



Experimental study of the tonal trailing-edge noise generated by low-reynolds number airfoils and comparison with numerical simulations

Gyuzel Yakhina

► To cite this version:

Gyuzel Yakhina. Experimental study of the tonal trailing-edge noise generated by low-reynolds number airfoils and comparison with numerical simulations. Other. Université de Lyon, 2017. English. NNT : 2017LYSEC008 . tel-01625208

HAL Id: tel-01625208

<https://theses.hal.science/tel-01625208>

Submitted on 27 Oct 2017

HAL is a multi-disciplinary open access archive for the deposit and dissemination of scientific research documents, whether they are published or not. The documents may come from teaching and research institutions in France or abroad, or from public or private research centers.

L'archive ouverte pluridisciplinaire **HAL**, est destinée au dépôt et à la diffusion de documents scientifiques de niveau recherche, publiés ou non, émanant des établissements d'enseignement et de recherche français ou étrangers, des laboratoires publics ou privés.



ÉCOLE
CENTRALE LYON

N° d'ordre NNT: 2017LYSEC08

Année 2017

THÈSE de DOCTORAT DE L'UNIVERSITÉ DE LYON
opérée au sein de l'École Centrale de Lyon

École Doctorale N° 162
Mécanique, Énergétique, Génie civil, Acoustique

Spécialité de Doctorat : Acoustique

Soutenue publiquement le 31/01/2017, par :

Gyuzel YAKHINA

Experimental Study of the Tonal Trailing-Edge Noise Generated by Low-Reynolds Number Airfoils and Comparison with Numerical Simulations

JURY

Pr.	GERVAIS	Yves	Université de Poitiers	Rapporteur
Pr.	GOLUBEV	Vladimir	Embry-Riddle Aeronautical University	Co-directeur de thèse
Pr.	MANKBADI	Reda	Embry-Riddle Aeronautical University	Rapporteur
Pr.	MOREAU	Stéphane	Université de Sherbrooke	Président du jury
Pr.	ROGER	Michel	École Centrale de Lyon	Directeur de thèse

Laboratoire de Mécanique des Fluides et d'Acoustique, UMR CNRS 5509
École Centrale de Lyon

Contents

Contents	I
List of Figures	V
List of Tables	XIII
Introduction	1
1 Theoretical Background of the Trailing-Edge Tonal Noise	7
1.1 Airfoil Self-Noise Mechanisms	8
1.2 Previous Experimental Investigations of the Trailing-Edge Tonal Noise	9
1.3 Aeroacoustic Feedback Loop Model	14
1.4 Role of the Separation Bubble	16
1.5 Concluding Remarks	19
2 Experimental Setup and Instrumentation	21
2.1 Setup Description and Instrumentation	22
2.2 Wind Tunnel Correction and Effective Angle of Attack.	25
2.3 Acoustic measurements	26
2.3.1 Remote Microphone Probes	26
2.3.2 Analytical Determination of the Transfer Function	27
2.3.3 In-Situ Calibration Procedure	32
2.3.4 Background-Noise Correction of Wall-Pressure Spectra	35
2.3.5 Effect of Wind-Tunnel Jet Shear Layers	36
2.4 Pressure Coefficient Measurements	37
2.5 Hot-Wire Anemometry	38

2.6	Flow Visualization	40
2.7	General Methods for Data Analysis	41
2.7.1	Cross-Spectral Analyses	41
2.7.2	Time-Frequency Analysis	42
2.7.3	Bicoherence Analysis	43
2.8	Uncertainty Assessment	44
2.9	Concluding Remarks	46
3	Experimental Results for the NACA-0012 airfoil	47
3.1	Ranges of Parameters of the Tonal Noise	48
3.2	Pressure Coefficient Measurements	50
3.3	Directivity Measurements	51
3.4	Far-field Acoustic Signature	55
3.4.1	Ladder-Type Structure	56
3.4.2	Influence of the Tripping Device	59
3.4.3	Influence of the Angle of Attack	60
3.4.4	Influence of the Chord Length	63
3.4.5	Influence of the Upstream Turbulence	63
3.4.6	Tracing of the Dominant Tone	67
3.5	Role of the Separation Bubble in Trailing-Edge Noise	68
3.5.1	Influence of Flow Velocity and Angle of Attack	68
3.5.2	Influence of the Upstream Turbulence on the Location of the Separation Bubble	73
3.5.3	Influence of the Separation Bubble on the PSD of the RMPs	74
3.5.4	Comparison with the Results of Previous Investigators . . .	76
3.6	Cross-Spectrum Analysis	78
3.6.1	Chordwise Analysis	78
3.6.2	Spanwise Correlation Length	82
3.7	Time-Frequency Analysis	84
3.8	Bicoherence of the Far-Field Microphone Signal	87
3.9	Concluding Remarks	90
4	Comparison with the ERAU Numerical Simulations. NACA- 0012 airfoil	95
4.1	Remarks about the Numerical Model	96
4.2	Comparison of Numerical and Experimental Data	97
4.3	Concluding Remarks	102
5	Analytical Modeling of the Tonal Noise Radiation	103
5.1	Theoretical Background	104
5.2	Convection Speed	106

5.3	Near-Field and Far-Field Pressures	108
5.4	Tone Level Prediction	110
5.5	Concluding Remarks	112
6	Experimental Results for the SD7003 Airfoil	115
6.1	Localization of the Noise Sources	116
6.2	Ranges of Parameters of the Tonal Noise	117
6.3	Pressure Coefficient	119
6.4	Far-Field Noise Signature	120
6.4.1	Influence of the Angle of Attack	120
6.4.2	Influence of Tripping	122
6.5	Location of the Separation Bubble for the SD7003 Airfoil	124
6.5.1	Influence of the Separation Bubble on the PSD of the RMPs	129
6.6	Comparison of Hot-Wire Velocity Spectra with Far-Field Acoustic Spectrum	130
6.7	Cross-Spectrum Analysis	131
6.7.1	Chordwise Analysis	131
6.8	Time-Frequency Analysis	134
6.9	Bicoherence of the Far-Field Microphone Signal	136
6.10	Concluding Remarks	138
7	Compared Numerical Simulations and Experimental Results for the SD7003 Airfoil	141
7.1	Numerical Simulation in ERAU	142
7.2	Numerical Simulation in OpenFOAM	145
	Conclusion	151
A	Tables of the Parameters of Experimental Investigation	155
B	Complementary Experimental Results for the NACA-0012 Airfoil	159
C	Complementary Experimental Results for the SD7003 Airfoil	165
D	Numerical Simulation with OpenFOAM	169
D.1	Geometrical Model	169
D.2	Mathematical Model	171
D.2.1	Governing Equations	171
D.2.2	Turbulence Model	172
D.3	Numerical Model	175
D.3.1	Computational Mesh	176
D.3.2	Boundary Conditions	179

D.3.3 Discretization Schemes	183
Bibliography	185

List of Figures

1.1	Effect of velocity on far-field vortex shedding tone frequencies, NACA-0012 full-span airfoil [1].	10
1.2	Typical noise spectrum of the NACA-0012 airfoil with 8 cm chord length at 20.2 m/s [2].	10
1.3	Reynolds number versus angles of attack plot for the NACA-0012 airfoil with bounds of the tonal and non-tonal areas from [3, 4]. Lowson <i>et al.</i> [3] (diamonds), Arcondoulis <i>et al.</i> [4](circles), Paterson <i>et al.</i> [1] (triangles). Solid markers represent tonal noise regimes, whereas empty markers represent non-tonal regimes. The tonal envelope and the maximum tonal amplitude were estimated by Lowson <i>et al.</i> [3].	12
1.4	Scheme of the feedback loop proposed by Tam [5].	14
1.5	Scheme of the feedback loop proposed by Longhouse [6].	15
1.6	Prediction of boundary layer separation at $\alpha^* = 0^\circ(\circ)$, $\alpha^* = 1.4^\circ(\square)$, $\alpha^* = 4.2^\circ(\nabla)$ and reattachment at $\alpha^* = 0^\circ(\times)$, $\alpha^* = 0^\circ(+)$. The locations are defined as fractions of the chord, x/c at the pressure surface of the NACA-0012 airfoil [7].	18
2.1	Grids producing upstream turbulence	23
2.2	Compared cross-sections of the NACA-0012 airfoil and of the SD7003 airfoil.	23
2.3	Photos and scheme of the experimental setup in ECL	24
2.4	Pin-hole locations and probe labels (red) of the wall-pressure RMP on the NACA-0012 mock-up. Relative position of the tripping device on the door side indicated as the black strip in subplot (a).	28
2.5	Pin-hole locations and probe labels (red) of the wall-pressure RMP on the SD7003 mock-up.	28

2.6	Sketch of the RMP.	29
2.7	Attenuation spectra as measured by the two-step calibration procedure (23 red plots), and as predicted by the analytical model. Sensitivity ratios are not taken into account. (a) - for the NACA-0012 airfoil, (b) - for the SD7003 airfoil.	33
2.8	Capillary-microphone junction acting as a Helmholtz resonator - Corrected probe model.	34
2.9	Typical wall-pressure spectra	36
2.10	PSD plots for far-field microphone. NACA-0012 airfoil at zero angle of attack and (a) - at 16 m/s, (b)- at 25 m/s. Red line - clean airfoil, blue line - test with a splitter plate.	37
2.11	Experimental setup for HWA	39
2.12	An example of the calibration curve.	40
3.1	Reynolds-number versus effective angle of attack chart for tonal noise of the NACA-0012 airfoil. (a) - present experiment, (b) - comparison with previous investigations[8, 4].	49
3.2	Pressure coefficient distribution for the NACA-0012 airfoil at 25 m/s with chord lengths 10 cm (\bullet for $\alpha = 0^\circ$, \circ for $\alpha = 5^\circ$) and 12 cm (\blacktriangle for $\alpha = 0^\circ$, \triangle for $\alpha = 5^\circ$). Configuration A.	50
3.3	Measured and computed pressure coefficients for the NACA-0012 airfoil of 12 cm chord length. ($-$ - XFoil simulation at $\alpha^* = 1.75^\circ$; \circ - experimental data at $\alpha = 5^\circ$)	51
3.4	Results of the directivity measurements for the NACA-0012 airfoil at 19 m/s and zero angle of attack. (a) angle-frequency radiation map; (b) directivity diagram of the main tones. Configuration A.	53
3.5	(a) angle-frequency radiation map for the NACA-0012 airfoil at zero angle of attack and at 16 m/s. Black line show the angle for which a PSD plot (b) was done. Configuration A.	53
3.6	Angle-frequency radiation maps for the NACA-0012 airfoil at zero angle of attack: (a) at 8 m/s; (b) at 25 m/s. Configuration A.	54
3.7	Angle-frequency radiation maps for the NACA-0012 airfoil at 5° and : (a) at 19 m/s; (b) at 30 m/s. Configuration A.	54
3.8	Angle-frequency radiation maps for the NACA-0012 airfoil at zero angle of attack and : (a) at 16 m/s; (b) at 19 m/s. Configuration B.	54
3.9	Frequency-flow speed chart of LBL-wave radiation for the NACA-0012 airfoil at zero angle of attack. Configurations A.	55
3.10	Noise spectra for the NACA-0012 airfoil in configuration A and at zero angle of attack.	57

3.11	Frequency-flow speed charts of LBL-wave radiation for NACA-0012 airfoil at zero angle of attack. (a) - Comparison of the power spectra density of configurations A,B,C at different speeds; (b) - Configuration B; (c) - Configuration C.	58
3.12	Frequency-flow speed chart for the NACA-0012 airfoil at 5° and the comparison of PSD plots for cases at 5° and 0°	61
3.13	Frequency-flow speed chart and PSD plot for the NACA-0012 airfoil with chord length 8 cm and 10 cm at zero angle of attack.	62
3.14	Frequency-flow speed chart for the NACA-0012 airfoil at zero angle of attack with small-scale turbulence and far-field sound spectra at configurations A and D. Flow speed 8 m/s.	64
3.15	Streamwise velocity spectra of the residual turbulence (black), and of the turbulence generated by the fine-mesh grid (red). 25 m/s.	65
3.16	Sound pressure level of the main tones as a function of flow velocity in configurations A (no tripping), B (tripping on the door side) and C (tripping on the wall side). The NACA-0012 airfoil at $\alpha = 0^\circ$ (a) and $\alpha = 5^\circ$ (b).	66
3.17	Sound pressure level of the main tones as a function of flow velocity. Comparison of the NACA-0012 airfoil at $\alpha^* = 0^\circ$ (a) and $\alpha^* = 1.75^\circ$ (b) with the results of Chong <i>et al.</i> [7]. Configuration A.	66
3.18	Example of flow visualization (a) and HWA results (b) for the NACA-0012 airfoil at $\alpha = 0^\circ$ and 19 m/s ($Re = 1.5 \times 10^5$). Tonal noise configuration.	69
3.19	Flow visualization for the NACA-0012 airfoil at $\alpha = 0^\circ$ and 33 m/s.	69
3.20	Results of near-wake measurements performed from the “door side” at the distance of 1.5 mm for the NACA-0012 airfoil at 19 m/s and zero angle of attack.	71
3.21	Flow visualizations for the NACA-0012 airfoil at 19 m/s ($Re = 1.5 \times 10^5$) and $\alpha = 5^\circ$ (pressure side). (a) - test with clean airfoil; (b) - test with the upstream small-scale turbulence.	73
3.22	The NACA-0012 airfoil at 19 m/s and zero angle of attack: (a) - location of the separation bubble; (b) - PSD plots for wall pressure probes and far-field microphone; (c) - chordwise coherence plots for doublets of wall pressure probes. Dotted lines mark tones.	75
3.23	Comparison of the mean (left) and rms (right) velocities measured by HWA ($-\circ-$ - test 1, $-\square-$ - test 2, $-\square-$ -shifted test 2) on the pressure (a) and the suction (b) sides with PIV data of Pröbsting ($- * -$). NACA-0012 airfoil.	77
3.24	Phase of cross-spectra of RMP №9 and №10 for the NACA-0012 airfoil at $\alpha = 0^\circ$ and $U_\infty = 25$ m/s. Configuration A.	80

3.25	Chordwise variations of PSD, coherence and phase of cross-spectra of RMP pairs for the NACA-0012 airfoil at $\alpha = 0^\circ$ and $U_\infty = 25 \text{ m/s}$. Configuration A.	81
3.26	Coherence surface for LBL wave radiation with and without acoustic feedback. NACA-0012 airfoil at $U_\infty = 16 \text{ m/s}$ and zero angle of attack. Door side.	83
3.27	Time signal (a) and its zoom (b) for the NACA-0012 airfoil at $U_\infty = 16 \text{ m/s}$ and zero angle of attack. Spanwise set of probes B (door side).	83
3.28	Time-frequency analysis for the NACA-0012 airfoil at 0° angle of attack. No tripping. Right plots: averaged far-field spectra. Case a: two averaged spectra for the two states of the switching regime.	86
3.29	Bicoherence of the far-field microphone (a) and zoomed part of the plot (b); (c) - PSD plot without calibration coefficient. NACA-0012 airfoil at 11 m/s and zero angle of attack.	88
3.30	Bicoherence of the far-field microphone (a) and zoomed part of the plot (b); (c) - PSD plot without calibration coefficient. NACA-0012 airfoil at 16 m/s and zero angle of attack.	89
3.31	Bicoherence of the far-field microphone (a) and zoomed part of the plot (b); (c) - PSD plot without calibration coefficient. NACA-0012 airfoil at 21 m/s and zero angle of attack.	89
3.32	The NACA-0012 airfoil at zero angle of attack. Configurations A, B and C. Noise signature contours marked by black solid, dashed and dotted lines, tonal noise regimes marked by colored lines and location of the separation bubble from the leading edge corresponding to some of regimes. 8 speeds are marked: 1 - 8 m/s ($Re_c = 0.63 \times 10^5$); 2 - 11 m/s ($Re_c = 0.87 \times 10^5$); 3 - 16 m/s ($Re_c = 1.26 \times 10^5$); 4 - 19 m/s ($Re_c = 1.5 \times 10^5$); 5 - 21 m/s ($Re_c = 1.6 \times 10^5$); 6 - 25 m/s ($Re_c = 2 \times 10^5$); 7 - 30 m/s ($Re_c = 2.4 \times 10^5$); 8 - 33 m/s ($Re_c = 2.6 \times 10^5$).	92
3.33	The NACA-0012 airfoil at 5° . Configurations A, B and C. Noise signature contours marked by black solid, dashed and dotted lines, tonal noise regimes marked by colored lines and location of the separation bubble from the leading edge corresponding to some of regimes. 8 speeds are marked: 1 - 8 m/s ($Re_c = 0.63 \times 10^5$); 2 - 11 m/s ($Re_c = 0.87 \times 10^5$); 3 - 16 m/s ($Re_c = 1.26 \times 10^5$); 4 - 19 m/s ($Re_c = 1.5 \times 10^5$); 5 - 21 m/s ($Re_c = 1.6 \times 10^5$); 6 - 25 m/s ($Re_c = 2 \times 10^5$); 7 - 30 m/s ($Re_c = 2.4 \times 10^5$); 8 - 33 m/s ($Re_c = 2.6 \times 10^5$).	93
4.1	Pressure coefficient distribution for the NACA-0012 airfoil at 16 m/s and $\alpha = 0^\circ$. Numerical simulation in freestream.	97

4.2	Comparison of the velocity spectra of NACA-0012 airfoil. (a) - mean velocity; (b) - rms velocity. — — — measurements; — — — numerical simulation.	98
4.3	(a) - instability amplification of the main tonal peak along the chord; (b) - velocity contours; (c) - friction coefficient. NACA-0012 airfoil at $\alpha^* = 0^\circ$ and $U_\infty = 25 \text{ m/s}$ ($Re = 1.8 \times 10^5$) [9].	100
4.4	Comparison of the separation bubble localization between experimental and numerical results.	101
5.1	Phase distribution of the cross-spectrum between the sensor 18 and the far-field microphone for the NACA-0012 airfoil at $U_\infty = 30 \text{ m/s}$ and $\alpha = 0^\circ$. Configuration A.	106
5.2	(a) Phase distribution of the cross-spectrum between sensors 20 and 23 for the NACA-0012 airfoil at $U_\infty = 30 \text{ m/s}$ and $\alpha = 0^\circ$. (b) PSD level of the RMPs №20 and №23. Configuration A.	107
5.3	(a): typical three-dimensional coherence plot versus frequency and separation η for the door-side spanwise-distributed set of RMPs on the NACA-0012 airfoil. The dashed line follows the dominant tone frequency. (b): Estimation of the acoustic wall-pressure distribution from the far-field pressure, according to Amiet's model.	109
5.4	Analytical predictions of the tonal noise. NACA-0012 airfoil. (a)- 16 m/s; (b)- 25 m/s. Upper and lower symbols pointed by arrows correspond to extreme values of the convection speed (0.29 to $0.7 U_0$).	111
6.1	Localization of the noise source for the main tone. SD7003 airfoil at 30 m/s and 3° . 1D antenna. The source map results from repeated color line.	116
6.2	Localization of the noise source for the harmonic tone. SD7003 airfoil at 30 m/s and 3° . 1D antenna. The source map results from repeated color line.	117
6.3	Reynolds-number versus geometrical angle of attack chart for the SD7003 airfoil.	118
6.4	Frequency versus geometrical angle of attack chart for the SD7003 airfoil.	118
6.5	Pressure-coefficient distributions. (a) - measured with the SD7003 airfoil of 12 cm chord length at different angles of attack. $Re_c = 12 \times 10^4$. (b) - experiment versus numerical simulation [10].	120
6.6	Frequency-flow speed charts of LBL-wave radiation for the SD7003 airfoil. Configuration A.	121
6.7	Frequency-flow speed charts of LBL-wave radiation for the SD7003 airfoil. Configurations B and C.	123

6.8	Far-field microphone measurements with tripping device. (a): sound pressure level of the main tones versus flow velocity. (b): PSD at several flow velocities (with vertical shifts by 50 dB). Configurations A, B and C. SD7003 airfoil at $\alpha = 2^\circ$	123
6.9	Flow visualization and HWA results for the suction side of the SD7003 airfoil at $\alpha = 2^\circ$ and 19 m/s.	125
6.10	HWA results on the pressure side of the SD7003 airfoil at $\alpha = 2^\circ$ and $U_\infty = 19$ m/s.	126
6.11	Flow visualization for the suction side of the SD7003 airfoil at $\alpha = 2^\circ$ and 25 m/s.	126
6.12	Flow visualization and HWA results for the suction side of the SD7003 airfoil at $\alpha = 5^\circ$ and 19 m/s.	127
6.13	Results of near-wake measurements along the pressure side at the distance of 1.5 mm for the SD7003 airfoil at 19 m/s and $\alpha = 2^\circ$	127
6.14	SD7003 airfoil at 19 m/s and 2° : (a) - location of the separation bubble; (b) - PSD plots for wall pressure probes and far-field microphone; (c) - coherence plots for wall pressure probes. Vertical dotted lines mark the dominant tones.	129
6.15	Hot-wire velocity spectra (dB, ref.1 m/s) for the SD7003 airfoil at the angle of attack of 2° and 19 m/s. (a) - locations of the HWA probe during the measurements; (b) - pressure side; (c) - suction side. Far-field acoustic spectrum shown for comparison (rel.dB).	130
6.16	Chordwise dynamic of PSD, coherence and phase of cross-spectrum of RMPs pairs on the suction side for the SD7003 airfoil at $\alpha = 2^\circ$ and $U_\infty = 25$ m/s.	132
6.17	Chordwise dynamic of PSD, coherence and phase of cross-spectrum of RMPs pairs on the pressure side for the SD7003 airfoil at $\alpha = 2^\circ$ and $U_\infty = 25$ m/s.	133
6.18	Time-frequency analysis for the SD7003 airfoil at 0° angle of attack. No tripping. Right plots: averaged spectra (black); filtered spectra (blue and red) for the switching regime, shifted by steps of 20 dB for clarity.	135
6.19	Bicoherence of the far-field microphone (a) and zoomed part of the plot (b); (c) - PSD plot without correction. SD7003 airfoil at 16 m/s and zero angle of attack. Filtered frequency equals 326 Hz.	136
6.20	Bicoherence of the far-field microphone (a) and zoomed part of the plot (b); (c) - PSD plot without correction. SD7003 airfoil at 16 m/s and zero angle of attack. Filtered frequency equals 371 Hz.	137
6.21	Bicoherence of the far-field microphone (a) and zoomed part of the plot (b); (c) - PSD plot without correction. SD7003 airfoil at 19 m/s and zero angle of attack.	137

6.22	Bicoherence of the far-field microphone (a) and zoomed part of the plot (b); (c) - PSD plot without correction. SD7003 airfoil at 25 m/s and zero angle of attack.	138
6.23	The SD7003 airfoil at 2° angle of attack. Configurations A, B and C. Noise signature contours marked by black solid, dashed and dotted lines, tonal noise regimes marked by colored lines and location of the separation bubble from the leading edge corresponding to some of regimes. 8 speeds are marked: 1 - 8 m/s ($Re_c = 0.63 \times 10^5$); 2 - 11 m/s ($Re_c = 0.87 \times 10^5$); 3 - 16 m/s ($Re_c = 1.26 \times 10^5$); 4 - 19 m/s ($Re_c = 1.5 \times 10^5$); 5 - 21 m/s ($Re_c = 1.6 \times 10^5$); 6 - 25 m/s ($Re_c = 2 \times 10^5$); 7 - 30 m/s ($Re_c = 2.4 \times 10^5$); 8 - 33 m/s ($Re_c = 2.6 \times 10^5$).140	
7.1	Comparison of the experimental and numerical results. ERAU (3D model in freestream at $\alpha^* = 0^\circ$) for the SD7003 airfoil at $U_\infty = 16$ m/s and $\alpha = 2^\circ$. (a) - pressure coefficient; (b) - skin friction coefficient. . . .	142
7.2	Comparison of the measured pressure coefficient at $\alpha = 2^\circ$ with numerical simulation in uniform freestream at $\alpha^* = 0^\circ$ as conducted at ERAU and when using OpenFOAM.	143
7.3	Time-average U-velocity (streamwise) contours: (a) 3D uniform ($\alpha = 0^\circ$) and (b) 2D freejet conditions ($\alpha = 2^\circ$) for the SD7003 airfoil at $U_\infty = 16$ m/s. ERAU simulations.	144
7.4	Comparison of computed velocity profiles with measured ones for the SD7003 airfoil at $U_\infty = 16$ m/s on the suction side. (a) - mean velocity, (b) - rms-velocity. — - numerical simulation ERAU at $\alpha^* = 0^\circ$ (uniform flow, 3D model) , - - - - experimental data.	144
7.5	Comparison of the experimental and numerical results for the SD7003 airfoil at $\alpha = 2^\circ$ and 16 m/s. (a) - pressure coefficient distribution; (b) - skin friction coefficient.	145
7.6	Comparison of mean velocity profiles for the SD7003 airfoil at $\alpha = +2^\circ$: ● - ECL experiment; — - OpenFOAM freestream; — - OpenFOAM open-jet case.	147
7.7	(a) - comparison of the experimental and numerical pressure coefficient distribution for the SD7003 airfoil at $\alpha = 5^\circ$ and 16 m/s. (b) - computed skin friction coefficient.	148
7.8	Mean streamwise velocity distribution for (a) freestream $\alpha^* = 1^\circ$ and (b) open-jet $\alpha = 5^\circ$ models.	148
7.9	Comparison of the experimental and numerical (only freestream model) results for the SD7003 airfoil at $\alpha = 7^\circ$ and 16 m/s. (a) - pressure coefficient distribution; (b) - skin friction coefficient.	149
7.10	Turbulent kinetic energy at $\alpha = +5^\circ$ in the open-jet model.	149

7.11	Mean pressure distribution around the airfoil for freestream $\alpha = +1^\circ$ (left) and open-jet $\alpha = +5^\circ$ (right) models.	150
7.12	Illustration of the trailing-edge tonal noise.	154
B.1	The NACA-0012 airfoil at 25 m/s and zero angle of attack: (a) - location of the separation bubble; (b) - PSD plots for wall pressure probes and far-field microphone; (c) - chordwise coherence plots for doublets of wall pressure probes. Dotted lines mark tones.	160
B.2	The NACA-0012 airfoil at 33 m/s and zero angle of attack: (a) - location of the separation bubble; (b) - PSD plots for wall pressure probes and far-field microphone; (c) - chordwise coherence plots for doublets of wall pressure probes. Dotted lines mark tones.	161
B.3	Chordwise dynamic of PSD, coherence and phase of cross-spectrum of RMPs pairs for the NACA-0012 airfoil at $\alpha = 0^\circ$ and $U_\infty = 16$ m/s. . .	162
B.4	Chordwise dynamic of PSD, coherence and phase of cross-spectrum of RMPs pairs on the suction side for the NACA-0012 airfoil at $\alpha = -5^\circ$ and $U_\infty = 25$ m/s.	163
C.1	PSD of the far-field microphone for the SD7003 airfoil. Configuration A at various flow velocities.	166
C.2	Flow visualization and HWA results for the pressure side of the SD7003 airfoil at $\alpha = 5^\circ$ and 19 m/s.	167
D.1	View of the computational domain in the first configuration.	170
D.2	View of the computational domain in the second configuration.	170
D.3	(a) Computational mesh for the freestream case. Mesh views of the freestream case: (b) around the airfoil, (c) zoom around the trailing edge.	177
D.4	(a) Computational mesh for the configuration with nozzle. Mesh views of the nozzle-flow case: (b) Mesh around the airfoil, (c) Mesh around the trailing edge.	178
D.5	Domain boundaries for the freestream case.	180
D.6	Domain boundaries for the nozzle case.	181

List of Tables

1.1	Parameters of reported experimental investigations of the trailing edge tonal noise for the NACA-0012 airfoil. c - chord length; H - span length; Re_c - chord-based Reynolds number; α - geometrical angle of attack; α^* - effective angle of attack.	13
3.1	Separation areas. Illustrative table for the NACA-0012 airfoil.	72
3.2	Compared extensions of the separation areas for the NACA-0012 airfoil with and without upstream grid. Percentage of chord.	74
5.1	Tone levels as predicted with analytical modeling (AM) and measured in the far-field (FF). NACA-0012 airfoil at 16 m/s and zero angle of attack. Probe numbers, related source levels (PSD) and convection speed are indicated.	113
5.2	Tone levels as predicted with analytical modeling (AM) and measured in the far-field (FF). NACA-0012 airfoil at 25 m/s and zero angle of attack. Probe numbers, related source levels (PSD) and convection speed are indicated.	113
6.1	Separation areas. Illustrative table for the SD7003 airfoil.	128
7.1	Illustrative table of the correspondence between freestream and open-jet condition angles of attack.	150
A.1	Flow speed range	156
A.2	Conducted measurements for the NACA-0012 airfoil	157
A.3	Conducted measurements for the SD7003 airfoil	158
D.1	Summary of the OpenFOAM computational cases.	179

D.2	The general conditions for the ECL experiment.	180
D.3	Boundary condition types for the freestream case.	181
D.4	Boundary condition types for the case with nozzle (for Inlet/Outlet the influx value is showed).	182

Nomenclature

α	geometrical angle of attack
α^*	effective angle of attack
ν	kinematic viscosity of air
ω	angular frequency
ρ_0	density
c	chord length
c_0	speed of sound
C_p	pressure coefficient
f_n	frequencies of discrete tones
f_s	tonal central frequency
$f_{n_{max}}$	frequencies of the strongest tone
H	hieght of the nozzle (equal to the span wise length of the airfoil)
k	wave number
L	distance between the maximum velocity point and the trailing edge of the airfoil
n	number of the tones
p_{rms}	root mean square sound pressure

Re	Reynolds number
Re_c	chord-based Reynolds number
U_∞	flow velocity
U_c	convection velocity
u_{rms}	root mean square velocity

Acknowledgments

This work was started in November 2013 as a collaboration project between Ecole Centrale de Lyon (ECL) and Embry-Riddle Aeronautical University (ERAU). I acknowledge the Air Force Office of Scientific Research (Award Number FA9550-12-1-0126, Program Manager Dr. D. Smith) for supporting it.

I am very grateful to my advisers Pr. Michel Roger and Pr. Vladimir V. Golubev for the exceptional opportunity to take part in the investigating project. I thank Michel Roger for his guidance and explanations, his support and patience during all this time. I appreciate his encouragements and advices. Vladimir Golubev despite of being quite far away motivated me by his questions to find possible explanations of the observed results.

For this dissertation I want to thank my committee members, Pr. Reda Mankbadi from ERAU, Pr. Yves Gervais from Université de Poitiers and Pr. Stéphane Moreau from Université de Sherbrooke for their time, important comments and insightful questions, which allowed to improve the manuscript.

All our measurements would not have been possible without Emmanuel Jondeau, who helped me to install the instrumentation for the experiments and carefully explained all the details. I also would like to thank Pascal Souchotte, Pierre Roland and Jean-Michel Perrin, who helped me during experimental campaigns.

I thank my college Lap Nguyen from ERAU who was responsible for the numerical simulation of the tonal noise phenomenon. Our fruitful discussions of the results allowed me to improve the understanding of the mechanisms.

I am grateful to my friends and colleagues who made this time enjoyable and unforgettable. I would like to thank Simon Bouley and Miguel Pestana for great music, a lot of laugh and squash. I also thank Nassim Jaouani who always was an example of highly motivated work. I am thankful to Romain Gojon for his nice sense of humor and his tennis partnership. I would like to thank Justine Giez for our tea breaks and long conversations, for her care and support. All these people helped me not to feel myself alone in the foreign country.

Special thanks to Pavel Kholodov who provided numerical simulations in Open-FOAM, which was very useful for determination of some parameters, and who is besides of that my husband. It is hard to express by words how meaningful was his support for me. He showed me that I can manage a lot of difficulties, even if it was hard to believe for myself.

I am grateful to my family: my grandparents and my parents for their care and love. I spent all possible holidays with them. And this time arose motivation to work harder and confidence that I was doing right things.

Résumé

Le bruit tonal rayonné au bord de fuite des profils à faible nombre de Reynolds est un phénomène observé sur les ailes de drones ou micro-drones qui sont utilisés partout dans la vie quotidienne. La diminution de ce bruit va augmenter la survivabilité et l'efficacité des appareils dans le domaine militaire. De plus, cela va augmenter le champ des applications civiles et minimiser la pollution par le bruit. La réduction efficace du bruit est indispensable et, par conséquent, une compréhension complète du processus de rayonnement du bruit tonal du profil est nécessaire. Malgré le fait que des essais dédiés aient été réalisés depuis les années 70, il reste beaucoup de détails à expliquer.

Le travail présenté est dédié à une étude expérimentale et analytique du bruit tonal. C'est une partie de collaboration entre l'École Centrale de Lyon et Embry-Riddle Aeronautical University. Le but est de réaliser une caractérisation exhaustive des paramètres acoustiques et aérodynamiques du bruit tonal de bord de fuite d'un profil et de produire une base de données qui pourra être utilisée pour valider les simulations numériques réalisées dans le futur.

Le profil symétrique NACA-0012 ainsi que le profil asymétrique SD7003 ont été testés pour une série d'angles d'incidence (de -10° à 10°) dans la soufflerie anéchoïque à jet ouvert de l'École Centrale de Lyon pour des nombres de Reynolds modérés ($0.6 \times 10^5 < Re_c < 2.6 \times 10^5$). Les mesures de pression aux parois et de pression acoustique en champ lointain pour différentes configurations ont permis d'observer une structure en escalier de la signature du bruit, de déterminer quel face du profil a produit le bruit et de distinguer le rôle de la boucle de

rétroaction. Des techniques supplémentaires de post-traitement comme l'analyse temps-fréquence ont montré l'existence de plusieurs régimes (un régime de commutation entre deux états, un régime d'une seule fréquence et un régime à plusieurs fréquences) de l'émission de bruit. L'analyse de bi-cohérence a montré qu'il y a des couplages nonlinéaires entre les fréquences.

Une étude par l'anémométrie à fil chaud et par des techniques de visualisation de l'écoulement a montré que la formation d'une bulle de décollement est une condition nécessaire mais pas suffisante pour la génération du bruit. De plus, la localisation de la bulle est aussi importante et elle doit être suffisamment proche du bord de fuite. En outre, l'analyse de stabilité linéaire des résultats de simulations numériques a montré que des ondes de Tollmien-Schlichting sont transformées en ondes de Kelvin-Helmholtz dans la zone du décollement.

Une prédiction analytique de l'amplitude des fréquences pures émises dans le champ lointain a été effectuée sur la base du modèle d'Amiet en supposant que le champ de pression pariétal est bidimensionnel. Les mesures de pression proches du bord de fuite du profil ont été prises comme données d'entrée. Les amplitudes prédites sont globalement en accord avec les mesures acoustiques.

Après l'analyse de tous les résultats la description suivante du processus de rayonnement de sons purs peut être proposée. Les ondes de Tollmien-Schlichting qui se développent initialement dans la couche limite se transforment en ondes de Kelvin-Helmholtz le long de la couche de cisaillement de la bulle de décollement. Au bord de fuite du profil elles sont converties en ondes acoustiques qui forment un couplage fort avec les instabilités de couche limite plus en amont de l'écoulement, pilotant elles-mêmes le déclenchement de ces instabilités.

Mots clés: aéroacoustique, profils d'aile, bruit tonal de bord de fuite, mesures en soufflerie, ondes de Tollmien-Schlichting, ondes de Kelvin-Helmholtz.

Abstract

The tonal trailing-edge noise generated by transitional airfoils is a topic of interest because of its wide area of applications. One of them is the Unmanned Air Vehicles operated at low Reynolds numbers which are widely used in our everyday life and have a lot of perspectives in future. The tonal noise reduction will increase the survivability and effectiveness of the devices in military field. Moreover it will enlarge the range of civil use and minimize noise pollution. The effective noise reduction is needed and therefore the complete understanding of the tonal noise generation process is necessary. Despite the fact that investigation of the trailing-edge noise was started since the seventies there are still a lot of details which should be explained.

The present work is dedicated to the experimental and analytical investigation of the tonal noise and is a part of the collaboration project between Ecole Centrale de Lyon and Embry-Riddle Aerospace University. The aim is to conduct an exhaustive experimental characterization of the acoustic and aerodynamic parameters of the trailing-edge noise and to produce a data base which can be used for further numerical simulations conducted at Embry-Riddle Aerospace University.

A symmetric NACA-0012 airfoil and a slightly cambered SD7003 airfoil at moderate angles of attack (varied from -10° to 10°) were tested in an open-jet anechoic wind tunnel of Ecole Centrale de Lyon at moderate Reynolds numbers ($0.6 \times 10^5 < Re_c < 2.6 \times 10^5$). Measurements of the wall pressure and far-field acoustic pressure in different configurations allowed to observe the ladder-type structure of the noise signature, to determine which side produced tones and to

distinguish the role of the acoustic feedback loop. Additional post-processing techniques such as time-frequency analysis showed the existence of several regimes (switching regime between two tones, one-tone regime and multiple-tones regime) of noise emission. The bicoherence analysis showed that there are non-linear relationships between tones.

The investigation of the role of the separation area by hot-wire anemometry and flow visualization techniques showed that the separation bubble is a necessary but not a sufficient condition for the noise generation. Moreover the location of the bubble is also important and should be close enough to the trailing edge. Furthermore the linear stability analysis of accompanying numerical simulation results showed that the Tollmien-Schlichting waves transform to the Kelvin-Helmholtz waves at the separation area. An analytical prediction of the tone levels in the far-field was done using Amiet's model based on the assumption of perfectly correlated sources along the span. The wall-pressure measurements close to the trailing edge were used as an input data. The comparisons of the predicted levels and measured ones showed a good agreement.

After analysis of all results the following description of the tonal noise mechanism is proposed. At some initial point of the airfoil the Tollmien-Schlichting instabilities start. They are traveling downstream and continued to Kelvin-Helmholtz waves along the shear-layer of the separation bubble. These waves reach the trailing edge, scatter from it as acoustic waves, which move upstream. The acoustic waves amplify the boundary layer instabilities at some frequencies for which the phases of both motions match and creates the feedback loop needed to sustain the process.

Keywords: aeroacoustics, airfoil, trailing-edge tonal noise, wind-tunnel measurements, Tollmien-Schlichting waves, Kelvin-Helmholtz waves.

Introduction

The airfoil self-noise caused by flow-acoustic interaction has been studied for more than 50 years because of its practical interest and of the variety of theoretical questions it induces. As airfoils are used in all spheres of human life the investigation of their noise is still of high importance. One component of the airfoil self-noise typical of rotors ore vehicles operated at low-Reynolds numbers is the trailing-edge noise. It is defined as a whistling or "singing" of the airfoil with one or several tones. Generally, trailing-edge noise is radiated by scattering of the boundary layer instabilities from the trailing edge coupled with a resonant feedback loop mechanism. This phenomenon has been observed in acoustic signatures of small aircraft, low-speed rotors, fans and wind-turbine blades.

The problem of the low-Reynolds number trailing-edge noise can be specifically attributed to the Micro Air Vehicles (MAVs) and Unmanned Air Vehicles (UAVs) or drones which operate in close proximity to people. Firstly, the military of the drones (reconnaissance, armed attack, etc) is limited by the radiated noise, which is easily detected. The main sources of the noise are the engine and the wings. As today electric motors can be used, the noise from the wing starts to play the main role. Therefore the trailing-edge noise reduction will increase the survivability and effectiveness of these vehicles. Secondly, above from the military context drones are widely used for civil goals (law enforcement, searching, and film making) and the low-noise performance would enlarge the range of possible missions and minimize the noise pollution.

Another field in which trailing-edge noise is a problem is the wind turbines,

which became widely used as a renewable source of energy. The enlargement of the wind energy farms in proximity to cities is limited partly because of the noise component.

Apriori the list cannot be extended to the trailing-edge noise radiated from aircraft wings during takeoff and landing, which is a problem for the airports located near the urban areas because the boundary layers are turbulent and lead to a broadband signature. But when testing small-scale mockups of wings in wind tunnels, the reduced Reynolds number corresponds to artificially laminar boundary layers; again tonal noise can be generated.

More and more stringent regulations in terms of noise pollution require an effective reduction of the trailing-edge noise. Therefore, a better understanding of the tonal noise mechanism and of the conditions of its generation is needed, in the continuation of a large number of experimental, numerical and theoretical studies. One of the first observations of the tonal trailing-edge noise was reported by Hersh & Hayden [11] as “[...] loud distinct tones” when they investigated the aerodynamic sound radiation from the NACA-0012 airfoil at low Reynolds numbers.

Paterson *et al.*[1] presented the first experimental study focused on the tonal noise radiated by the symmetric NACA airfoils used in helicopter rotors. They found that the noise signature can be described by the frequency dependence on the flow velocity and that it has a ladder-type structure of tones. Tam [5] explained the tonal staging by a feedback-loop mechanism. Later this idea was developed in the experimental work by Arbey & Bataille [2]. Moreover their results confirmed the observations of Paterson *et al.*[1]. A narrow range of discrete frequencies superimposed on a broader hump was found. The interpretation of this phenomenon was proposed by Longhouse [6], who attributed it to the Tollmien-Schlichting(T-S) instability waves developing in the boundary layer, scattering as a sound waves from the trailing edge and being amplified by the acoustic feedback-loop at some frequencies. However Lawson *et al.*[3] using experimental data concluded that the instability waves were not a sufficient condition for the tonal noise radiation. Some separation bubble on the pressure side of the airfoil was believed to play a key role in the process. Furthermore, the sound intensity was correlated with the length of the separation bubble. Later Nash *et al.*[12] in their serie of experiments on the NACA-0012 airfoil failed to observe the ladder-type structure of the determinant tone frequency in contrast to Paterson *et al.*[1] and Arbey & Bataille [2]. Their LDA measurements confirmed the theory of Lawson *et al.*[3] about the necessity of the separation bubble existence near the trailing edge for effective tonal noise radiation. Nevertheless, Arcondoulis *et al.*[4, 13] in an experimental research on

Introduction

the NACA-0012 airfoil observed behavior of the noise signature similar to [1, 2]. New experimental techniques allow to obtain more and more parameters of the process.

At the same time the analytical modeling of trailing-edge noise (more dedicated to broadband applications) was not behind the experimental research. The first analytical model proposed by Ffowcs Williams & Hall [14] was further completed with alternative formulations by Amiet [15] and Howe [16]. Howe [16], for example, points out three theories based on (1) Lighthill's acoustic analogy, (2) the solution of linearized hydroacoustic problems and (3) *ad hoc* aerodynamic source models. Roger & Moreau [17, 18, 19] proposed a back-scattering correction to Amiet's model and got a good agreement of their predictions with the alternative theories and with measurements. A special version of the theory can be used in the case of the tonal noise, as shown in this thesis.

Another possible way to explore the phenomenon is a numerical simulation. First numerical simulations (DNS) presented by Desquesnes *et al.*[20] showed that the tone frequency selected by the boundary layer is amplified by the separation bubble. The authors also assumed the existence of a second feedback loop on the suction side which also plays a role in the process. Sandberg & Jones in their works [21, 22] conducted DNS of the airfoil self-noise at low Reynolds numbers. In particular, the performed linear stability analysis points out that the most amplified instability wave frequency was higher than the measured tone frequency. Tam & Ju [23] also made a DNS study for the low Reynolds-number airfoil and observed only one tone, which coincides with the measurements of Nash *et al.*[12]. They attributed the multiple tones to a bad isolation of the airfoil, which remains a questionable explanation.

The present PhD work is one part of a collaboration project between the Embry-Riddle Aeronautical University (ERAU) and the Ecole Centrale de Lyon (ECL), aimed at investigating the tonal noise of the low-Reynolds number airfoils by experimental, theoretical and numerical means. The numerical simulation was done at the ERAU. ECL was in charge of for the experimental research and the analytical modeling. The aim of the present PhD thesis was to address and solve some controversial questions which remain open even after all the decades of investigation. For example, the role of the separation bubble and the influence of its parameters (size, location) on the tonal trailing-edge noise is not enough understood. Some details as the influence of the airfoil design or chordlength and of the upstream turbulence should be also clarified. The need was recognized to generate a complete database with various flow parameters, the relevance of which is confirmed by the comparison with selected reference results. It should be men-

tioned that the effect of a different airfoil design is also needs to be more deeply examined. Apart from a recent study by Padois *et al.*[24] the reported investigations are mostly dealing with the NACA-0012 airfoil. Therefore, a cambered SD7003 airfoil is tested as well as reference symmetric NACA-0012 airfoil. The created database was used for the verification of the numerical simulation provided by ERAU. Another issue is that the trailing-edge noise mechanism seems to be sensitive to the parameters of the experimental setup. This explains why two experimental investigations can have different results. This fact complicates the understanding of the tonal noise mechanism. It is believed that the combination of different investigation methods will increase its physical knowledge.

The thesis contains seven chapters. The first one describes the tonal noise phenomenon and reviews the previous researches on the subject. The tonal noise generation mechanism is explained in its main features. The analysis of the literature contributes to elucidate the unsolved questions which partly motivated this study.

The chapter 2 reports about the experimental setup, the measurement techniques and the post-processing methods used for the investigation of the tonal noise. The parameters of the installation and of the flow are described. In particular, the remote-microphone probes used for surface pressure measurements are discussed. The role of the separation bubble in the process is also investigated by flow visualization and hot-wire anemometry. Advanced post-processing by means of cross-spectral, bicoherence and time-frequency analyses is applied to get more detailed in formation.

The results of the experimental investigation on the symmetric NACA-0012 airfoil are discussed in the chapter 3. The limits of parameters such as the Reynolds numbers and angles of attack within which the tonal noise is heard during tests are compared with other researches. The acoustic signature is described. Its dependence on the presence of a tripping device, on the angle of attack, chord length and upstream turbulence is analyzed. Another important result of examination - the role of the separation areas in the tonal noise is discussed. The cross-spectrum analysis is used to give the coherence in the spanwise direction and provides some evidence of the acoustic or aerodynamic nature of the measured pressure. The bicoherence analysis shows the non linear relationship of tones. Several regimes of the tonal noise are highlighted by the time-frequency analysis. Some results are compared with the references.

The chapter 4 is dedicated to the comparison of the experimental data and numerical simulations performed at ERAU. An analysis of the possible reasons of

Introduction

disagreements is done.

The chapter 5 addresses the analytical prediction of the tonal noise using Amiet's theory. The surface pressure measurements are used as input data and the noise calculations are compared with the far-field acoustic measurements.

The chapter 6 describes the experimental results obtained for the cambered SD7003 airfoil. Similar results as for the NACA-0012 are reported as well as a comparative analysis. In the chapter 7 the results of two numerical simulations are discussed. The first one was done at ERAU with the same approach as for the NACA-0012 airfoil. The second one was conducted using the OpenFOAM software and provides a better agreement with the experimental data.

Finally, the conclusion presents summarizing remarks and review of the main results of the present work.

Chapter 1

Theoretical Background of the Trailing-Edge Tonal Noise

A literature review of the tonal noise problem is presented in this chapter. The main conclusions and some characteristic points of previous works are addressed. The most important questions, still to be investigated, are the roles of the acoustic feedback loop and of the separation bubble.

1.1 Airfoil Self-Noise Mechanisms

Brooks *et al.*[25] introduced airfoil self-noise as “[...] the interaction between airfoil blade and the turbulence produced in its own boundary layer and near wake” and described several types of the self-noise depending of the flow conditions:

- Vortex-shedding noise produced by a laminar boundary layer;
- Vortex-shedding noise produced by the trailing-edge bluntness;
- Separationstall noise attributed to moderate and high angles of attack;
- Trailing-edge noise produced by a turbulent boundary layer;
- Tip vortex formation noise.

It is worth noting that the first two aforementioned types fundamentally differ. The vortex shedding of a blunted trailing edge corresponds to the formation of a von Kármán vortex street in the wake. In contrast the so-called vortex shedding associated with a laminar boundary layer is more the continuation of disturbances which grow upstream of the edge. For this reason it is considered here that the first and fourth types above are two declination of the trailing-edge mechanism.

All types of airfoil self-noise are important in various applications such as fan noise, high-lift device noise and UAV-MAV and have been widely investigated in the literature. However, the present work focused on the noise associated with the laminar boundary layers developing on an airfoil at moderate Reynolds numbers and angles of attack.

Generally speaking, the process can be described in the following way. At low Reynolds numbers, hydrodynamic pressure fluctuations develop along the surface of the airfoil as instability waves. These waves, characteristic of laminar boundary layers, are referred to as Tollmien-Schlichting (T-S) waves. This process is a transitional step between the laminar and fully turbulent boundary layers. The T-S waves travel downstream and encounter different conditions when they reach the sharp trailing edge. Because of this they are scattered into acoustic pressure waves and give rise to secondary vorticity in the wake. The organized nature of the name of “vortex shedding” noise. During the experiments for such flow conditions usually one or several peaks frequencies which have nearly a 20 dB emergence comparing with the broadband signature are observed. This phenomenon is called tonal noise and it is often associated not only with vortex shedding but also with an acoustic feedback mechanism (see section 1.3).

1.2 Previous Experimental Investigations of the Trailing-Edge Tonal Noise

The investigation of the trailing-edge tonal noise was started from the 70s, when Paterson *et al.*[1] published the curious result of their careful experimental investigation with the symmetrical NACA-0012 airfoil. The authors wanted to determine vortex shedding characteristics of typical helicopter rotor sections by measurements of the far-field acoustic spectrum. During the experiments at low Reynolds numbers and moderate angles of attack the “ladder-type” structure of the noise signature had been observed (see figure 1.1). Indeed the plot of the dominant tone in the tone frequencies as a function of velocity exhibit a signature with a main slope according to the equation

$$f_s = \frac{0.02 \times U_\infty^{3/2}}{\sqrt{c \times \nu}} \quad (1.1)$$

and several lines which followed the law $U_\infty^{0.8}$. It was observed that the frequency of the strongest tone $f_{n_{max}}$ is close to the central frequency f_s . At some velocities discrete tones and secondary tones with smaller amplitude were detected. The authors could not explain this phenomenon. They just assumed that its origin was aerodynamic in nature. The autocorrelation and cross-correlation measurements showed that the pressure disturbances were located near the trailing edge. A phase shift between these measurements demonstrated that the measured noise source was a dipole. The authors found that the existence of the tonal noise phenomenon is observed only when the boundary layer is laminar at least on the pressure side.

The study of Paterson *et al.* roused great interest of the scientific community and since that time the question of the trailing-edge noise was investigated from different points of view.

The experimental study of the NACA-0012 airfoil was carried out by Arbey & Bataille [2] in an open-jet wind tunnel for a better understanding of the role of the instability of the boundary layer. The “ladder-type” structure was confirmed during the experiments. More precisely, the acoustic radiation was found to be made of two contributions, namely a hump-like spectral signature that is associated with the spectrum of the unstable frequencies, and a superimposed series of tones. The existence of the discrete tones is illustrated in figure 1.2. As a result the

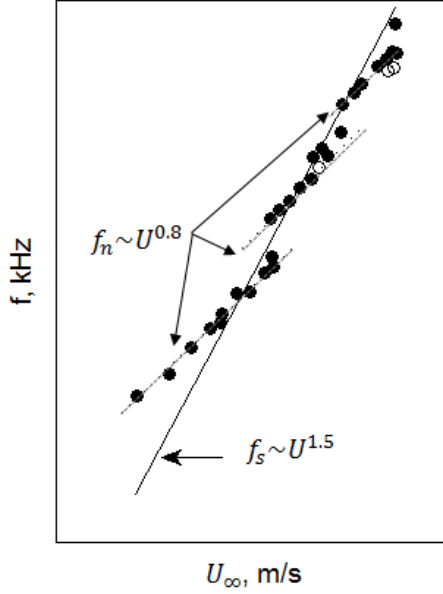


Figure 1.1: Effect of velocity on far-field vortex shedding tone frequencies, NACA-0012 full-span airfoil [1].

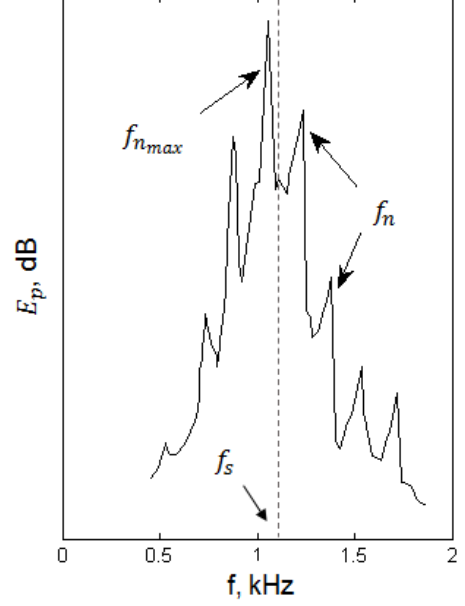


Figure 1.2: Typical noise spectrum of the NACA-0012 airfoil with 8 cm chord length at 20.2 m/s [2].

authors assumed that the noise signature combines two mechanisms which are connected with the broadband contribution and discrete components.

Nash *et al.*[12, 26] in another experimental investigation of the NACA-0012 airfoil in a closed-section wind tunnel did not observe the “ladder-type” structure and declined its necessity for the tonal noise production. The authors affirmed that three components such as T-S waves on the pressure side, sound generation at the trailing edge and a feedback loop are responsible for the tonal noise.

Another series of experiments was conducted by Arcondoulis *et al.* and presented in papers [4, 27, 13]. The NACA-0012 airfoil was tested in an open-section anechoic wind tunnel at low Reynolds numbers varied from 0.5×10^5 to 1.75×10^5 . The authors addressed the influence of the angle of attack and flow velocity on the tonal noise signature. The results of acoustic measurements, flow visualization and hot-wire anemometry were presented. A “ladder-type” structure was also observed during the research.

Inasawa and coworkers [28] studied experimentally the feedback loop mechanism between T-S waves and the trailing edge of the NACA-0012 airfoil at low

Reynolds number by hot-wire anemometry and acoustic measurements. They observed that the side which produces tonal noise changes depending on the Reynolds number. The boundary layer on the suction side generates tones at Reynolds numbers below 1.3×10^5 . At higher Reynolds numbers the separation on the pressure side is responsible for the tones. Later on this was confirmed by Pröbsting [29].

Chong *et al.*[7] investigated the relationship between the frequencies of the tones and the T-S waves on the pressure side and concluded that the T-S waves must be firstly amplified by a separation bubble.

Plogmann *et al.*[30] produced acoustic measurements for the NACA-0012 airfoil by Coherent Particle Velocity (CPV) along with oil flow visualization. They observed the influence of the separation zone on the tone generation. The tests with tripping confirmed make the flow turbulent near the trailing edge, suppress the discrete tones and only broadband noise can be observed. They observed a narrow band of discrete tones which were depending on the Reynolds numbers, the angle of attack and on whether the boundary layer is laminar or turbulent on the pressure side near the trailing edge.

As a preliminary to the present work experimental and numerical efforts were conducted by Golubev *et al.*[31] with NACA-0012 airfoils of chord lengths 8 cm and 10 cm to re-examine the acoustic feedback loop mechanism and its contribution to the trailing-edge noise. The tests with tripping on the suction and pressure sides demonstrated that the ladder-type structure may exist without interaction of the main and secondary feedback loops assumed by Desquesnes *et al.*[20]. The presented data were very close to previous results by Arbey & Bataille. Moreover it was concluded that at lowest flow velocities up to 28 m/s the suction side produced tones, whereas at higher velocity tones are produced by the pressure side. The authors noted that during the tests with a small amount of upstream turbulence the main trace of the noise signature was practically unchanged, whereas the tones associated with the acoustic feedback loop were suppressed.

One of the most recent experimental researches with the NACA-0012 airfoil was conducted by Pröbsting *et al.*[32, 29]. The authors used particle image velocimetry (PIV) for the tests with moderate angles of attack and Reynolds numbers from 1×10^5 to 2.7×10^5 in open-jet wind tunnel. On the basis of time-resolved analysis it was concluded that the dominant tone frequency corresponded to the frequency of the vortices at the trailing edge. The authors also mention the difference of the coherence levels depending on the airfoil side. Vortices on the pressure side were recognized as responsible for the tonal noise by virtue of a much higher coherence. The detailed investigation of the separation region showed that it amplifies the

instability waves.

Substantial differences are identified between the experimental results obtained by various investigators. As the parameters and characteristics of the experimental setup is varied from one reference to another, the summarized table of the experiments with the NACA-0012 airfoil presented by Pröbsting [8] was complemented by additional researches. It is shown in table 1.1.

The big amount of experimental data allowed to produce a plot of the trailing-edge noise radiation area depending on the Reynolds number and on the angles of attack. This plot is presented in figure 1.3.

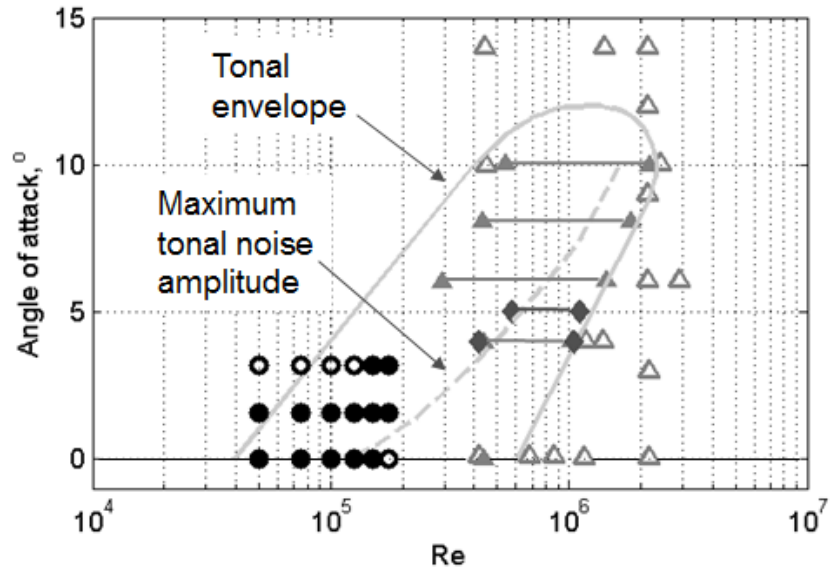


Figure 1.3: Reynolds number versus angles of attack plot for the NACA-0012 airfoil with bounds of the tonal and non-tonal areas from [3, 4]. Lawson *et al.*[3] (diamonds), Arcondoulis *et al.*[4](circles), Paterson *et al.*[1] (triangles). Solid markers represent tonal noise regimes, whereas empty markers represent non-tonal regimes. The tonal envelope and the maximum tonal amplitude were estimated by Lawson *et al.*[3].

Most of the works about tonal trailing-edge noise affirm that the boundary layer instabilities can produce tones only if an acoustic feedback loop and a separation bubble take place at least on one side of the airfoil. Therefore these two aspects should be reviewed in more details. They are the main motivation of the present work.

Table 1.1: Parameters of reported experimental investigations of the trailing edge tonal noise for the NACA-0012 airfoil. c - chord length; H - span length; Re_c - chord-based Reynolds number; α - geometrical angle of attack; α^* - effective angle of attack.

Author	c , mm	H , mm	$Re_c \times 10^5$	α	α^*
Paterson <i>et al.</i> [1]	228.6	787.4	3 to 29.4	$4^\circ, 6^\circ, 10^\circ$	$2.6^\circ, 3.9^\circ, 6.6^\circ$
Arbey & Bataille [2]	80, 160	150	1 to 7	0°	0°
Nash <i>et al.</i> [12]	300	600	1 to 14.5	$2^\circ, 3^\circ, 4^\circ, 5^\circ$	closed
Arcondoulis <i>et al.</i> [4]	67	275	0.5 to 1.5	$0^\circ, 5^\circ, 10^\circ$	$0^\circ, 1.6^\circ, 3.2^\circ$
Inasawa <i>et al.</i> [28]	150	300	0.48 to 4.3	2°	
Golubev <i>et al.</i> [31]	80, 100	300	0.5 to 3	$-5^\circ, 0^\circ, 5^\circ$	
Chong <i>et al.</i> [7]	150	450	1 to 6	$0^\circ, 5^\circ, 15^\circ$	$0^\circ, 1.4^\circ, 4.2^\circ$
Pröbsting <i>et al.</i> [32]	100	400	1 to 2.7	$0^\circ, 2^\circ, 4^\circ$	$0^\circ, 1.5^\circ, 2.9^\circ$

1.3 Aeroacoustic Feedback Loop Model

At low Reynolds number in case of tonal noise at least one boundary layer on the surface of the airfoil is laminar but unstable. The hydrodynamic instabilities called Tollmien-Schlichting (T-S) waves grow in the boundary layer, and produce noise at the trailing edge. The corresponding power spectral density plot exhibits a series of tones over the same frequency range as the broad hump. A number of studies concluded that the former result from some selective amplification of the latter. The frequency of the highest tone is in a good overall agreement with the center frequency of the main broadband hump.

The ladder-type structure and velocity dependence of the frequencies motivated the scientists to interpret the phenomenon. One of the explanations was proposed by Tam [5], who assumed that the amplification of the tones was caused by a self-excited aerodynamic feedback loop. He supposed that disturbances produced in the near wake from the trailing edge propagate downstream with increasing amplitude. When the amplitude of the disturbances is high enough they force the wake to vibrate. This point where vibration starts is the noise source and part of the acoustic waves propagates upstream, reaches the trailing edge and forces the boundary layer and near wake to oscillate. However, even if it can predict multiple discrete tones this feedback loop model was not able to explain the origin of the ladder-type structure. It is worth noting that Tam's investigation was proposed for very low Reynolds numbers and therefore the near wake was laminar, which is not the case for the present research.

A theory about the origin of the feedback loop was reported by Archibald[33]

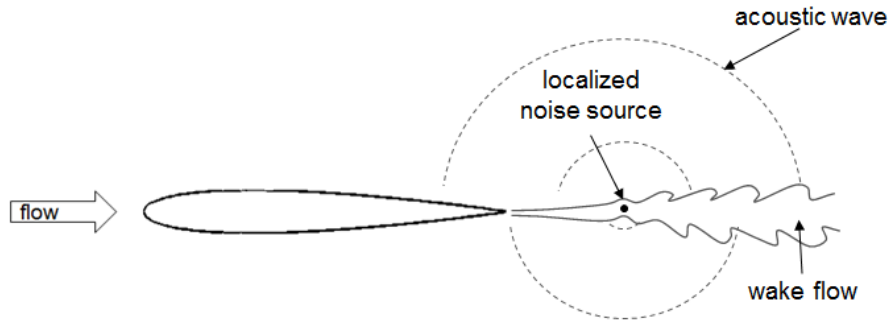


Figure 1.4: Scheme of the feedback loop proposed by Tam [5].

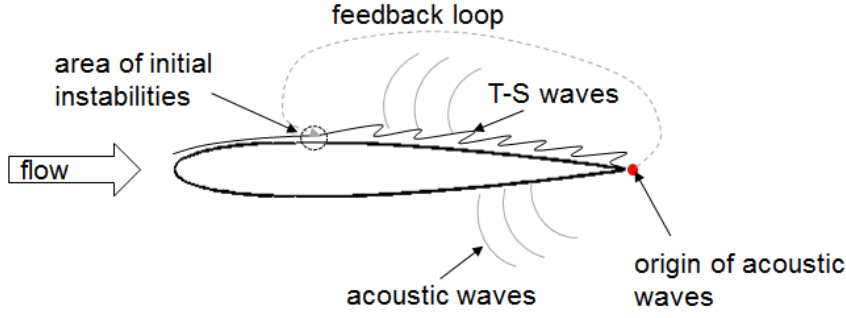


Figure 1.5: Scheme of the feedback loop proposed by Longhouse [6].

who suggested that the feedback was produced by acoustic standing waves in the wind tunnel used for the experiment. This theory was not confirmed later.

Longhouse [6] relied on experimental studies of fans to improve the feedback loop model (see figure 1.5). He considered that the T-S waves are generated far enough upstream of the trailing edge, then travel downstream and scatter from the trailing edge. After that the generated acoustic waves propagate upstream and amplify the starting instability waves. Therefore there are three necessary conditions for the tonal noise production: interaction of the T-S waves with the trailing edge, acoustic feedback and amplification of the T-S waves. The research refuted Tam's [5] statement that the wake instability moves back to the trailing edge.

In 1983 Arbey & Battaille [2] used as a basis for interpretation the feedback model and carried out careful experiments. They assumed that acoustic waves disturb the boundary layer at the point of maximum flow velocity, the airfoil surface where T-S waves are generated. The authors associated the broadband component with the primary radiation of the T-S waves without feedback. In order to explain the jumps of maximal frequency of the tones, they proposed the following formula for selected frequencies f_n :

$$f_n = \left(n + \frac{1}{2}\right) \frac{K}{L} U_\infty^{0.85} \quad (1.2)$$

where $K = 0.89 \pm 0.05$. This formula is based on the assumption that amplification occurs as the time taken by a T-S wave to travel from their starting point to the trailing edge, plus the time taken by the scattered acoustic waves to propagate upstream to the starting point, must be a multiple of the period of oscillation. It is in complete agreement with Longhouse's argument.

Yet some authors [26, 12] reject the necessity of the feedback loop for the tonal noise generation. Another view point based on the results of DNS simulations was proposed by Desquesnes *et al.*[20]. They assumed the existence of a second feedback loop on the suction side at non-zero angle of attack. However this was refuted by Pröbsting *et al.*[34].

The theoretical prediction of the discrete tone frequencies f_n produced by the feedback loop was addressed more accurately by Kingan & Pears [35] who showed a good agreement with the experimental results.

Chong & Joseph [36] trying to understand the role of the feedback loop mechanism in the ladder-type structure concluded that the jumps of the maximal tonal frequency are caused by the frequency lag between the maximal TS-wave amplification and the multiple discrete tones.

On the basis of aforementioned studies it can be concluded that the natural boundary layer instabilities need to be amplified to produce high-amplitude tonal noise.

1.4 Role of the Separation Bubble

The interest for the influence of a separation bubble on the tonal noise generation arose from the researches of the role of each side of the airfoil in this process. From the very beginning researchers used tripping devices to investigate the responsibility of each side in the generation of the trailing-edge noise. Even Paterson *et al.* [1] mentioned that only tripping on the pressure side suppresses the tonal noise, whereas on the suction side it produces no significant difference if any. Similar results were described in [26]. However the question of which side is producing tones was controversial. Some aforementioned works [28, 29] reported that the side producing tones can change depending on the Reynolds number and on the angle of attack. Longhouse [6] performed experiments on the fans and connected the existence of the tonal noise with the presence of the separation bubble. After his studies he asked the question of whether the laminar separation bubble influences the noise level and of whether the bubble instabilities have an effect on the frequencies of the tonal noise or not.

Looking ahead several sub-questions can be raised.

- Is the separation bubble a necessary condition for tonal noise generation?
- Is the separation bubble a sufficient condition for tonal noise generation?
- Is the location of the separation bubble important?
- What is the role of the separation bubble in the process?

Available published works address these issues in one way or another.

Lowson *et al.* [3] identified a laminar separation bubble as a necessary component which should amplify the T-S waves for an effective radiation of the trailing-edge noise. Later, the role of the separation bubble as an amplifier was confirmed experimentally in [12, 7, 29] as well as numerically in [20]. Moreover, Chong *et al.* [37] trying to reduce tonal noise by means of serrations noted that the separation bubble should be completely suppressed for this task. McAlpine *et al.* [26] noted that the tonal noise was in strong dependence of the existence of a separation bubble located near the trailing edge. The authors also stressed that the feedback occurred on the side with the separation bubble.

At the same time Nash *et al.* [12] assumed that the separation was not enough to generate tones. As a result of an experimental and theoretical investigation they proposed a revised mechanism for tonal noise generation. They attributed the tonal noise to the amplification of the T-S waves by the separating laminar shear layer near the trailing edge of the airfoil. They also observed a triple-peak structure of the streamwise velocity fluctuations which was described like a feature of the tonal noise emission. However, the latter argument was refuted by Pröbsting *et al.* [32].

In numerical simulations for the NACA-0012 airfoil Desquesnes *et al.* [20] concluded that the separation bubble acted as an amplifier but was not a generator of the tonal noise. This hypothesis was confirmed by the experimental study of Chong *et al.* [7]. The authors compared calculations with measured noise spectra and concluded that the noise radiation by scattering of the hydrodynamic pressure in the vicinity of the trailing edge required the incoming instability waves to be first amplified by a separation region. The authors predicted the location of the separation bubble depending on the Reynolds number (figure 1.6).

Pröbsting *et al.* [29] observe that the reattachment of the separated layers on both sides of the airfoil moves upstream with increasing Reynolds number. With increasing angle of attack; the reattachment on the suction side shifts upstream whereas on the pressure side it moves downstream (the same behavior was observed in [38]). Therefore the authors divided the Reynolds versus angle of attack plot into pressure- and suction-side-dominated areas.

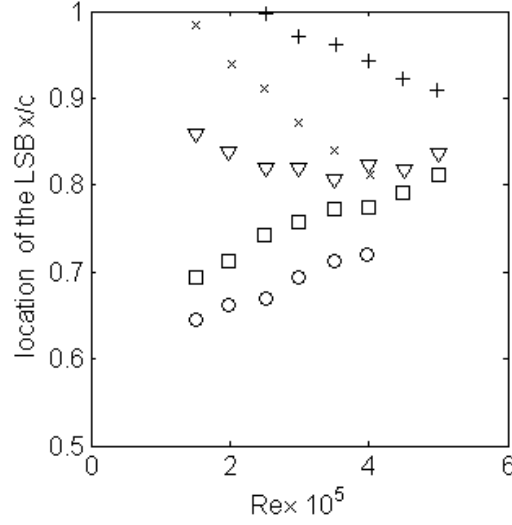


Figure 1.6: Prediction of boundary layer separation at $\alpha^* = 0^\circ$ (\circ), $\alpha^* = 1.4^\circ$ (\square), $\alpha^* = 4.2^\circ$ (∇) and reattachment at $\alpha^* = 0^\circ$ (\times), $\alpha^* = 0^\circ$ ($+$). The locations are defined as fractions of the chord, x/c at the pressure surface of the NACA-0012 airfoil [7].

Dealing with boundary layer instabilities vocabulary issues must be clarified, in the sense that Tollmien-Schlichting (T-S) waves and Kelvin-Helmholtz (K-H) waves should be distinguished. According to the work of Atassi [39] when separation takes place the situation is equivalent to free shear layers and the underlying physics is rather that of K-H instabilities. However, because the thickness of the separation bubble is very small in the present case scientists still argue about the terminology especially because the vicinity of the wall could make the oscillations of the separated layer differ from true free shear-layer oscillations. In order to avoid confusions and misunderstanding in the present work T-S waves as well as K-H waves will be called laminar boundary layer (LBL) instabilities.

All aforementioned works refer to the NACA-0012 airfoil. The other airfoil investigated in the present study is the SD7003 airfoil, which is well documented from the aerodynamic view point. Typically Galbraith *et al.* [10] used Implicit Large Eddy Simulation (LES) for investigation of the laminar separation bubble (LSB) at low Reynolds numbers ($10^4 < Re < 9 \times 10^4$). They observed a large recirculation region on the suction side at $Re = 10^4$. As the Reynolds number increased the LSB moved to the leading edge of the airfoil.

1.5 Concluding Remarks

This chapter presents an overview of the trailing-edge tonal noise problem. Some typical features such as a ladder-type structure of the discrete-tone frequencies dependence on the flow velocity were discussed. As was figured out by most investigators there are two components in the tonal noise mechanism: boundary layer instabilities and feedback loop. Some of the researchers also argued that the separation bubble plays a key role in the phenomenon. As the trailing-edge noise is very sensitive to the parameters of the flow a lot of significant differences were observed in previous investigations. This motivated the present experimental study, aimed at checking some previous theories, investigating the role of the separation bubble and creating a database for comparison with numerical simulations. The next chapter will describe the experimental setup used for the measurements and the post-processing methods. The analysis of the results will be addressed in subsequent chapters.

Chapter 2

Experimental Setup and Instrumentation

For the creation of the data base for a NACA-0012 and a SD7003 airfoils a set of acoustic and aerodynamic measurements was decided. This chapter presents an overview of the experimental setup and of the measurement techniques addressing unsteady surface pressure, acoustic far-field spectra and directivity, and mean pressure coefficient. For the investigation of the separation bubbles hot-wire anemometry and flow visualization were used. Advanced methods of data analysis such as cross-spectra, bicoherence and time-frequency analysis are also reported. Finally, uncertainties of the measurements are discussed in this chapter.

2.1 Setup Description and Instrumentation

Experimental investigations were conducted in the anechoic open-jet wind tunnel, which consists in a fan system connected with an anechoic room of dimensions $4m \times 5m \times 6m$ by a long duct. The room is enclosed in a concrete box which is isolated from the building basement by a layer of sand to prevent transmission of low-frequency vibration. A clean laminar flow in the outlet section is ensured by filters inserted in the duct just upstream of the nozzle contraction. The noise from the fans is absorbed by liners distributed in the duct well upstream of the nozzle.

The flow is delivered in the anechoic room by a set of 6 axial-flow fan stages labeled S1 to S6 that can be turned on and off independently. The fan S6 has a potentiometer that allows adjusting the flow speed at any desired value by associating it with other fan stages. The investigated flow speeds which were measured using a Pitot tube and a FC0510 micro-manometer of National Instruments are listed in table A.1 (appendix). They have been measured with and without additional turbulence grids in the nozzle in order to correct the effect of additional pressure losses due to the grids.

Two grids (figure 2.1) installed inside of the nozzle were used for more detailed research on the effect of turbulence on the noise generation process.

- The small grid for generation of fine-scale turbulence has square cells of side 1 cm and is made of thin rods of diameter 1.5 mm.
- The large grid for generation of large-scale turbulence which suppresses LBL waves has square cells of side 5 cm and is made of flat rods with a width of 1 cm.

The outlet section has a working area of 30 cm (height) \times 15 cm (width).

A mock-up of the NACA-0012 and a mock-up of the SD7003 airfoil were made of aluminum. The difference of cross-section is shown in figure 2.2. The leading edges of the airfoils were located 11 cm downstream of the nozzle outlet section (figure 2.3). The chord length is 12 cm and the span length is 30 cm in both cases. The airfoil ends are fixed in discs that are embedded in the end plates of the setup. This allowed simply adjusting the geometrical angle of attack at any desired value. The mock-up rotates around its center-chord point and its chord line is along the axis of the nozzle exit at zero angle of attack. For each mock-up a block of resin

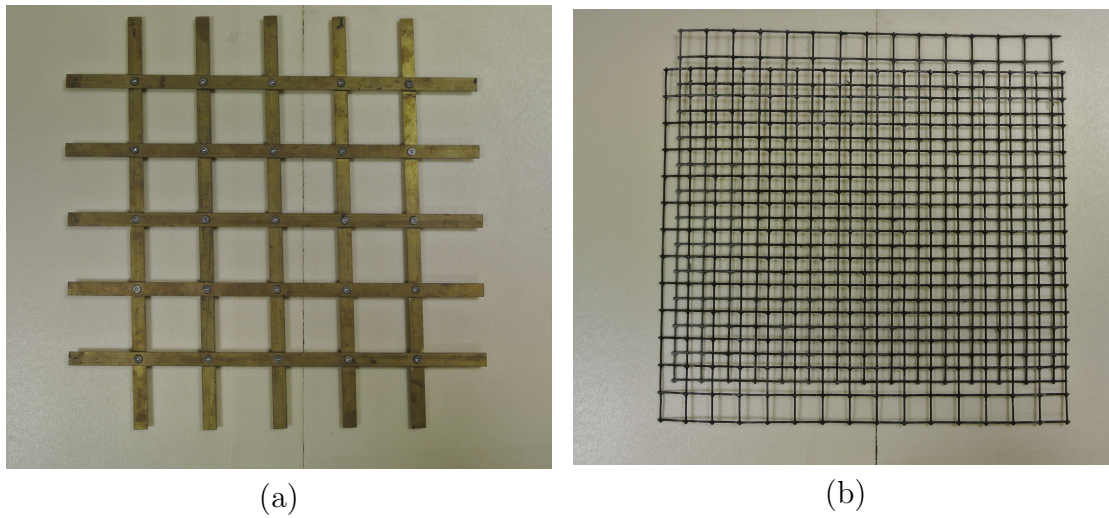


Figure 2.1: Grids producing upstream turbulence: (a) - large-scale grid, (b) - small-scale grid.

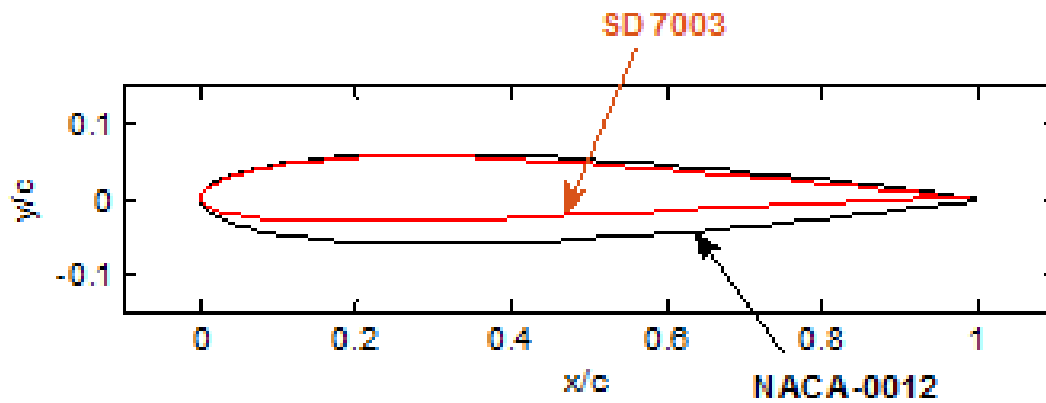


Figure 2.2: Compared cross-sections of the NACA-0012 airfoil and of the SD7003 airfoil.

is used above the upper disc to maintain the junctions of the capillary tubes with their PVC extensions and with the measuring microphones (see figures 2.3 - 2.6).

In some tests an optional tripping strip was added on the surface of an airfoil to force the transition to turbulence on one or on the other side. This device is made of a medical adhesive plaster of 2.5 cm width. It has been positioned around the maximum thickness area at the distance 7.5 cm from the trailing edge for

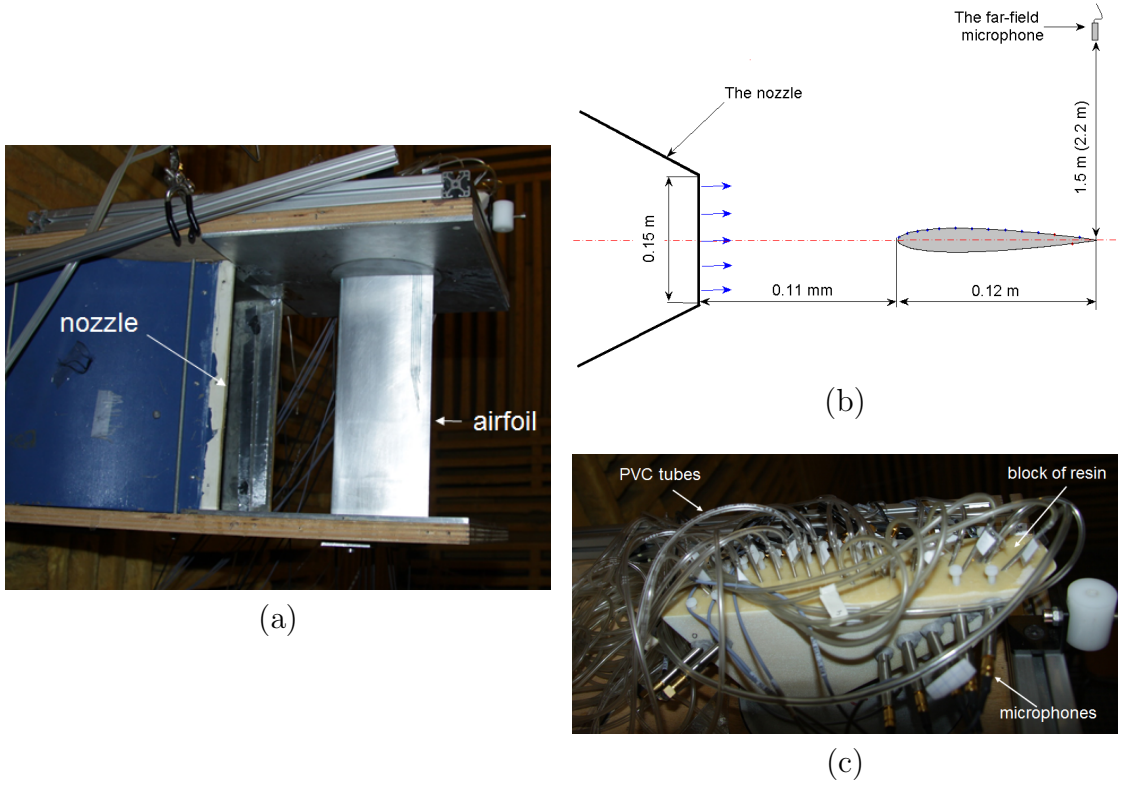


Figure 2.3: Anechoic wind tunnel of ECL: (a) photo of an installed mockup; (b) sketch of the experimental setup for acoustic measurements (top view); (c) detail of top-plate instrumentation, showing the microphones and the RMP tubes embedded in a block of resin.

the NACA-0012 airfoil. In the case of the asymmetric SD7003 airfoil the tripping strip was located on the pressure side at the distance 7.2 cm and on the suction side at the distance 7.6 cm again measured from the trailing edge. Tripping the boundary layer is a classical way of suppressing the LBL waves and the associated tone generation. It was used also to ensure that only one side remains laminar.

Various flow conditions with different angles of attack and with or without tripping have been tested in the experiments. Because the NACA-0012 is a symmetric airfoil, for clarity the one side facing the entrance of the anechoic room is called the door side and the opposite one facing the wall is called the wall side. The following configurations were investigated:

- Configuration A: clean oncoming flow without tripping. In this case the residual turbulence of the wind-tunnel allows the onset of LBL waves rein-

forced by acoustic feedback.

- Configuration B: clean oncoming flow with tripping on the door side.
- Configuration C: clean oncoming flow with tripping on the wall side.
- Configuration D: clean oncoming flow with tripping on both sides. This case forces turbulent boundary layers on both sides and only produces broadband trailing-edge noise.
- Configuration E: small-scale upstream turbulence produced by a grid, without tripping. This case corresponds to laminar and unstable boundary layers, expectedly free of acoustic feedback at moderate speeds, and probably to turbulent boundary layers close to the trailing edge at higher speeds.
- Configuration F: large-scale upstream turbulence produced by a grid, without tripping. This case corresponds to the usual turbulence-impingement noise configuration. It is not thoroughly investigated but just cited for comparison.

All measurements which were conducted for both airfoils are summarized in tables A.2, A.3 (appendix).

2.2 Wind Tunnel Correction and Effective Angle of Attack.

Several angles of attack were tested for both airfoils. Since the dimension of the nozzle is limited the flow deviates from the nozzle axis at non-zero angle of attack. This effect is one of the disadvantages of the open-jet wind tunnel. It reduces the airfoil loading and corresponds to conditions that would be encountered in an infinite flow at smaller angle of attack. Two definitions are introduced, as the geometrical angle of attack α (measurements) and the effective angle of attack α^* (used for numerical simulation and comparison with other works). For the NACA-0012 airfoil the correction proposed by Books *et al* [25] was used:

$$\alpha^* = \alpha / \xi \tag{2.1}$$

where

$$\xi = (1 + 2\sigma)^2 + \sqrt{12\sigma} \tag{2.2}$$

and

$$\sigma = (\pi^2/48)(c/H)^2 \quad (2.3)$$

On the basis of this calculation $\xi = 2.86$ and $\alpha = 5^\circ$ corresponds to $\alpha^* = 1.75^\circ$.

For the SD7003 airfoil no correction formula is available and the only way to determine the effective angle of attack is a comparison of the pressure coefficient distribution with a numerical simulation. This will be addressed in chapter 7.

2.3 Acoustic measurements

The preliminary tests were conducted to determine the boundaries of the parameter space in which the tonal noise is observed. This is essentially achieved by directly listening at the sound produced as a function of the Reynolds numbers and angles of attack.

For quantitative measurements, a single Bruel & Kjaer 1/2" type 2671 microphone on a rotating arm provided far-field spectral directivity measurements. For the NACA-0012 airfoil the microphone was located at the distance 1.5 m normal to the airfoil (90° with respect to the oncoming flow direction) for frequency versus flow-speed measurements of airfoil tonal noise and at 2.2 m for directivity measurements. This difference is explained by practical reasons associated with measurements made at different periods. In all cases the far-field conditions are fulfilled. For the SD7003 airfoil the distance for all measurements was 2.2 m. The measured levels can be transposed at any other distance, for comparison, according to the spherical attenuation of waves.

The interval between acoustic measurements at different speeds was more than 15 s to ensure the stabilization of the flow.

2.3.1 Remote Microphone Probes

The Remote Microphone Probe (RMP) technology used for measuring wall-pressure fluctuations at a point on the surface of an airfoil is aimed at characterizing the development of instability waves or turbulence in the boundary layers. In aeroacoustics this is often equivalent to get information not on the sound itself

but on the flow features that are the sources of the sound. In principle the nature of the measured pressure fluctuation can have hydrodynamic and/or acoustic origin depending on boundary layer features. For example, if the boundary layer is turbulent or transitional both types of fluctuation are measured but the hydrodynamic ones are much bigger than the acoustic ones. In contrast when the probes are covered by a laminar boundary layer they can measure only acoustic fluctuations. Therefore values measured close to the trailing edge have a hydrodynamic origin and are a trace of the source of the sound. It should be mentioned that the nature can change depending on the frequencies. The RMP technology is based on capillary tubes put in spanwise-aligned grooves that are blocked up again (for details see section 2.3.2).

There are a spanwise and a chordwise sets of RMPs for each airfoil mock-up. The chordwise set is located at the midspan (0.15 m from each end plate) of the airfoil to prevent any possible influence of the end plates and to have acceptable two-dimensional flow condition. The distance between probes varies from 5 mm to 20 mm. The aim was to investigate the changes of PSD level, coherence, *etc.* Therefore probes are uniformly distributed along the chord. Close to the trailing edge the minimal possible distance allowed by the manufacturing technology was achieved. The spanwise set is located as close to the trailing edge as it was technically possible. In particular the sets of spanwise probes allow to measure the spanwise coherence associated with the LBL waves. The NACA-0012 airfoil has 15 chordwise probes on the wall side and 4 and 5 spanwise probes on the wall and door side correspondingly. It should be mentioned that the probe 15 had not worked because of technical problems. The SD7003 airfoil has 12 chordwise probes and 5 spanwise probes on the suction side, as well as 5 chordwise probes on the pressure side.

The RMPs are equipped with Bruel & Kjaer, type 4935 microphones.

The wall-pressure level was expressed with the same definition as for acoustic levels:

$$SPL_{dB} = 20 \log_{10} \frac{p_{rms}}{2 \times 10^{-5}} \quad (2.4)$$

2.3.2 Analytical Determination of the Transfer Function

The transfer function between the meaning point and the microphone can be determined analytically based on the theory of sound waves in very narrow tubes.

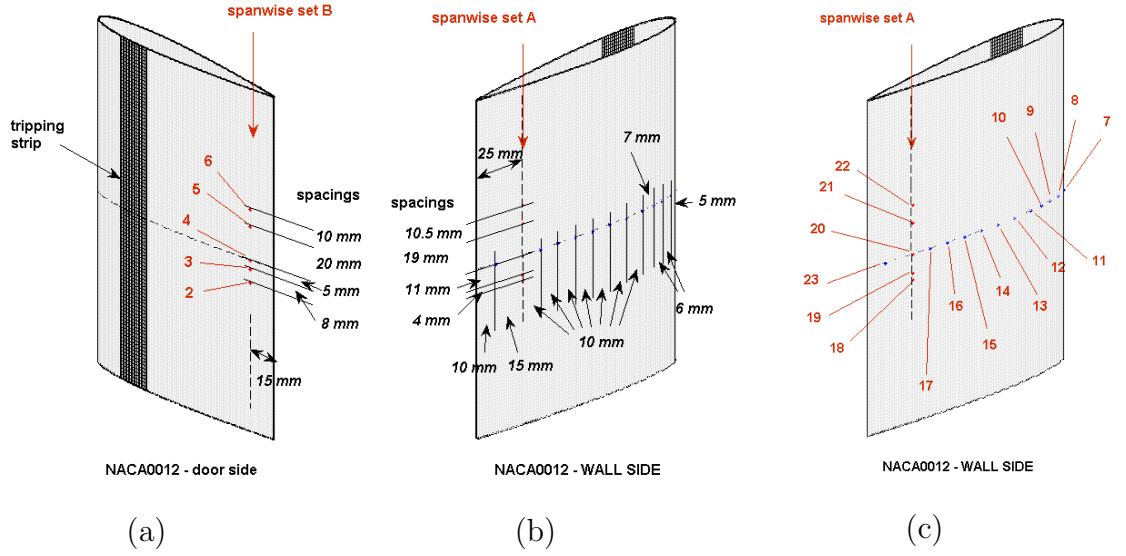


Figure 2.4: Pin-hole locations and probe labels (red) of the wall-pressure RMP on the NACA-0012 mock-up. Relative position of the tripping device on the door side indicated as the black strip in subplot (a).

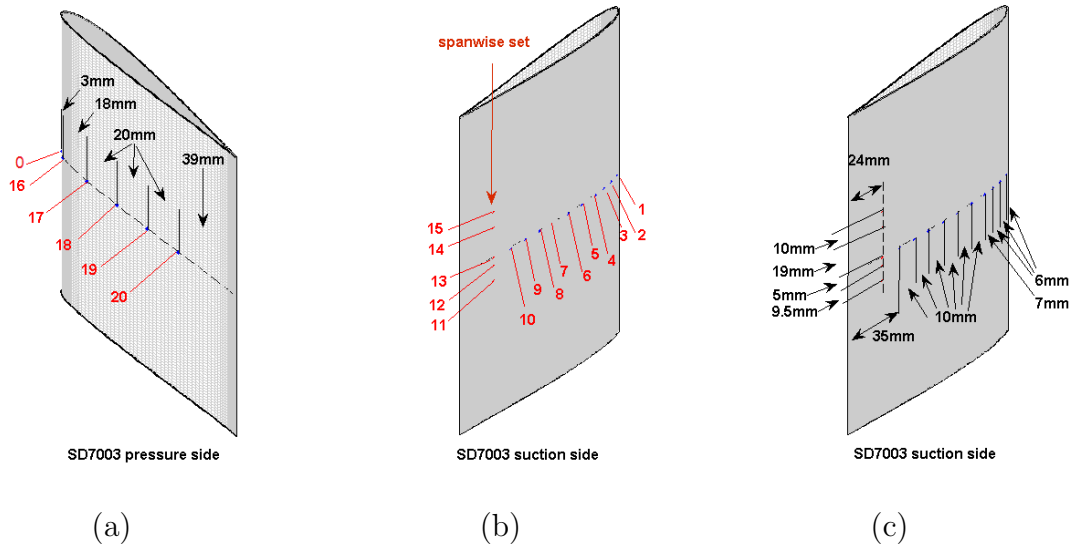


Figure 2.5: Pin-hole locations and probe labels (red) of the wall-pressure RMP on the SD7003 mock-up.

It has been first derived in a simplified form by Pérennès [40]. A more complete form is proposed in this section.

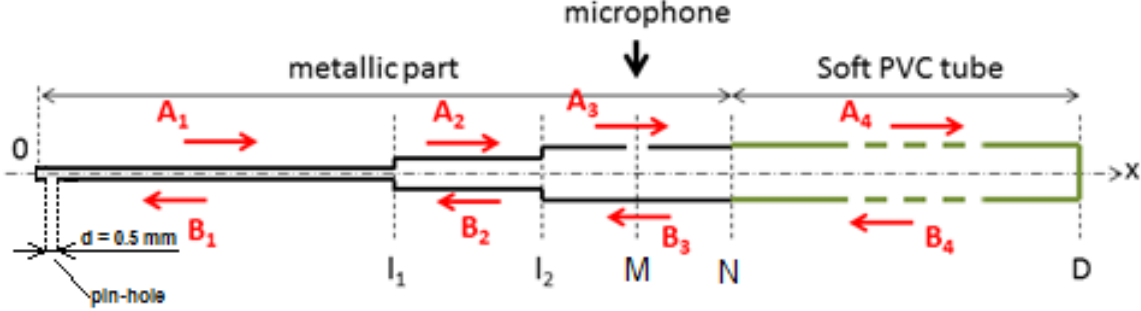


Figure 2.6: Sketch of the RMP.

As was mentioned by Pierce [41] an acoustic plane wave is exponentially attenuated in a narrow tube because of viscous effect and the modified wavenumber is expressed as

$$K = k + (1 + i)\zeta \quad \text{with} \quad k = \omega/c_0 = 2\pi f/c_0 \quad \text{and} \quad \zeta = \frac{0.0102}{c_0} \frac{\sqrt{f}}{r} \quad (2.5)$$

where r is the inner radius of the capillary cross-section. The imaginary part accounts for the attenuation (with the present convention of monochromatic waves with time dependence $e^{-i\omega t}$). This attenuation reaches 25 dB at 20 kHz with the present technology, which seems quite large, but the use of microphones for aerodynamic wall-pressure measurements remains reliable above that value, as reported in previous studies [42].

The probe design of figure 2.6 involves three capillary tubes of progressively increasing cross-section diameters. The smallest tube of outer diameter 1 mm (inner 0.7 mm diameter) ensures a reasonable access quite close to the trailing edge of narrow airfoils (typically down to 2 mm thickness of the material, thus 1 cm from the trailing-edge for a NACA-0012 airfoil). The biggest tube is laterally perforated (coordinate M in figure 2.6) and connected to a nearly-flush mounted microphone by means of a block of resin in which the tube and the microphone barrel are embedded, in such a way to avoid leakage. The end of the biggest tube is then connected to a long soft-wall (PVC) tube aimed at progressively damping

the acoustic waves (junction at the coordinate N in figure 2.6). This PVC tube, of about 2 m long, expectantly ensures anechoic conditions at its end. It is closed in order to avoid any mean flow in the probe. With this technology, incident sound waves are partially reflected and transmitted at each section discontinuity, but only plane waves are regenerated; therefore two forward and backward-propagating waves result on each side of a discontinuity. First analytical determinations of the response function [40] assumed that the waves transmitted in the last tube are measured by the microphone and then attenuated in the soft-wall termination with negligible reflections (assumption $B_4 = 0$ in the model below). This has been shown to be justified for most self-noise studies (airfoil trailing-edge noise in clean inflow) for which very low frequencies can be ignored. Yet recent measurements of the wall-pressure spectra in the presence of upstream turbulence, for which large fluctuations are generated at low frequencies, show evidence of residual oscillations typically below 300 Hz. This is why the formulation has been readdressed to account for some non-zero end reflection at low frequencies.

The first equation of the transfer-function model expresses the continuity of acoustic motion at the probe entrance; it relates the amplitudes of the pressure waves inside the capillary of index 1, say A_1 and B_1 , to the amplitude of the incident pressure wave A_0 . It reads

$$2A_0 = (A_1 + B_1) + \frac{Z_0}{\rho_0 c_0} (A_1 - B_1) \quad (2.6)$$

and involves the acoustic inlet impedance

$$\frac{Z_0}{\rho_0 c_0} = R_0 + ik\delta_0, \quad \text{with} \quad R_0 = \frac{k^2 S_0}{2\pi} \quad \text{and} \quad \delta_0 = \frac{8\sqrt{S_0}}{3\pi^{3/2}} \quad (2.7)$$

where S_0 is the orifice area[41]. Other relations arise by imposing the continuity of wave pressure and flow rate on both sides of each cross-section change, according to the generic equations

$$A_j e^{iK_j l_j} + B_j e^{-iK_j l_j} = A_{j+1} e^{iK_{j+1} l_j} + B_{j+1} e^{-iK_{j+1} l_j} \quad (\text{pressure}) \quad (2.8)$$

$$A_j e^{iK_j l_j} - B_j e^{-iK_j l_j} = \frac{K_{j+1} S_{j+1}}{K_j S_j} (A_{j+1} e^{iK_{j+1} l_j} - B_{j+1} e^{-iK_{j+1} l_j}) \quad (\text{flow rate}) \quad (2.9)$$

where l_j stands for the coordinate of the j^{th} singularity and K_j , S_j for the associated wavenumber and cross-section area. At the end of the PVC tube the residual sound wave is totally reflected with a zero-velocity condition. It is worth noting that the attenuation is increased by the soft walls of the tube, but its value remains unknown. Solving the system of equations provides the ratio of the complex amplitudes of the pressure waves at the microphone location and at the orifice as a function of frequency. The predicted attenuation is plotted in decibels as the dashed line in figure 2.7.

In the analytical response model the pin-hole is considered to have equivalent inlet acoustic impedance, which is *a priori* valid only for acoustic excitation. (It is also assumed that the attenuation inside the RMPs is not depending on the external flow speed.) As long as the characteristic length of the actual wall-pressure fluctuations remains larger than the pin-hole diameter of 0.5 mm hydrodynamic and acoustic excitation are assumed equivalent for the capillary response. But the validity of this assumption is still an open question. It is also known in the physics of flush-mounted pressure sensors that the active sensor area averages the true wall-pressure fluctuations. This causes an artificial high-frequency decrease of the response as the aerodynamic wavelengths get smaller than the sensor area, as pointed out by Corcos [43] in the sixties. This effect becomes only significant with the present RMP technology at very high frequencies, well above the range of interest for the study. It could be critical at very low flow speeds because small aerodynamic length scales produce lower frequencies at lower flow speeds, but the investigated sounds also have lower frequencies at lower flow speeds.

According to aforementioned elements, the effect of larger capillary lengths is to increase the amount of attenuation. Therefore the optimal length is the smallest possible one, keeping in mind that all microphones must be kept outside the mock-up, beyond the end-plates used to hold it. Quite logically in the present experiment, most sensors are clustered around mid-span, and the spanwise sets are centered also at mid-span and located at an interval around 50 mm. Furthermore for convenience all sensors are manufactured identical in order to have to consider only one common response function. This defines part of the design rules, keeping in mind that the most of them are empirical.

The actual wall-pressure information is lost only when the measured signal goes below the electronic background noise, easy to identify: the latter produces a flat horizontal spectral signature at very high frequencies whereas the true information produces a physically consistent decrease. The flat background noise is observed only at very high frequencies for low-speed measurements, but again remains out of the range of the investigated phenomena.

Manufacturing issues might result in some uncertainties about the RMP parameters. Furthermore the perforation is not exactly at the end of the smallest capillary tube for practical reasons, but slightly displaced. This is why a corrected length has been considered in the model in such a way that the theoretical humps and dips of the RMP response coincide at best with the measured ones. The capillary parameters are listed below:

- inner radii (mm) of the capillary tubes $r_1 = 0.00035 \text{ m}$; $r_2 = 0.00053 \text{ m}$; $r_3 = 0.00075 \text{ mm}$;
- distances from wall perforation to cross section changes (see definition on the sketch of figure 2.6) $l_1 = 0.22 \text{ m}$; $l_2 = 0.23 \text{ m}$;
- distance from wall perforation to microphone $M = 0.27 \text{ m}$;
- length of the metal part $N = M + 0.05 \text{ m}$;
- total length $D = N + 2.1 \text{ m}$.

2.3.3 In-Situ Calibration Procedure

Because of the sensibility of the analytical response to small manufacturing errors (errors in capillary lengths) some uncertainty is expected at high frequencies. This uncertainty might cause spurious small-amplitude oscillations in a broadband spectrum. Furthermore the model assumptions can be questionable, or at least need being validated, in some frequency ranges. This is why a dedicated acoustic calibrator has been designed at ECL. The calibrator is made of a small-size loudspeaker embedded in a box and continued by a tube of inner diameter 1 cm. The end of that tube is equipped laterally by the microphones B&K $1/4''$ microphone that delivers a signal X_{CAL} and its opening acts as a piston for most frequencies of interest, typically up to 18 kHz. The opening is placed successively over the pin-hole of the RMP to be calibrated and over another reference B&K $1/4''$ microphone flush mounted in a rigid flat plate. This second microphone delivers a signal X_{REF} . The loudspeaker is excited by a broadband noise generator. Two transfer functions are acquired: the RMP to calibrator, say X_M/X_{CAL} , and the calibrator to reference X_{CAL}/X_{REF} . Forming the ratio of both provides the transfer function between the RMP and what a flush-mounted B&K $1/4''$ would measure, X_M/X_{REF} . Because this calibration is purely acoustic and makes sense

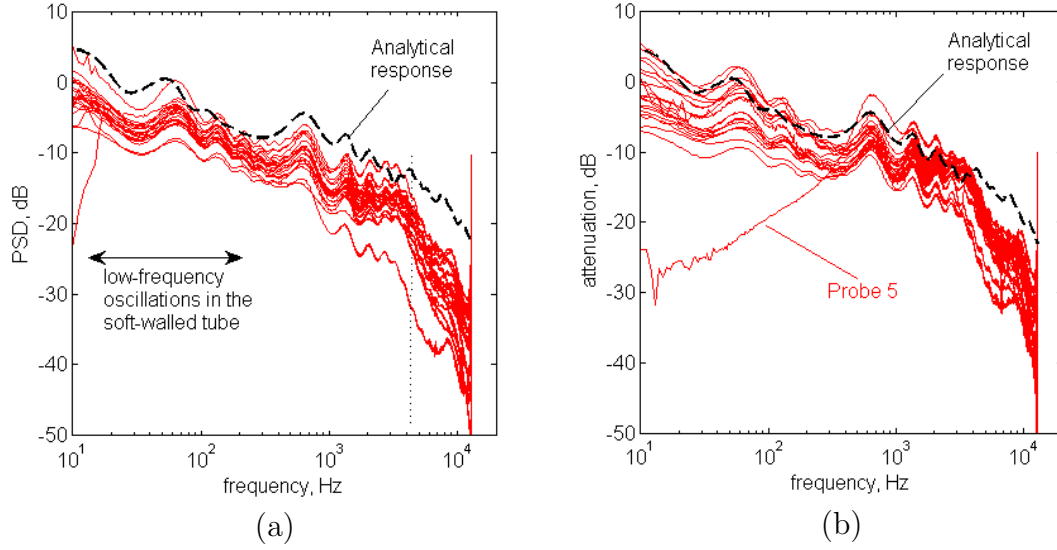


Figure 2.7: Attenuation spectra as measured by the two-step calibration procedure (23 red plots), and as predicted by the analytical model. Sensitivity ratios are not taken into account. (a) - for the NACA-0012 airfoil, (b) - for the SD7003 airfoil.

for a frequency range in which the diameter of the B&K $\frac{1}{4}$ " microphone remains well compact, it is reliable. Yet the calibrator positioning may not be perfect on some curved parts of airfoil surfaces or close to a trailing edge. Therefore the in-situ calibration sometimes requires additional use of a ductile seal. The analytical and measured response functions can be used jointly: the calibration is satisfying when both methods provide similar corrections.

In the two-step calibration procedure the sensitivity σ_M of the RMP microphone differs from the sensitivity σ_{REF} of the reference flush-mounted microphone. The sought transfer function is therefore simply expressed by $(\sigma_{REF}/\sigma_M)X_M/X_{REF}$. Typical direct measurements (uncorrected for sensitivity differences) are plotted in figures 2.7.

Theoretical and measured attenuations deviate from each other above 5 kHz, where the latter are more pronounced. Furthermore the high-frequency hump measured around 8-9 kHz (or the dip at 6-7 kHz depending on the way of interpreting both) is not found with the theoretical response. These discrepancies can be attributed either to a limitation of the analytical model or to the calibration itself. Anyway a hump at 8-9 kHz is observed in the measured spectra with no evidence of physical consistency. The reference $\frac{1}{4}$ " microphone used for the calibration is flush-mounted with its protection grid removed. This was found to

attenuate the response at high frequencies and could explain the aforementioned deviation. The $\frac{1}{4}$ " microphones of the RMPs still have their protection grids. But the connection with the laterally perforated tube is ensured by means of a pinhole of 0.5 mm diameter in the tube itself and a conical drilling in the resin block. This expectedly acts as an equivalent Helmholtz resonator the resonance of which can only be estimated.

As shown in figure 2.7(b) the analytical response for the SD7003 airfoil is in a good agreement with the calibration curves. However, the probe 5 has a big deviation at low frequencies. For this case the analytical function was used for the correction.

The general expression for the impedance of a Helmholtz resonator (figure 2.8) reads [44]

$$Z_R = (1 + i) \frac{\rho_0 L_e \sqrt{2\omega\nu}}{\pi(d/2)^3} + i \left(\frac{\omega \rho_0 (L_e + \pi d/4)}{\pi(d/2)^2} - \frac{\rho_0 c_0^2}{\omega V} \right) \quad (2.10)$$

The half apex angle of the cone is 45° , therefore the resonance frequency is estimated as

$$f_R = \frac{c_0}{2\pi} \sqrt{\frac{A}{VL}}, \quad \text{with} \quad V = \frac{\pi(D-d)}{24} (D^2 + Dd + d^2) \quad (2.11)$$

where A and L_e are the neck cross-section and length (the latter corresponds to the capillary tube thickness), V the volume of the conical cavity and D and d the diameters of the microphone and of the neck, respectively. ν is the kinematic

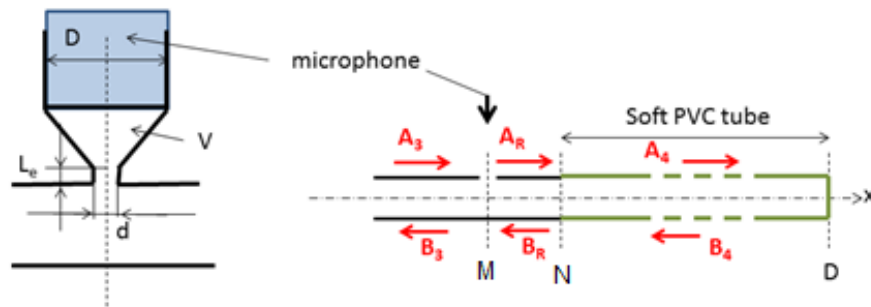


Figure 2.8: Capillary-microphone junction acting as a Helmholtz resonator - Corrected probe model.

viscosity. This estimation is compatible with the aforementioned hump/dip artifact. But the implementation of the resonator branch impedance in the model did not produce significant changes in the response of the probe. Because the frequency range of the resonance is beyond the interval covered by LBL waves no further effort has been attempted. The main concern with the analytical response function is that it is shifted systematically around 12 dB from the experimentally determined ones. The origin of this shift has not been identified. This is why the measured response functions are used to correct the wall-pressure spectra. The overall agreement between the model and measured corrections in terms of humps and dips allows understanding their physical origin.

2.3.4 Background-Noise Correction of Wall-Pressure Spectra

At low speed, the wall-pressure fluctuation level is very low and the high-frequency content is possibly hidden by the electronic background noise. The latter can be measured by just turning the wind tunnel off. It is responsible for a high-frequency plateau. The decontamination by spectral subtraction is better achieved after reducing the spectral resolution because the background noise suffers from very large scatter. This is illustrated on a low-speed acquisition in figure 2.9, where all signals of the 23 sensors on the airfoil are plotted after subtraction with both resolutions of 1 Hz (standard in the present experiments) and 16 Hz (produced by further averaging), not accounting for the transfer function of the capillary tubes. The configuration E for the NACA-0012 airfoil is selected, for which Tollmien-Schlichting waves without acoustic feedback are expected. The drop at high frequencies below 0 dB (red plots) cannot be reproduced with $\Delta f = 1 \text{ Hz}$. It must be noted that the probe-response correction can only be applied if the background noise is eliminated. Otherwise applying the correction causes non-physical growth of the high-frequency level. Anyway the results make no sense anymore above 2 kHz, whereas they are reliable up to the limit of 25 kHz in figure 2.9. The indicative threshold for wall-pressure measurements with the present technique is around -3 dB at the remote microphones, in equivalent acoustic decibels (ref. $2 \times 10^{-5} \text{ Pa}$).

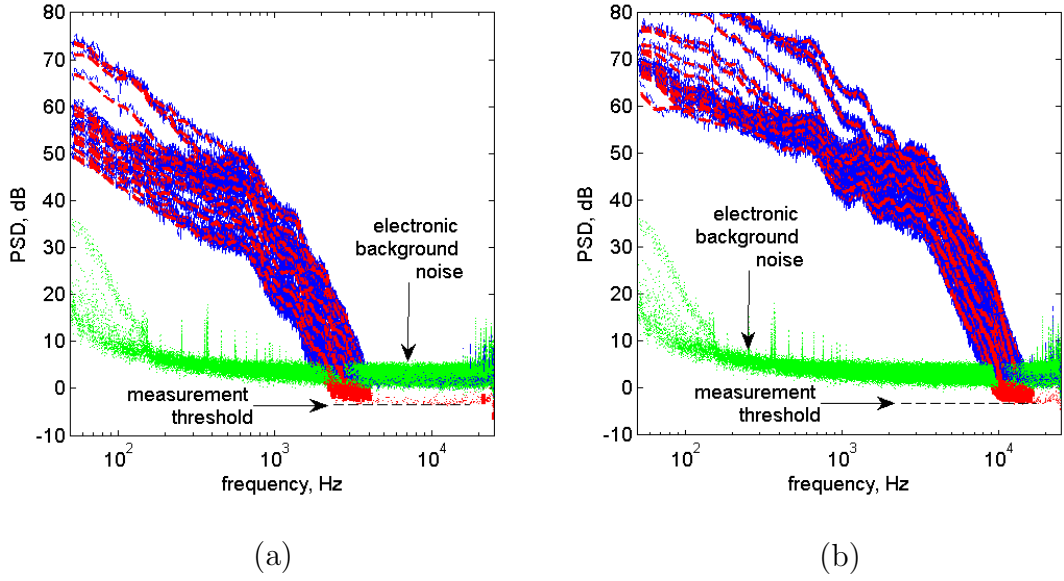


Figure 2.9: Typical wall-pressure spectra measured at low level (a) and high level (b) for transitional boundary layers without acoustic feedback. RMP response not included. — - subtracted background noise, — - spectra at 1 Hz, — - spectra at 16 Hz.

2.3.5 Effect of Wind-Tunnel Jet Shear Layers

In open-jet wind-tunnel experiments for which the flow width is not large when compared to the airfoil chord, a possible contamination of the local flow over the airfoil by the oscillations of the developing shear layers of the jet is expected. This is the case in the present study. A simple test has been performed to check that point. In the test, the airfoil being installed, an additional splitter plate of 3 cm chord and 30 cm span is placed at the boundary of the jet shear layer close to the streamwise location of the airfoil leading edge. The splitter plate radiates additional noise at the frequencies of the aforementioned oscillations, but its location has been chosen so that the tonal noise of the airfoil is not significantly modified.

This test provides a way of assessing the frequency range in which the contamination is possible (though it can be ineffective in practice). The results are reported in figure 2.10 for two flow speeds.

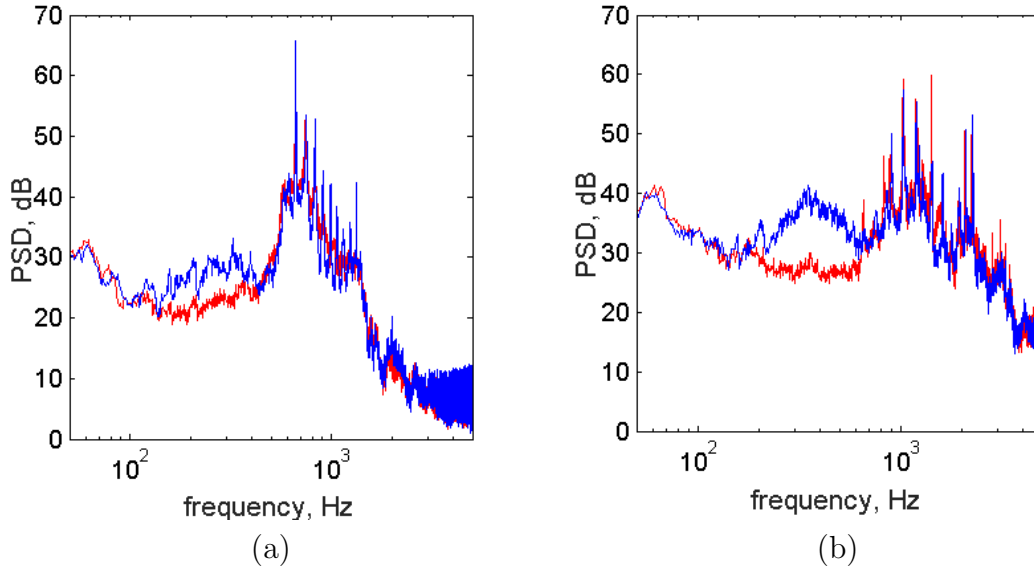


Figure 2.10: PSD plots for far-field microphone. NACA-0012 airfoil at zero angle of attack and (a) - at 16 m/s, (b)- at 25 m/s. Red line - clean airfoil, blue line - test with a splitter plate.

An extraneous broad hump is observed in a limited low-frequency range (from 100 Hz to 450 Hz at the flow speed of 16 m/s and from 180 Hz to 650 Hz of 25 m/s). In both configurations the tonal noise attributed to the laminar instabilities developing on the airfoil radiates at substantially higher frequencies and is not modified. However the splitter plate can act as a wave-scattering body, which probably explains the differences in the number and/or level of the tones.

It is concluded that the natural oscillations of the wind-tunnel jet do not question the observations of the LBL-wave radiation. However coherence spectra between pairs of wall-pressure probes could exhibit high values if the frequency range of the jet oscillations.

2.4 Pressure Coefficient Measurements

The pressure coefficient measurements were made by connecting the PVC tubes with the manometer. Before that the orifices receiving the microphones on the top instrumentation part of the airfoil were covered by plasticine to prevent leakages which may be a reason of incorrect results. The temperature was measured by

a thermometer before every data registration. After the connection of the probe with the manometer a pause of about 10 s was done to stabilize the flow.

The pressure coefficient was calculated by the formula [45]:

$$C_p = \frac{p - p_{atm}}{\frac{1}{2}\rho_0 U_\infty^2} \quad (2.12)$$

where p is the pressure at the point at which pressure coefficient is being evaluated; p_{atm} is the pressure in the freestream; ρ_0 is the freestream fluid density.

2.5 Hot-Wire Anemometry

Hot-wire measurements in the boundary layers of low Reynolds numbers airfoils allow to determine the separation bubble involved in the noise generation process.

The principle of the hot-wire anemometry is the following. As an electric current is circulating through the wire, heat generation and is balanced by the heat exchange with the surrounding fluid. With velocity changes the convective heat transfer coefficient changes too. Therefore the temperature of the wire changes and becomes the indicator of flow velocity variations. More details can be found in [46].

For the present measurements a single small-size sensor Dantec DYNAMICS, probe-type 55 P01, with a sensor resistance of $3.15\ \Omega$ was used. It has been verified that the probe and its support have no effect on the acoustic signature. The motorized supporting system allowed to move the probe normal to the incident flow direction, thus nearly normal to the wall. It was displaced at a series of chordwise locations. The initial measuring point was defined by visually making the probe nearly touch the wall, taking the coincidence of the probe with its shadow under an oblique light as indication but some inaccuracy remains that has been evaluated about 0.5 mm with the present driving system. As the wall of the airfoil is in metal sometimes the first measuring point is only indicative because of heat-conduction issues. During the measurements the probe was moved automatically across the boundary layer by steps of 0.1 mm to 0.5 mm, along a path of 2 to 4 mm depending on the chordwise location.

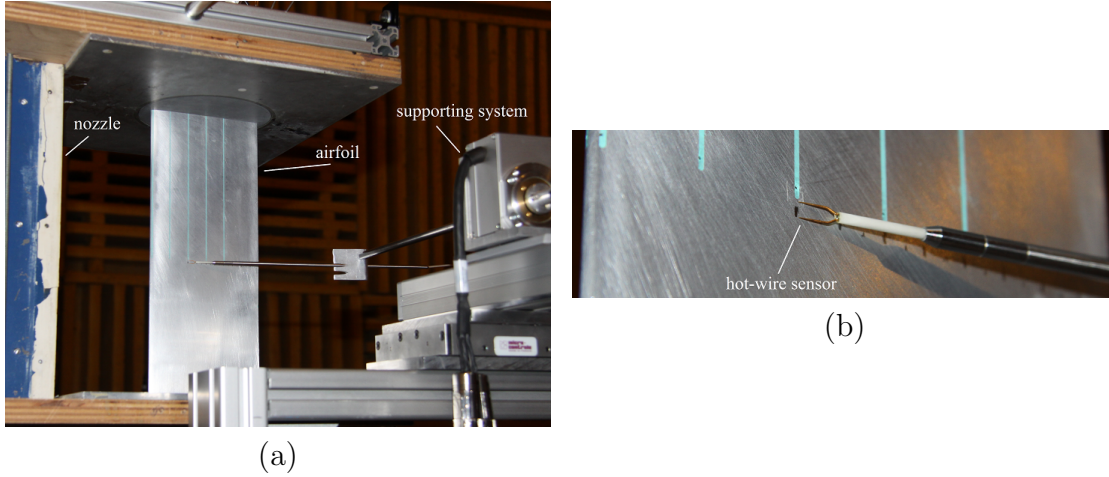


Figure 2.11: Experimental setup for HWA: (a) - picture of the experimental mockup during hot-wire anemometry measurements; (b) - detail of the active part of the hot-wire probe and RMP locations, showing the ends of refilled grooves.

The calibration of the system has been done twice per day because of the sensitivity of the measurements to temperature. For this the probe is exposed to a set of known velocities and the output voltage is recorded. The calibration curve (see figure 2.12) is used as a transfer function for converting data records from voltages into velocities. This is the reason of another disadvantage of the method. As the mean flow approaches zero the value becomes inaccurate (see the calibration curve in figure 2.12), as especially as the hot-wire theory assumes that the velocity fluctuates around a non-zero mean value. Therefore part of the measurements are indicative.

The hot-wire measurements provide values of the local mean-flow speed and of the root-mean-square velocity component parallel to the mean-flow direction. In principle the fluctuating velocity normal to the wall could be accessed with a cross-wire probe of larger size; this was not attempted here in order to ensure the targeted resolution in the data and to avoid intrusiveness.

As the time signals were recorded on acquisitions of 30 s at every point the PSD for flow velocities can be produced. A couple of wall-pressure signals have been acquired simultaneously in order to also compute indicative pressure-velocity correlations.

The velocity profiles were measured at different locations from 40% of chord to the near wake at a distance of about 1-2 mm beyond the trailing edge. It must be kept in mind that the hot-wire anemometry cannot discriminate upstream and

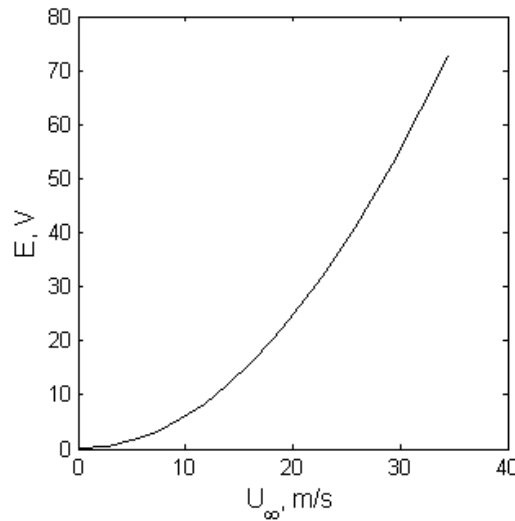


Figure 2.12: An example of the calibration curve.

downstream fluid motions; in the case of a reversed flow in a separation area the negative value of the velocity is measured as positive.

2.6 Flow Visualization

Surface flow visualization was used as an additional method for the determination of separation areas. By the way, this method sometimes allows to observe a reversed flow that cannot be registered by hot-wire anemometry.

Several tests were conducted with different types of mixture, varying flow velocities and angles of attack. After several tests a mixture made of carbon soot, benzol and white spirit was chosen because of suitable characteristics. Two positions of the airfoil, vertical and horizontal, were tested. Both of them have some advantage and some weakness. On the one hand during the data registration in vertical position the drops influenced by gravitation go down especially near the trailing edge. On the other hand this happen if separation takes place. And in case of reattachment the drops change their direction of motion, which is a good indication of the border of the separation bubble. In horizontal position the stagnation of drops near the trailing edge takes place and can change the characteristics of

the flow.

The mixture was applied on the surface of the airfoil by a brush. Videos were made by a Canon 550d camera.

2.7 General Methods for Data Analysis

2.7.1 Cross-Spectral Analyses

The spectral coherence γ^2 is a statistics that can be used to examine the degree of linear relationship between two signals or data sets. It is defined as:

$$\gamma^2(f) = \frac{|G_{xy}(f)|^2}{G_{xx}(f)G_{yy}(f)} \quad (2.13)$$

where $|G_{xy}(f)|$ is the magnitude of the cross-spectral density between the signals $x(t)$ and $y(t)$, $G_{xx}(f)$ and $G_{yy}(f)$ are the autospectral densities of x and y respectively. As a level of linear relationship between signals coherence can be interpreted in different ways.

Two probes close enough to each other in chordwise direction are should have a quite high level of coherence even if they corresponds to hydridynamic information (because the assumption of the frozen hydrodynamic motion is only valid over short distance). This is *a fortiori* true for acoustic motion. In case of turbulent motion which is random the doublet of probes probably has a small coherence level. If the coherence is high, the streamwise pair of probes gives access to a characteristic phase speed.

The coherence between signals of aerodynamic nature measured simultaneously at several spanwise locations by a set of probes provides the spanwise correlation length l_y of the wall-pressure fluctuations. It is a key information to characterize the radiation efficiency of trailing-edge noise sources if taken at a short chordwise

distance to the trailing edge.

$$l_y(\omega) = 2 \int_0^{\infty} \sqrt{\gamma^2(\omega, \eta)} d\eta \quad (2.14)$$

In practice only a limited number of values of the separation η can be obtained in an experiment. It is understood that they are fitted by some theoretical law to allow the computation of the integral.

As acoustic wave motion is linear two acoustic (in nature) signals taken from the same acoustic field have a coherence level equal to 1. This can be observed between two far-field microphones, two wall-pressure sensors where the pressure fluctuations are associated with only acoustic motion (usually beneath a laminar and stable boundary layer), or between an acoustic wall-pressure sensor and a far-field microphone. In such cases it is possible to recover the sound propagation speed on the basis of a cross-spectrum.

A drop or a loss of coherence does not mean that there is no relationship between the two signals of interest; a relationship other than linear can exist, or the linear part of the relationship is overwhelmed by another mechanism.

2.7.2 Time-Frequency Analysis

The acoustic signature as heard during the experiments obviously exhibits variations with large characteristic time scales when compared to the acoustic periods, such as intermittency or sudden changes. The associated statistical quantities are not stationary, making the classical Fourier analysis not relevant because of the underlying averaging procedure. This is why time-frequency analysis was performed, either to extract stationary parts of the signals or to track the sound level and frequency content of the signals as functions of a slowly-varying time. The observation of various acoustic signatures in the same configuration could be the origin of discrepancies between measured and computed signals, because most numerical simulations are performed on very short time intervals. They are also possibly related to an extreme sensitivity of the mechanism to installation effects which differ from an experimental investigation to another. As a result the detailed mechanisms of TS-wave radiation can be observed and more convincing comparisons can be made. In the present study the short-term Fourier transform with an overlap of 50% of adjacent samples was applied.

2.7.3 Bicoherence Analysis

Bispectral analysis is a higher-order spectral analysis that has been used to examine data for quadratic nonlinearities in a variety of applications (more details in [47]). It is applied to a single time signal. The bicoherence, the normalized version of the bispectrum, measures the proportion of the signal energy at any couple of frequencies that is quadratically phase coupled. Phase coupling is observed when two frequencies f_1 and f_2 are simultaneously present in the signal with their sum or difference. The sum of the phases Φ_1 and Φ_2 of these frequency components remains constant. The bicoherence is usually normalized in the same way as a correlation coefficient and a classical coherence. It is close to 1 when the signal contains three frequencies that satisfy the relations $f_1 + f_2 = f$ and $\Phi_1 + \Phi_2 = \Phi + cst$, otherwise it is close to 0 (or a low residual level due to the non-converged statistics). The intermediate value of bicoherence can present a part of energy came from coupling between two components ([48]). It is written as

$$b(f_1, f_2) = \frac{|\sum_n F_n(f_1)F_n(f_2)F_n^*(f_1 + f_2)|}{\sqrt{\sum_n |F_n(f_1)|^2 |F_n(f_2)|^2 |F_n^*(f_1 + f_2)|^2}} \quad (2.15)$$

where F is the Fourier transform of the signal, $(.)^*$ denotes the complex conjugate (note that the Fourier transform and the bispectrum are complex-valued quantities), and n denotes the sample index of the averaging procedure.

The bispectral analysis of the numerical signal conducted by Kim & Powers [48] allows to distinguish the self-excited oscillations and "secondary" oscillations produced by non-linear interaction.

As was described by Soreefan [49] there are several main combinations between frequencies f_k, f_l and f_m ($f_k < f_l < f_m$):

- $f_k + f_k \longrightarrow 2f_k$: where $2f_k$ is a harmonic of primary frequency f_k ;
- $f_k + f_l \longrightarrow f_m$: secondary frequency f_m was generated by non-linear interaction of two primary frequencies f_k and f_l ;
- $f_m - f_k \longrightarrow f_l$: secondary frequency f_l produced by non-linear interaction of the f_m and f_k ;
- $f_m - f_l \longrightarrow f_k$: f_k is a result of non-linear interaction of the primary frequencies f_m and f_l .

Traces in the bicoherence chart confirm partial phase-coupling between the frequencies. But this kind of analysis is very complicated for interpretation. Spots would indicate sharply defined unchanging locked frequencies. It is often stated that lines are due to a single mode interacting with a broad range of frequencies. Two interacting oscillators (continuously exchanging energy) also produce lines in the bicoherence plot. In this thesis the bicoherence is identified as a possible way of highlighting some features of the TS-wave radiation mechanism, typically nonlinear.

To compute the bicoherence the acoustic signal is divided into 60 samples of 25600 Hz.

2.8 Uncertainty Assessment

A measurement is the determination of some characteristic parameters of an object or an event, which can be compared with parameters of an other object or event. However, any real measurement is an approximation of the true value with a positive or negative deviation. The causes of the deviation can exist because of instrumentation, data acquisition, environmental conditions and so on [50]. Therefore a recorded measurement is complete only when it includes an estimate of its uncertainty. An uncertainty of measurement is the doubt that exists about the result of any measurement and gives an idea about its quality.

As the present investigation was carried out at transitional regimes the phenomenon is very sensitive to the effects of the set-up and possibly any small variation of the conditions. The calculated values may explain some controversial points of experimental results. It should be mentioned that information about uncertainties is useful if the test are to be repeated in future. The complete calculation of the uncertainty is a complicated task, which requires to have enough repeated measurements or some statistical information. However the quantity of the tests is limited and a statistical database is not available. Therefore, the analysis of the possible uncertainty sources has been done as a first step.

For recognition of the possible sources of uncertainties the analysis of the whole process of measurements should be done. Initial tests showed that the key parameters of the flow such as flow velocity and angle of attack are responsible for significant changes in observed phenomenon. Therefore the uncertainty of these

parameters may have an influence on all types of measurements. The angle of attack was changed manually according to the scale marked on the plates of the experimental set-up. The possible deviation of the value can be estimated as $\pm 0.5^\circ$. The flow velocity was determined by a Pitot tube and a micro-manometer Furness FCO 510, which has the accuracy of calibration to 0.25% of readings. In principle the Pitot tube should be located along the axis of the airfoil chord on the nozzle plane. Obviously, the location may be not exact. The values of the flow velocity were defined according to the display on the manometer and were expressed in round numbers (the uncertainty is around ± 0.5 m/s). The uncertainty of round numbers may also be associated with the pressure coefficient (around ± 0.5 Pa). The theoretical basis of the Pitot tube measurements is Bernoulli's equation where the density of the flow is taken into account. Hence the variation of temperature of the surrounding atmosphere depending of the season may have some effects on the value of the flow velocity. But it should be mentioned that the sets of measurements, for example for the pressure coefficient, were taken during the short time periods and it is believed that the temperature should not produce a big deviation during each period.

As was described in the section 2.6 for flow visualization several types of mixture were tested. The viscosity plays a key role in this case. If the viscosity is too high the mixture accumulates at some parts of the airfoil and may slightly change the parameters of the flow. Indeed the separation layers to be identified are very thin (~ 1 mm order of magnitude). The location of the separation bubble was defined visually, which is also a source of some deviation between results. Several tests at the same configurations were provided and in general the deviation between locations of the separation bubble was limited to ± 5 mm.

The results of the flow visualization were completed by the hot-wire anemometry measurements. This type of measurements has high sensitivity to temperature of environment. Thus the calibration procedure (see the section 2.5) was conducted twice per day to avoid uncertainty due to the temperature variation. Another source of uncertainty is the initial location of the hot-wire probe provided manually. Besides, the measurements were conducted at chordwise locations varied from 5 mm to 10 mm, which could not guarantee the exact determination of the separation bubble location.

The high precision of the location of the separation bubble is not a required result because differences of a couple of millimeters do not change the understanding of the whole mechanism. Yet the true location can be important for a quantitative comparison with simulations.

A calibration of the microphones was done (see section 2.3.3). Another important parameter is therefore the sensitivities of the microphones (the smallest signal measured by an instrument) which were measured and used for correction of the spectra. The level of the background noise was investigated also (see section 2.3.4). Hence these facts were excluded from the uncertainty estimation.

2.9 Concluding Remarks

The parameters of the experimental setup and the main measuring techniques were described in this chapter. A symmetric NACA-0012 airfoil and a slightly cambered SD7003 airfoil with 12 cm chordlengths were used for the investigation of the trailing-edge noise. Apart from the far-field microphone measuring the noise signature, remote microphone probes RMP were used to measure the surface pressure. This provides a better understanding of the boundary layer instabilities. A calibration procedure of the remote microphone probes was described also. The electronic back ground noise from the RMP signals was measured as well as the wind-tunnel background noise; they are low enough to allow a clear interpretation of the results. It was also observed that the wind-tunnel jet shear layers influence the measured data at low frequencies which are below the area of interest. The pressure coefficient was measured as a reference parameter representative of the operating point of the tested airfoil; this allows defining some identity of the experimental and numerical flows. For the investigation of a separation bubble the hot-wire anemometry and the flow visualization were conducted. The basis of the post-processing methods applied later on, such as cross-spectral, time-frequency and bicoherence analyses were explained. Finally, an estimation of the uncertainty was done. The obtained experimental results for the symmetric NACA-0012 airfoil are reported in the next chapter.

Chapter 3

Experimental Results for the NACA-0012 airfoil

This chapter surveys the experimental results of the NACA-0012 airfoil. The ranges of angle of attack and flow speed of the tonal noise phenomenon coincide with those reported by other investigators. The determination of the equivalent load allows to compare the parameters of the flow with numerical simulation. The detailed investigation of the acoustic signature and its dependence on the angle of attack, chord length and upstream turbulence is discussed. It is demonstrated that the separation bubble is a necessary condition for the high-intensity trailing-edge noise. As the NACA-0012 airfoil is well documented the comparison with previous researches provides reasonable agreement and confirms that the measurements are reliable.

Coherence plots of the wall-pressure signals in chordwise and spanwise directions are also presented. The bicoherence analysis shows the existence of non-linear relationship between tones. Several regimes of the noise emission are observed and some intermittency is indicated by the time-frequency analysis.

3.1 Ranges of Parameters of the Tonal Noise

The ranges of flow-speed or associated Reynolds numbers and of angle of attack in which the tonal trailing-edge noise of an airfoil is observed is a key step in the characterization. The first acoustic data was registered by simply listening the sound for determining the limiting conditions of the tonal trailing-edge noise. At several velocities ($0.6 \times 10^5 < Re < 2.6 \times 10^5$) the geometrical angles of attack were changed from -15° to 15° . Filming the angle of attack graduation and registering the sound were done for further analysis. Configurations with tripping devices were also tested.

The clean airfoil exhibits several regimes of the tonal noise generation. This fact motivated the detailed investigation with time-frequency analysis which is described in section 3.7. The first one is a regime with a stable strong single tone. Another one is a switching regime where two non simultaneous tones switch between each other. The last one is a regime of multiple tones which can be observed simultaneously.

The registered data were transposed into the Reynolds-number versus effective angle of attack plot (figure 3.1(a)).

The “primary” noise (empty circles) without clear tones was registered as a preliminary step for the emission of tonal noise. A low-level narrow-band signature is heard. It may be associated with starting instabilities in the boundary layer without amplification by the feedback loop. The area of the tonal noise is indicated by the solid circles. With the increase of the flow velocity the range of the angles of attack enlarges. A slight asymmetry around 0.5° of the tonal noise area is noted.

Using the tripping device allowed to “switch off” one side of the airfoil and determine the role of each one in the noise generation. As shown on the plot by the stars (*) at low flow velocities the suction side is producing the tones. However the large area at higher speeds involves the pressure side. The same phenomenon was observed by Inasawa *et al.*[28] and Pröbsting [8]. The surprising fact is the disappearance of the tones at 33 m/s ($Re_c = 2.6 \times 10^5$) around zero angle of attack. It is possible that at this combination of flow conditions one of the necessary components of the tonal trailing-edge noise such as instability waves, feedback loop or separation bubble is suppressed.

The experimental data were compared with the results of Arcondoulis *et al.*[4] and Pröbsting [8](figure 3.1(b)). Pröbsting in his work pointed that the limits of the tonal noise (solid black line) calculated by Lowson *et al.*[3] should be re-

calculated for the effective angle of attack. He also determined separated areas (hatched areas) where the suction or pressure side produced tones. The solid symbols are for tonal cases and the empty symbols are for non tonal cases. The tonal area of Pröbsting is considerably wider than the one observed by Arcondoulis *et al.*[4]. The upper limit is more than 4.5° at Reynolds numbers around 10^5 . The present study has tonal noise limits at a similar angle, but at higher flow velocity ($Re = 2.6 \times 10^5$). Arcondoulis *et al.*[4] registered tones at $Re = 1.5 \times 10^5$ for an angle of attack around 3° . The area of tonal noise in the present study (marked by grey color) is in reasonable agreement with aforementioned data. Moreover, the limits where the suction side produces tones as mentioned by Pröbsting coincide. Another interesting fact is that the gap of the tonal noise at high velocities close to the zero angle of attack was also reported by Arcondoulis *et al.*[4]. The differences are attributed to the sensitivity of the phenomenon to the parameters of the experimental setup.

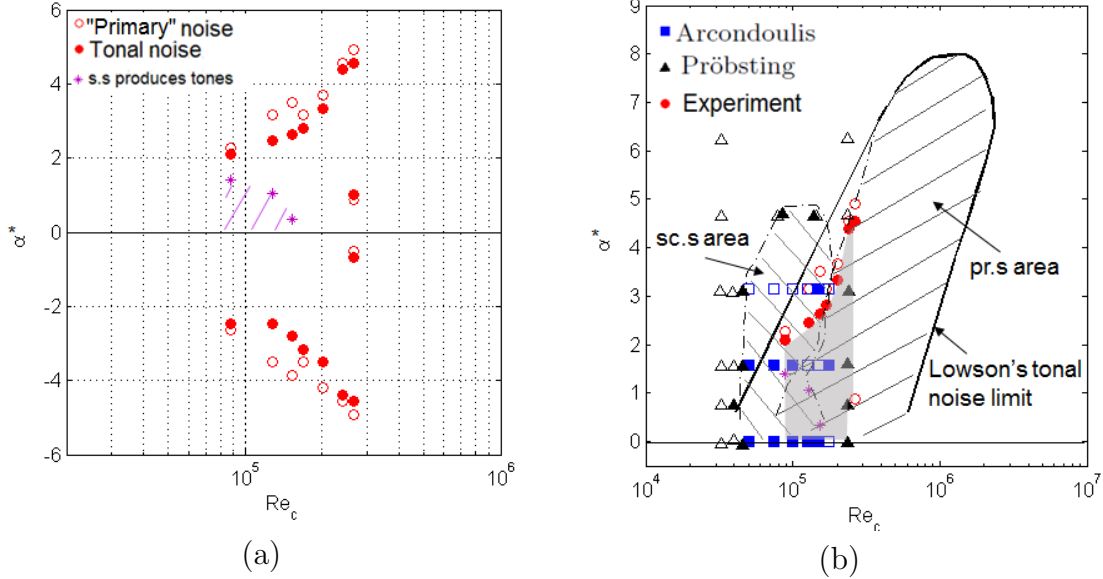


Figure 3.1: Reynolds-number versus effective angle of attack chart for tonal noise of the NACA-0012 airfoil. (a) - present experiment, (b) - comparison with previous investigations[8, 4].

3.2 Pressure Coefficient Measurements

The pressure coefficient is a necessary parameter for comparison with numerical simulation to ensure that the airfoil loadings corresponds to each other. For the symmetric NACA-0012 airfoil the measurements at $\alpha = 0^\circ$ were performed as well as at $\alpha = 5^\circ$ and $\alpha = -5^\circ$ which allows to get more precise data for the pressure and suction sides. The measurements were conducted at 25 m/s. The results for airfoils with two different chord lengths (10 cm and 12 cm) are summarized in figure 3.2. The values are close to each other. The small differences are attributed to a moderate effect of the Reynolds number. Furthermore the installation effect differs for both airfoils. This leads to a smaller effective angle of attack as shown by a different coefficient in Brook's formula. The presence or not of the tripping device has not been found to produce a significant difference on the C_p distribution.

The pressure-coefficient distribution for the NACA-0012 airfoil at 5° angle of attack is also compared with a simulation in figure 3.3. The computation has been performed with the XFOIL software assuming an infinite flow extension. The

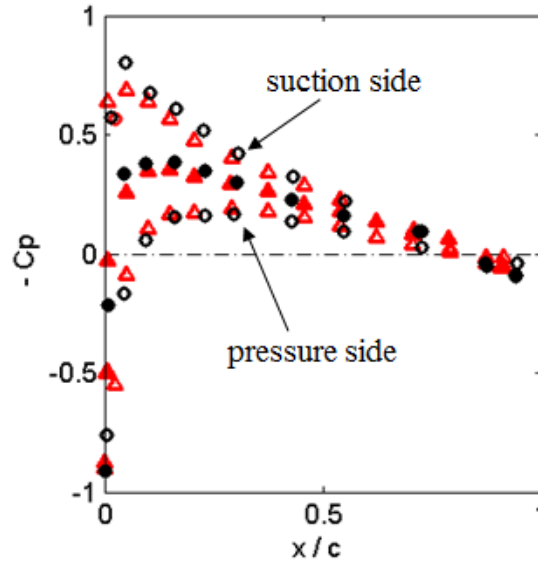


Figure 3.2: Pressure coefficient distribution for the NACA-0012 airfoil at 25 m/s with chord lengths 10 cm (\bullet for $\alpha = 0^\circ$, \circ for $\alpha = 5^\circ$) and 12 cm (\blacktriangle for $\alpha = 0^\circ$, \triangle for $\alpha = 5^\circ$). Configuration A.

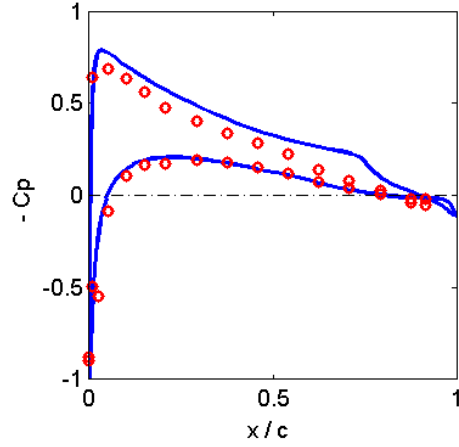


Figure 3.3: Measured and computed pressure coefficients for the NACA-0012 airfoil of 12 cm chord length. (— Xfoil simulation at $\alpha^* = 1.75^\circ$; \circ - experimental data at $\alpha = 5^\circ$)

predicted pressure drop in the rear part of the airfoil is not seen in the experiment in spite of the correction leading to the effective angle of attack. As was mentioned by Moreau *et al.*[51] the free-jet wind-tunnel experiments have a strong effect on the loading and flow parameters. Therefore a simulation should take explicitly into account the nozzle configuration.

3.3 Directivity Measurements

The directivity measurements complete the characterization of the source of sound. A typical result is presented as a color map or so called radiation map in figure 3.4(a), where the sound level is shown as a function of angle of attack and frequency. The white band between -15° and 15° corresponds to the angular range covered by the wind tunnel jet, where measurements are contaminated by the pseudo-sound pressure of the jet mixing. On both sides and low frequencies the trace of the pseudo-sound is still visible. The sound field seems to be symmetric with respect to the plane of the airfoil. The lower-frequency part of the map is attributed to the background noise, essentially residual jet noise and the noise from the flow over the end-plates. Two tones are clearly identified at frequencies 744 Hz and 840 Hz, which are presented in the directivity diagram in figure 3.4(b)

to emphasize the symmetry. The drop at small angles is characteristic of the dipole-like sources of the trailing-edge noise. The lobed patterns are similar for both frequencies, which remain relatively quite close to each other.

For a more complete description, radiation maps at lower (8 m/s) and higher (25 m/s) flow velocities are shown in figure 3.6. As one can note the horizontal yellow-to-red traces associated with the tonal noise radiation move up with increasing flow velocities. As frequency increases the sound is weaker at small observation angles close to the jet area. The level of the background noise also increases with flow speed.

Angle-frequency radiation maps show evidence of secondary low-frequency tone emergence associated with multiple amplified frequencies, as pointed out in figures 3.5 and 3.6(a) (at least up to 16 m/s). The low-frequency tone is sometimes more pronounced on the wall-side and has a frequency close to $(f_2 - f_1)/2$ when the two tones at frequencies f_1 and f_2 are observed in the LBL wave range. This can be interpreted differently, either from the linear superposition of two intrinsic frequencies or from the modulation of the intermediate frequency by a much lower envelope frequency, in extrapolation of the formula

$$\begin{aligned} & \cos(2\pi f_1 t + \phi_1) + \cos(2\pi f_2 t + \phi_2) \\ &= 2 \cos \frac{2\pi(f_1 + f_2) + (\phi_1 + \phi_2)}{2} \cos \frac{2\pi(f_1 - f_2) + (\phi_1 - \phi_2)}{2} \end{aligned} \quad (3.1)$$

Therefore the question arises of whether the tones are inherently selected by the feedback mechanism on LBL waves and give rise to the low-frequency emergence or if they result from the modulation of a single frequency by another low-frequency oscillation that could be caused by the experimental setup. Low-frequency oscillations can be found in the instabilities of the free shear layers of the nozzle jet in the present experiment. This is why the tracking of the low-frequency tones becomes crucial.

Increasing the angle of attack up to 5° reduces the PSD level and shift the tones to higher frequencies. The second harmonic tones are clearly shown in figure 3.7(b). It should be mentioned that because of the flow deviation the influence of the pseudo sound pressure from the jet became considerable at small observation angles. At the flow velocity of 30 m/s (figure 3.7(b)) several harmonic tones at high frequencies with low sound pressure level are observed, which was not the case at zero angle of attack.

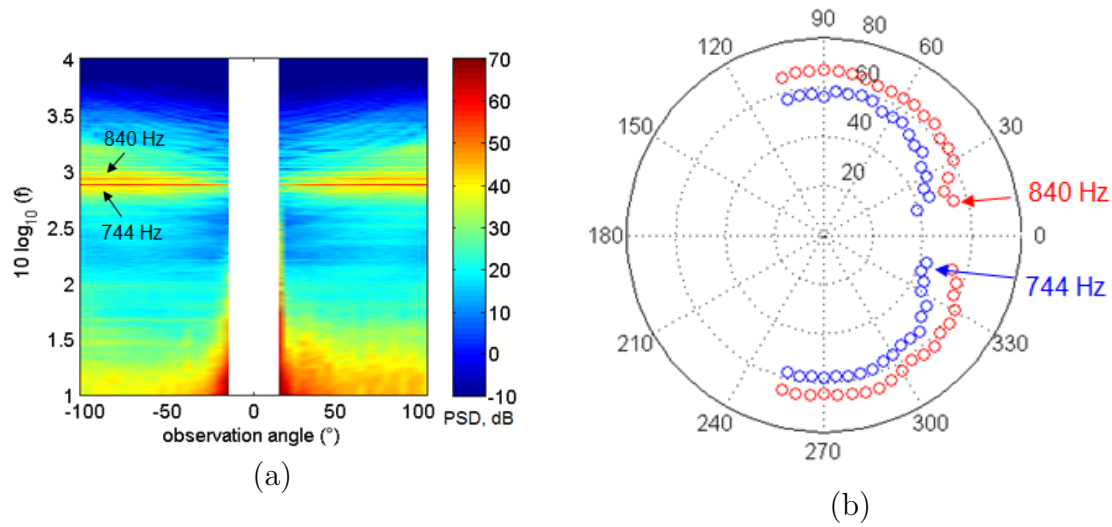


Figure 3.4: Results of the directivity measurements for the NACA-0012 airfoil at 19 m/s and zero angle of attack. (a) angle-frequency radiation map; (b) directivity diagram of the main tones. Configuration A.

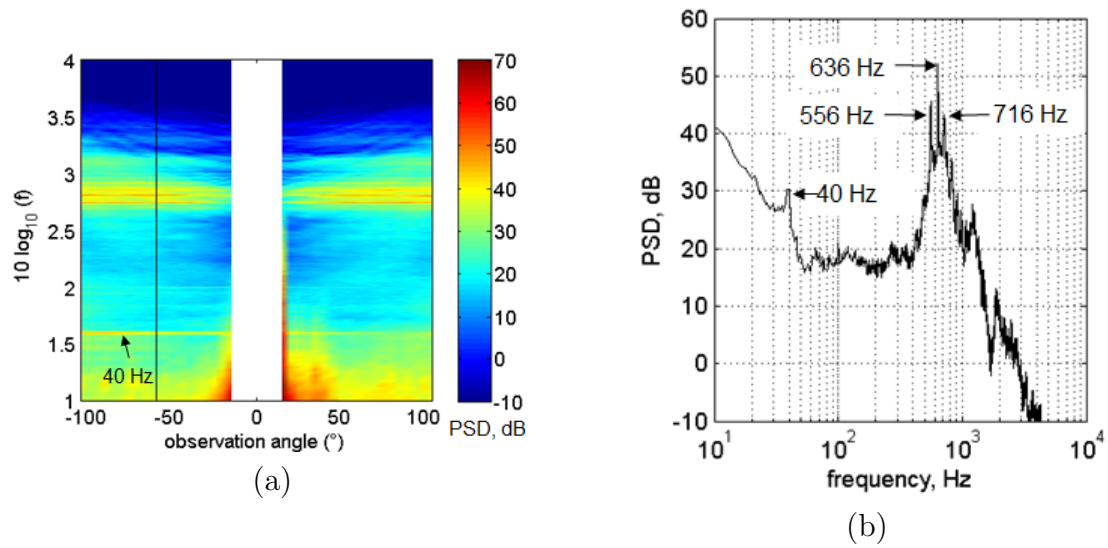


Figure 3.5: (a) angle-frequency radiation map for the NACA-0012 airfoil at zero angle of attack and at 16 m/s. Black line show the angle for which a PSD plot (b) was done. Configuration A.

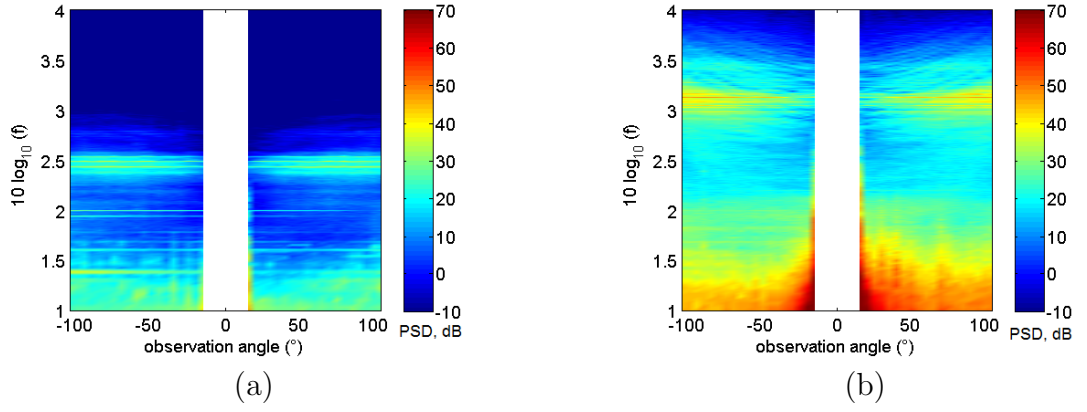


Figure 3.6: Angle-frequency radiation maps for the NACA-0012 airfoil at zero angle of attack: (a) at 8 m/s; (b) at 25 m/s. Configuration A.

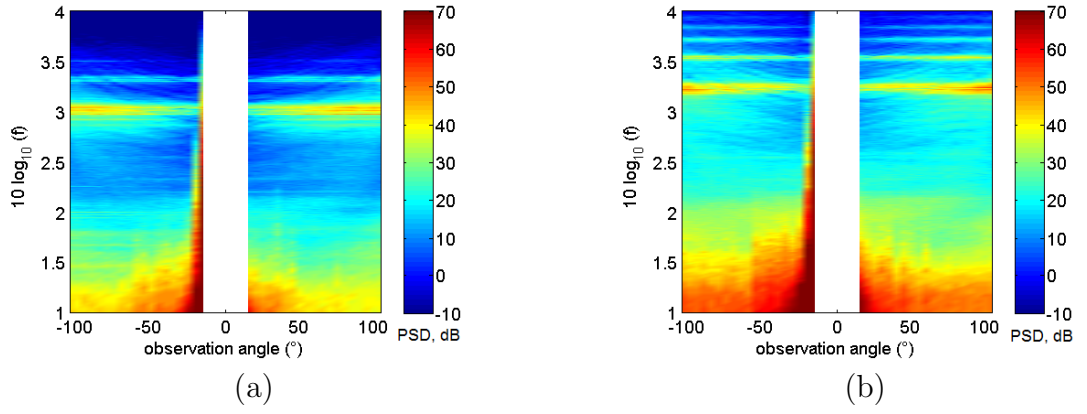


Figure 3.7: Angle-frequency radiation maps for the NACA-0012 airfoil at 5° and : (a) at 19 m/s; (b) at 30 m/s. Configuration A.

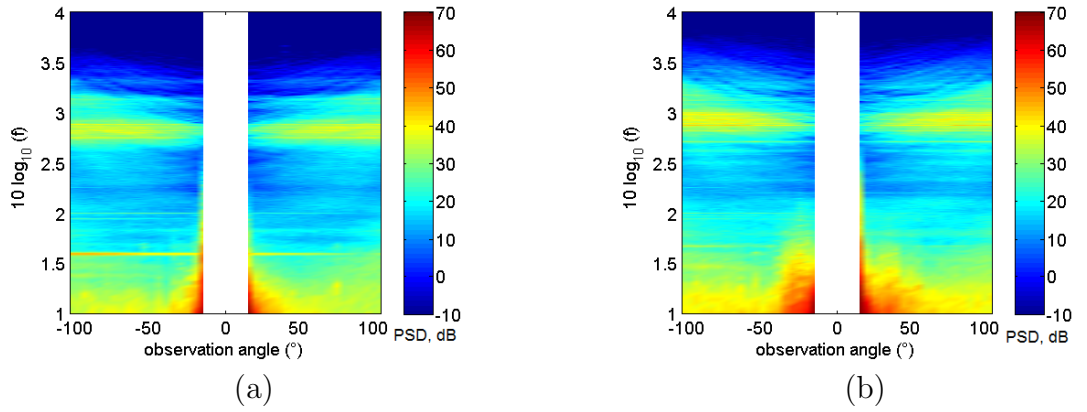


Figure 3.8: Angle-frequency radiation maps for the NACA-0012 airfoil at zero angle of attack and : (a) at 16 m/s; (b) at 19 m/s. Configuration B.

Tests with a tripping device on the door side of the airfoil show the decreasing of the sound level (compare with figure 3.4), but the general noise signature remains the same (see figure 3.8(a)). At 16 m/s (figure 3.8(b)) an asymmetrical tone at low frequency is also found.

3.4 Far-field Acoustic Signature

The first evidence of the ladder-type structure of the tonal noise was reported by Paterson *et al.*[1] during inspection of the far-field area for a NACA-0012 airfoil with nearly 23 cm chord length. The special scaling laws $U_\infty^{1.5}$ and $U_\infty^{0.8}$ for the tone frequencies were proposed. The observation of the ladder-type structure confirms that the experimental setup is reliable, in view of what has been observed by previous investigators.

The details of the far-field measurements were described in chapter 2.3.

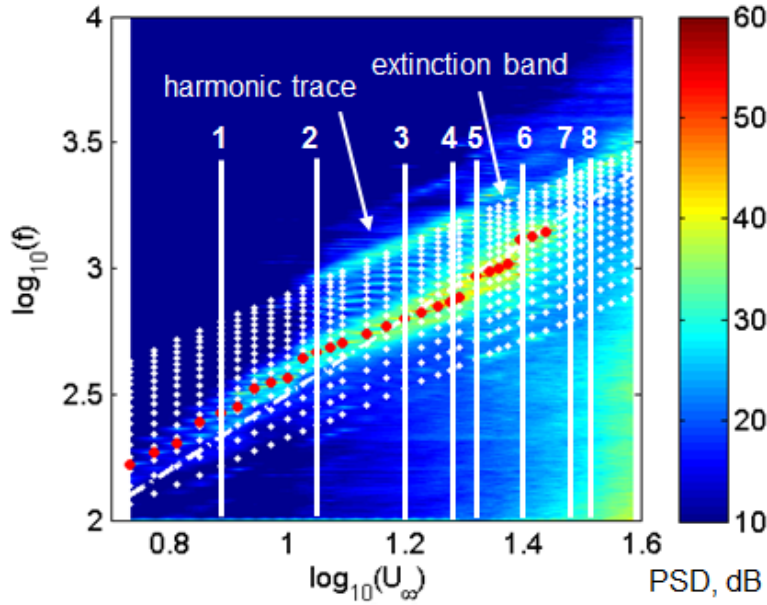


Figure 3.9: Frequency-flow speed charts of LBL-wave radiation for the NACA-0012 airfoil at zero angle of attack. Configuration A. 8 speeds are marked: 1 - 8 m/s ($Re_c = 0.63 \times 10^5$); 2 - 11 m/s ($Re_c = 0.87 \times 10^5$); 3 - 16 m/s ($Re_c = 1.26 \times 10^5$); 4 - 19 m/s ($Re_c = 1.5 \times 10^5$); 5 - 21 m/s ($Re_c = 1.6 \times 10^5$); 6 - 25 m/s ($Re_c = 2 \times 10^5$); 7 - 30 m/s ($Re_c = 2.4 \times 10^5$); 8 - 33 m/s ($Re_c = 2.6 \times 10^5$).

3.4.1 Ladder-Type Structure

The noise signature of the NACA-0012 airfoil in the far-field can also be plotted as a color map versus frequency and Reynolds numbers. In this map the dominant tones are indicated by red dots which as can be seen from the figure 3.9 generate a ladder-type structure discussed in [1, 2, 36, 7]. The main trace corresponding to the hump generated by boundary layer instabilities scales like $f \sim U_\infty^{1.5}$, whereas the “steps” of the ladder are in agreement with $f \sim U_\infty^{0.8}$. The jumps take place when the dominant tone gets too far from the main trace axis.

In the case of configuration A with clean airfoil the noise signature covers a wide range of flow velocities. Moreover the main trace is accompanied by the thinner and parallel harmonic trace at higher velocities. The map is sometimes cut by horizontal extinction bands at $10\log_{10}(f) = 3.25$, which does not depends on the flow velocity. In figure 3.9(a) the oblique dotted lines are produced by a simplified expression of the feedback loop formula relating the expected frequencies of the tones to the length L over which the process takes place. The tones are predicted at the values f_n such that

$$\frac{f_n L}{U_\infty} = \left(n + \frac{1}{2}\right) \left[a + \frac{M_\infty}{1 - M_\infty}\right]^{-1} \quad (3.2)$$

where $a = U_\infty/U_c$ is the ratio of the external flow speed to the averaged convection speed of the instability waves and M_∞ is the Mach number. The factor $1/2$ has been identified as associated with the trailing-edge scattering [2]. The formula is abusively simplified in the sense that it assumes constant values of velocities that are in fact local and thus variable quantities along the airfoil. Yet it is consistent if the feedback length L is adjusted. A refined feedback formula can be written if the convection speed is determined from the linear-stability theory of parallel flows, for instance [52]. Equation (3.2) is compatible with the observed traces in the charts because it predicts a variation of the frequencies f_n close to $U_\infty^{0.8}$.

For a more detailed analysis eight flow velocities were chosen, indicated by the white vertical lines in figure 3.9.

The far-field spectra for eight investigated velocities in figure 3.10 illustrate the behavior of the ladder-type structure. Note that successive spectra are shifted by 50 dB from each other for clarity. The increase of the dominant tone frequency is shown by arrows. At 8 m/s the broadband hump is slightly noticeable with a dominant tone close to its central frequency and two lower tones on both sides.

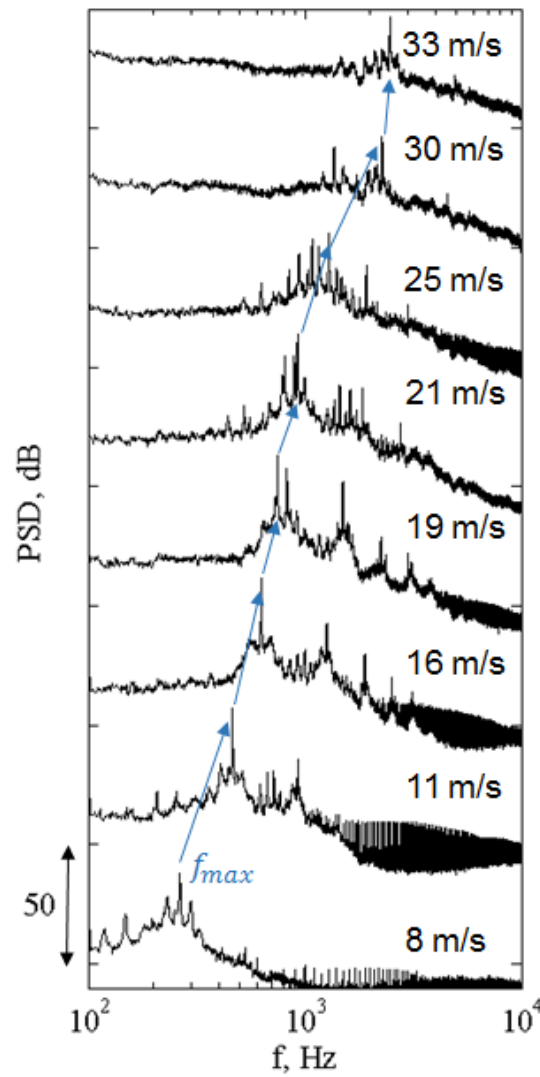


Figure 3.10: Noise spectra for the NACA-0012 airfoil in configuration A and at zero angle of attack.

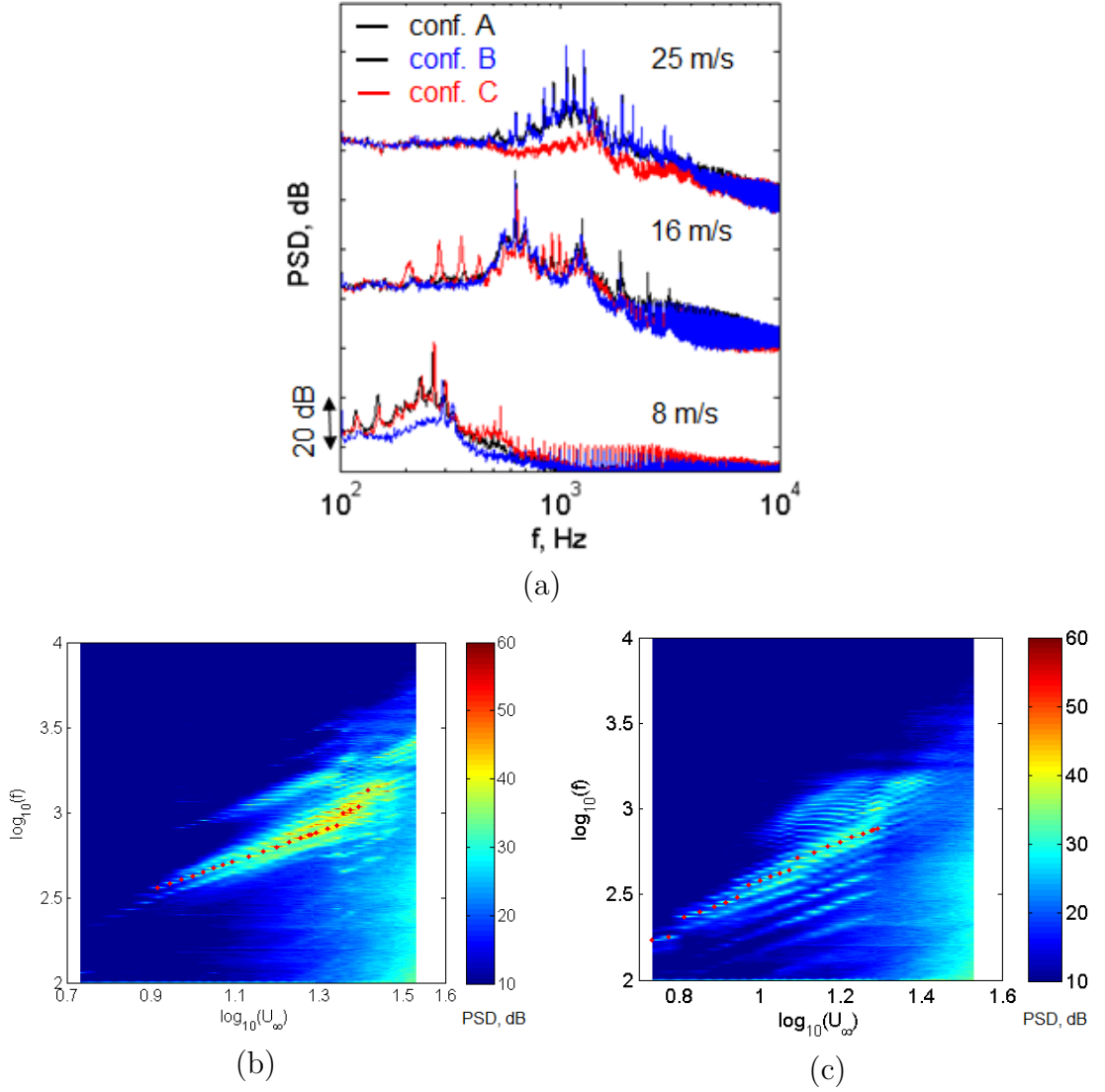


Figure 3.11: Frequency-flow speed charts of LBL-wave radiation for NACA-0012 airfoil at zero angle of attack. (a) - Comparison of the power spectra density of configurations A,B,C at different speeds; (b) - Configuration B; (c) - Configuration C.

At 11 m/s the hump is more visible with a marked dominant tone and a second harmonic hump. At 19 m/s two tones with very similar levels are observed at similar distances from the central frequency. At 25 m/s one can notice multiple discrete tones with a significant level. At higher velocities the single dominant tone can be noticed but with lower intensity.

Previously it was found (see [26, 12]) that the central frequency of the broadband hump correspond to the frequency of the most amplified LBL wave, which provides clear evidence that the broadband hump can be associated with LBL waves.

3.4.2 Influence of the Tripping Device

The aim of the test with a tripping device was to elucidate which side of the airfoil produces sound. Tripping has the effect of forcing transition to turbulence in the boundary layer, allowing for coherent motion associated with LBL waves only on the untripped side. Therefore the chart without tripping in figures 3.9(a), 3.12(a) can be interpreted as a combined effect of LBL waves developing on both sides, but the combination might not be a simple linear sum of effects.

Similar investigations were performed by Paterson *et al.*[1], Nash *et al.*[12] where the authors conclude that the pressure side was responsible for tonal noise generation by the NACA-0012 airfoil. The investigation of Inasawa *et al.*[28] found that the side which produces tonal noise changed with the Reynolds numbers: the suction side became dominant in this process at low flow velocities and angles of attack. This was proved also by Pröbsting *et al.*[29].

Both sides of the NACA-0012 airfoil were tested with tripping at $\alpha = 0^\circ$ (figure 3.9(c),(d)). Unexpected differences were observed despite the fact that the configuration without tripping is totally symmetric. The configuration B (figure 3.9(c)) has a very similar noise signature in comparison with the clean airfoil even with harmonic trace. The noise radiation in this case starts from slightly higher flow velocities. The configuration C (figure 3.9(d)) shows that the door side has weak contribution in noise signature. However at low flow velocities (see 3.9(b) 8 m/s) the spectra of this configuration coincides with the clean airfoil signature, which means that the door side plays a key role for these parameters. At moderate flow velocity 16 m/s the contribution of both sides can be observed. Further increasing the speed makes the wall side dominant. The same process can be observed in the case $\alpha = 5^\circ$ presented in figures 3.12(c),(d). The result supports the conclusions of section 3.1 and confirms the conclusions of previous researchers

for the NACA-0012 airfoil with different chord lengths [28, 29, 34] that depending on the Reynolds numbers the side responsible for the tonal noise changes.

The imbalance even at $\alpha = 0^\circ$ was also mentioned by Pröbsting *et al.*[29] and can be attributed to the uncertainty of the angle of attack, which leads to asymmetry in the flow conditions. However this unexpected imbalance was impossible to suppress by slightly adjusting the angle of attack on the setup. Therefore firstly it was attributed to some asymmetry of the mock-up because of the instrumentation on the wall side which creates some roughness of the surface. The same test has been repeated by reversing the airfoil bottom up in the setup in order to state about a possible effect of the instrumentation, leading to the same results. It has been concluded that the groove instrumentation does not introduce detrimental roughness but that a residual asymmetry in the wind-tunnel itself was probably incriminated.

The possibility of the flow relaminarisation was also assumed. It may be possible that a tripping device forces a boundary layer from laminar to turbulent, but that at some distance the flow can turn back to laminar because of the local conditions. This assumption was assessed by using a second tripping device at 2 cm downstream from the first one. However it does not change significantly the noise signature, which proves that one tripping device is enough for this kind of tests and the asymmetry can not be associated with relaminarization of the flow.

3.4.3 Influence of the Angle of Attack

Some scientists (for example Lawson *et al.*[3]) mentioned that even small changes of angle of attack of 1° can influence the data. This fact was confirmed earlier by the Reynolds-number versus angle of attack plot.

For the NACA-0012 airfoil the effect of increasing the angle of attack was only investigated at 5° . The configuration A at 5° (see figure 3.12(a)) in comparison with 0° (figure 3.9) exhibits a much narrower noise signature in the flow velocity range, but wider in the frequency range. At low flow velocities up to 15 m/s around 10 parallel traces scaled by the law $f \sim U_\infty^{0.8}$ are seen. At high frequency two secondary harmonics traces are observed. This is also illustrated by figure 3.12(b) for 16 m/s which presents the difference of the far-field sound PSD between 0° and 5° of angle of attack. The tones emitted at very close frequencies for both angles of incidence up to 25 m/s. But there is no agreement between tones at high flow velocities.

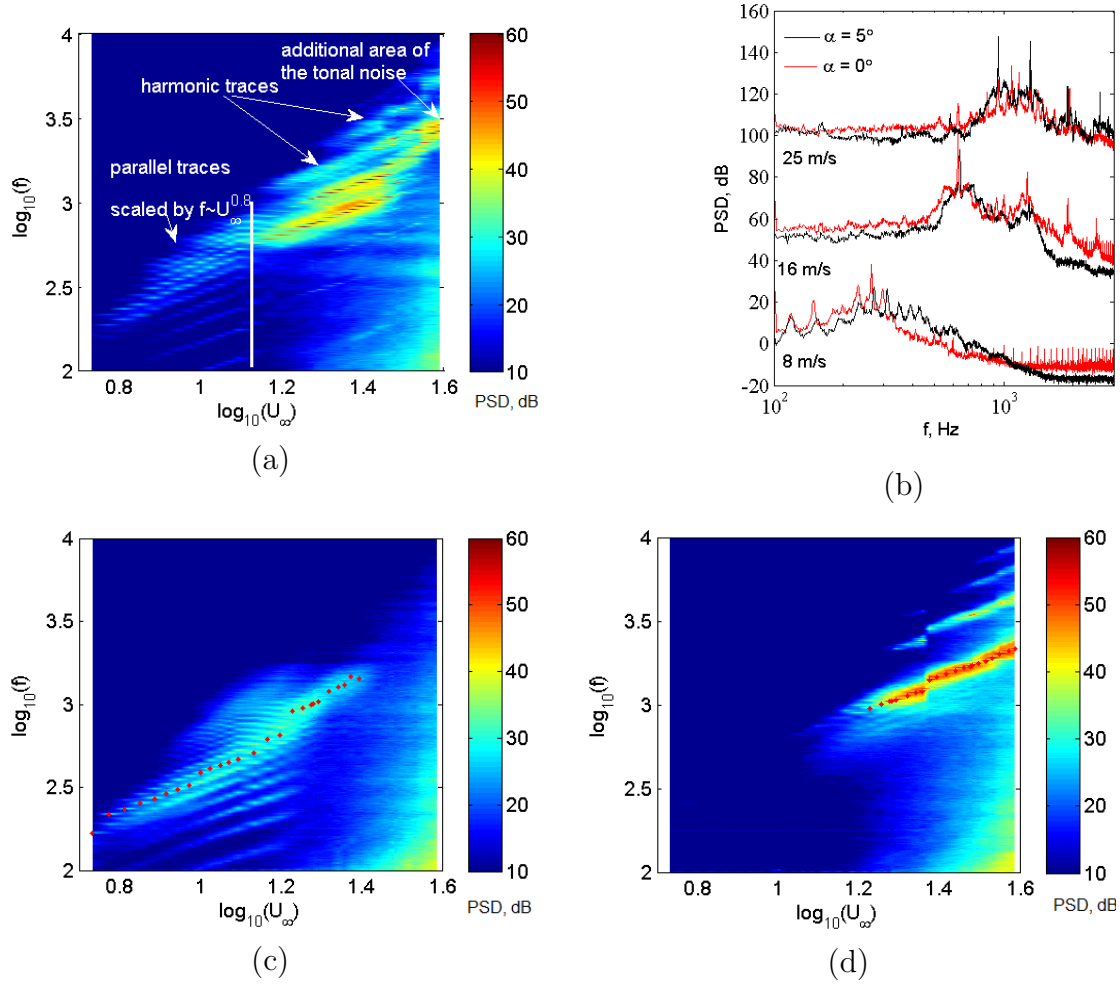


Figure 3.12: Frequency-flow speed charts and spectra of LBL-wave radiation for the NACA-0012 airfoil: (a) at 5° ; (b) the comparison of PSD plots for cases at 5° and 0° ; (c) - tripping on the pressure side; (d) - tripping on the suction side.

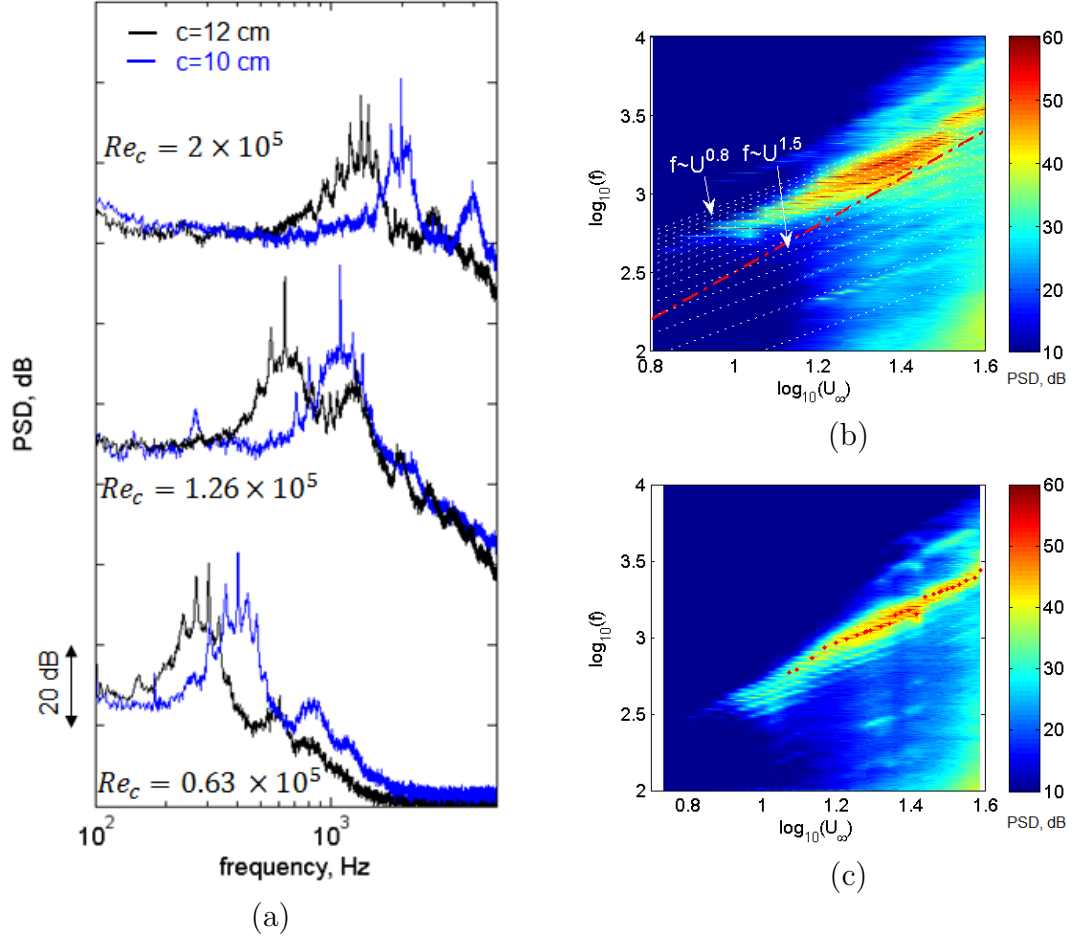


Figure 3.13: (a): PSD plot for comparison of noise signature depended on the chord length of the airfoil. (b) and (c): frequency-flow speed chart of LBL-wave radiation for the NACA-0012 airfoil with chord length 8 cm and 10 cm at zero angle of attack correspondingly.

3.4.4 Influence of the Chord Length

The present measurements for the configuration A with the NACA-0012 airfoil of 12 cm chord at zero angle of attack are compared with previously obtained data for the airfoil of 8 cm chord (more details are given in [31]) in figure 3.13 in order to understand the effect of airfoil size on its noise signature.

The behavior of each airfoil changes with increasing of the flow velocity (see figure 3.13). The comparison of the PSD levels between $c = 12$ cm and $c = 10$ cm at several Reynolds numbers is shown in figure 3.13(a). Each pair of spectra shifted vertically by 50 dB for clarity. The smaller airfoil has slightly higher tonal level at higher frequency range. At $Re_c = 1.26 \times 10^5$ airfoil with 12 cm chord length has second harmonic hump, which is not presented for airfoil with 10 cm chord length. At higher Reynolds number bigger airfoil has multiple tones with PSD level close to the level of the main tone, whereas airfoil with 10 cm still has distinguished main tone. In order to emphasize on the multiple tones white dotted theoretical lines are superimposed on the charts, based on the simplified feedback formula equation 3.2. The equation predicts that the amplified frequencies of same order n are inversely proportional to the chord length of the airfoil. This supposes that the difference in Reynolds number does not question the flow regime. Furthermore the frequency range actually activated in the LBL instabilities, not determined from equation 3.2 is also shifted to higher frequencies as the chord length is reduced.

3.4.5 Influence of the Upstream Turbulence

One of the key features pointed by previous investigators is that the LBL waves are amplified by the acoustic feedback, leading to the emergence of tones. In order to produce an action on the acoustic waves, tests have been repeated inserting a turbulence grid upstream in the nozzle before the contraction (configuration E). The grid is made of wires of approximate mesh size 10 mm and diameter 1.5 mm. It generates small-scale turbulence at a low turbulence rate, less than 1%. The results are shown in figure 3.14 for the NACA-0012 airfoil at zero angle of attack. The radiated sound is of much lower amplitude in this case but some of its features are unchanged. Typically the same oblique trace with the $U_\infty^{1.5}$ scaling is seen in the frequency-versus flow speed chart as shown in figure 3.14(a) but the steps of the

ladder-type structure have disappeared. Looking at the far-field sound spectrum for a given flow speed (figure 3.14(b)) confirms that the tones are suppressed. The acoustic signature only includes a broad hump. The hump extends over the same characteristic frequency range as in the clean-inflow configuration A.

The test suggests that the acoustic signature combines two effects, one associated with the hump and another one associated with the tones. The interpretation is that a weak small-scale homogeneous and isotropic turbulence in the external flow is able to deactivate the acoustic feedback whereas the boundary layer remains fundamentally laminar and unstable; the external turbulence is not strong enough to force transition in the boundary layers. Natural LBL waves develop free of acoustic feedback. As a result the primary sound emission from the scattering of these waves at the trailing edge is preserved but neither amplification nor frequency selection occurs. Figure 3.14(b) also stresses that in clean flow the emergence of the tones is also accompanied by harmonic humps that are not observed with the fine-scale turbulence. The residual turbulence in the wind-tunnel flow, the spectral extent of which is well separated from that of the natural LBL waves, has no noticeable effect on the investigated mechanism. In contrast as a sufficient level of turbulence is present in the flow over the frequency range covered by the instability waves the acoustic feedback can be deactivated. This intermediate regime is different from the leading-edge noise (or turbulence-impingement noise) that would be produced with a higher turbulence rate.

Going into the details, the figure 3.15 displays the streamwise-velocity spectra

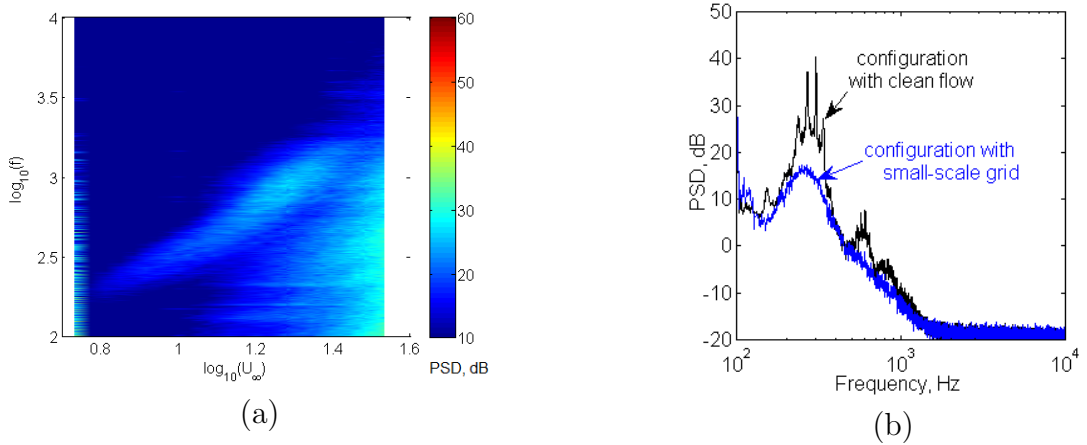


Figure 3.14: (a): frequency-flow speed chart for the NACA-0012 airfoil at zero angle of attack with small-scale turbulence; (b): compared far-field sound spectra in configurations A and D. Flow speed 8 m/s.

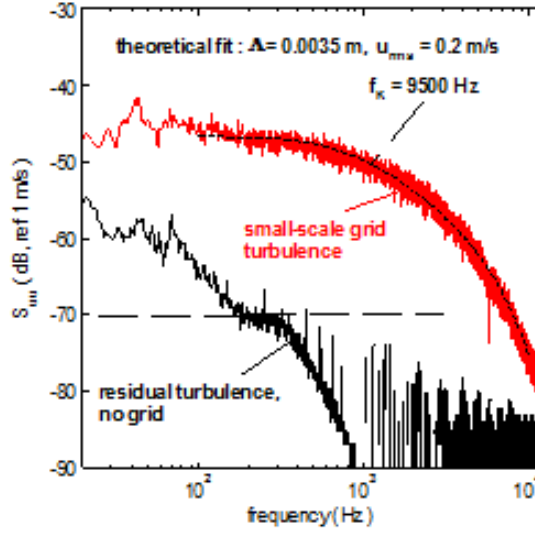


Figure 3.15: Streamwise velocity spectra of the residual turbulence (black), and of the turbulence generated by the fine-mesh grid (red). 25 m/s.

as measured with a single hot-wire probe at the location of the airfoil leading edge (but with the airfoil removed). The black plot stands for the residual turbulence of the wind tunnel. The indicative threshold of -70 dB corresponds to a rms value of 3×10^{-4} m/s; it is only exceeded below 200 Hz. The fluctuation level at the same frequency in the presence of the fine grid is about 5×10^{-3} m/s. This value corresponds to 100 dB of acoustic pressure whereas the former corresponds to 76 dB. At higher frequencies the residual turbulence is of lower amplitude than typical sound waves in the present experiment, but the grid turbulence is not. It appears that in any experiment the background turbulence of the wind tunnel must be characterized by its spectrum and evaluated with regards to the sound level of the primary LBL wave radiation (without feedback). Different declinations of the sound radiation are expected depending on the level of turbulence.

It is worth noting that an acoustic signature similar to that of figure 3.14(a) has been also obtained with the SD7003 airfoil at the angle of attack 5° but in clean flow condition. This suggests that the primary LBL-wave radiation can occur without feedback amplification even in clean flow, though the physical reason is unexplained.

The influence of the upstream turbulence on the location of the separation bubble will be discussed in section 3.5.2.

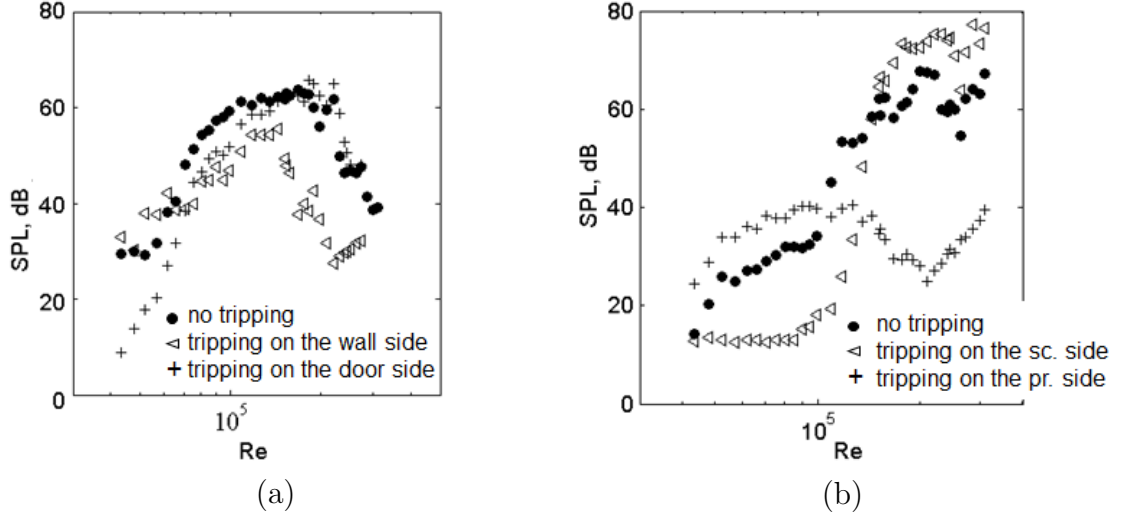


Figure 3.16: Sound pressure level of the main tones as a function of flow velocity in configurations A (no tripping), B (tripping on the door side) and C (tripping on the wall side). The NACA-0012 airfoil at $\alpha = 0^\circ$ (a) and $\alpha = 5^\circ$ (b).

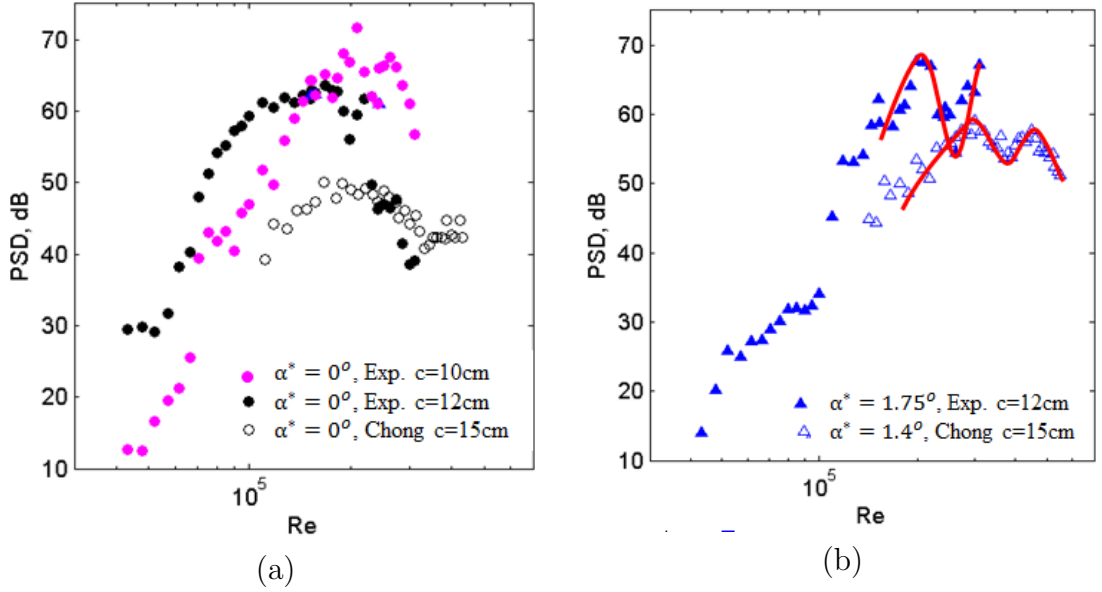


Figure 3.17: Sound pressure level of the main tones as a function of flow velocity. Comparison of the NACA-0012 airfoil at $\alpha^* = 0^\circ$ (a) and $\alpha^* = 1.75^\circ$ (b) with the results of Chong *et al.* [7]. Configuration A.

3.4.6 Tracing of the Dominant Tone

The sound pressure level of the dominant tone measured by far-field microphone for the NACA-0012 airfoil is shown in figure 3.16(a). SPL increases with the flow velocity till the velocity threshold $U_\infty = 20 \text{ m/s}$ and decreases at higher velocities. The same behavior was mentioned for the CD airfoil by Padois *et al.*[24]. On the one hand the SPL of the tone results from the pressure level at the acoustic source, which is directly related to the flow velocities. On the other hand it depends on the coherence of the flow needed for the feedback loop, which forces the acoustic waves (see 3.4.2 and 3.4.5). As the increasing of the flow velocity produces more non-linearity in the flow, both the coherence level and therefore the amplification by the feedback loop decrease. This can explain why beyond some limit flow velocity (for the present case it is 20 m/s) the level of the tones decreases. This plot also leads to the similar conclusions as comparison of the noise signature color maps (figure 3.9). Depending on flow velocity different sides responsible for the trailing-edge noise (this is also shown in figure 3.16(a)).

In figure 3.17 the comparison of the sound pressure level as a function of Reynolds numbers of the present study with results of Chong *et al.* [7] is shown for two angles of attack. A correction of the level according to the distance between noise source and far-field microphone was applied. The chord lengths of the airfoils are different: 10 cm, 12 cm and 15 cm. With increasing chord length the sound pressure level decreases. The threshold for the smallest chord is around 70 dB. The maximal level for the NACA-0012 airfoil with 12 cm is around 64 dB. The reference result of Chong *et al.* shows a threshold at 45 dB. The behavior of the plot for all three cases at zero angle of attack is similar. Following the dominant tones produces a main hump. At higher angle of attack a second hump can be observed (figure 3.17(b)).

3.5 Role of the Separation Bubble in Trailing-Edge Noise

As was mentioned in section 1.4 the role of the separation bubble in the tonal noise generation is incontestable. The analysis of the separation bubble characteristics was done on the basis of the results of flow visualization and hot-wire anemometry (HWA), which complement each other. The procedures of the flow visualization and HWA are described in sections 2.6 and 2.5.

During the tests several types of flow were observed, listed below.

- Separation with clearly reversed flow at the trailing edge.
- Separation with reattachment.
- Separation without visible reattachment.
- Attached flow.

3.5.1 Influence of Flow Velocity and Angle of Attack

During the flow visualization tests the flow velocity was set to 19 m/s, 25 m/s and 33 m/s. The tested geometric angles of attack for the symmetric airfoil were $\alpha = 0^\circ, 5^\circ, 10^\circ$.

A typical combination of the flow visualization and hot-wire anemometry results is presented in figure 3.18. In the photo of flow visualization the existence of the separation bubble (area where liquid concentrates) is evidenced by the stagnation of the mixture. Yet near the trailing edge over a distance of 3-4 mm a different patterns visible. The video which was registered during the tests shows that for this case a reversed flow takes place. This feature is impossible to prove on the basis of HWA because the direction of the local flow is not accessible. The bounds of the separated area differ by about 10% in the two techniques: flow visualization 54% - 100% and HWA 58%-100%. The level of the u_{rms} increase twice moving to the trailing edge and reach 4 m/s. It seems that at $x/c = 0.5$ the hot-wire probe

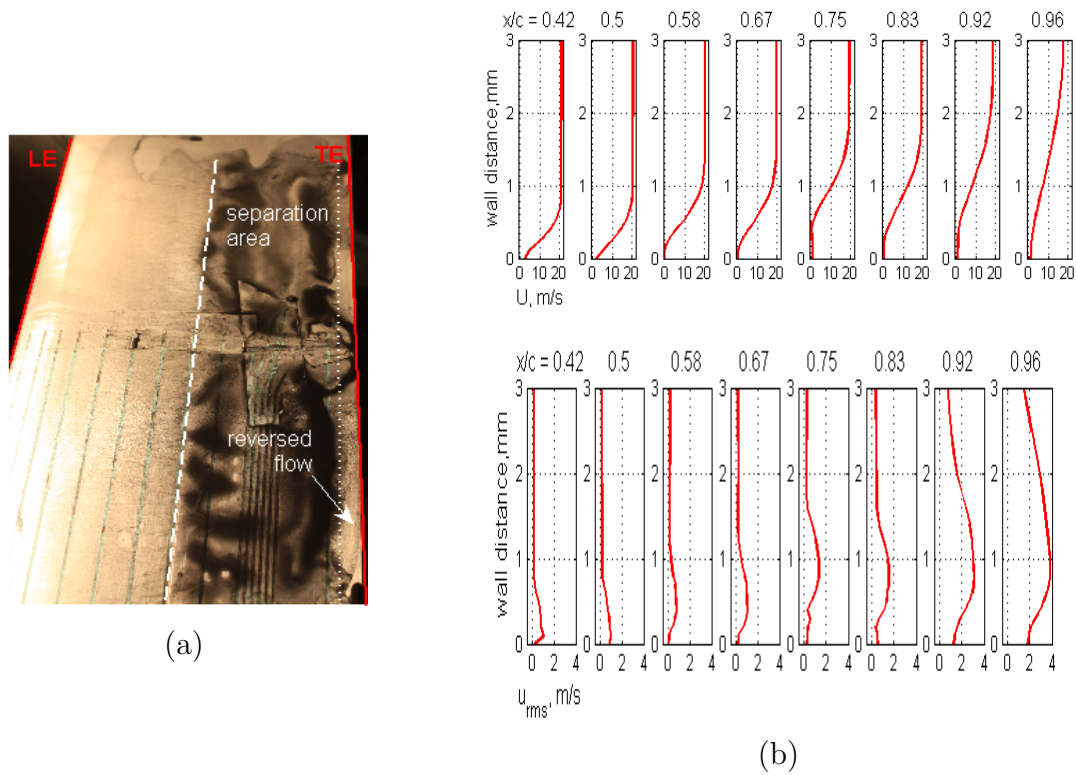


Figure 3.18: Example of flow visualization (a) and HWA results (b) for the NACA-0012 airfoil at $\alpha = 0^\circ$ and 19 m/s ($Re = 1.5 \times 10^5$). Tonal noise configuration.

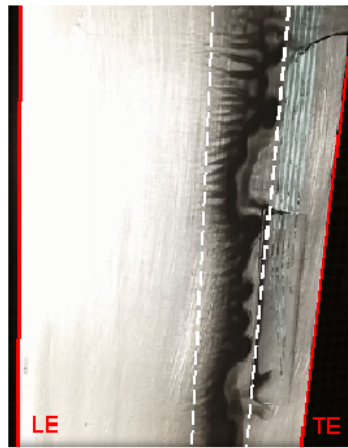


Figure 3.19: Flow visualization for the NACA-0012 airfoil at $\alpha = 0^\circ$ and 33 m/s showing quite a large reattachment area before the trailing edge (TE). Tonal noise is not observed.

was not close enough to the surface of the airfoil and that the profile should be shifted a little.

In all tonal noise cases the separation bubble extends down to the vicinity of the trailing edge on the pressure side. The tests with tripping devices confirmed that the bubble is responsible for the tonal noise. The increasing of the angle of attack and/or flow velocity moves the initial point of the separation bubble on the suction side closer to the leading edge and reduces the surface covered by bubble. On the contrary, on the pressure side the separation bubble moves closer to the trailing edge and in most cases there is no reattachment. The case without tones (see figure 3.19) at $U_\infty = 33 \text{ m/s}$ and $\alpha = 0^\circ$ is characterized by the fact that the separation bubble is more than 20% of chord away from the trailing edge.

The results for the NACA-0012 airfoil are summarized in table 3.1. Red marks indicate the boundaries of the separation bubbles. A single mark means that there is no clear reattachment of the separation area. The absence of marks corresponds to a fully attached flow. A small arrow indicates the reversed flow. On the basis of the results it is possible to say that the separation bubble is a necessary condition for the high-intensity trailing-edge noise. Moreover the location of the bubble plays an important role in the process. If the separation bubble is too far away from the trailing edge there is no tone generation.

Measurements were conducted in the very near-wake at about 1.5 mm from the trailing edge. They are presented in figure 3.20(a). Slight asymmetry which can be explained by the uncertainty of the geometrical angle of attack and a possible asymmetry of the flow is observed. The results also suggest that the flow has reattached just before the trailing edge. Indeed the mean-velocity and turbulent-intensity profiles are similar to these for attached boundary layer.

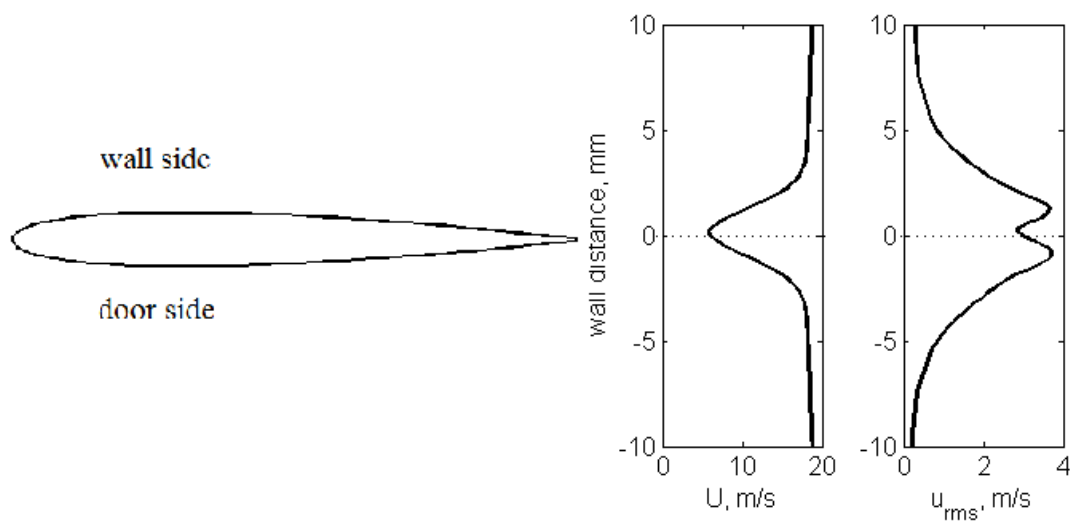
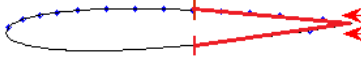
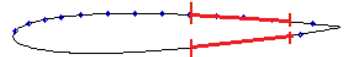
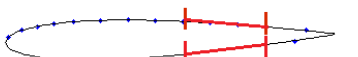
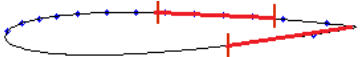
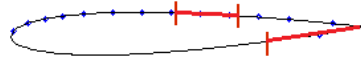
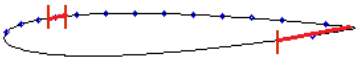


Figure 3.20: Results of near-wake measurements performed from the “door side” at the distance of 1.5 mm for the NACA-0012 airfoil at 19 m/s and zero angle of attack.

Table 3.1: Separation areas. Illustrative table for the NACA-0012 airfoil.

α	U_∞ 19 m/s		25 m/s	33 m/s
	Flow Visualization	HWA	FV	FV
0°	54% 	42% - 92% 58%-100%	54% - 85 % 	57% - 80%  NO TONE
5°	sc.s 40% - 80%  pr.s 60%	33%-88% 33%-79% 67%-100%	sc.s 45% - 62%  pr.s 62%	
10°				sc.s 10% - 17%  pr.s 80%

3.5.2 Influence of the Upstream Turbulence on the Location of the Separation Bubble

The acoustic investigation with the small-scale grid shows that a slight increase of the upstream turbulence level suppresses the tonal noise (see section 3.4.5). The energy of the acoustic waves is not enough for overcoming the turbulence and force the starting instabilities in the boundary layer. Flow visualization tests were conducted to check whether the upstream turbulence changes the location of the separation bubble or not. Since the acoustic feedback is suppressed in this case, the test is also a way to assess the effect of the feedback on the separation.

Figure 3.21 shows flow visualization results for pressure side of the NACA-0012 airfoil at $U_\infty = 19 \text{ m/s}$ and $\alpha = 5^\circ$ with and without upstream grid. One can see that the differences in the location of the separation bubble are negligible and can be attributed also to the effect of the viscosity of the visualizing mixture.

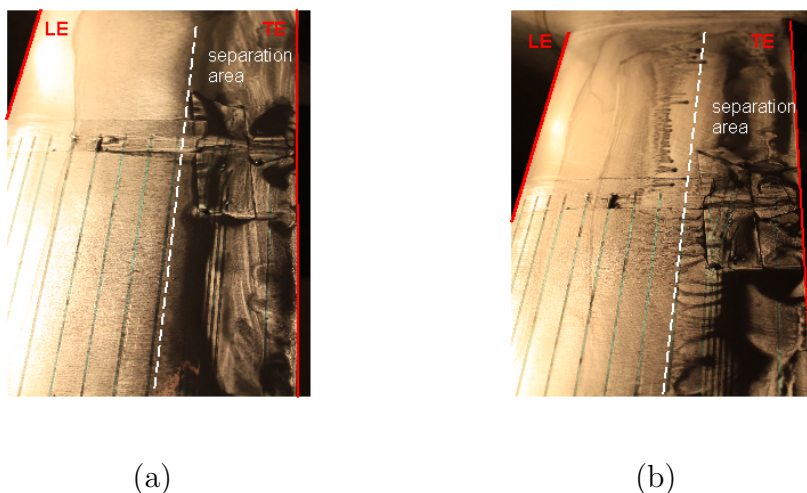


Figure 3.21: Flow visualizations for the NACA-0012 airfoil at 19 m/s ($Re = 1.5 \times 10^5$) and $\alpha = 5^\circ$ (pressure side). (a) - test with clean airfoil; (b) - test with the upstream small-scale turbulence.

The results for of this set of tests are summarized in table 3.2. The differences are around 5% of the chord length. So the small-scale upstream turbulence does not significantly change the location of the separation bubble nor suppress it. It can be concluded that the separation bubble is necessary but not a sufficient condition for the tonal noise, which is suppressed without acoustic feedback loop

even if the separation bubble exists. Further in chapter 4 will be proved by numerical simulation that the transition of the weak Tollmien-Schlichting waves to Kelvin-Helmholtz waves takes place at the separation area. The Kelvin-Helmholtz waves are strong enough to generate acoustic waves at the trailing edge of the airfoil, which affect the growth of the T-S waves at some frequencies through the receptivity mechanism (acoustic feedback loop). The small-scale upstream turbulence disorganizes the flow in such a way that the acoustic waves lose part of their coherence and cannot amplify the Tollmien-Schlichting waves anymore (see also [53, 54]). Therefore without amplification of the instabilities only broadband noise with low SPL can be generated as was shown in section 3.4.5.

Table 3.2: Compared extensions of the separation areas for the NACA-0012 airfoil with and without upstream grid. Percentage of chord.

α	U_∞	without grid	with grid
0°	19 m/s	54% - rev	54% - 92%
	25 m/s	54% - 85%	58% - 80%
5°	19 m/s	60%-100%	62%-100%
10°	33 m/s	80% - rev	80% - 100%

3.5.3 Influence of the Separation Bubble on the PSD of the RMPs

It can be assumed that the separation bubble protects the RMPs from the oscillations of the shear layer and blocks a part of the information to measure. This encourages to track the influence of the separation bubble on the PSD measured by wall pressure probes. The idea is to compare PSD plots of probes out of the separation bubble with those that are covered by it. Turning back to the configuration at $\alpha = 0^\circ$ and $U_\infty = 19 \text{ m/s}$ for the NACA-0012 airfoil several probes were chosen for this analysis. These are the probe №14 located before the separation bubble; the probe №16, the probe №20 and the probe №23 covered by the separation area (figure 3.22(a)). The PSD plots (figure 3.22(b)) for probes №14 and №16 coincide with each other and have only a moderate level difference ($\sim 10 \text{ dB}$) with the plot of the probe №20. However for the probe №23 the difference is nearly 20 dB. The higher level of the PSD for the probe №20 and the probe №23 can be explained by the location of the aforementioned probe closer to the trailing edge (source of the tonal noise) where the growth of the instability

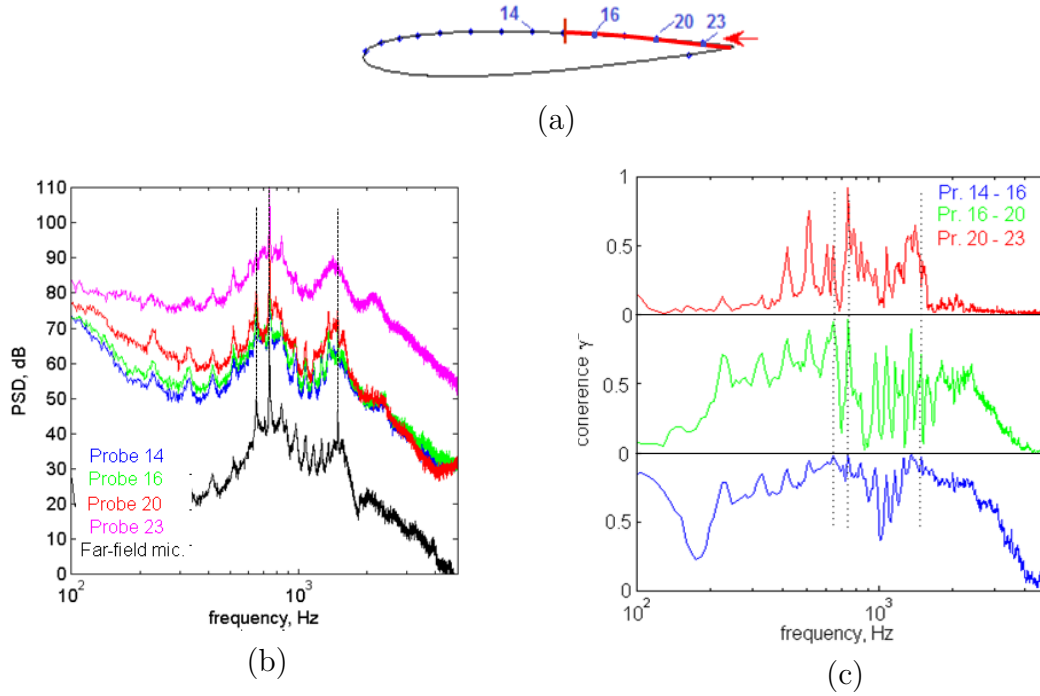


Figure 3.22: The NACA-0012 airfoil at 19 m/s and zero angle of attack: (a) - location of the separation bubble; (b) - PSD plots for wall pressure probes and far-field microphone; (c) - chordwise coherence plots for doublets of wall pressure probes. Dotted lines mark tones.

is larger. This indicates that the separation bubble causes no loss in the wall pressure measurements. Therefore the latter are a reliable trace of the developing instabilities.

The question whether the information measured by RMPs is of aerodynamic or acoustic nature has also a high priority. For this reason the coherence between doublets of RMPs was calculated at various chordwise locations. It is well known that the acoustic waves have a high level of coherence as well as organized hydrodynamic fluctuations, unlike turbulent disturbances. It can be noted that moving downstream on the airfoil surface the level of coherence between probes decreases for the NACA-0012 airfoil at 19 m/s (see figure 3.22(c)). For the middle part of the airfoil the information has a clear acoustic character up to about 3 kHz or at least corresponds to a very coherent motion. Approaching the trailing edge the measured data becomes aerodynamic below 400 Hz and beyond 1800 Hz. The tones on the PSD plots are marked by dotted lines and coincide with the peaks of

coherence. These features are observed for all configurations at different angles of attack and flow velocities.

For the flow velocity 25 m/s (see appendix B figure B.1) the starting point of the separation bubble is the same as in the previous case and the signals from the probes №14 and №16 are in a good agreement again. The difference between probes №16 and №20 is bigger. The reattachment takes place between probes №20 and №23. The levels of the spectra of these probes have discrepancies of nearly 20 dB. But it should be taken in account that the probe 23 is the closest to the trailing edge where the maximum level is expected. It is interesting that for the following case at 33 m/s (see appendix B figure B.2) the humps of the spectra for the probes №17 (covered by the separation bubble) and №20 (located at the end of the separation bubble) coincide, whereas the other curves have a 15 dB difference.

3.5.4 Comparison with the Results of Previous Investigators

The numerical investigation by Desquesnes *et al.*[20] for the NACA-0012 airfoil at effective angle of attack $\alpha^* = 2^\circ$ and $Re = 2 \times 10^5$ showed that the separation area started at 76% of the chord with reattachment at 96%. This differs from the similar case (NACA-0012 airfoil at $\alpha^* = 1.75^\circ$ (geometrical $\alpha = 5^\circ$) and $Re = 2 \times 10^5$) of the present study by 14% at the beginning of the separation (62%). Furthermore, the reattachment was not observed. The difference may be explained by the fact that the angles of attack, and also probably the pressure-coefficient distributions, are not exactly the same.

The flow visualization reported by Arcondoulis *et al.*[13] on the NACA-0012 airfoil with a chord length of 67 mm at effective angles of attack 0° , 1.58° and $Re_c = 1.5 \times 10^5$ is comparable with the present results. At $\alpha^* = 0^\circ$ the separation bubble extends from 60% to 95% of chord. This is 6% closer to the trailing edge than in the present study. However, the reversed flow observed in the present measurements cannot be confirmed. Arcondoulis' data at $\alpha^* = 1.58^\circ$ showed a separation area starting from 65% on the pressure side and from 31% on the suction side; a reattachment was observed, but with no indication of its exact location. These results differ from ours by less than 10% .

Pröbsting *et al.*[32] reported PIV measurements of the boundary layer for the NACA-0012 airfoil at $\alpha^* = 1.5^\circ$ and $U_\infty = 24 \text{ m/s}$ which can be compared ac-

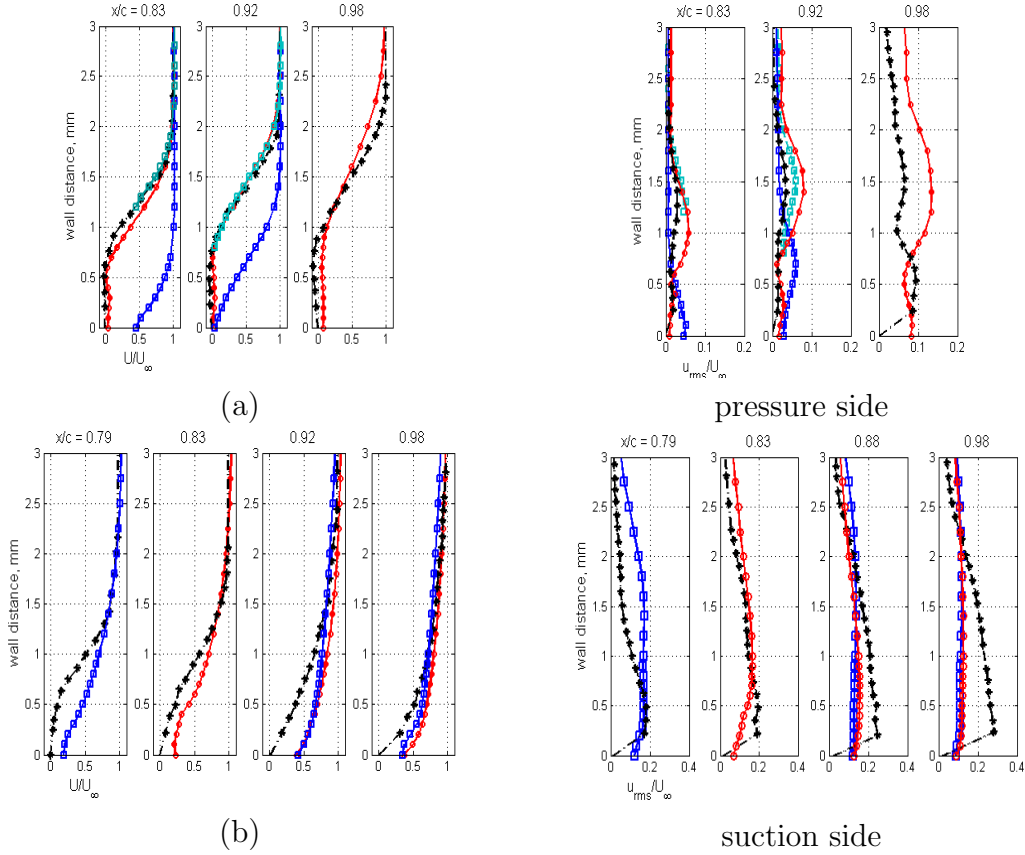


Figure 3.23: Comparison of the mean (left) and rms (right) velocities measured by HWA (—○— test 1, —□— test 2, —□—shifted test 2) on the pressure (a) and the suction (b) sides with PIV data of Pröbsting (—*—). NACA-0012 airfoil.

cording to the Reynolds number (based on the chord length) with the HWA measurements for the present NACA-0012 airfoil at $\alpha^* = 1.75^\circ$ and $U_\infty = 19 \text{ m/s}$ (see figure 3.23). Because an asymmetrical flow was observed even at zero angle of attack on the experimental set-up, it was decided to repeat the HWA measurements at the same positive (test 1) and negative (test 2) angles in order to assess the differences in the boundary layers.

On the pressure side the mean-velocity difference between test 1 and test 2 is considerable. The test 1 and Pröbsting's reference results are in a good agreement, except very near the trailing edge where the present velocity profile exhibits a smoother slope. The difference between the tests is attributed to an inaccuracy of the initial positioning of the probe for test 2 due to unavoidable contact of the probe support with the wall. Indeed if the profiles for test 2 are shifted by 1.2 mm at 83% of chord and 0.8 mm at 92% of chord the agreement becomes much better.

In contrast the present u_{rms} level is higher for both tests than in the reference. Yet the positions of the maximum levels coincide, except again near the trailing edge (98%). The fact that the measurements were not performed exactly at the same position may cause the deviation.

An opposite situation is faced on the suction side. Tests for positive and negative angles of attack coincide. This confirms the aforementioned positioning issue of the probe. A discrepancy on the mean velocity corresponding to a shift of 1 mm from the wall remains between the present results and Pröbsting's. The level of the reference u_{rms} is now twice higher near the trailing edge than in the present measurements. Such differences stress the high sensitivity of the mechanisms involved in the transitional boundary layers. It should be mentioned that Pröbsting *et al.*[32] use a circular nozzle with a cross-section of diameter 600 mm. This is equivalent to a possible additional spanwise inhomogeneity and a different confinement which may be a reason for discrepancies. In particular for the NACA-0012 airfoil the flow on the suction side is very unstable and sensitive to changes of the flow parameters.

An overall qualitative agreement is finally obtained between the present results and previous investigations. The fact that the phenomenon of the tonal noise emission is very sensitive to installation effects can explain why the quantitative agreement is hard to obtain.

3.6 Cross-Spectrum Analysis

3.6.1 Chordwise Analysis

As was mentioned in section 2.7.1 the cross-spectrum analysis is a way of estimating the level of correlation between two signals and other features such as the convection speed. The influence of the flow velocity and the angle of attack on the coherence of the oscillatory motion along the chord length should give indications about changes in the linear relationships between probes. There are 11 pairs of RMPs along the chord line for the NACA-0012 airfoil. The analyzed signals were measured simultaneously.

Figure 3.25 presents the results of a cross-spectrum analysis for the NACA-0012 airfoil (configuration A) at 25 m/s and zero angle of attack. On the PSD

plot the red line corresponds to the 1st probe in pair, the black line to the 2nd one. On the phase plot the blue line is the phase of cross-spectrum for a resolution of 1 Hz, the black one for 8 Hz. An abscissa of the PSD and coherence plots presents frequency in logarithmic scale, whereas for phase plots the linear format was used for clarity. The analysis was done from the leading edge to the trailing edge. A comparison can be made with the NACA-0012 airfoil at $U_\infty = 16 \text{ m/s}$, $\alpha = 0^\circ$ (figure B.3) and at $U_\infty = 25 \text{ m/s}$, $\alpha = -5^\circ$ (figure B.4).

The two probes №7 and №8 produce very similar PSD spectra. The coherence peaks are close to 1 for a very narrow frequency range around 1300 Hz which corresponds to the tones on the PSD plot. A less coherent secondary peak is seen around the harmonic frequency of 2600 Hz. At other frequencies the coherence is 0.2. At higher flow velocities the tones have lower coherence levels. A high coherence level can be associated, firstly, with the acoustic nature of the signals, secondly, with the hydrodynamic and coherent signals that can be encountered with instability waves. In general the area close to the leading edge can be quite questionable, because several physical processes such as starting instabilities, acoustic propagation and diffraction effects may exist. The behavior of the phase plot is very irregular with values close to 0 in the frequency ranges corresponding to the main hump and its harmonic, whereas in general random oscillations are observed. More precisely, for the main tonal noise hump the phase is below 0 and for the second hump it is above 0. The hump on the coherence plot at low frequencies up to 250 Hz is clearly visible for this pair of probes but also can be recognized for other combinations of probes. This hump is in a range of contamination by the jet shear-layer oscillations (see section 2.3.5). At 16 m/s (see figure B.3) the behavior of the plots for the same probes is very similar.

The next pair of probes №8 and №9 at 25 m/s exhibits a significant increase of coherence for the whole broad-band hump and its harmonic. The coherence plot has two humps with a small decrease of the level between. At high frequencies the level of the coherence decreases gradually. But the difference in the phase plot becomes significant. The phase plot deviates around $\pm 30^\circ$ without visible slopes which will be discussed for the next pair of probes. At 16 m/s the phase oscillations have higher amplitude at high frequencies.

The third pair of probes №9 and №10 has a similar character of the coherence plot but with drops to 0.6 in a frequency range from 700 Hz to 1000 Hz before the instability hump. The phase plot has a gentle negative slope changed by the small hump around 5500 Hz (figure 3.24). The slope can be used for the determination

of some phase velocity between two probes using the formula

$$U_c = \frac{\Delta x \Delta \omega}{\Delta \phi} \quad (3.3)$$

where Δx is the distance between two RMPs, $\Delta \omega$ is the difference between angular frequencies and $\Delta \phi$ is the difference of phase.

The slope takes place in the range from zero to 4500 Hz, so $\Delta \omega = 4500 \text{ Hz}$. The difference of phase is $\Delta \phi = -50^\circ$ and the distance between probes is $\Delta x = 0.006 \text{ m}$. This gives a phase velocity equal to -173 m/s, where the minus means the upstream direction of movement. This value is neither corresponding to a clear acoustic motion nor a convective motion. It should be mentioned that the value of the convection speed in some cases can be questionable, because sometimes the way of choosing the slope for the calculation can significantly change the value. There are also several cases with two different convection speeds for the same pair of probes (see section 5.2).

At lower flow velocities the plots of the probes №9 and №10 are similar to the №8 and №9.

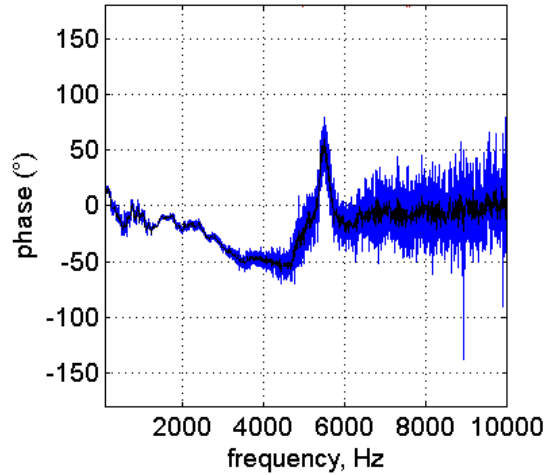


Figure 3.24: Phase of cross-spectra of RMP №9 and №10 for the NACA-0012 airfoil at $\alpha = 0^\circ$ and $U_\infty = 25 \text{ m/s}$. Configuration A.

The probes №10, №11 and №12 have a drop of coherence less than 0.6 just before the broadband hump. However the harmonic humps are easily detected on

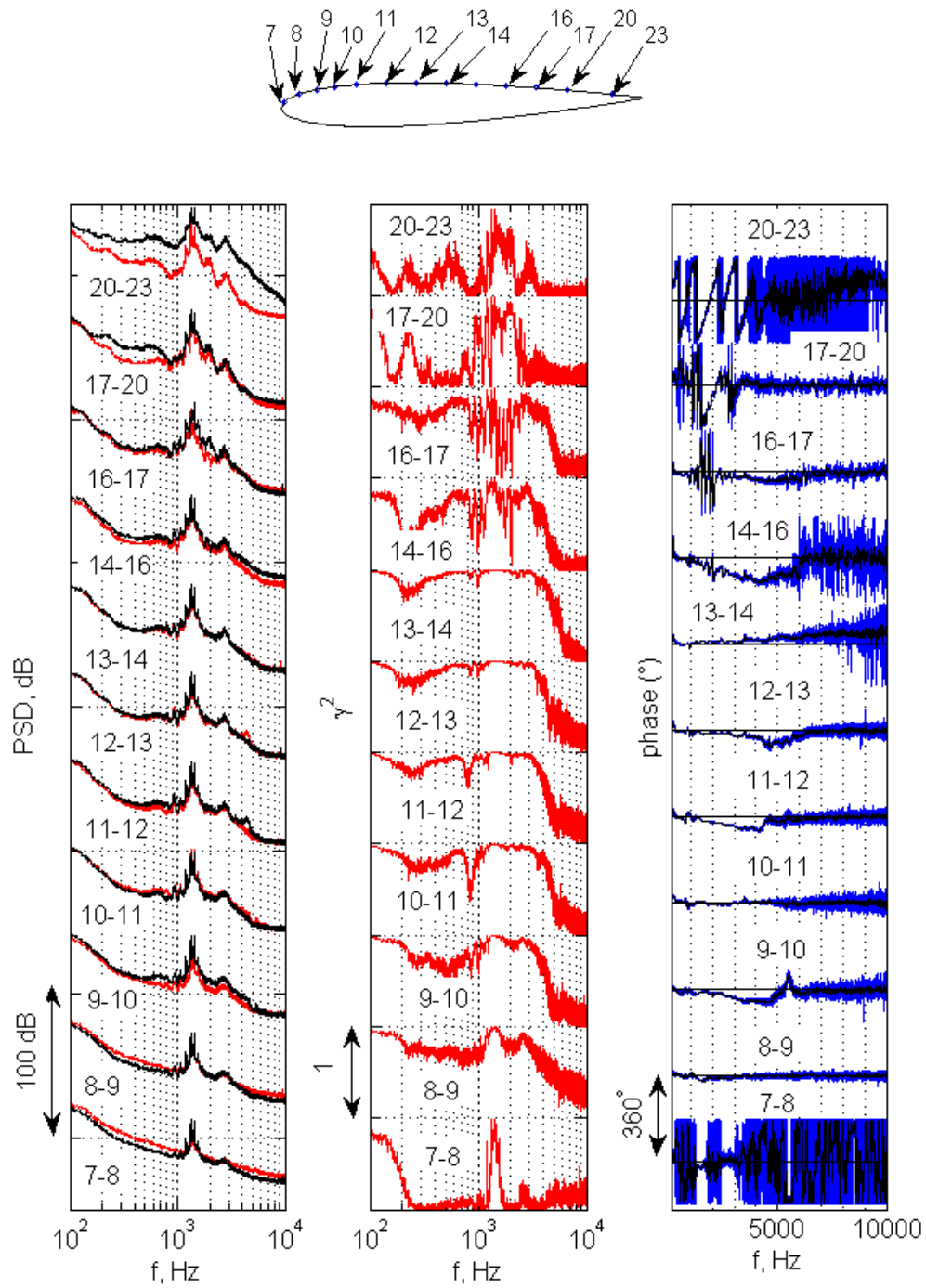


Figure 3.25: Chordwise variations of PSD, coherence and phase of cross-spectra of RMP pairs for the NACA-0012 airfoil at $\alpha = 0^\circ$ and $U_\infty = 25 \text{ m/s}$. Configuration A.

the coherence plots at 16 m/s. At both flow velocities the phase between probes №10 and №11 has no a clear slope, whereas a slope can be identified between probes №11 and №12 as well as for №12 and №13 at 25 m/s. At 16 m/s the last pair of probes has no a clear slope. The overall of coherence significantly decreases for probes №12, №13 and №14 at both velocities. The phase between the signals from №13 and №14 has no slope whereas a clear slope is seen again for the phase between №14 and №16 (same at 16 m/s). The level of the coherence for this pair of probes decreases and humps become easier to identify. A very similar coherence plot is produced by the probes №16 and №17. At 25 m/s in the aft part of the airfoil the phase plot has a saw-tooth shape with an increasing slope at frequencies corresponding to the tonal hump. More clearly this shape is presented on the phase plot for probes №17, №20 and №23 closer to the trailing edge. The saw-tooth phase plot allows to calculate the convection speed between probes №20 and №23 (see section 5.2), which is necessary for the analytical modeling. The general coherence level for the last two pairs of probes is lower.

The influence of the angle of attack was also investigated. In general the coherence level at 25 m/s and -5° (figure B.4) on the suction side is lower than in the configuration at 0° . The aforementioned drop of coherence level for probes №10, №11 and №12 is not observed. The significant changes start from the probe №14 where only the hump and the tones have a coherence level higher than 0.2. The character of the coherence plots on the pressure side is very similar to the configuration at 0° . The characteristic saw-tooth shape of the phase plot can be observed from the pair of probes №11 and №12.

3.6.2 Spanwise Correlation Length

The spanwise correlation length l_y can be deduced from a series of measurements of the coherence between various couples of sensors distributed along the span at the same chordwise location. This information makes sense as close as possible to the trailing edge. In this section the example of the spanwise set B (door side) is taken for illustration. The three-dimensional surface plots of the coherence as a function of sensor separation and frequency in logarithmic scale are plotted in figure 3.26 for the configuration A (LBL-wave radiation with acoustic feedback) at 16 m/s and the configuration E (with small-scale upstream turbulence) at 16 m/s.

In the first case (figure 3.26(a)) the coherence remains close to 1 at the tone

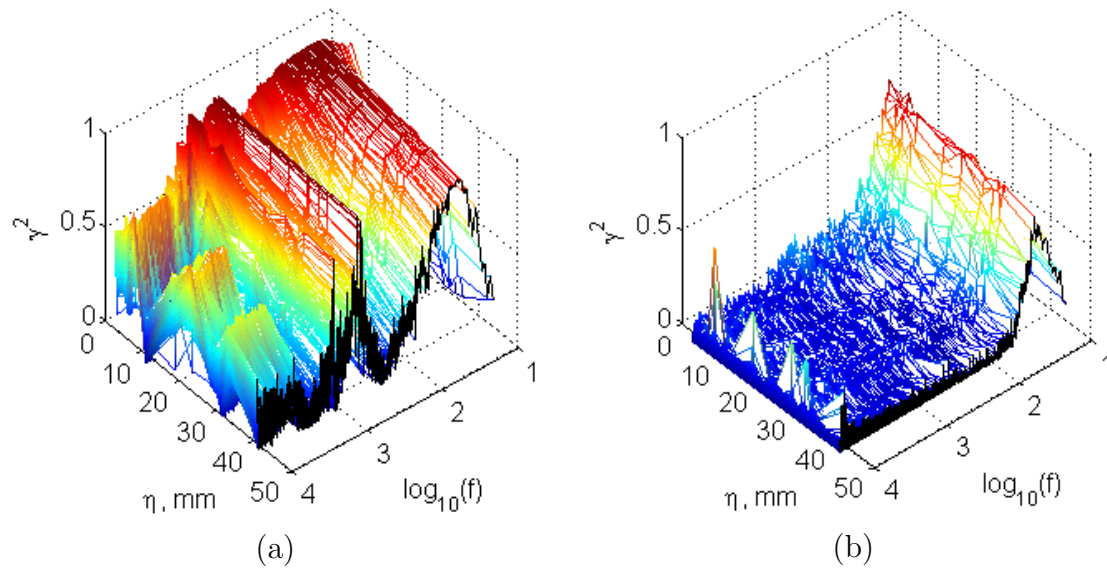


Figure 3.26: Coherence surface for LBL wave radiation with and without acoustic feedback. NACA-0012 airfoil at $U_\infty = 16 \text{ m/s}$ and zero angle of attack. Door side.

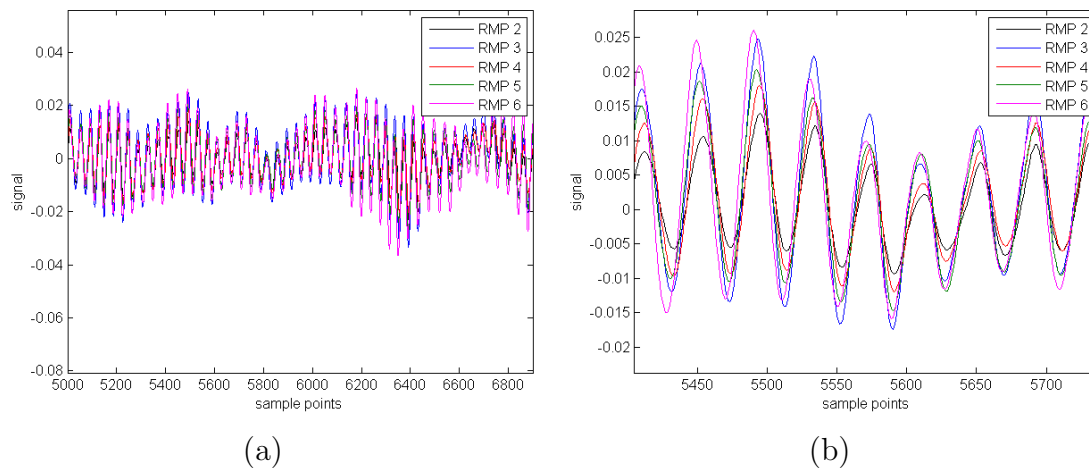


Figure 3.27: Time signal (a) and its zoom (b) for the NACA-0012 airfoil at $U_\infty = 16 \text{ m/s}$ and zero angle of attack. Spanwise set of probes B (door side).

frequencies that are amplified by the acoustic feedback (around 1 kHz), at least for the accessible values of the separation η . This suggests either that the fluid motion becomes two-dimensional, because the upstream propagating waves tend to trigger the instabilities in phase along the span, or that coherent oblique waves form with well-defined spanwise phase speed. In contrast the coherence drops with increasing separation at other frequencies. The two-dimensional motion is confirmed by the time signal plot for the spanwise probes from the door-side set (figure 3.27). Indeed fact if the instabilities were three-dimensional, then the time signals measured by the probes should exhibit consistent delays. However the fluctuations have no significant shift and are in phase. Figure 3.27 also illustrates an amplitude modulation.

If small-scale turbulence is introduced in the flow upstream of the airfoil, the feedback is deactivated and no triggering is possible. The spanwise coherence is very poor in this case, as shown by figure 3.26. On both plots the coherence remains very high below 200 Hz. This range is not related to the development of boundary-layer instabilities; it is attributed to large-scale oscillations of the wind-tunnel jet and must be ignored in the analysis. The very crucial difference of coherence between both cases explains why the feedback makes the LBL waves much noisier.

3.7 Time-Frequency Analysis

The acoustic signature as heard during the experiments obviously exhibits variations with large characteristic time scales when compared to the acoustic periods, such as intermittency or sudden changes. The associated statistical quantities are not stationary, making the classical Fourier analysis not relevant because of the underlying averaging procedure. This is why time-frequency analysis was performed, either to extract stationary parts of the signals or to track the sound level and frequency content of the signals as functions of a slowly-varying time. The observation of various acoustic signatures in the same configuration could be the origin of discrepancies between measured and computed signals, because most numerical simulations are performed on very short time intervals. They are also possibly related to an extreme sensitivity of the mechanism to installation effects which differ from an experimental investigation to another. As a result the detailed mechanisms of LBL-wave radiation can be observed and more convincing comparisons can be made. In the present study the short-term Fourier transform with an overlap of 50% of adjacent samples was applied.

As an example figure 3.28 presents 6-seconds portions extracted from signals of total duration 60 seconds. Different regimes of LBL-wave radiation are identified, all observed at different velocities for the NACA-0012 airfoil in configuration A. In each sub-plot the left side displays the sonogram and the right side presents the averaged spectrum.

The first regime at 11 m/s is characterized by two dominant tone frequencies of similar averaged amplitudes and nearly symmetrical locations with respect to the central frequency of the broadband hump. The flow is intermittently switching between two states of different frequency contents. As a result averaged spectra produced by isolated stable parts of the signals would exhibit only one dominant tone, as illustrated in figure 6.18 for the SD7003 airfoil in section 6.8. This means that in some configurations the two tones might not be observed simultaneously. This “switching” regime corresponds to the area around the vertical line 2 which indicates flow velocity in figure 3.11(a). With increasing flow velocity a second regime is reached, illustrated here at the flow speed of 16 m/s corresponding to the line 3 in figure 3.11(a). For this regime a single dominant tone is observed, quite stable in time in view of the sonogram. The frequency of this tone nearly coincides with the central frequency of the hump. On the averaged PSD plot higher harmonics of the hump and of the tone are also noted, with less tonal emergence. It is worth noting that Arbey & Bataille’s analysis based on the feedback loop formula (3.2) confirms that with progressively increasing flow speed one or two tones can dominate. Indeed the center frequency of the hump typically increases with $U_\infty^{1.5}$ whereas the individual amplified frequencies f_n approximately increase with a scaling law between $U_\infty^{0.8}$ and $U_\infty^{0.85}$. The present result confirms that the flow preferentially selects the tonal frequency that is closest to the center frequency of the hump and that it switches between two states if two tones are nearly at equal distances from this frequency. But of course the interpretation only holds with a well-identified and ideal bell-shaped hump. A deeper look at figure 3.28(a) shows that in fact two contiguous tones are emitted simultaneously with one of them dominating in both states of the switching regime: two doublets (f_n, f_{n+1}) and (f_{n+1}, f_{n+2}) sometimes alternate.

Around the higher flow speed of 21 m/s the averaged spectrum again exhibits a dominant tone and multiple tones of lower amplitudes, superimposed on a much broader hump. On the sonogram the main tone has a dashed trace revealing some intermittency. The multiple frequencies are observed simultaneously. Again making connections with the feedback-loop model, the broader hump corresponds to a wider frequency range in which the LBL waves develop, allowing for more frequencies f_n to be amplified. But because the hump is broader the identification of a center frequency for it becomes ambiguous. It is worth noting that without

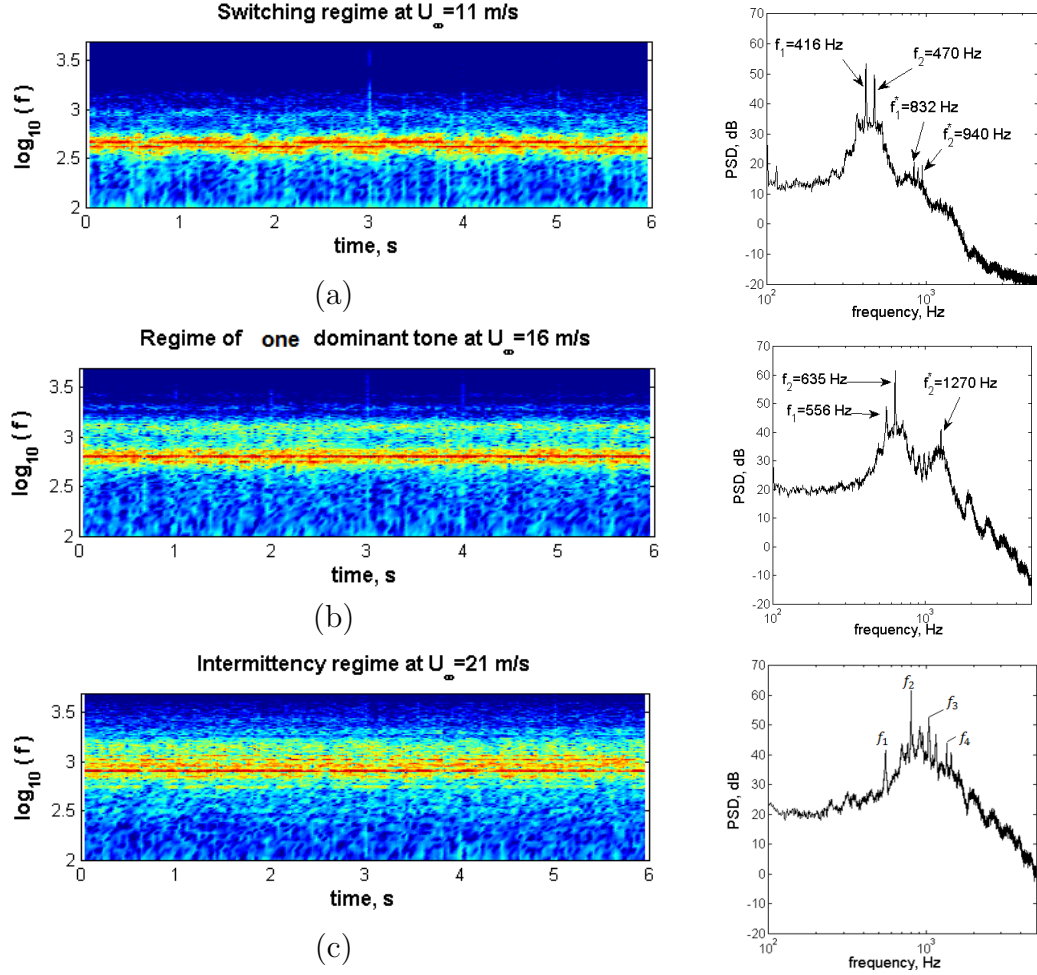


Figure 3.28: Time-frequency analysis for the NACA-0012 airfoil at 0° angle of attack. No tripping. Right plots: averaged far-field spectra. Case a: two averaged spectra for the two states of the switching regime.

tripping both sides of the airfoil possibly radiate LBL tonal noise with different frequency contents because of the imbalance noted in section 3.4.2.

Increasing the geometrical angle of attack up to 5° suppresses the variety of the regimes observed at 0° . At low flow velocities separated points are observed. With increasing of the flow velocity the stable single tone is registered with one or several harmonic tones.

3.8 Bicoherence of the Far-Field Microphone Signal

The bicoherence is calculated for regimes which were detected by time-frequency analysis. The results are presented in figures 3.30, 3.30, 3.31 like two-dimensional maps of frequency versus frequency. The top right map is a zoomed picture with the marked points with highest bicoherence level. The additional PSD plot without calibration coefficients is also presented for a clear matching of the bicoherence maximum level with the dominant tones frequencies.

For the switching regime at 11 m/s (figure 3.30) the maximum level of the bicoherence $b(f_2, f_2)$ of 0.62 is observed for the self coupling of the second frequency $f_2 = 470$ Hz. For $f_1 = 416$ Hz the bicoherence is of 0.44. The combination of the main frequencies has a lower level $b(f_1, f_2) \approx 0.2$. There is a second harmonic hump on the PSD plot which is more visible in figure 3.28(a). Indeed the tone at $f_1^* = 832$ Hz is the first harmonic of the primary tone at $f_1 = 416$ Hz. The associated bicoherence level is $b(f_1^*, f_1) = 0.2$.

The regime of a single dominant tone at $f_2 = 635$ Hz exhibits a maximum bicoherence exhibited the maximum value of 0.51 (figure 3.30). On the PSD plot a harmonic hump is also noted with a tone at $f_2^* = 2 \times 635 = 1270$ Hz. The bicoherence for two aforementioned frequencies $b_{f_2^*, f_2}$ equals 0.51, which indicates that part of the energy in the signal was produced by non-linear interaction.

The intermittency regime is a more interesting configuration. Obviously the highest bicoherence level of 0.44 is observed at $f_2 = 802$ Hz, the frequency of the strongest tone. Another value $b(f_4, f_1) = 0.26$ is found at the frequency $f_4 = 1353$ Hz. This frequency is a combination of the $f_1 = 551$ Hz and $f_2 = 802$ Hz.

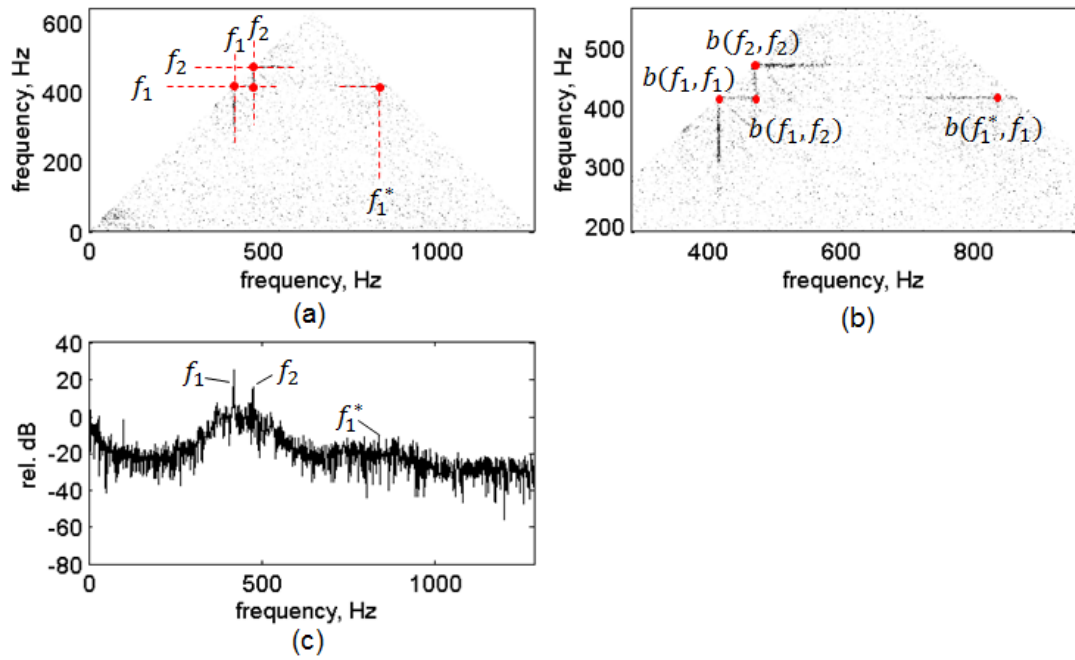


Figure 3.29: Bicoherence of the far-field microphone (a) and zoomed part of the plot (b); (c) - PSD plot without calibration coefficient. NACA-0012 airfoil at 11 m/s and zero angle of attack.

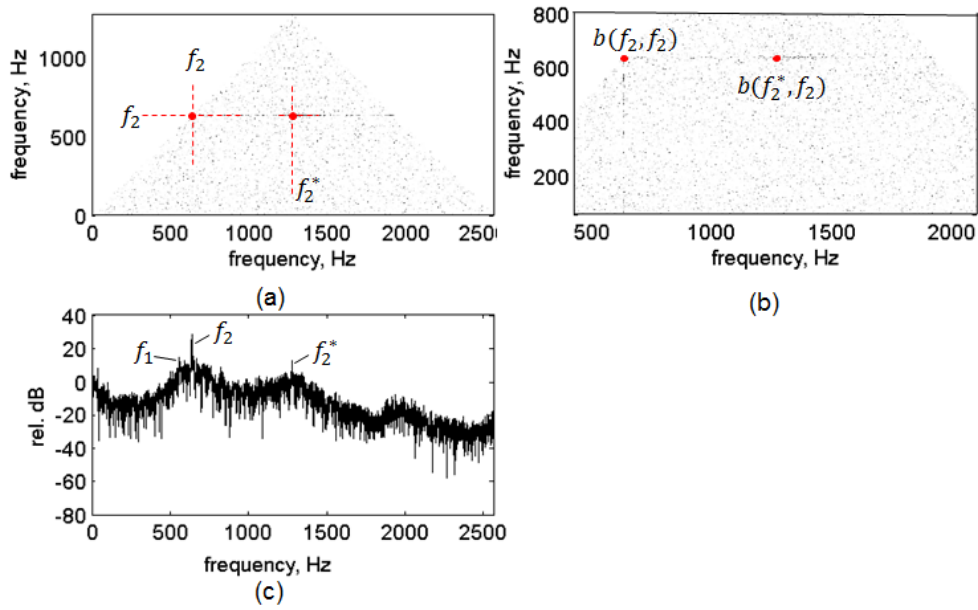


Figure 3.30: Bicoherence of the far-field microphone (a) and zoomed part of the plot (b); (c) - PSD plot without calibration coefficient. NACA-0012 airfoil at 16 m/s and zero angle of attack.

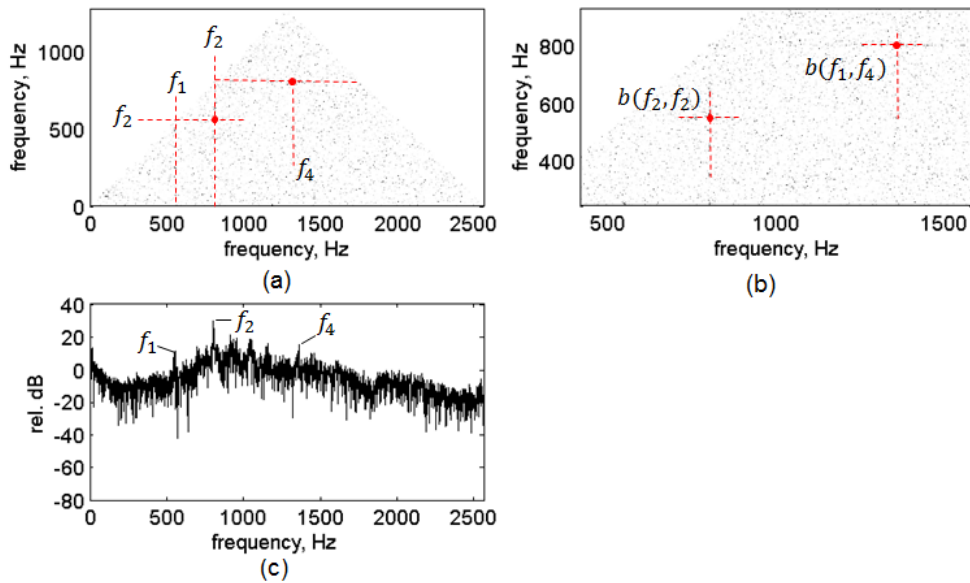


Figure 3.31: Bicoherence of the far-field microphone (a) and zoomed part of the plot (b); (c) - PSD plot without calibration coefficient. NACA-0012 airfoil at 21 m/s and zero angle of attack.

The same time-frequency and bicoherence analysis for a Controlled Diffusion (CD) airfoil was described by Padois *et al.*[55]. The authors also observed several regimes of the tonal noise emission. The peaks at high frequencies were associated with the non-linear interaction of the fundamental and harmonic tones.

3.9 Concluding Remarks

The work presented in this chapter enlarged an experimental data base for the NACA-0012 airfoil. The experimental investigation of this airfoil showed that the range of the tonal noise for the present set-up coincided with the results of previous investigators. In particular the switching between suction and pressure sides as responsible for the tones was already mentioned by previous works. The frequency-flow velocity color maps in combination with the SPL plots featuring the main tones helped to see more clearly the transition from one side to the other. This transition area takes place at lower angles of attack with increasing flow velocity (from $\sim 2^\circ$ at 11 m/s to $\sim 0.5^\circ$ at 19 m/s).

As a complementary result, the angle-frequency radiation maps produced by the directivity measurements showed the bounds of the domain where the measurements are not achievable because of the contamination by the pseudo-sound pressure. The contamination is not an issue because the signature of the pseudo-sound in terms of directivity and frequency content does not influence with that of the tonal noise.

The far-field measurements confirmed and clarified the ladder-type structure which was in a good agreement with Paterson's formula. The effect of the chord length has been shortly addressed. Increasing of the chord length extends the trace of the tonal noise to lower frequencies and flow speeds in the frequency-speed map.

The tests with the small-scale turbulence grid proved that the tonal trailing-edge noise involves a combination of the feedback loop and LBL waves. Indeed the spectral signature without turbulence is made of a hump with superimposed tones, whereas the signature with turbulence only exhibits the hump, at a substantially lower level. It is concluded that the hump corresponds to the direct trailing-edge noise associated with the instabilities and that the tones correspond to an additional selective amplification caused by the feedback.

Another important question about the role of the separation bubble was also addressed. It was figured out that the separation bubble should exist and extend

close to the trailing edge on the side which is responsible for the tones in order to produce high sound levels. For the NACA-0012 airfoil and the investigated parameters the pressure side produced the tones. However the separation bubble is not a sufficient condition for the tonal noise production, because it is still observed when the turbulence grid is installed. Again the feedback loop appears as necessary.

The time-frequency analysis revealed several regimes with different characters of the tonal noise emission depending on the flow velocity. The switching regime with two non simultaneous tones transformed to the regime with single tone at central frequency of the hump with increasing of the flow velocity. At high flow velocities the main tone became unstable and accompanied by the multiple weaker tones.

Figures 3.32, 3.33 summarize the information. The contours of the noise signature (the solid line for configuration A, dashed line for configuration B and dotted line for configuration C) are superimposed. The regimes as identified from the time frequency analysis of the 8 flow speeds are indicated by color lines for each configuration. The percents of chord stand for the location of the separation bubble from the leading edge on the side which produces tones. It should be reminded that using the tripping device on one side has no significant influence on the location of the separation bubble on the opposite side. Therefore for the case at zero angle of attack the location of the separation bubble is the same for all configurations A,B and C. As at non-zero angle of attack the locations of the separation bubbles on the pressure side and suction side are different, the values for the pressure side are presented in configuration B at 5° and for the suction side in configuration C. This figure emphasizes the asymmetry of the experimental setup. It also shows that the regimes are sensitive and depend on the combination of factors (flow velocity, angle of attack and configuration). Another interesting point is the configuration C (at 5°) or configuration B (at -5°) where the pressure side a priori responsible for the tones is tripped. In this case tonal noise is still observed, which can be explained by the fact that this configuration is very close to the area (low flow velocities and angles of attack) where the suction side is responsible for the tones. However the separation bubble ends not close enough to the trailing edge and the amplitude of LBL instabilities is attenuated when they reach the trailing edge.

The bicoherence analysis indicated that the relations between the main tone and harmonic its tones had a non-linear character.

Some results of this chapter were discussed in [56].

The next two chapters present numerical simulations and analytical modeling for the NACA-0012 airfoil.

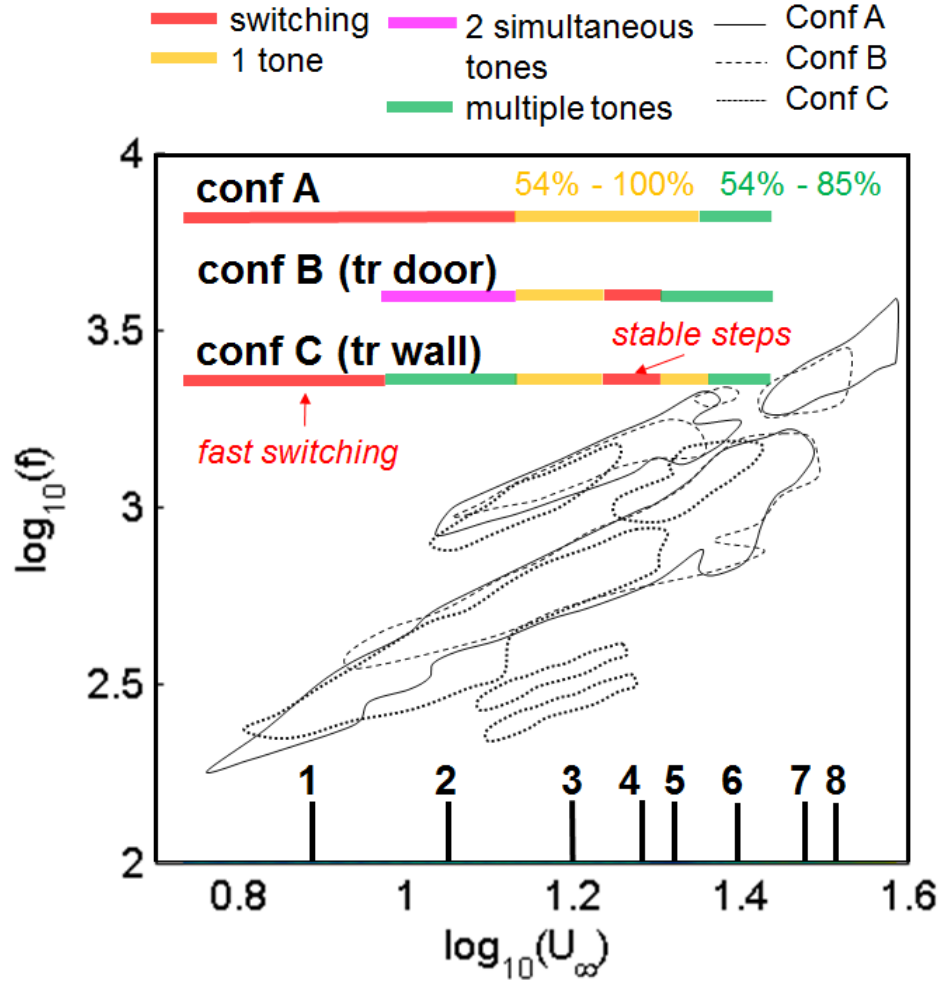


Figure 3.32: The NACA-0012 airfoil at zero angle of attack. Configurations A, B and C. Noise signature contours marked by black solid, dashed and dotted lines, tonal noise regimes marked by colored lines and location of the separation bubble from the leading edge corresponding to some of regimes. 8 speeds are marked: 1 - 8 m/s ($Re_c = 0.63 \times 10^5$); 2 - 11 m/s ($Re_c = 0.87 \times 10^5$); 3 - 16 m/s ($Re_c = 1.26 \times 10^5$); 4 - 19 m/s ($Re_c = 1.5 \times 10^5$); 5 - 21 m/s ($Re_c = 1.6 \times 10^5$); 6 - 25 m/s ($Re_c = 2 \times 10^5$); 7 - 30 m/s ($Re_c = 2.4 \times 10^5$); 8 - 33 m/s ($Re_c = 2.6 \times 10^5$).

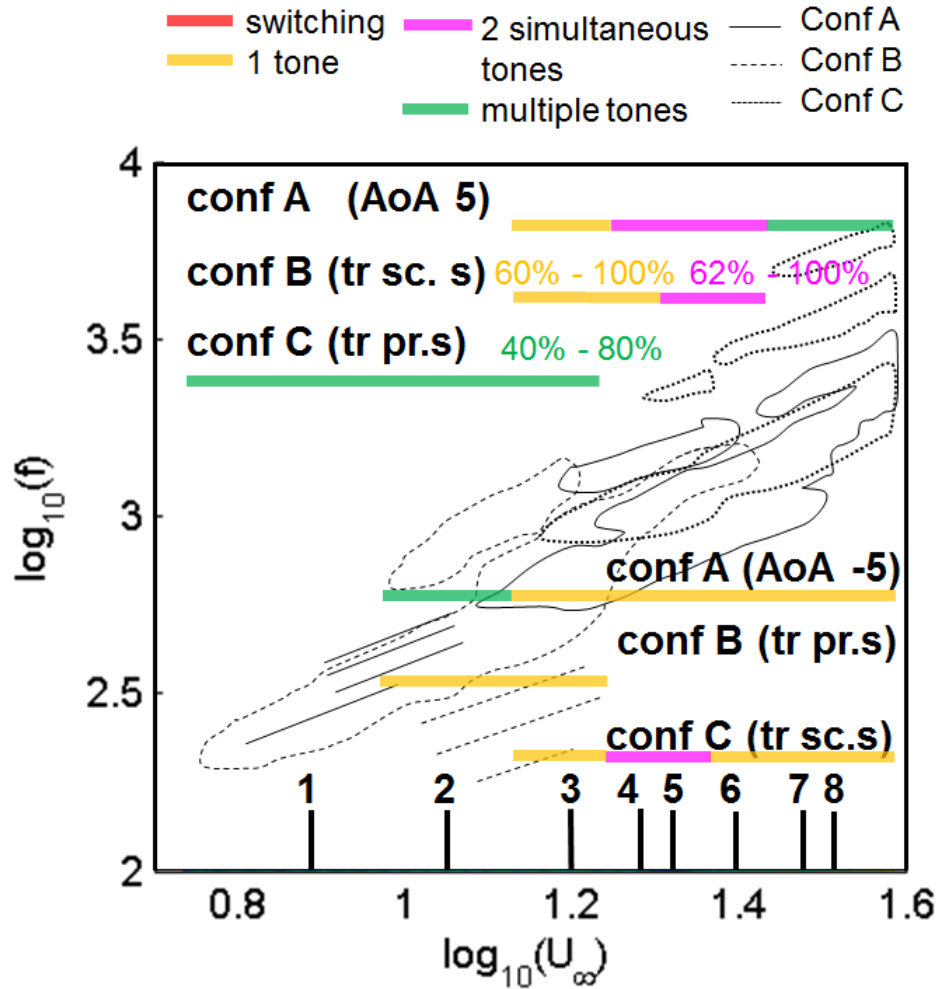


Figure 3.33: The NACA-0012 airfoil at 5° . Configurations A, B and C. Noise signature contours marked by black solid, dashed and dotted lines, tonal noise regimes marked by colored lines and location of the separation bubble from the leading edge corresponding to some of regimes. 8 speeds are marked: 1 - 8 m/s ($Re_c = 0.63 \times 10^5$); 2 - 11 m/s ($Re_c = 0.87 \times 10^5$); 3 - 16 m/s ($Re_c = 1.26 \times 10^5$); 4 - 19 m/s ($Re_c = 1.5 \times 10^5$); 5 - 21 m/s ($Re_c = 1.6 \times 10^5$); 6 - 25 m/s ($Re_c = 2 \times 10^5$); 7 - 30 m/s ($Re_c = 2.4 \times 10^5$); 8 - 33 m/s ($Re_c = 2.6 \times 10^5$).

Chapter 4

Comparison of ERAU Numerical Simulations with the Experimental Results for the NACA-0012 Airfoil

The numerical investigation of the transitional flow (and associated noise) over the airfoils tested in this thesis was conducted at Embry-Riddle Aeronautical University. A short description of the computational model is mentioned in this chapter. Some results for the NACA-0012 airfoil are compared with experimental data produced at Ecole Centrale de Lyon. Some discrepancies are identified. In particular for some cases in the computations, tones are observed, whereas during the experimental campaign the equivalent configuration did not produce high-level noise.

4.1 Remarks about the Numerical Model

As a part of the collaborative work a numerical simulation of the flow over transitional airfoil was done at ERAU (see details in [57, 9]). It was expected that the numerical investigation will improved the understanding of the phenomenon and highlight details which are hard to observe during the experiments.

Sets with 2D and 3D studies in freestream flow were performed. The computational mesh of the pseudo-2D model had the following size in terms of number of cells $1281 \times 789 \times 3$ (in streamwise, normal and spanwise direction), whereas the size for the 3D case was $1281 \times 789 \times 101$. The 3D configuration was conducted for the spanwise extension of $0.1c$ with periodic conditions applied at the span end planes. Moreover, a 2D configuration with the nozzle for the SD7003 airfoil was tested at identical flow conditions as in the freestream model. The physical time step was 0.675×10^{-6} sec for the 2D model and 0.16875×10^{-6} sec for the 3D. To prevent transient processes the steady-state flow conditions were first reached after marching for 20 characteristic cycles. The pressure values were recorded for 720000 steps. So for the baseline set-up collecting the data sample for 0.487 sec with the sampling rate 33.6 kHz achieved the frequency resolution of $\Delta f = 2.05$ Hz. The numerical solution was successfully validated against the DNS analysis performed by Desquensnes *et al.*[20].

The Numerical studies are based on a high-fidelity Implicit Large Eddy Simulation (ILES) code [58] which solves the compressible Navier-Stokes equations with a 6th-order scheme. The code uses a finite-difference approach to descretize the governing equations with all the spatial derivatives obtained using the high-order compact-differencing scheme (more details in [59]).

During the numerical simulation the following questions were investigated:

- effect of 2D and 3D modeling;
- effect of upstream turbulence;
- effect of angle of attack ($\alpha^* = 0^\circ, 2^\circ, 4^\circ, 6^\circ, 8^\circ, 10^\circ$ and 12° at $Re_c = 1.8 \times 10^5$) in a configuration which corresponds to the experimental case $U_c = 25$ m/s);
- effect of flow velocity ($Re_c = 1.44 \times 10^5, 1.8 \times 10^5, 2.16 \times 10^5, 2.52 \times 10^5, 2,88 \times 10^5$ and 3.24×10^5 at $\alpha^* = 2^\circ$, see chapter 7.2);

- effect of freejet upstream flow conditions (only for the SD7003 airfoil at $Re_c = 1.66 \times 10^5$ and $\alpha = 2^\circ$).

The 3D modelling shows a better overall agreement with the experiments. Therefore only the results of the 3D freestream simulation will be discussed. For more details the reader can address the references [60, 57, 9].

4.2 Comparison of Numerical and Experimental Data

The pressure coefficient is a key indicator which allows to determine if the flows in the experiment and in the numerical simulation are comparable. The measurements were described in section 2.4 and some results were presented in section 3.2. A typical comparison with the numerical simulation conducted at ERAU is shown in figure 4.1.

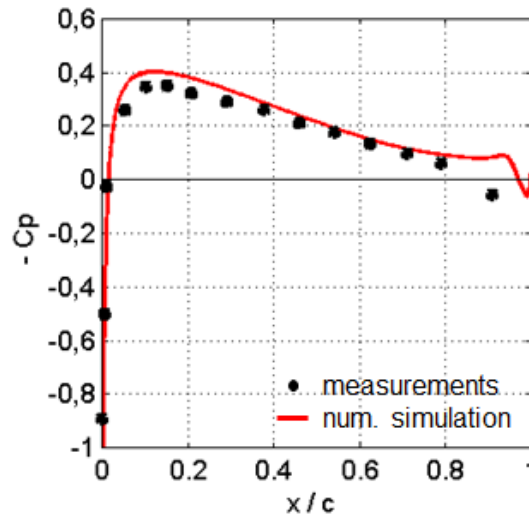


Figure 4.1: Pressure coefficient distribution for the NACA-0012 airfoil at 16 m/s and $\alpha = 0^\circ$). Numerical simulation in freestream.

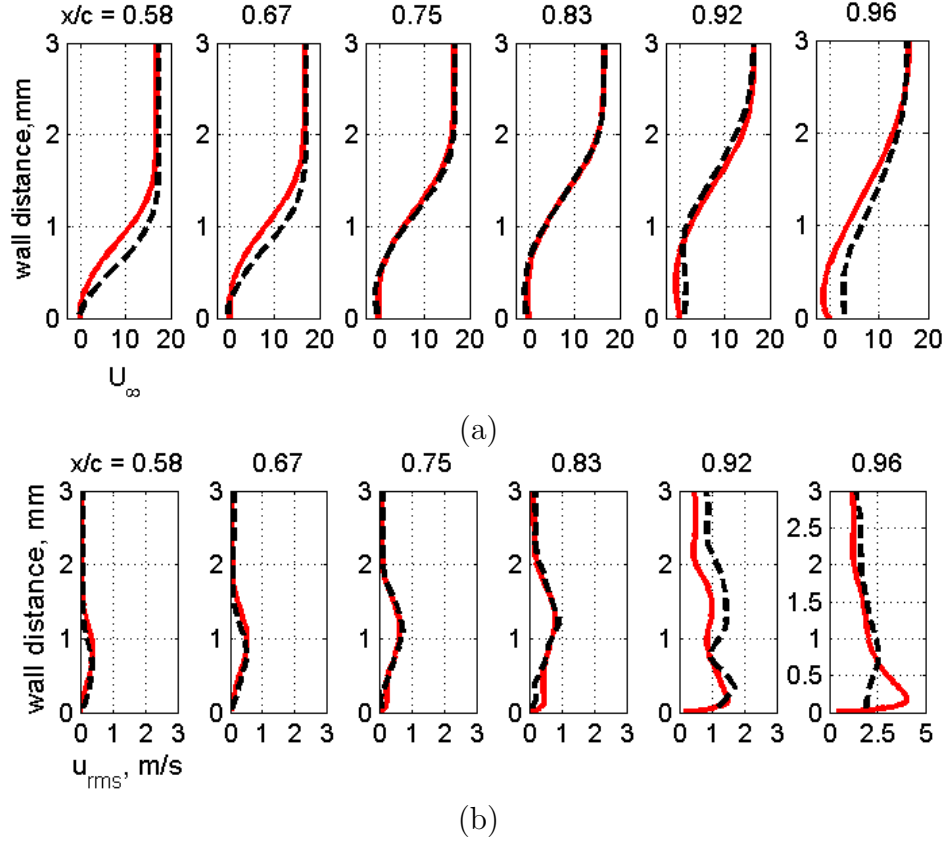


Figure 4.2: Comparison of the velocity spectra of NACA-0012 airfoil. (a) - mean velocity; (b) - rms velocity. — — measurements; — — numerical simulation.

The difference between the measured and computed C_p is significant close to the trailing edge where the computational results show a separation area starting from 60% of the chord length. The measured data do not exhibit the same feature despite the trend observed at $x/c = 0.8$. This could be because of the limited number of probes close to the trailing edge. But the last measuring point at $x/c = 0.9$ deviates strongly from the simulation. This coincide with the conclusions of the flow visualization and hot-wire anemometry tests which showed a separation bubble from 54% of the chord length. As was mentioned previously (section 3.2) it could be associated with the influence of the nozzle (see also [51]).

The compared measured and simulated velocity profiles are presented in figure 4.2. The agreement is satisfactory. The differences are larger close to the trailing edge. They can be explained by differences in airfoil loading or overall flow conditions. Furthermore the HWA measurements become less accurate at the mean flow velocity approaches zero. In particular it must be pointed that the HWA

does not discriminate the either upstream or downstream motion, which possibly explains the discrepancies on the mean-velocity profiles at 98% of chord. The u_{rms} velocity profiles differ more significantly especially near the trailing edge. The location of the maximum at the last point 95% does not coincide and the numerical data have a higher level than the experimental one.

The investigation of the influence of angle of attack and mean flow velocity allows determining the boundaries of the tonal noise regime. As expected with increasing angle of attack the separation bubble on the pressure side moves upstream whereas on the suction side it moves downstream from the initial symmetrical position at zero angle of incidence.

The only contradiction between of experimental and numerical results is the area where the tonal noise is observed and the role of each side of the airfoil in this mechanism. In the experimental study the highest effective angle of attack for which tonal noise was observed was around 4.5° . Moreover, for all tonal noise cases a separation bubble was observed on the pressure side close to the trailing edge. This was indicated as a necessary condition for the tone production. However in the simulations tones were observed at 6° with a separation bubble on the suction side from 9% to 25% near the leading edge and a attached flow on the pressure side.

In the accompanying numerical study performed by ERAU the linear stability theory was used to analyze the roles of both sides of the airfoil in the tonal noise generation. Figure 4.3 presents the amplification of the tonal frequency 1550 Hz, a velocity colormap and a plot of the friction coefficient on both sides of the NACA-0012 airfoil at zero angle of attack and 25 m/s. The vertical blue dotted lines show the flow separation and reattachment detected from the friction coefficient plot. It was observed that the instability starts growing in the region where the separation bubble is located. Similar amplification by the separation bubble was observed on the suction side of the NACA-0012 airfoil close to the leading edge at $\alpha^* = 6^\circ$. For the non-tonal cases of the numerical simulations the frequency modes are also amplified near the leading edge but disappear farther downstream. All details can be found in [9].

The increase of the flow velocity reduces the surface of the separation bubble on the suction side, whereas on the pressure side it stays stable. Despite this stability the amplification increases with the flow velocity. This can be interpreted in the sense that at low flow velocities the suction side produces tones, but that at higher velocities the pressure side contributes to the mechanism. The same effect was observed during the experiments and was also described in [28, 29].

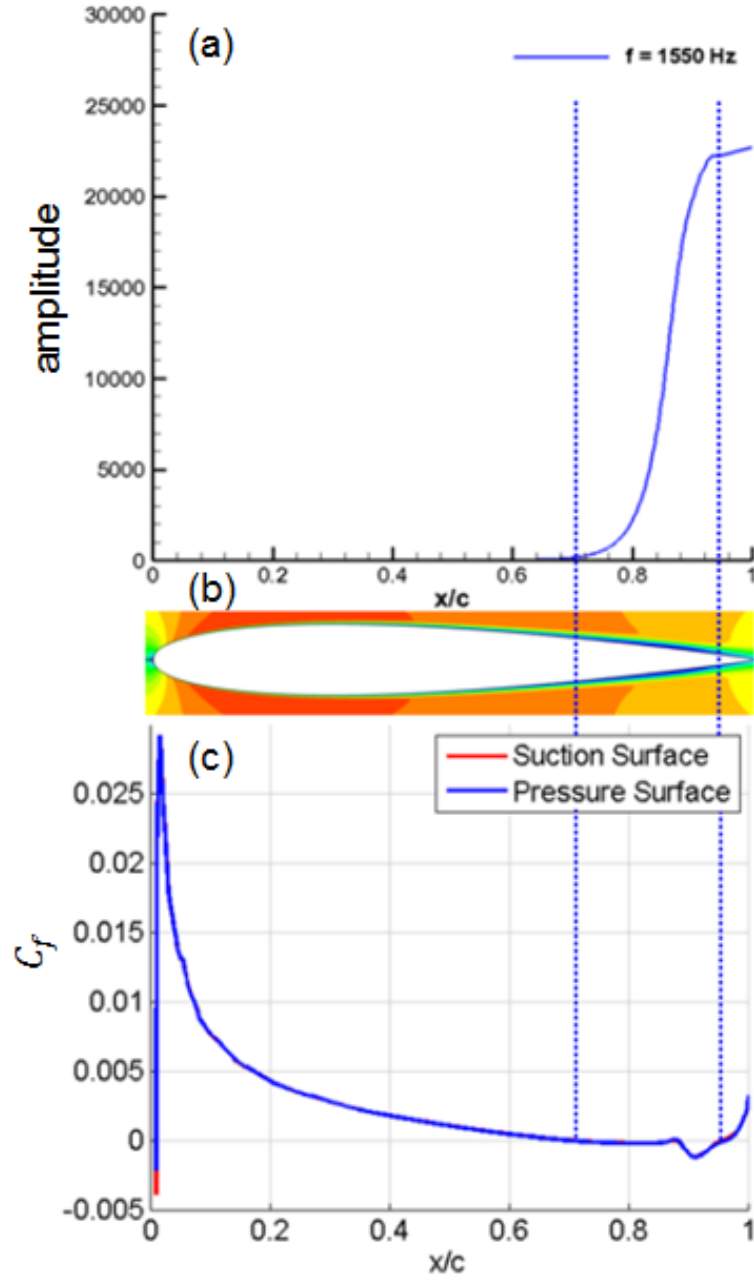


Figure 4.3: (a) - instability amplification of the main tonal peak along the chord; (b) - velocity contours; (c) - friction coefficient. NACA-0012 airfoil at $\alpha^* = 0^\circ$ and $U_\infty = 25$ m/s ($Re = 1.8 \times 10^5$) [9].

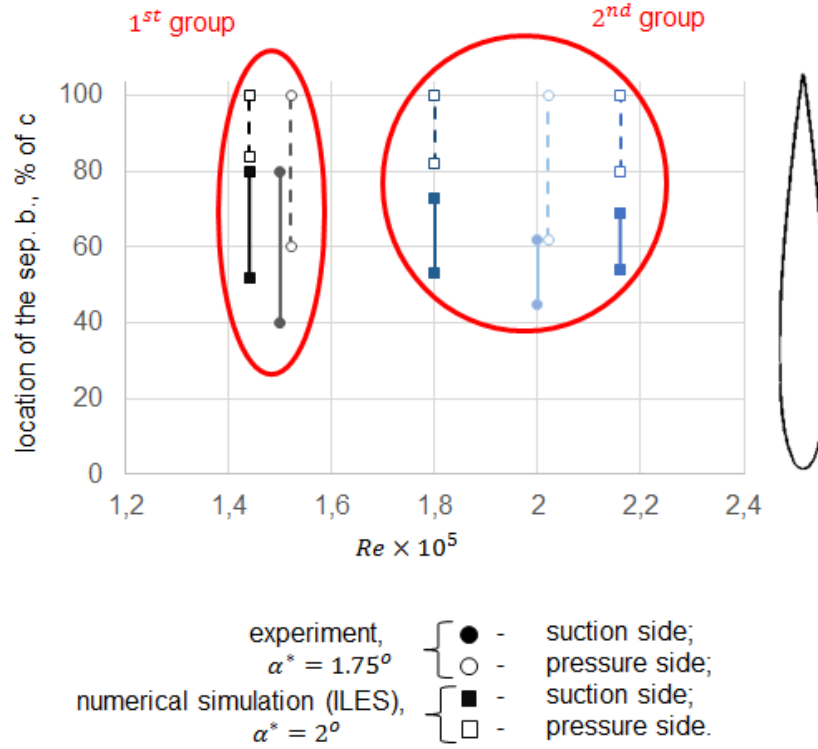


Figure 4.4: Comparison of the separation bubble localization between experimental and numerical results.

As a summarizing scheme the locations of the separation bubble on both sides of the airfoil is presented in figure 4.4 for effective angles of attack that are considered close enough to each other. The results are divided into two groups according Reynolds number. This was done because the values Reynolds number in numerical and experimental studies were close to each other but not the same. So the closest Reynolds number was chosen for comparison. The experimental pressure side results are shifted at $Re_c = 0.02 \times 10^5$ for clarity because of crossing with separation bubble on the suction side. The first one is at a Reynolds number around 1.5×10^5 . The differences of the beginning of the separation bubble between numerical simulation and experiments are nearly 10%. The location of the reattachment takes place at 80% of the chord length for both. On the suction side according to the measurements developing of the separation bubble starts at 60% when numerical simulation registered it only at 82%. The second group includes experimental data at $Re_c = 2 \times 10^5$ and numerical simulation at $Re_c = 1.8 \times 10^5$ and $Re_c = 2.16 \times 10^5$. Flow visualization showed the separation area from 45% to 62% on the suction side and from 62% to 100% on the pressure side. The increasing of Reynolds number

slightly moves the reattachment closer to the leading edge on the suction side and leaves unchanged pressure side in the numerical simulation. As for the previous group the beginning of the flow separation on the both sides starts earlier and separation surface on the pressure side is much longer in the experiments.

4.3 Concluding Remarks

The numerical simulations of the trailing-edge tonal noise were conducted at the Embry-Riddle Aeronautical University (ERAU). The effects of the angle of attack and of the Reynolds number were investigated for the NACA-0012 airfoil in freestream simulations. Tonal and non-tonal regimes were included in the test cases. The measured and calculated pressure coefficients were in a good agreement except in the area close to the trailing edge and showed that the flow parameters in experiments and simulations are close to each other. The importance of the separation bubble for tonal noise was proved by the experiments and described in a previous chapter, so the comparison was focused on the location of the separation bubble. The velocity profiles are in good agreement with some differences close to the trailing edge of the NACA-0012 airfoil. In general the measured separation bubbles are more extended to the leading edge on the pressure side as well as on the suction side. The discrepancies can be explained by the uncounted features of the experimental setup in the freestream simulations. It should be mentioned that as pointed out by Mankbadi *et al.*[61] the Tollmien-Schlichting waves became three dimensional forming the resonant triad. This can not be captured in the numerical simulations due to the lack of spanwise length and may also influence on the discrepancies.

One of the important conclusions from the numerical simulation is the explanation of the separation bubble role in the trailing-edge tonal noise. The linear stability theory showed that the separation bubble amplifies the instability waves. In other words the Tollmien-Schlichting waves transform to the Kelvin-Helmholz waves. The previously mentioned switching between the sides responsible for the sound with increasing flow velocity was numerically confirmed and was explained by the amplitude of the amplification in the separation area on each side.

However the question about the limit values of the parameters for the emission of tonal noise is still controversial. The calculations showed tonal noise at much higher angles of attack than what was observed during the experiment. The most likely explanation is the influence of the experimental set-up and some differences in flow parameters.

Chapter 5

Analytical Modeling of the Tonal Noise Radiation

The analytical models based on the acoustic analogies usually solve a problem in an approximate way and provide fast and cheap results. They can concentrate the basic physical mechanisms and give an idea of what happens during experimental researches. Of course, the analytical models can not reproduce the same details as numerical simulations, but they are highly useful to assess, for instance, cause to effect relationships.

The analytical prediction of the tonal noise of an airfoil using Amiet's model is illustrated in this chapter. The wall pressure measurements near the trailing edge are used as input data. The predicted tone level corresponds to the level measured by the far-field microphone. One of the issues for using the analytical model is a determination of the convection speed, which is needed for the calculations. Finally this value was estimated on the basis of some experimental data, numerical simulation and results of previous researches.

5.1 Theoretical Background

The interpretation of airfoil tonal noise in terms of feedback mechanism is based on the assumption of instability waves driven by external acoustic waves. Both the hydrodynamic and the acoustic motions have very different characteristic scales at low Mach numbers; indeed the acoustic-to-hydrodynamic wavelength ratio is inversely proportional to the mach number that is very small in our case. As a result the acoustic motion is nearly in phase over quite large portions of the airfoil chord. Intuitively this is compatible with a feedback between the maximum-velocity point A and the trailing edge only if the instabilities are receptive to acoustic forcing in the vicinity of A and not elsewhere. This condition is fulfilled as long as the instabilities grow exponentially to reach high amplitudes away from the point A. In order to confirm the hypothesis, estimates of the orders of magnitude of the various involved motions are needed, which requires resorting to relevant models and/or measured quantities. The instability growth and overall level can be inferred from wall-pressure measurements performed at various chordwise locations. The other measured quantity is the far-field sound at 90° from the streamwise direction. Because LBL-wave radiation is just a declination of trailing-edge noise any validated model of that noise can be used to quantify the source-to-sound relationship and therefore help to interpret various measurements.

As noted by Howe [16] there are three categories of classified analytical models for predicting trailing-edge noise, according to the way the flow interaction with the edge of a plate is described. The first ones are based on Lighthill's acoustic analogy in which aerodynamic fluctuations are represented by a distribution of quadrupole acoustic sources. This view was for instance used by Ffowcs Williams & Hall [14] for the analysis of the scattering by sharp edges. The next ones are theories based on the linearized unsteady-aerodynamics equations. One of them is Amiet's model [15], which is used in the present study. The last category is *ad hoc* models where the strengths and multipole types of the source distribution are determined empirically [62, 63]. Howe [16] proposed an analytical model that relates the acoustic field to the turbulent velocity field, discussed the connection of the surface pressure fluctuations and the noise spectrum and also stressed the dual possibility of applying Kutta and no-Kutta conditions. This model can be applied only to low Mach numbers flows.

Some experimental researches, for example by Brooks & Hodgson [64], aimed at confirming and complementing the analytical theories. The authors provided a prediction scheme on the basis of the wall pressure statistics close to the trailing edge. A good agreement between experimental data and analysis proved the cor-

rectness of the theoretical assumptions. As another indicative example Schlinker & Amiet [65] developed and validated a prediction model for the helicopter rotor trailing-edge noise using the analytical model from [15] and experiments for an isolated cambered airfoil.

The present work addresses the tonal noise associated with LBL instabilities using the linearized theory of Amiet [15]. Not going further into the details, all aforementioned works addressed broadband trailing-edge noise associated with boundary-layer turbulence.

Amiet's solution is in two steps. The first step provides an expression for the unsteady lift or pressure distribution induced along the airfoil surface by the scattering of boundary-layer disturbances into sound at the trailing edge. This distribution can be seen as the trace of the acoustic motion at the wall, from which the far-field sound is calculated by a radiation integral. It also represents the acoustic near-field pressure that is actually forcing the developing hydrodynamic instability waves. In the second step the far-field pressure is calculated from the induced unsteady lift.

A possible use of Amiet's trailing-edge noise model is to confirm the cause-to-effect relationship between the measured wall-pressure close to the trailing edge and the far-field sound by calculating the former from the latter. This is also attempted here for the tones, assuming that the associated spanwise correlation length is very large because of the feedback process. This last point is crucial. It has been confirmed by the coherence measured between probes from the spanwise set B of the NACA-0012 airfoil shown in figure 2.4, leading to the surface plot in figure 5.3(a). In the plot the low-frequency part below 100 Hz must be ignored and the attention focused on the peak around 1 kHz. In fact LBL waves correspond to coherent motion even if the acoustic feedback is ignored, when compared to the random motion in turbulent boundary layers. As the instabilities are reinforced by the feedback, two-dimensionality is triggered in the flow because the acoustic wavelengths are much larger than the hydrodynamic wavelengths at low Mach number. This explains why no decrease is found of the measured coherence in figure 5.3(a) along the dashed black line, even at the larger separation of 50 mm, and justifies that a fully two-dimensional model is used to describe the sources of the trailing-edge noise in this case, at least for a first insight. Such a simplification is needed because Amiet's trailing-edge noise model can only be used in two limit cases. One is the turbulent boundary layer for which the spanwise correlation length is substantially smaller than the span, leading to a closed-form expression of the far-field pressure PSD [17]. The other one is the presently assumed case of perfect correlation for which a deterministic calculation can be made at a single frequency.

5.2 Convection Speed

One of the crucial input parameters for the model is the convection speed U_c , which characterizes the velocity of the instability waves developing near the wall of the airfoil. There are several ways to get this value. The first one and the most preferable is the determination from the phase of the cross-spectrum of the two chordwise RMPs closest to the trailing edge (see formula 3.3).

The same method allows checking the relationship between wall-pressure fluctuations and the acoustic waves. For instance the calculation from the cross-phase plot of the sensor №18 near the trailing edge and the far-field microphone at the distance 1.5 m provides the phase speed 336 m/s, which is very close to the speed of sound (see figure 5.1).

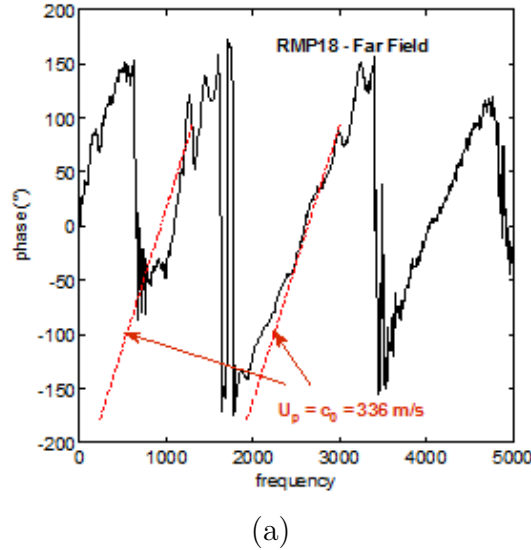


Figure 5.1: Phase distribution of the cross-spectrum between the sensor 18 and the far-field microphone for the NACA-0012 airfoil at $U_\infty = 30 \text{ m/s}$ and $\alpha = 0^\circ$. Configuration A.

More unexpectedly the cross-spectrum phase between the wall-pressure probes №20 and №23 (figure 5.2) for the NACA-0012 airfoil at free-stream velocity 30 m/s and zero angle of attack shows two possible convection speeds 22.5 m/s ($U_c/U_\infty = 0.75$) and 12 m/s ($U_c/U_\infty = 0.4$). The distance between probes is 0.015 m (see figure 2.4). The value 22.5 m/s is found in the range from 1200 Hz to 3200 Hz (main hump on the PSD of) and from 3800 Hz to 5000 Hz (secondary hump). The

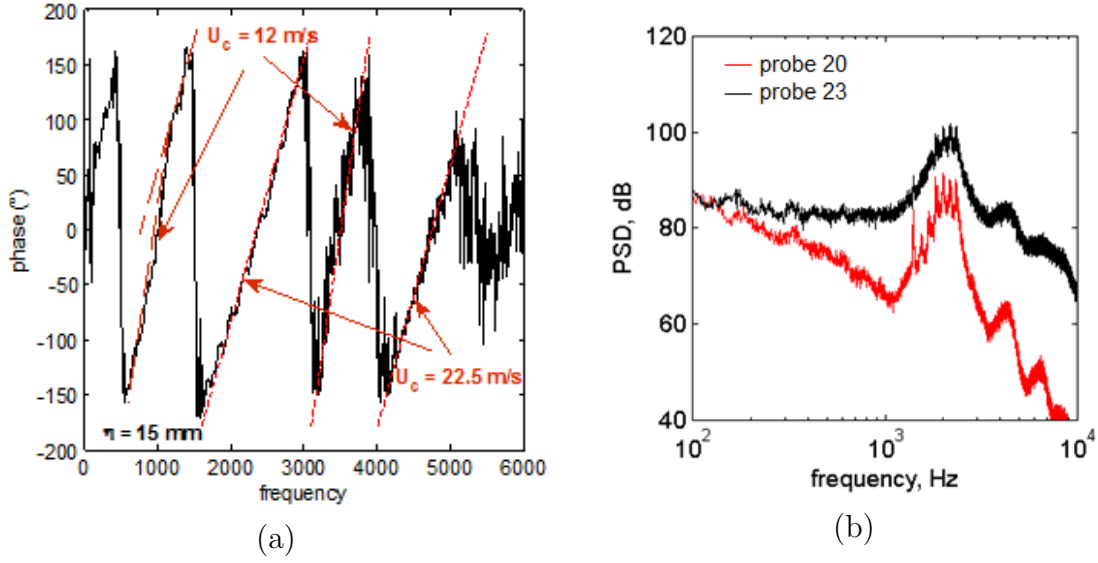


Figure 5.2: (a) Phase distribution of the cross-spectrum between sensors 20 and 23 for the NACA-0012 airfoil at $U_\infty = 30 \text{ m/s}$ and $\alpha = 0^\circ$. (b) PSD level of the RMPs №20 and №23. Configuration A.

second value 12 m/s is found between the two aforementioned humps and below 1200 Hz.

However, for some cases the phase slope is questionable and not easy for interpretation. In the presence of the acoustic back-reaction the true linear relationships are not simply either pure convection of the aerodynamic frozen patterns at the wall or source-to-sound relationships from wall-pressure to acoustic far-field. Trailing-edge noise sources are generated by different boundary layers developing on both sides of the airfoil and measurements on one side are possibly contaminated by the contribution from the other side.

Another opportunity to estimate the value of the convection speed is to take into account the statistical data obtained by previous investigators in similar experiments. Arcordoulis *et al.* [13] analyzed the spectrogram of the phase difference for measurements taken at every 1 mm from the trailing edge at the frequency of a tone and concluded that at Reynolds numbers equal to 0.5×10^5 , 1×10^5 , 1.5×10^5 the ratio U_c/U_∞ equals 0.32, 0.38 and 0.42 respectively.

Pröbsting [8] estimated the convection speed on the basis of a wavenumber-frequency spectrum as $U_c/U_\infty = 0.75$, which corresponds to the U_c/U_∞ range provided by Brooks & Hodgson [64] from 0.58 to 0.9. This value is close to the

highest value obtained in the present study whereas Arcordoulis' values are closer to the smallest one.

The third way to estimate the convection speed is the numerical simulation which was conducted at ERAU. The results of a dispersion analysis showed that for the NACA-0012 airfoil at 25 m/s the convection speed is 7.25 m/s (or $U_c/U_\infty = 0.29$), which again confirms quite a small value. No clear explanation has been found for the quite large differences.

In view of the variety of results, it was decided to vary the convection speed from $0.29 \times U_\infty$ to $0.7 \times U_\infty$ and to investigate the influence of this parameter on the model results.

5.3 Near-Field and Far-Field Pressures

Assuming a two-dimensional motion, the expression of the amplitude of the near-field wall pressure induced on the airfoil by trailing-edge scattering is simply

$$|p_{NF}| = |1 - (1 - i) E(-BX)|$$

for a unit amplitude of the source, with $B = a\bar{K} + (1 - M_\infty)\mu$, $\bar{K} = \omega c/(2U_\infty)$, $\mu = \bar{K}M_\infty/\beta^2$, $\beta = \sqrt{1 - M_\infty^2}$, $X = x/c$ being the negative coordinate to the trailing-edge made dimensionless by the half chord, $a = U_\infty/U_c$ being the ratio of the external flow speed to the convection speed of the hydrodynamic disturbances and ω is the angular frequency. E is the Fresnel integral defined as

$$E(\xi) = \int_0^\infty \frac{e^{it}}{\sqrt{2\pi t}} dt$$

The second step of the model leads to the approximation of the far-field pressure amplitude as (see Roger & Moreau [17] for details)

$$|p_{FF}| \simeq \frac{k H c}{4 \pi C R} \left| 1 - (1 - i) E(2B) + (1 - i) \sqrt{\frac{B}{\mu}} e^{2iC} E(2\mu) \right|$$

where $C = a\bar{K} + M_0\mu$, H is the span length, R the microphone distance and k the acoustic wavenumber. Forming the ratio $|p_{NF}|/|p_{FF}|$ and multiplying by the amplitude of the measured far-field sound restores the needed acoustic trace on

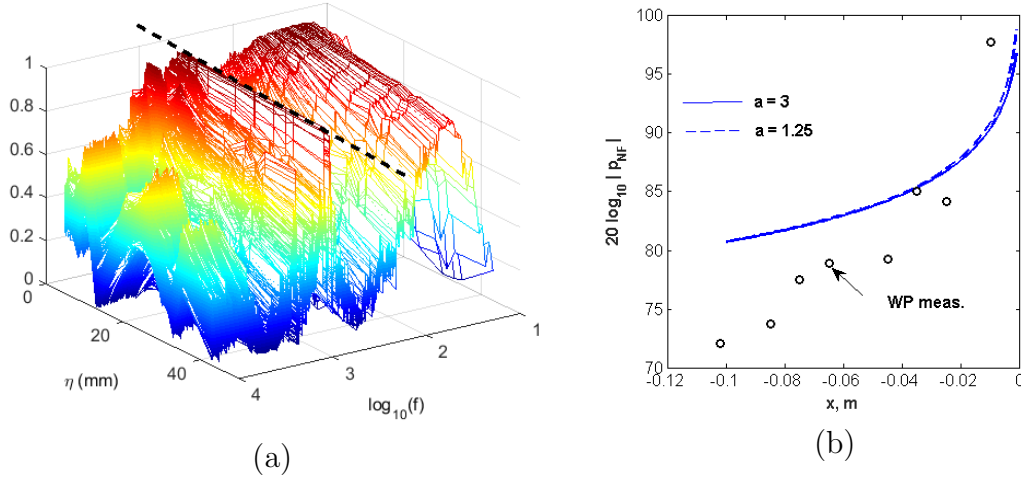


Figure 5.3: (a): typical three-dimensional coherence plot versus frequency and separation η for the door-side spanwise-distributed set of RMPs on the NACA-0012 airfoil. The dashed line follows the dominant tone frequency. (b): Estimation of the acoustic wall-pressure distribution from the far-field pressure, according to Amiet's model.

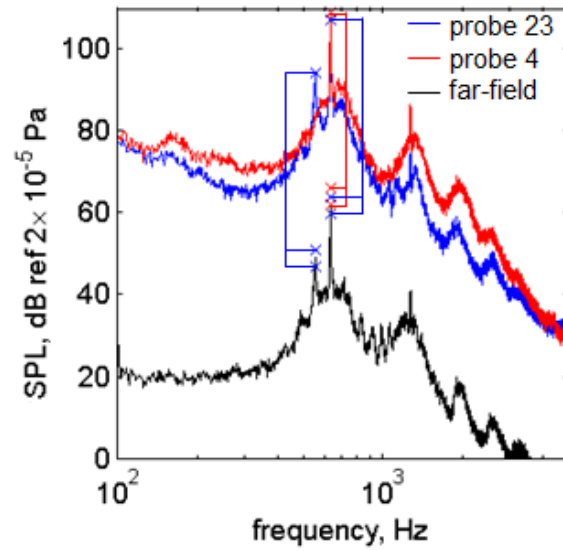
the wall as a function of the distance to the trailing edge. The result is plotted in figure 5.3(b) for a tone frequency of 800 Hz, a flow speed of 21 m/s and a measured sound of 60 dB at the distance of 1.5 m. The parameter a strongly determines the amplitude of trailing-edge noise generation but it has a negligible effect on the aforementioned ratio. Indeed it is given two values here, namely 3 and 1.25, without producing significant changes. The acoustic near-field is expected close to 100 dB directly upstream of the trailing edge, corresponding to the dominant tone shown in figure 3.28(c). The near-field acoustic pressure is expected slightly above 80 dB around the location of point A according to this prediction. Unexpectedly the measured peak level at the wall is well below this value except in the aft part of the airfoil whereas the RMP capture the total pressure field, combining acoustic and hydrodynamic pressures.

The estimate must be taken with care because of ignored effects that are expected to occur close to the wall. The mean-velocity gradient in the boundary layer is responsible for refraction of upstream-propagating sound waves away from the wall. This possibly explains the results of figure 5.3(b). Anyway in view of the results the growing instabilities are probably not receptive to acoustic forcing in the last 30% of chord. But they could be forced farther upstream. This makes the hypothesis of a feedback loop physically acceptable.

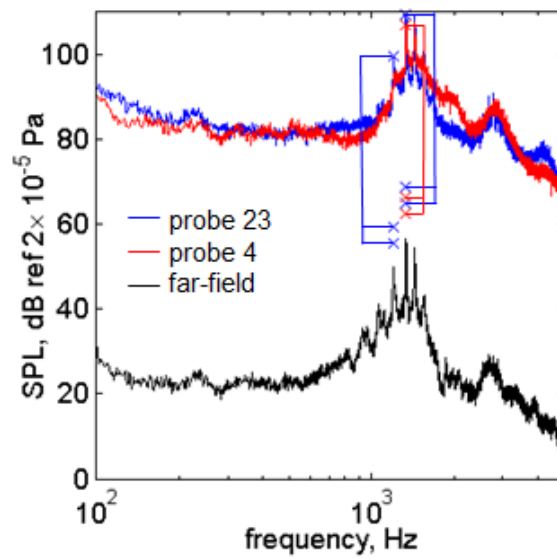
5.4 Tone Level Prediction

When addressing quantitative sound predictions from a specified amplitude in the hydrodynamic field, the convection speed must be known with a reasonable accuracy. Facing the difficulty of determining it for tones by the usual examination of the phases of cross-spectra between chordwise distributed sensors, the aforementioned stability calculations performed at ERAU of the paper have been used instead. The theoretical convection speed is found below 30% of the external flow speed in the trailing-edge area. Higher convection speeds more representative of attached turbulent boundary layers have also been tested, leading to a range of values that can be interpreted as an uncertainty in the input data. Moreover the analytical prediction from the measured wall spectra is made difficult for various reasons. Firstly, both sides of the airfoil contribute, therefore calculations are to be performed for each; but the way the contributions interfere is not elucidated. Secondly the wall-pressure is measured only at some distance upstream of the trailing edge, whereas the instability waves are continuously amplified (or possibly damped) down to the trailing edge where they are scattered as sound. This makes some underestimate (or overestimate) expected. Finally the reattachment of the separated layers in the very vicinity of the trailing edge presumably modifies the properties of the noise emission. The tests reported in figure 5.4 for the two flow speeds of 16 m/s and 25 m/s are made with the wall-pressure tone levels measured at RMP 4 (door side) and 23 (wall side) as input data. This provides two estimates of the far-field sound that must be summed to be compared to the microphone measurements.

At 16 m/s (figure 5.4(a)) the results are reported in table 5.1. The tone at 556 Hz is only emitted from the door-side probe, as a results of the imbalance between both sides attributed to the installation and already mentioned in section 2.3. The dominant tone at 635 Hz is emitted from both sides with nearly equivalent source levels, though the overall wall-pressure level at probe 4 is lower than that at probe 23. This level difference is also possibly attributed to the larger distance to the edge at RMP location 4 (see figure 2.4). The associated sound levels are 49 dB and 61.5 dB for the lower and the higher frequencies, respectively. Amiets model predicts sound levels ranging from 47.2 dB to 51 dB at 556 Hz for the extreme values of convection speeds $0.29 U_\infty$ and $0.7 U_\infty$, higher convection speeds leading to higher sound predictions. At 635 Hz the predictions range from 60.3 dB to 64 dB and from 62 dB to 66 dB depending on either the input data are considered at RMP 4 or RMP 23, respectively. In most cases a slight over-prediction takes place. A reduction of the predicted level around -1.6 dB can be achieved by reducing the span length to 0.25 m instead of 0.3 m. This is a way of taking into account the



(a)



(b)

Figure 5.4: Analytical predictions of the tonal noise. NACA-0012 airfoil. (a)- 16 m/s; (b)- 25 m/s. Upper and lower symbols pointed by arrows correspond to extreme values of the convection speed (0.29 to $0.7 U_0$).

fact that the end-plate boundary layers reduce the effective spanwise extent the stability waves. This makes the comparison quite satisfactory.

Surprisingly the same test repeated at 25 m/s (see table 5.2) leads to larger overestimates as indicated by the plot in figure 5.4(b). Indeed for the frequencies 1200 Hz, 1333 Hz and 1432 Hz the measured tone levels are 50 dB, 55.6 dB and 54.41 dB whereas the predictions produced by both probes range from 55 dB to 59 dB, from 62 dB to 69 dB and from 63 dB to 68 dB, respectively. As can be seen at this flow velocity the over-prediction is systematic. It is not excluded (though not proved) that between the wall-pressure measurement point and the trailing edge, some reduction of the amplitude of the LBL waves operates in this case.

5.5 Concluding Remarks

A short review of the analytical models was done in the present chapter. Amiet's model was used for prediction of the far-field PSD. As an input data the surface pressure measurements were used. The most tricky step was the estimation of the convection speed. After analysis of all possible values it was decided to make the investigation in a range from $0.29 \times U_\infty$ to $0.7 \times U_\infty$ for the investigation. It was concluded that Amiet's trailing-edge noise model based on the assumption of perfectly correlated sources along the span for the reinforced tones is compatible with the experimental results.

Table 5.1: Tone levels as predicted with analytical modeling (AM) and measured in the far-field (FF). NACA-0012 airfoil at 16 m/s and zero angle of attack. Probe numbers, related source levels (PSD) and convection speed are indicated.

	frequency 556 Hz				frequency 635 Hz		
	PSD, dB	U_c/U_∞	AM, dB	FF, dB	PSD, dB	AM, dB	FF, dB
pr 4	94.4	0.29	47.2	49	107.2	60.3	61.5
		0.5	49.6			62.7	
		0.7	51			64.2	
pr 23		0.29			109.2	62.3	
		0.5				64.7	
		0.7				66.2	

Table 5.2: Tone levels as predicted with analytical modeling (AM) and measured in the far-field (FF). NACA-0012 airfoil at 25 m/s and zero angle of attack. Probe numbers, related source levels (PSD) and convection speed are indicated.

	frequency 1200 Hz				frequency 1333 Hz			frequency 1432 Hz		
	PSD, dB	U_c/U_∞	AM, dB	FF, dB	PSD, dB	AM, dB	FF, dB	PSD, dB	AM, dB	FF, dB
pr 4	99.6	0.29	55.4	49.9	109.5	65.1	56.7	109.1	64.45	54.4
		0.5	57.8			67.5			66.9	
		0.7	59.3			69			68.3	
pr 23		0.29			107	62.6		107.8	63.2	
		0.5				65			65.6	
		0.7				66.5			67.1	

Chapter 6

Experimental Results for the SD7003 Airfoil

This chapter presents the experimental results obtained with the SD7003 airfoil. Various angles of attack from -3° to 7° were investigated because of the sensitivity of the flow and its acoustic signature to this parameter. All results correspond to the geometrical angle of attack, because there is no simple formula to calculate the effective angle of attack. For this reason an additional numerical simulation was used to determine the effective angles of attack from the pressure-coefficient distributions (see section 7.2). Directivity measurements were missing for the cambered airfoil. However a one-dimensional source-localization technique has been performed. The investigation of the acoustic signature and the area of a tonal noise in terms of the angle of attack and Reynolds number has been defined. The necessity of the separation bubble for the phenomenon is confirmed. Different tonal noise regimes are also observed and described with the time-frequency analysis. The comparative analysis with the results of NACA-0012 airfoil is presented.

6.1 Localization of the Noise Sources

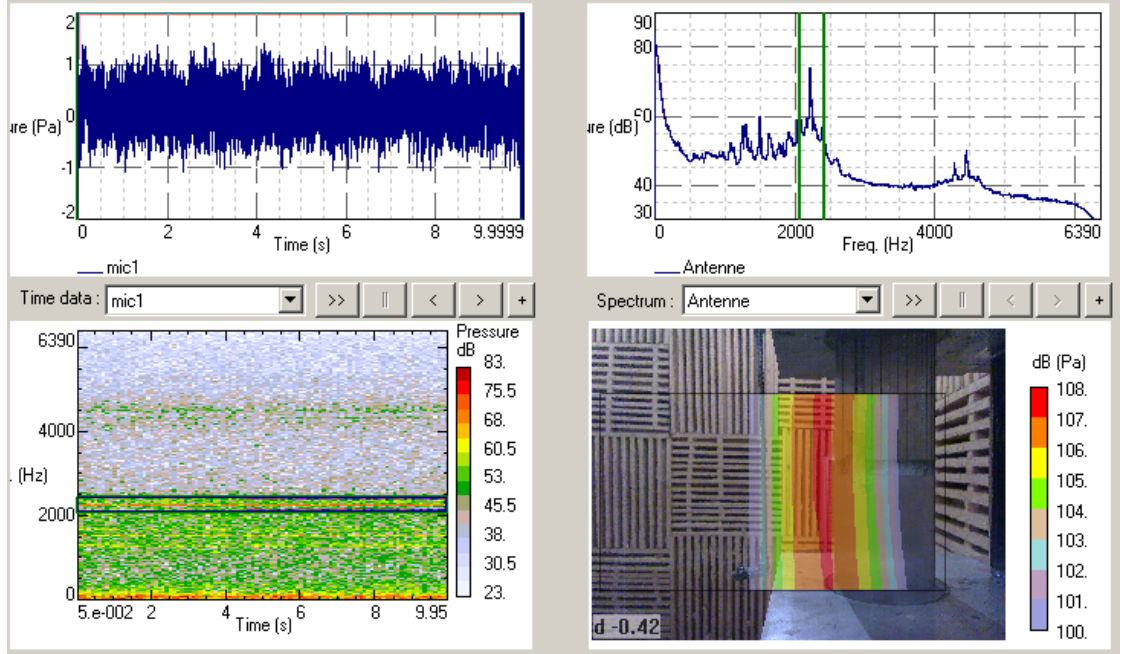


Figure 6.1: Localization of the noise source for the main tone. SD7003 airfoil at 30 m/s and 3° . 1D antenna. The source map results from repeated color line.

The localization of the noise sources was not initially included in the aim of the present work. However an indicative test has been performed as a complement, for curiosity. The measurements were done by an antenna with horizontally distributed microphones in a plane distant of 50 cm from the airfoil plane. The figures 6.1 and 6.2 show the registered signal (left top), and associated PSD (right top), a time frequency plot (left bottom) and a color map of the source localization (right bottom). In fact both figures 6.1 and 6.2 are presenting measurements for the same flow conditions but for the main tone and its harmonics respectively. The color maps confirm that the source of the main tone is located at the trailing edge as well as the source of the second harmonic tone. It must be noted that the 1D-antenna is not able to discriminate the vertical coordinate of the sources and artificially provides a band in the map. Furthermore, no correction for sound refraction through the jet shear layers is applied here. Therefore the apparent source location is shifted downstream by an amount $M_0 h$ where M_0 is the flow Mach number and h the thickness of the flow from the trailing edge to the shear layer. This

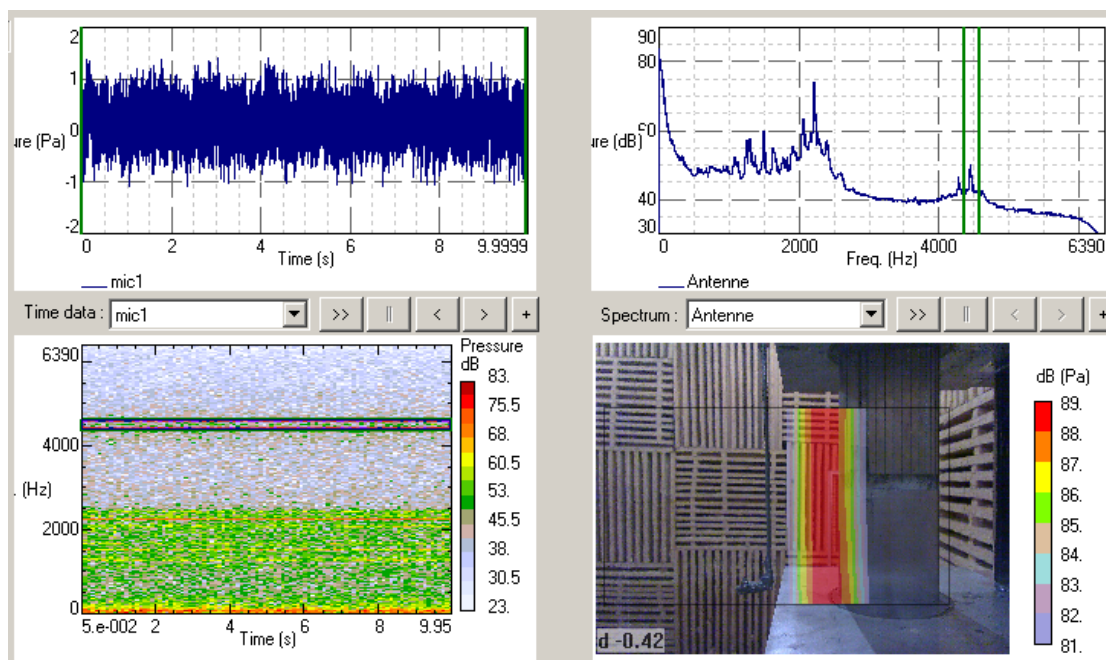


Figure 6.2: Localization of the noise source for the harmonic tone. SD7003 airfoil at 30 m/s and 3° . 1D antenna. The source map results from repeated color line.

shift is about 4 mm in the present case, which explains why the traces are found slightly downstream of the trailing edge in the pictures of the figures 6.1 and 6.2 - bottom right. In both pictures the airfoil and its upper and lower end-plates are visible. The flow is going from right to left.

6.2 Ranges of Parameters of the Tonal Noise

Figure 6.3 presents the tonal noise area for the SD7003 airfoil depending on the Reynolds numbers and angles of attack. Unlike the case of the NACA-0012 airfoil the present one has a horse shoe shape. The SD7003 airfoil has a much more limited range of angles of attack (note that in figure 6.3 geometrical angles of attack are considered). There is also an extinction of the tonal noise around the zero angle of attack (empty circles on the plot) at low flow velocities around 10 m/s for the cambered airfoil, whereas for the NACA-0012 airfoil this was observed at 30 m/s. Furthermore, tests with the tripping device show that the suction side of the airfoil is always responsible for the tones.

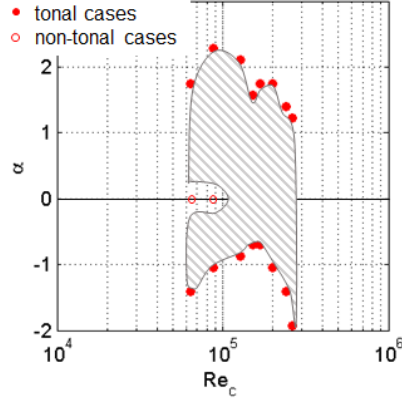


Figure 6.3: Reynolds-number versus geometrical angle of attack chart for the SD7003 airfoil.

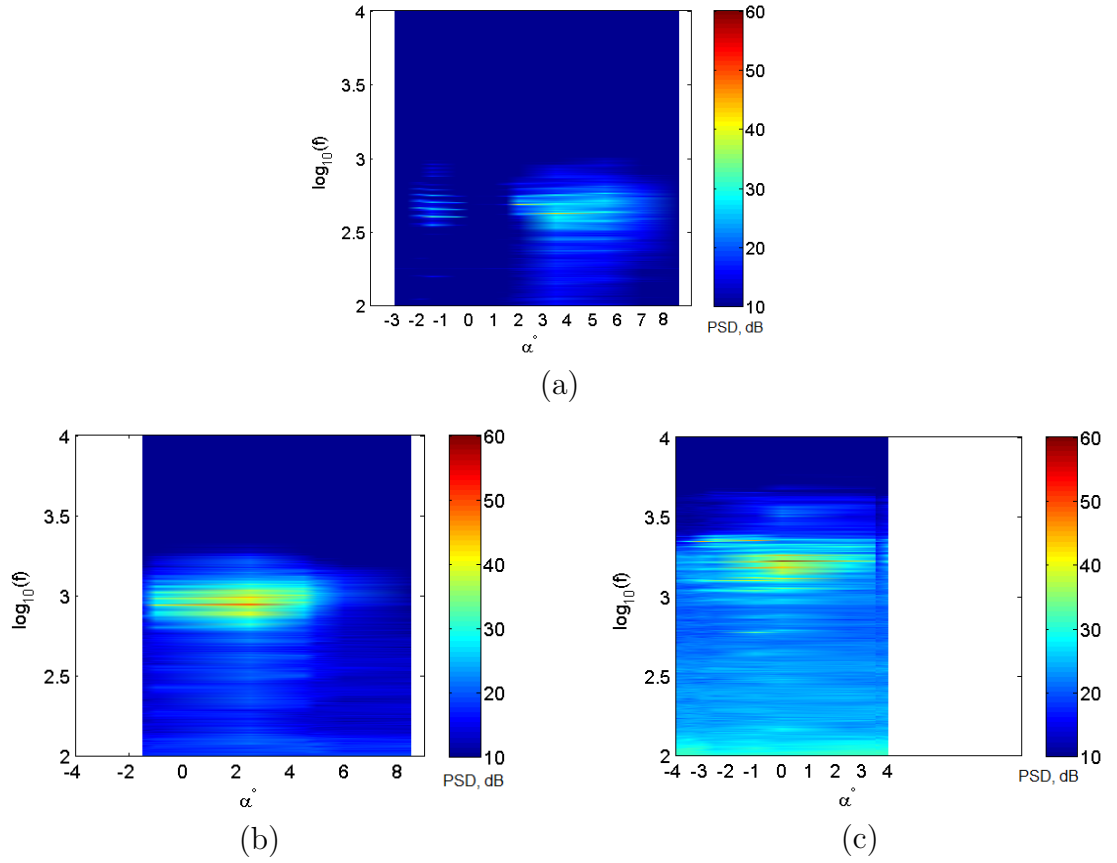


Figure 6.4: Frequency versus angle of attack chart for the SD7003 airfoil. (a): at 11 m/s ($Re_c = 0.87 \times 10^5$); (b): at 19 m/s ($Re_c = 1.5 \times 10^5$) and (c): at 30 m/s ($Re_c = 2.4 \times 10^5$).

It was observed that the cambered airfoil is much more sensitive to a change of angle of attack, leading to several regimes at same the flow velocity. Therefore it was decided to produce the frequency versus geometrical angle of attack plots in figure 6.4 to identify the areas of tonal noise more clearly. Because of the uncertainty of the determination of the angle of attack, the presented data are a qualitative representation of the noise behavior. At 11 m/s the noise signature is divided into two parts with extinction of the tonal noise around 0° . The highest tonal noise is found at 19 m/s with one stable tone from 0° to 4° . With increasing flow velocity up to 30 m/s the tonal noise area concentrates around 0° .

6.3 Pressure Coefficient

Most numerical simulations reported in the literature address the aerodynamic of the airfoil in infinite stream whereas the measurements are performed in a narrow wind-tunnel flows. In absence of empirical correlation formula, the distribution of the pressure coefficient is the only way of determining an effective angle of attack.

Figure 6.5(a) reports measurements of the pressure coefficient for the SD7003 airfoil at various geometrical angles of attack and at $Re_c = 12 \times 10^4$. The last 20% of chord are not accessible for the capillary technology because of the small thickness of the airfoil. At 7° on the suction side a small drop which is sometimes associated with a separation bubble can be observed.

The SD7003 airfoil was also simulated numerically in reference [10]. The numerical simulation was conducted for $Re_c = 6 \times 10^4$ and the experiment has been repeated for the same Reynolds number and twice that value, 12×10^4 . The measured C_p distribution at 7° is selected for the comparison in figure 6.5(b) as the most comparable to the simulated configuration at 2° . A complete fit cannot be found whatever the adjustment of the angle of attack might be. This is attributed to an effect of the limited flow width in the wind-tunnel testing (see Moreau *et al* [51] for the discussion). But as long as the pressure gradient is the same the development of the boundary layers is expected to be the same, except for additional Reynolds-number effects. Typically in the present case the experiment at the highest Re_c starts capturing a pressure drop around 65% of chord whereas the last measuring point for the smallest Re_c does not exhibit that drop, in accordance with the simulation.

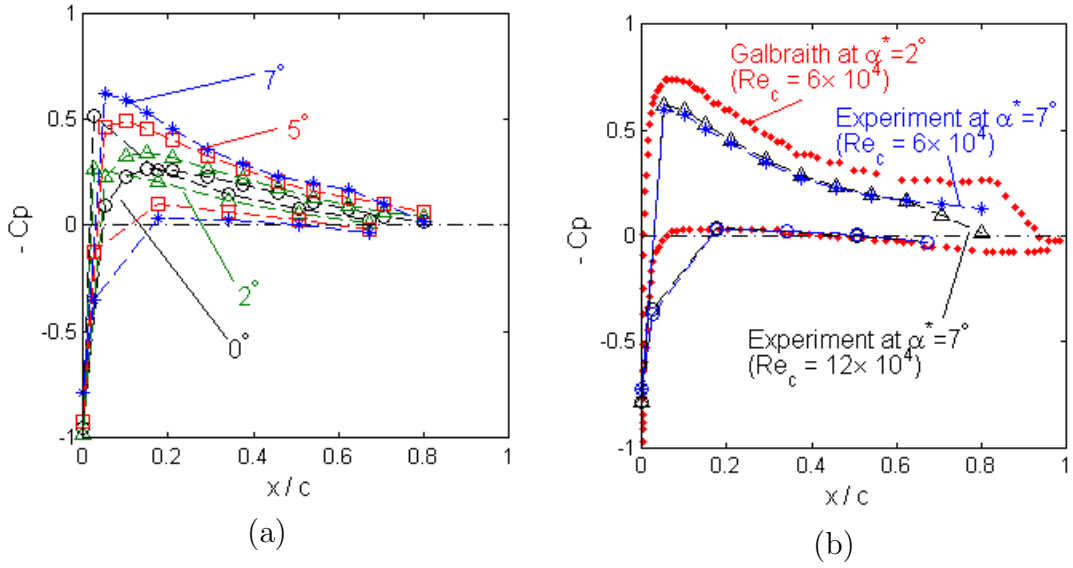


Figure 6.5: Pressure-coefficient distributions. (a) - measured with the SD7003 airfoil of 12 cm chord length at different angles of attack. $Re_c = 12 \times 10^4$. (b) - experiment versus numerical simulation [10].

6.4 Far-Field Noise Signature

6.4.1 Influence of the Angle of Attack

The acoustic characterizations were done at following angles of attack: 7° ; 5° ; 2° ; 0° ; -2° and -3° . All of them show differences in tonal noise signature, but the ladder-type structure can be distinguished in every case. The experimental results are in a good agreement with power laws proposed by Paterson: $f_{max} \sim U_\infty^{1.5}$ and $f \sim U_\infty^{0.8}$.

At $\alpha = 5^\circ$ (figure 6.6(a)) the noise signature is weak with a low level of the tonal hump. Tones are hardly distinguished from the general level of the hump (see also appendix C figure C.1(a)). The color maps (see figure 3.9) at 2° and 0° are similar to each other. Both of them exhibit 2 tones with similar PSD level at equal distance from the central frequency of the hump. At zero angle of attack harmonic traces are observed at low frequencies and high flow velocities. At -2° multiple tones distributed all over the hump are observed. With increasing flow velocity the intensity of the tones increases.

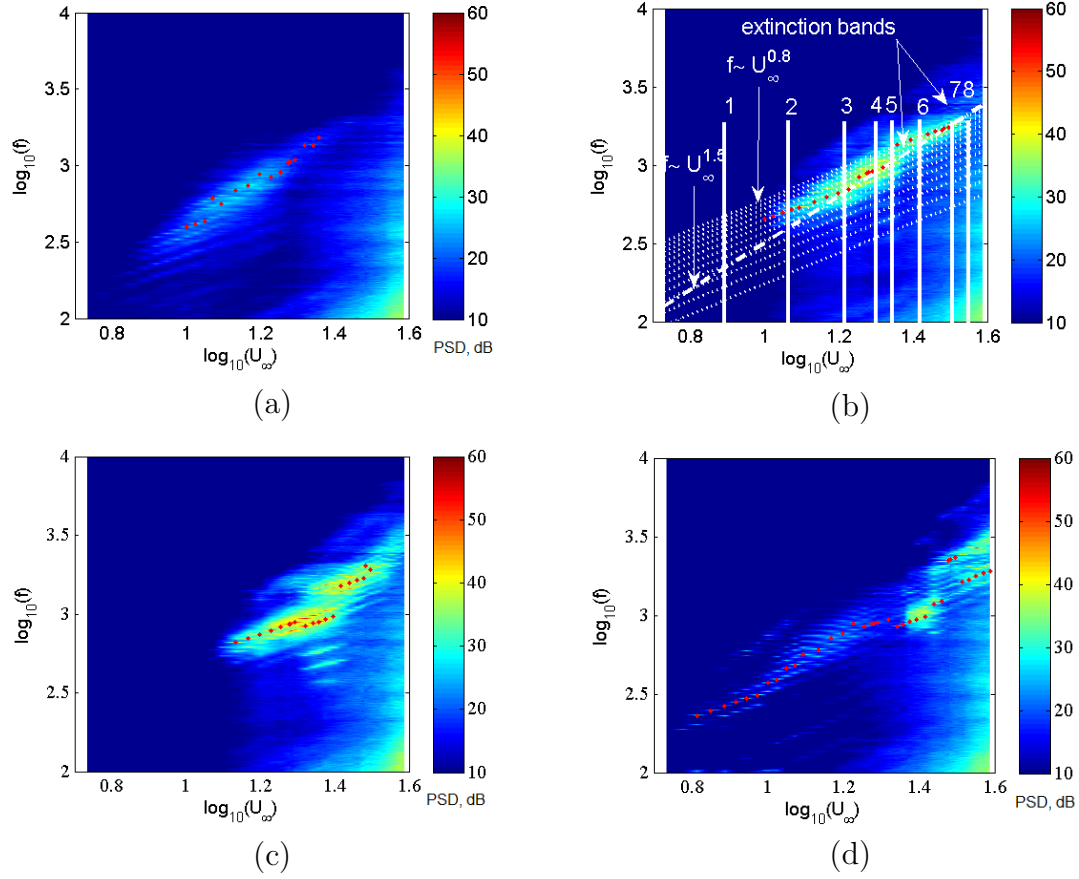


Figure 6.6: Frequency-flow speed charts of TS-wave radiation for the SD7003 airfoil. Configuration A. (a) - at $\alpha = 5^\circ$; (b) - at $\alpha = 2^\circ$; (c) - at $\alpha = 0^\circ$; (d) - at $\alpha = -2^\circ$. 8 speeds are marked: 1 - 8 m/s ($Re_c = 0.63 \times 10^5$); 2 - 11 m/s ($Re_c = 0.87 \times 10^5$); 3 - 16 m/s ($Re_c = 1.26 \times 10^5$); 4 - 19 m/s ($Re_c = 1.5 \times 10^5$); 5 - 21 m/s ($Re_c = 1.6 \times 10^5$); 6 - 25 m/s ($Re_c = 2 \times 10^5$); 7 - 30 m/s ($Re_c = 2.4 \times 10^5$); 8 - 33 m/s ($Re_c = 2.6 \times 10^5$). Dominant tone levels marked by red dots.

It was assumed and further confirmed by numerical simulation (see section 7.2) that the geometrical angle of attack 2° is equivalent to the effective angle 0° . Therefore the acoustic signature of the SD7003 airfoil at 2° can be compared to the NACA-0012 airfoil at 0° (figure 3.9(a)). The noise signature of the former is shorter than of the latter. The tonal noise begins at higher flow velocities. The SD7003 airfoil does not produce harmonic traces. However the horizontal extinction bands are observed at $10\log_{10} = 3.1$ and 3.3 for all angles of attack. At geometrical angles of attack higher than 2° the tonal noise is much weaker in comparison with the NACA-0012 airfoil at geometrical angle 5° (effective angle 1.75°).

In general it can be noted that the cambered airfoil has a narrower tonal noise area and is much more sensitive to the angle of attack than the NACA-0012 airfoil.

6.4.2 Influence of Tripping

Color maps for configurations with tripping device at $\alpha = 2^\circ$ (see figure 6.7) confirm that for the SD7003 airfoil the suction side produces tonal noise. When the pressure side is tripped and the suction side works alone (configuration B) the noise signature is very similar to the one of the clean airfoil (configuration A presented in figure 6.6(b)). The level of the noise is lower. The pressure side plays a role only at very high flow velocities.

Figure 6.8 demonstrates more clearly the role of each side in the noise generation. It presents the sound pressure level of the main tones versus flow velocity for the SD7003 airfoil. The configurations A, B and C are compared. At low flow velocities the signature of the clean airfoil (A) corresponds to the case when only the suction side is responsible for tones (B). At velocities higher than 25 m/s the tonal noise generated by the pressure side coincides with clean airfoil. The tonal noise threshold is close to 60 dB.

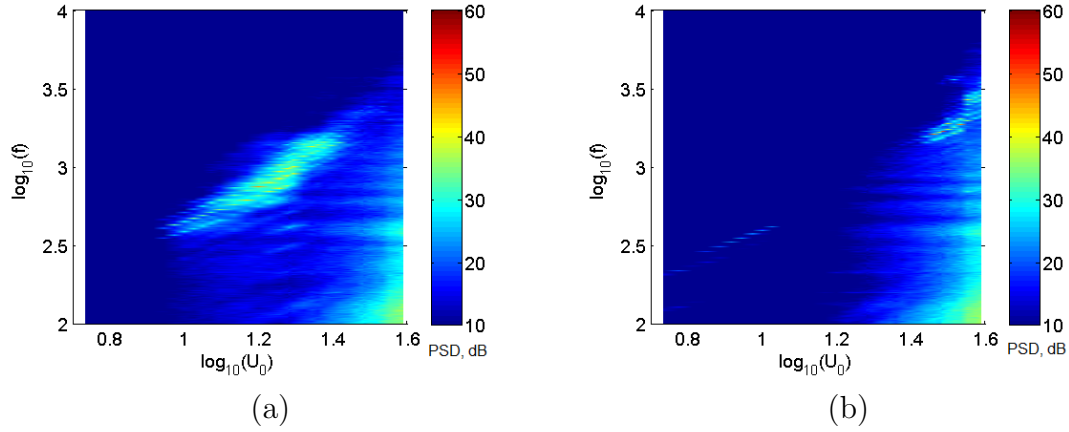


Figure 6.7: Frequency-flow speed charts of TS-wave radiation for the SD7003 airfoil at $\alpha = 2^\circ$. (a) - configuration B, tripping on the pressure side; (b) - configuration C, tripping on the suction side.

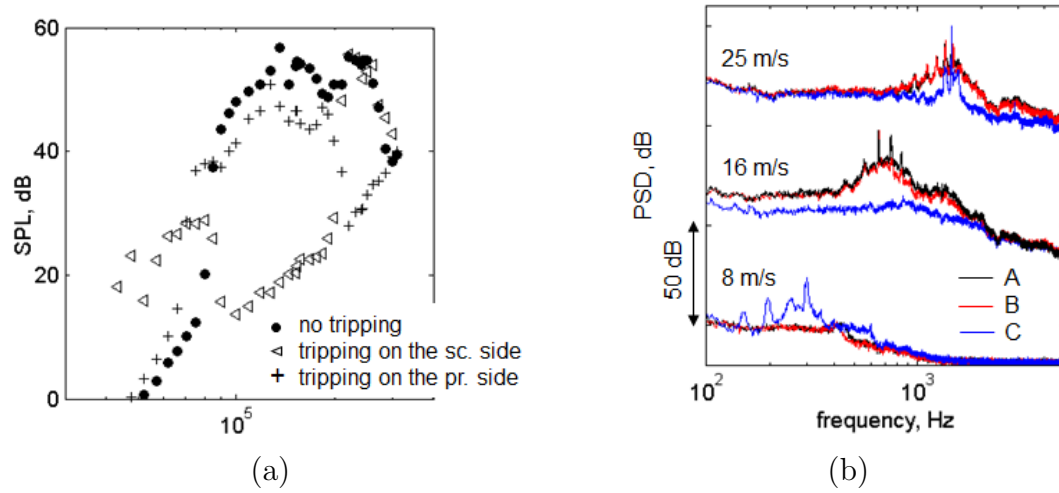


Figure 6.8: Far-field microphone measurements with tripping device. (a): sound pressure level of the main tones versus flow velocity. (b): PSD at several flow velocities (with vertical shifts by 50 dB). Configurations A, B and C. SD7003 airfoil at $\alpha = 2^\circ$.

6.5 Location of the Separation Bubble for the SD7003 Airfoil

The study of the separation bubble for the cambered SD7003 airfoil was conducted at four geometrical angles of attack ($\alpha = 0^\circ, 2^\circ, 5^\circ, -2^\circ$).

In general the behavior of the separation bubble as observed with flow visualization can be described as follows. On the suction side which produces the tones the separation bubble moves downstream closer to the trailing edge with increasing flow velocity. This was also noted by Olson *et al.*[66], for example. On the contrary an increase of the angle of attack makes the separation area move upstream. For all described cases an attached flow was observed on the pressure side. In some cases the boundaries of the separation bubble were not constant in the spanwise direction, which can be associated with an inhomogeneous flow.

In the configuration $\alpha = 2^\circ$ and $U_\infty = 19 \text{ m/s}$ which produces tonal noise (see figure 6.9(a)) the separation area starts from 54% of chord and has no reattachment on the suction side. According to the HWA the separation area for this case is wider and starts from 46%. The flow visualization of the pressure side shows an attached flow, whereas the hot-wire anemometry (figure 6.10) suggested a separation bubble. The numerical simulation results (section 7.2) will be shown to agree with the first case. It can be assumed that hot-wire probe forced the boundary layer to separate in this case. However, this is not proved.

Figure 6.11 clearly shows streamwise vortical structure for the case at $\alpha = 2^\circ$ and 25 m/s. The effect of the supporting plates on the flow is also highlighted.

For a more complete investigation two cases without tones were tested. The SD7003 airfoil at $\alpha = 5^\circ$ and 19 m/s exhibits a separation area on the suction side which extends from 42% to 62%, as seen in figure 6.12, and an attached flow on the pressure side. The HWA indicates the separation on the suction side (33% - 80%) as well as on the pressure side (33% to 98%). At the moment there is no explanation for the differences. But even if the separation on the pressure side takes place there is no big difference because the suction side is responsible for the tones. The results for the pressure side can be found in appendix C, figure C.2.

One of the results of the hot-wire measurements in the near-wake is shown in figure 6.13. The minimum of the velocity is slightly shifted vertically because

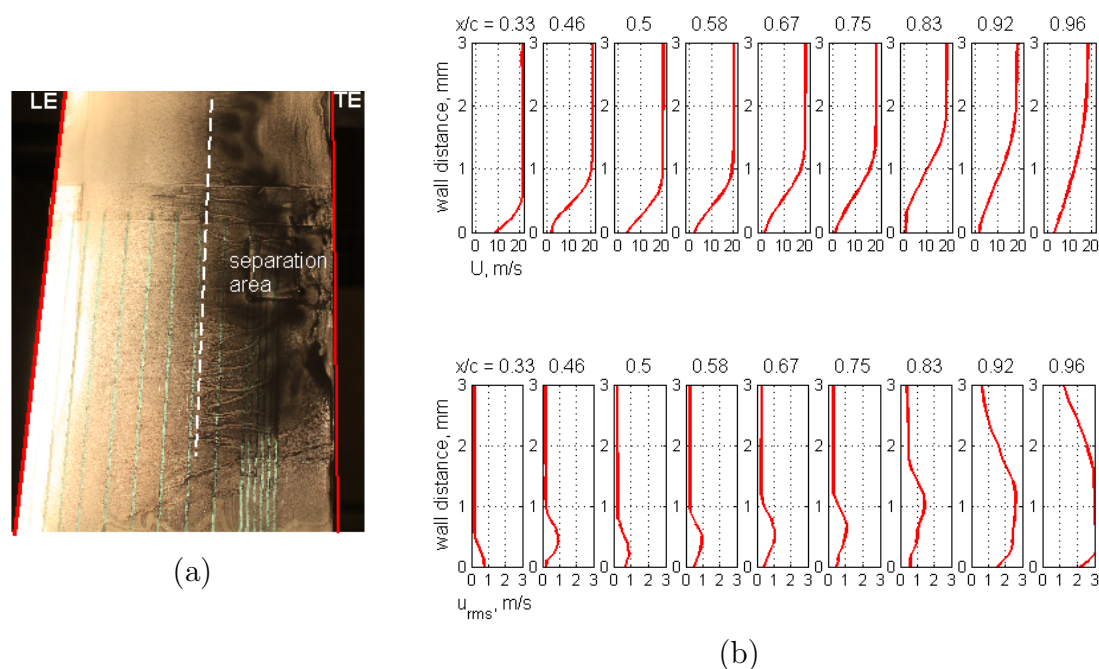


Figure 6.9: Flow visualization (a) and HWA results (b) for the suction side of the SD7003 airfoil at $\alpha = 2^\circ$ and 19 m/s. Tonal noise is observed. LE - leading edge, TE - trailing edge.

of the camber and the angle of attack. The maximal level of the u_{rms} is on the suction side.

All observations are summarized in table 6.1. It was assumed that the flow on the pressure side remained attached in view of the flow visualization and the numerical simulation. As can be seen from the table all configurations which produce tonal noise have a separation bubble with or without reattachment close to the trailing edge. In contrast in the case at $\alpha = 5^\circ$ without tones the separation bubble reattaches 30% before the trailing edge, which is obviously too far away to get favorable conditions.

The general results for the cambered airfoil allow to make the same conclusions as for the NACA-0012 airfoil. They prove that a separation bubble located on any side close enough to the trailing edge, is one of the necessary conditions for the tonal noise generation.

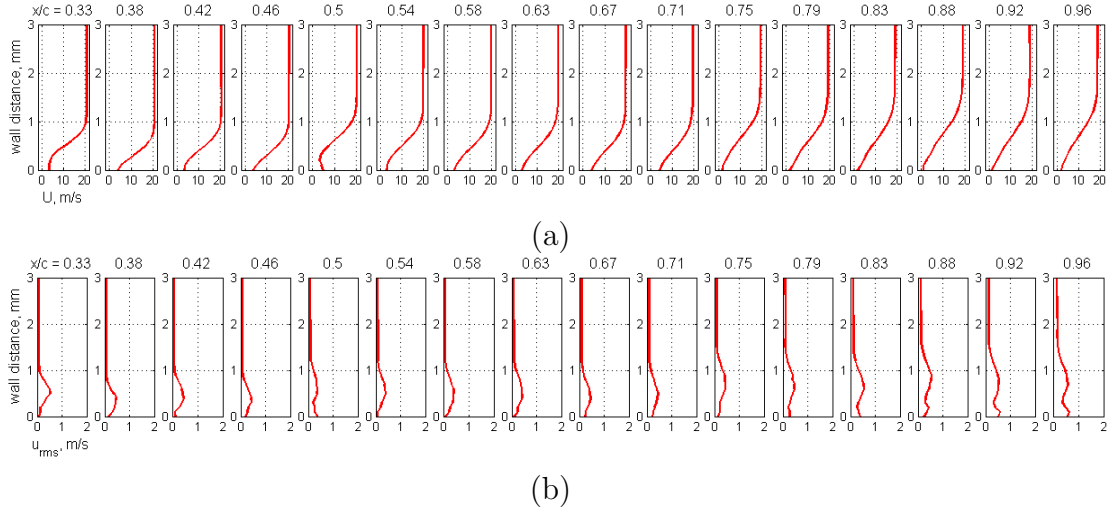


Figure 6.10: HWA results on the pressure side of the SD7003 airfoil at $\alpha = 2^\circ$ and $U_\infty = 19 \text{ m/s}$.

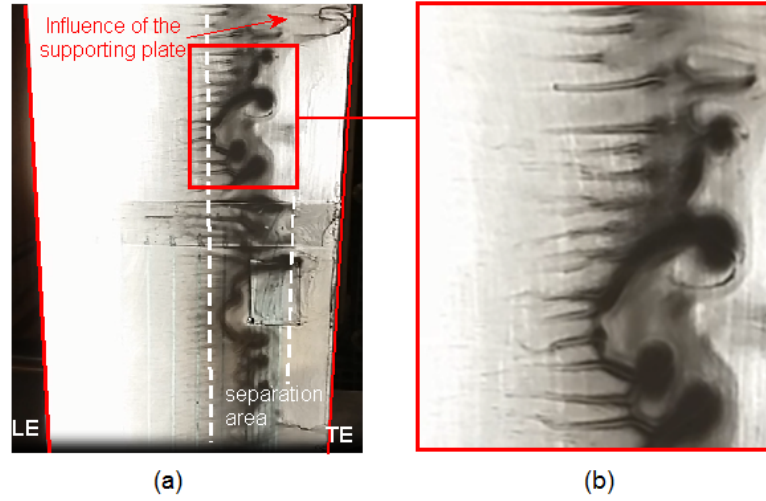


Figure 6.11: Flow visualization (a) results and traces of vortices (b) for the suction side of the SD7003 airfoil at $\alpha = 2^\circ$ and 25 m/s . Tonal noise is observed.

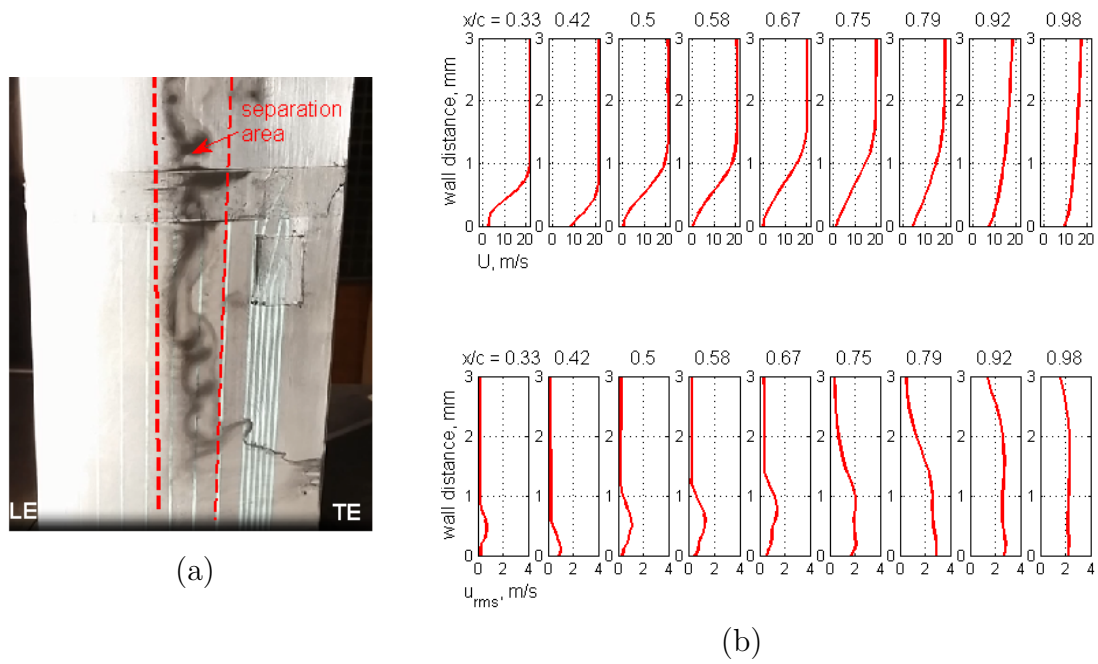


Figure 6.12: Flow visualization (a) and HWA results (b) for the suction side of the SD7003 airfoil at $\alpha = 5^\circ$ and 19 m/s. Tonal noise is not observed.

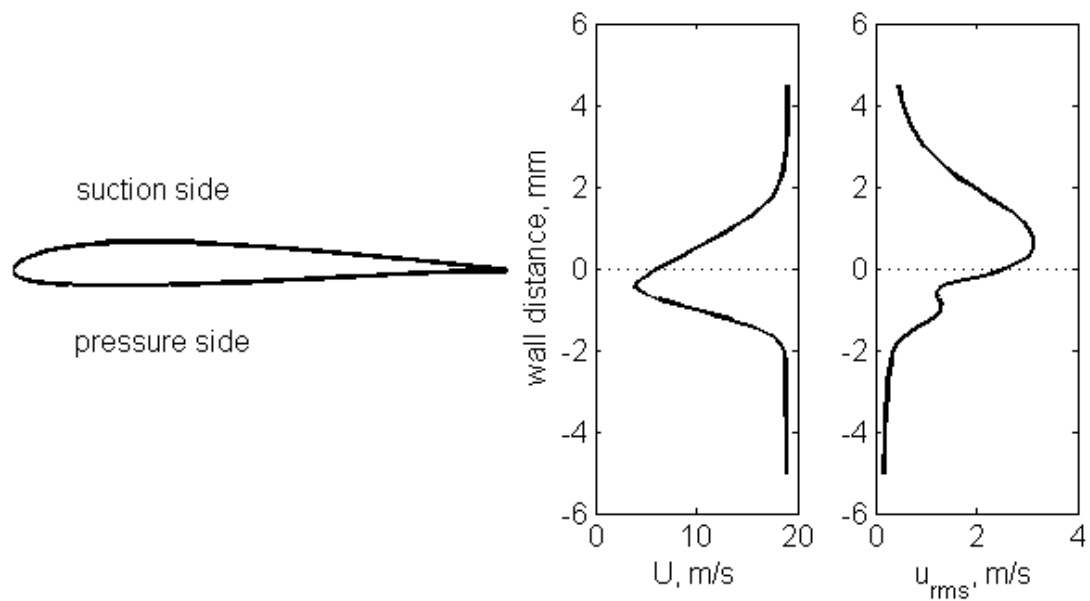
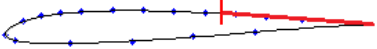
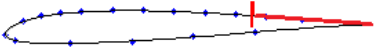
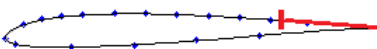
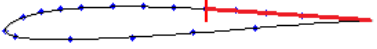
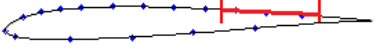
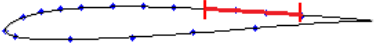
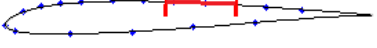

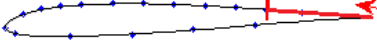
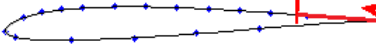
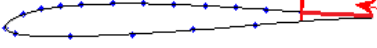


Figure 6.13: Results of near-wake measurements along the pressure side at the distance of 1.5 mm for the SD7003 airfoil at 19 m/s and $\alpha = 2^\circ$.

Table 6.1: Separation areas. Illustrative table for the SD7003 airfoil.

$\alpha \backslash U_\infty$	19 m/s		25 m/s	33 m/s
	Flow visualization	HWA		
0°	sc.s, 58%  pr.s, attached flow		sc.s, 67%  pr.s, attached flow	sc.s, 72%  pr.s, attached flow
2°	sc.s, 54%  pr.s, attached flow	46%-92% 33%-96%	sc.s, 60%-90%  pr.s, attached flow	sc.s, 54%-80%  pr.s, attached flow
5°	sc.s, 42% - 62%  pr.s, attached flow NO TONES	33%-75% 33%-98%	sc.s, 46% - 62%  pr.s, attached flow NO TONES	
-2°	sc.s, 71%  pr.s, attached flow		sc.s, 77%  pr.s, attached flow	sc.s, 80%  pr.s, attached flow

6.5.1 Influence of the Separation Bubble on the PSD of the RMPs

Figure 6.14 supports the conclusion of the section 3.5.3 that the separation bubble has no dramatic influence on the measurements of the RMPs. The differences of the spectra of probes 7, 8 and 9 which are close to each other are negligible. The higher level of the spectrum of probe 13 is explained by the closer location to the trailing edge, associated with a higher amplification of the instabilities. The level of the coherence decreases when moving downstream and suggests that the measured information becomes more aerodynamic than acoustic (though the hydrodynamic motion is probably significantly coherent). The hump of the coherence at low frequencies from 100 Hz to 450 Hz for the first two pairs of probes is associated with the effect of wind-tunnel jet shear layers.

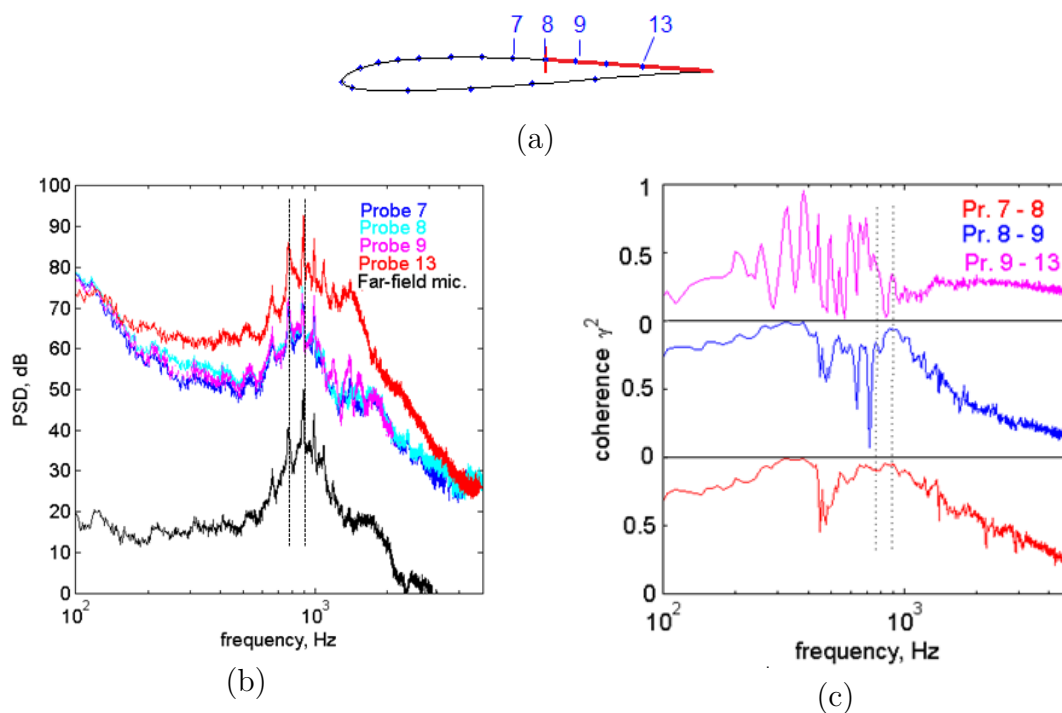


Figure 6.14: SD7003 airfoil at 19 m/s and 2°: (a) - location of the separation bubble; (b) - PSD plots for wall pressure probes and far-field microphone; (c) - coherence plots for wall pressure probes. Vertical dotted lines mark the dominant tones.

6.6 Comparison of Hot-Wire Velocity Spectra with Far-Field Acoustic Spectrum

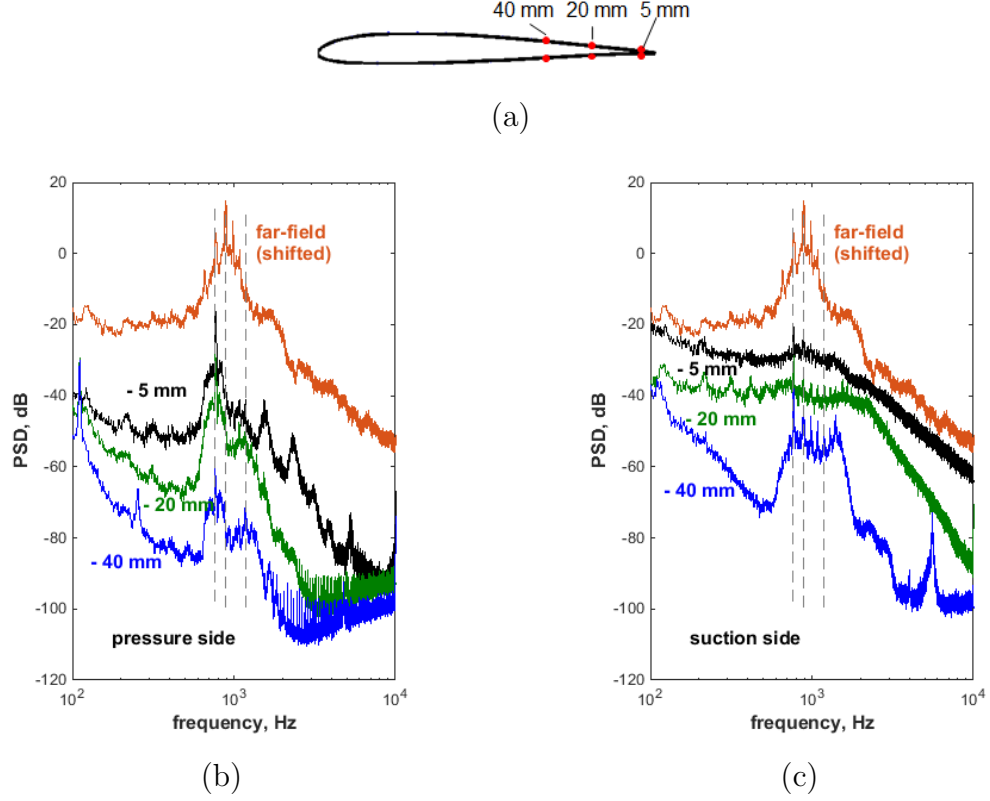


Figure 6.15: Hot-wire velocity spectra (dB, ref.1 m/s) for the SD7003 airfoil at the angle of attack of 2° and 19 m/s. (a) - locations of the HWA probe during the measurements; (b) - pressure side; (c) - suction side. Far-field acoustic spectrum shown for comparison (rel.dB).

Examples of velocity spectra deduced from hot-wire measurements are plotted in figure 6.15 for the SD7003 airfoil at 2° angle of attack and a flow speed of 19 m/s. Three locations along the chord at 40 mm, 20 mm and 5 mm from the trailing edge are selected, both on the suction side and on the pressure side. The far-field pressure spectrum is reported in figure in a relative dB scale for the sake of comparison. The results must be analyzed in view of the velocity profiles in figure 6.15, bearing in mind that the probe captures only the fluctuating motions

in the direction of the mean flow, therefore ignoring the fluctuations normal to the wall. Furthermore the acoustic velocity can be measured by the hot wire especially close to its source because of the high sound level. Except for the dominant tone measured close to the trailing edge for which the level is similar on both sides, the overall level of oscillation is much higher on the suction side. Moreover the frequencies of the tones heard in the far field are clearly identified in the hot-wire spectra for the suction side. This confirms that the suction-side boundary layer is responsible for the sound radiation, as already concluded from the wall-pressure measurements. The measured spectra on the pressure side are more probably of acoustic nature.

6.7 Cross-Spectrum Analysis

6.7.1 Chordwise Analysis

The chordwise cross-spectrum analysis was conducted for 10 pairs of RMPs along the chord line on the suction side of the SD7003 airfoil at $\alpha = 2^\circ$ and $U_\infty = 25 \text{ m/s}$ (figure 6.16). The general behavior of the plots is very similar to what was observed with the NACA-0012 airfoil in section 3.6.1.

All PSD plots present two tones at 674 Hz and 725 Hz. For the probes №1 and №2 there is a difference of 10 dB between PSD levels. The coherence plot has maxima at tonal frequencies, whereas the general coherence level is low. There is no hump at low frequencies possibly associated with the effect of the wind-tunnel shear layers, as observed for the NACA-0012 airfoil. The phase signals from the probes exhibit a large scatter. The next three pairs of probes №2, №3, №4 and №5 are very similar. The spectra coincide with each other. The coherence levels are quite high and the hump around the tonal frequencies can be observed. At the dominant tonal frequency the coherence is systematically 1. That can be associated with the probable acoustic nature of signal. The phase plots are stable and close to zero.

Another quaternion of probes №5, №6, №7 and №8 have no big changes in PSD plots, but a drop of coherence level can be observed in the range from 350 Hz to 550 Hz. This creates a hump at low frequencies up to 500 Hz, which is in the range of the possible effect of wind-tunnel shear layers. The hump can be observed

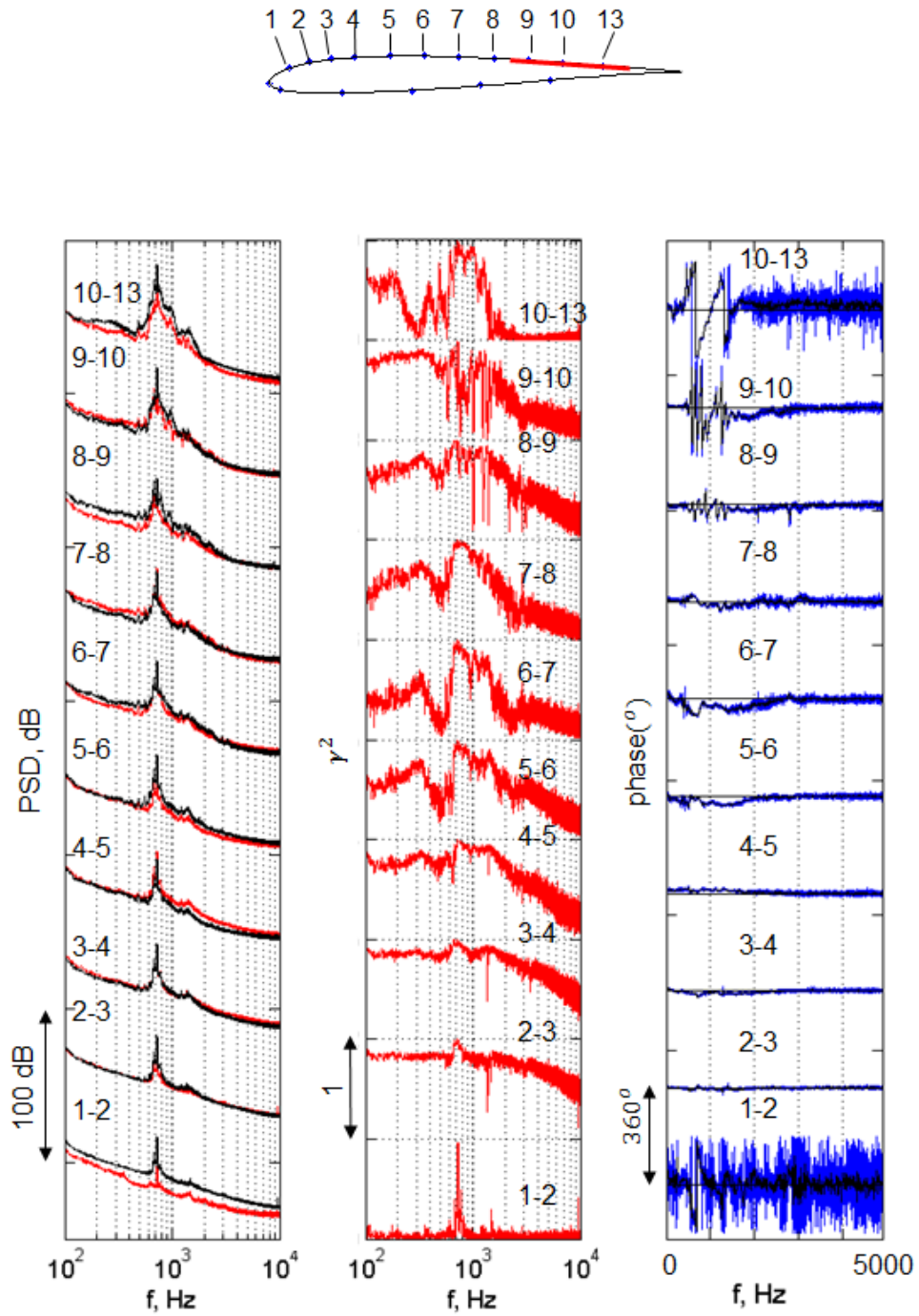


Figure 6.16: Chordwise dynamic of PSD, coherence and phase of cross-spectrum of RMPs pairs on the suction side for the SD7003 airfoil at $\alpha = 2^\circ$ and $U_\infty = 25 \text{ m/s}$.

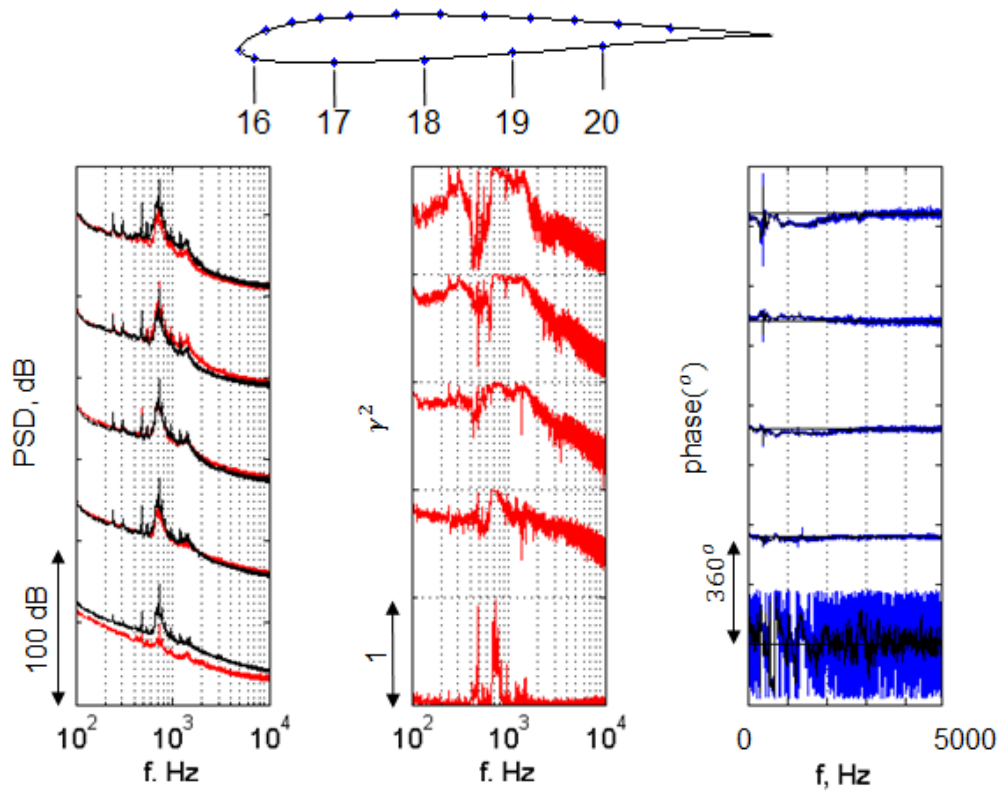


Figure 6.17: Chordwise dynamic of PSD, coherence and phase of cross-spectrum of RMPs pairs on the pressure side for the SD7003 airfoil at $\alpha = 2^\circ$ and $U_\infty = 25 \text{ m/s}$.

for other pairs of probes moving to the trailing edge. The phase plot is also quite stable, but some slopes can be observed at frequencies below 2000 Hz. The next triplet of probes №8, №9 and №10 does not have significant differences of PSD and coherence plots comparing to the previous probes, except the fact that there are more drops at frequencies from 1 kHz. But the phase plots now have a saw-tooth shape at frequencies up to 1500 Hz associated with a clear convective motion. At higher frequencies the phase oscillates around zero.

The last pair of probes №10 and №13 exhibits bigger differences in PSD levels. The general coherence level is lower and tonal frequencies can be distinguished more easily. The shape of the main hump can be clearly observed. There is still a hump at low frequencies up to 300 Hz. At high frequencies from 1.1 kHz the coherence is close to zero. The phase plot has a saw-tooth shape up to 1500 Hz like the previous pair, but at higher frequencies oscillations are much bigger. The calculated convection speed is around 4 m/s for probes №9 and №10 and 7 m/s for №10 and №13.

The analysis of the signals for the same configuration but on the pressure side (see figure 6.17) produces very similar results. The saw-tooth shape is not observed anymore close to the trailing edge because the motion there is more probably of dominant acoustic nature.

6.8 Time-Frequency Analysis

A similar time-frequency analysis as already discussed for the NACA-0012 airfoil has been performed for the SD7003 airfoil at zero angle of attack. The results are reported in figure 6.18. The switching regime is more illustrative in this case, so that two signals can be easily reconstructed by separating time intervals when one tone or the other one dominates. This produces two ‘filtered’ spectra plotted in red and blue in the right plot of figure 6.18(a) and shifted by steps of 20 dB with respect to the averaged spectrum for clarity. Not only the dominant tone but also the broader hump are not positioned at the same frequencies. Further research is needed to elucidate how this can be related to time changes of the length of the feedback loop or of the separation areas. A regime of two simultaneous tones with a harmonic hump was registered at 19 m/s (see figure 6.18(b)). At higher flow velocities multiple tones are observed (see figure 6.18(c)). Finally both airfoils seem to have similar steps of transition from one regime to another depending on flow velocity.

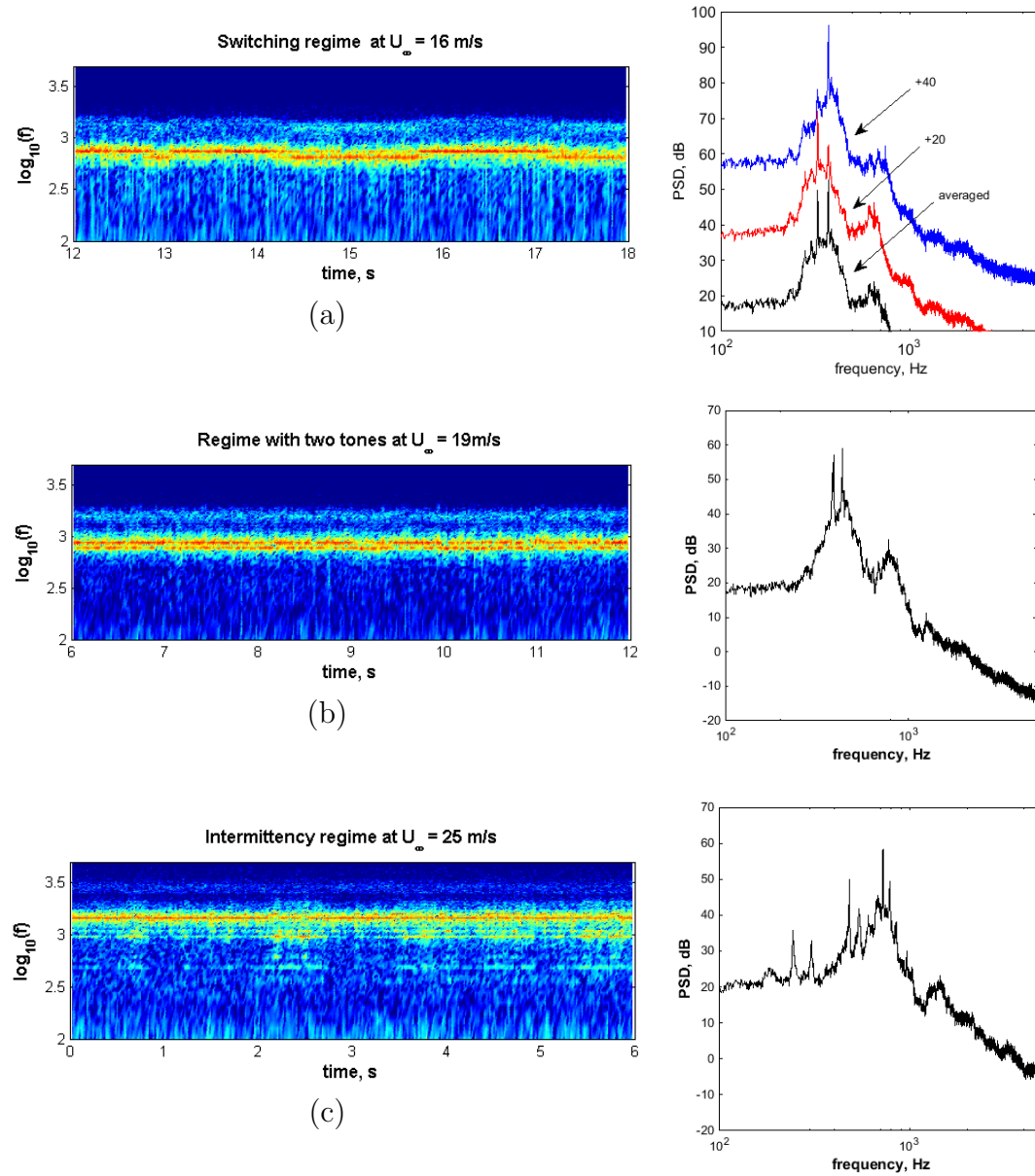


Figure 6.18: Time-frequency analysis for the SD7003 airfoil at 0° angle of attack. No tripping. Right plots: averaged spectra (black); filtered spectra (blue and red) for the switching regime, shifted by steps of 20 dB for clarity.

6.9 Bicoherence of the Far-Field Microphone Signal

For switching regime the bicoherence analysis was done for filtered time signal for each frequency of the main tone. The maximal level of the bicoherence $b(f_1, f_1)$ up to 0.88 exhibits at $f_1 = 326$ Hz (figure 6.19). The bicoherence $b(f_2, f_2)$ equals 0.55 for the second switching tone at $f_2 = 372$ Hz (figure 6.20).

The bicoherence equals 0.65 and 0.5 at $f_1 = 388$ Hz and $f_2 = 434$ Hz correspondingly with increasing of the flow velocity (the regime of two simultaneous tones). The harmonic hump is also observed for this case and the highest tone there is at $f_1^* = 2 \times 388 = 776$ Hz which generated partly by the non-linear interaction of the dominant tone.

At the flow velocity of 25 m/s one principal tone at $f_2 = 723$ Hz accompanied by multiple tones with lower level is presented by the PSD plot in the figure 6.22. Surprisingly that the maximum bicoherence level $b(f_1, f_2)$ around 0.57 is observed at combination of $f_1 = 243$ Hz and f_2 , whereas $b_{f_2, f_2} = 0.55$.

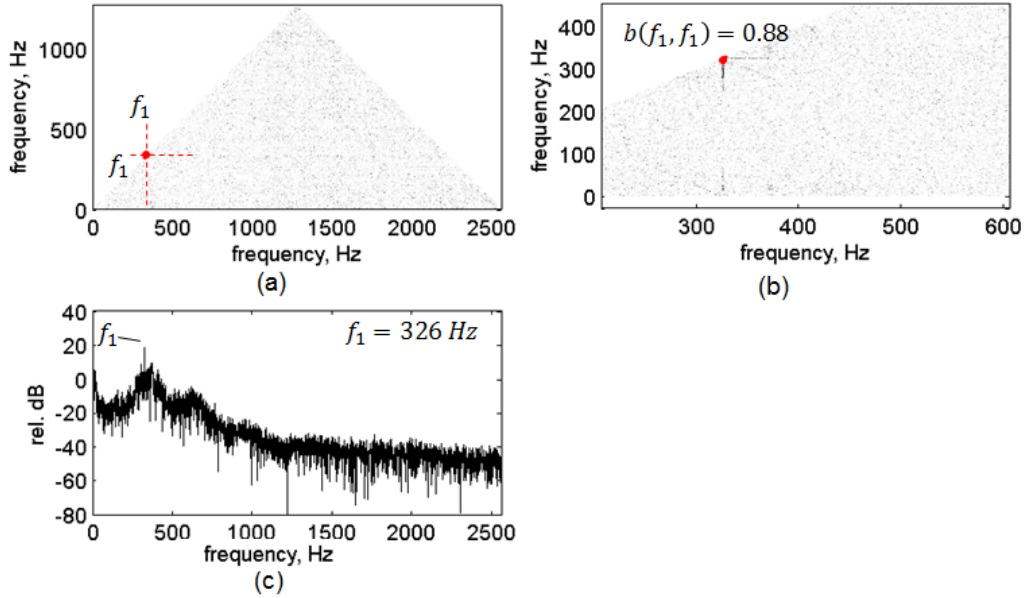


Figure 6.19: Bicoherence of the far-field microphone (a) and zoomed part of the plot (b); (c) - PSD plot without correction. SD7003 airfoil at 16 m/s and zero angle of attack. Filtered frequency equals 326 Hz.

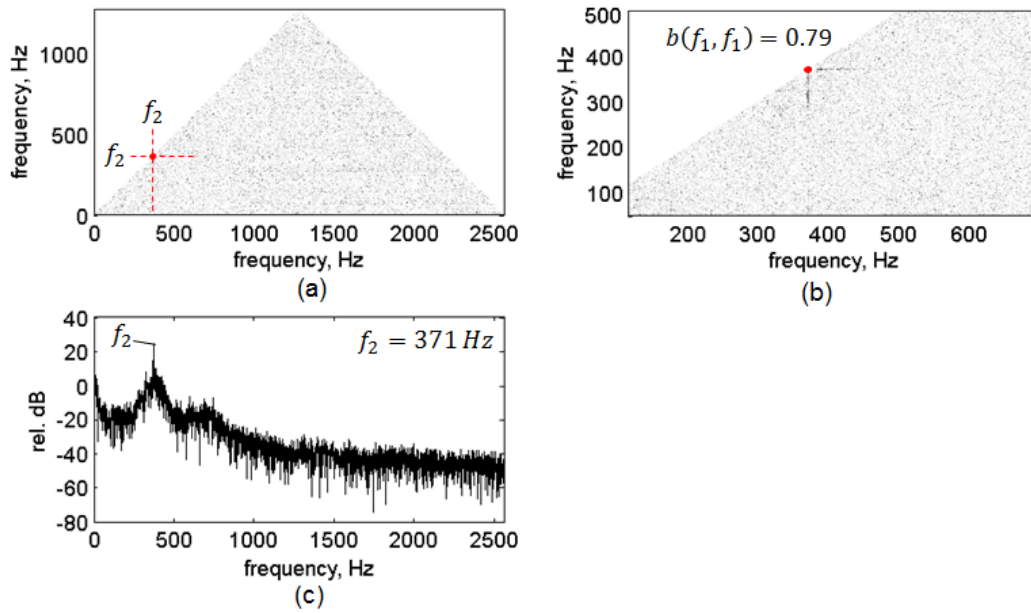


Figure 6.20: Bicoherence of the far-field microphone (a) and zoomed part of the plot (b); (c) - PSD plot without correction. SD7003 airfoil at 16 m/s and zero angle of attack. Filtered frequency equals 371 Hz.

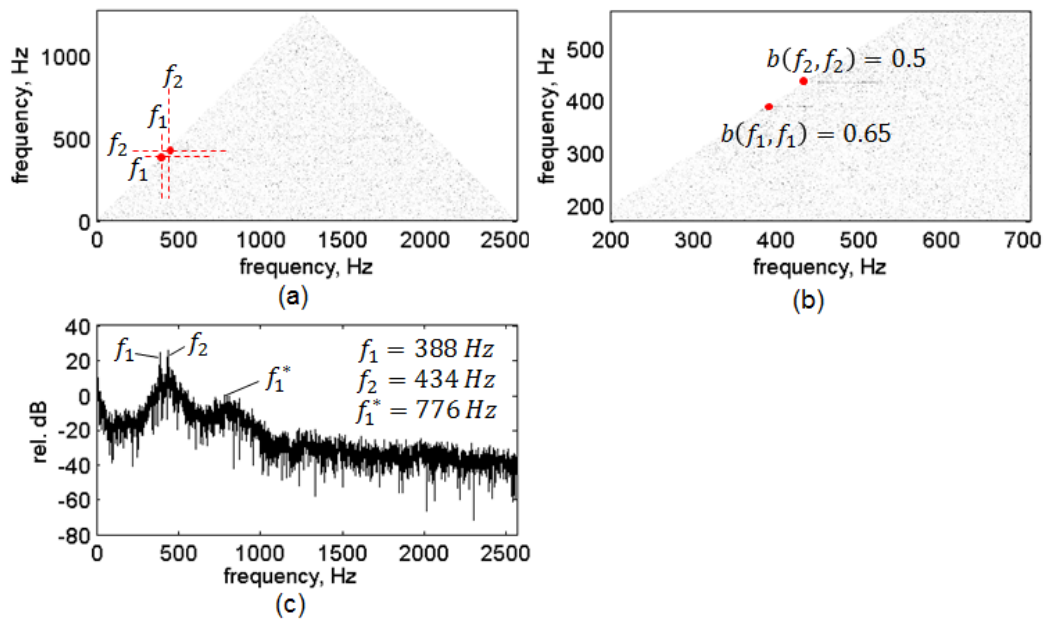


Figure 6.21: Bicoherence of the far-field microphone (a) and zoomed part of the plot (b); (c) - PSD plot without correction. SD7003 airfoil at 19 m/s and zero angle of attack.

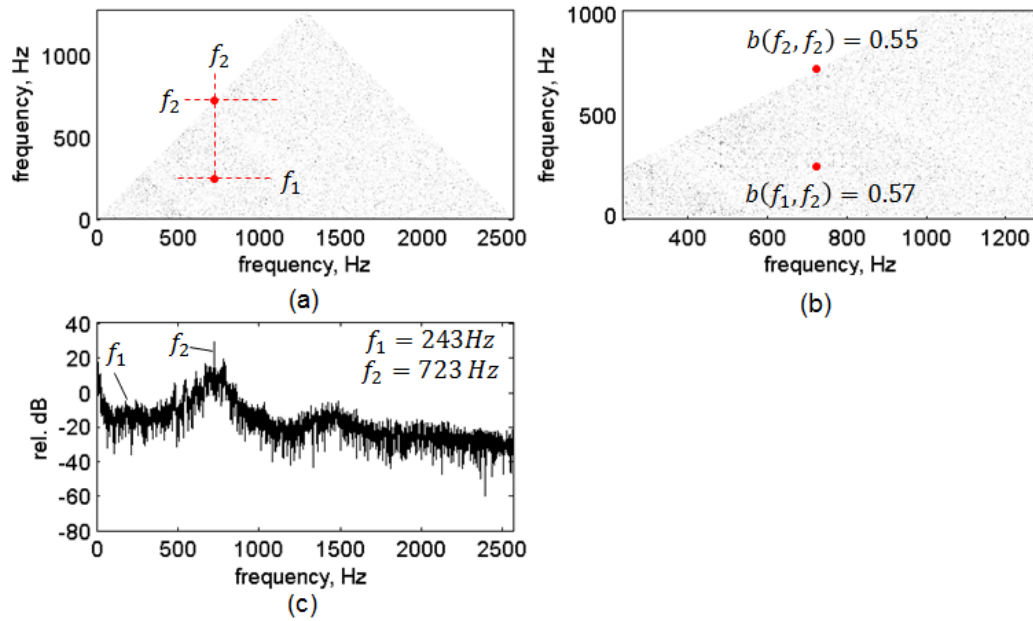


Figure 6.22: Bicoherence of the far-field microphone (a) and zoomed part of the plot (b); (c) - PSD plot without correction. SD7003 airfoil at 25 m/s and zero angle of attack.

6.10 Concluding Remarks

Experiments with the cambered SD7003 airfoil led to the similar conclusions as was made for the symmetric NACA-0012 airfoil. The ladder-type structure was observed, but the cambered airfoil is more sensitive to the change of the angles of attack and produces tonal noise in more limited borders. Test with tripping device show that the suction side is responsible for the noise production. The tonal noise dependence from the existence and location of the separation bubble also was proved. The airfoil produces trailing-edge noise when the separation bubble located on the suction side close to the sharp edge. The leading role of the suction side is also confirmed by the good correspondence of the tones of the far-field spectra and hot-wire velocity spectra. The chordwise coherence analysis presents that the character of the measured information changed with the movement downstream from acoustic to aerodynamic, because the level of the

coherence decrease except for the tonal frequencies for which it always equals 1. During time-frequency analysis three regimes depending on the flow velocities are observed: switching regime, regime with one tone and intermittency regime. The bispectral analysis of this regime shows that the non-linear relationships of the frequencies partly cause the second harmonic tones.

Figure 6.23 summarizes information about regimes, location of the separation bubble and noise signature. The same symbols as in case with the NACA-0012 airfoil were used. There are only two regimes: regime of the one tone and multiple tones regimes are observed at this angle of attack. Noise signatures and regimes at configurations A and B are in a good agreement what emphasizes that the suction side is responsible for the tones.

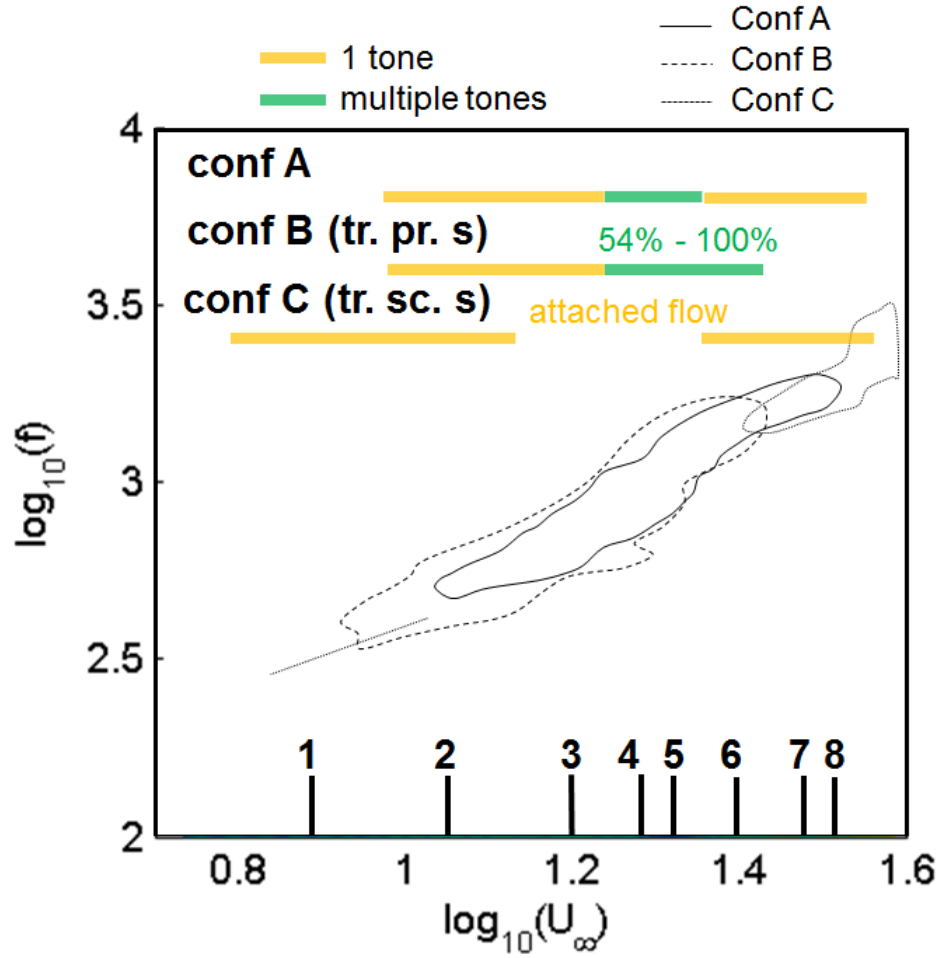


Figure 6.23: The SD7003 airfoil at 2° angle of attack. Configurations A, B and C. Noise signature contours marked by black solid, dashed and dotted lines, tonal noise regimes marked by colored lines and location of the separation bubble from the leading edge corresponding to some of regimes. 8 speeds are marked: 1 - 8 m/s ($Re_c = 0.63 \times 10^5$); 2 - 11 m/s ($Re_c = 0.87 \times 10^5$); 3 - 16 m/s ($Re_c = 1.26 \times 10^5$); 4 - 19 m/s ($Re_c = 1.5 \times 10^5$); 5 - 21 m/s ($Re_c = 1.6 \times 10^5$); 6 - 25 m/s ($Re_c = 2 \times 10^5$); 7 - 30 m/s ($Re_c = 2.4 \times 10^5$); 8 - 33 m/s ($Re_c = 2.6 \times 10^5$).

Chapter 7

Compared Numerical Simulations and Experimental Results for the SD7003 Airfoil

This chapter describes the results of two sets of numerical simulations for the SD7003 airfoil. The main reason for the additional simulation with OpenFOAM was the difference of aerodynamic results between the experiment and the numerical simulation conducted at ERAU. In particular, the pressure distribution does not allow to determine the effective angle of attack, which is needed for a relevant comparison of the results. The investigation of the aerodynamics in OpenFOAM was conducted for the freestream configuration as well as for the freejet. The agreement finally achieved with the measurements allows to define the correspondence between geometrical and effective angles of attack for the SD7003 airfoil.

7.1 Numerical Simulation in ERAU

As was mentioned previously there is no formula to calculate the effective angle of attack for the SD7003 airfoil from the knowledge of the geometrical angle of attack and of the installation. The comparison of airfoil loading should show if the flow conditions of experiment and numerical simulation are similar to each other. As the agreement of numerical simulations conducted at ERAU and experimental results was hardly achieved in a first step the accompanying numerical simulation with OpenFOAM was used for the determination of the effective angle of attack (see section 7.2). Finally, the results from ERAU were improved (see figure 7.1). However, the OpenFOAM simulation provides a better fit (see figure 7.2(b) and section 7.2).

In figure 7.1(b) the skin friction coefficient calculated at ERAU shows the separation area on the suction side from 40% to 80% of the chord length, whereas on the pressure side an attached flow is observed.

The figure 7.1(a) shows the pressure coefficient measured at $U_\infty = 16 \text{ m/s}$ and $\alpha = 2^\circ$ in comparison with calculated results in an infinite, uniform flow at

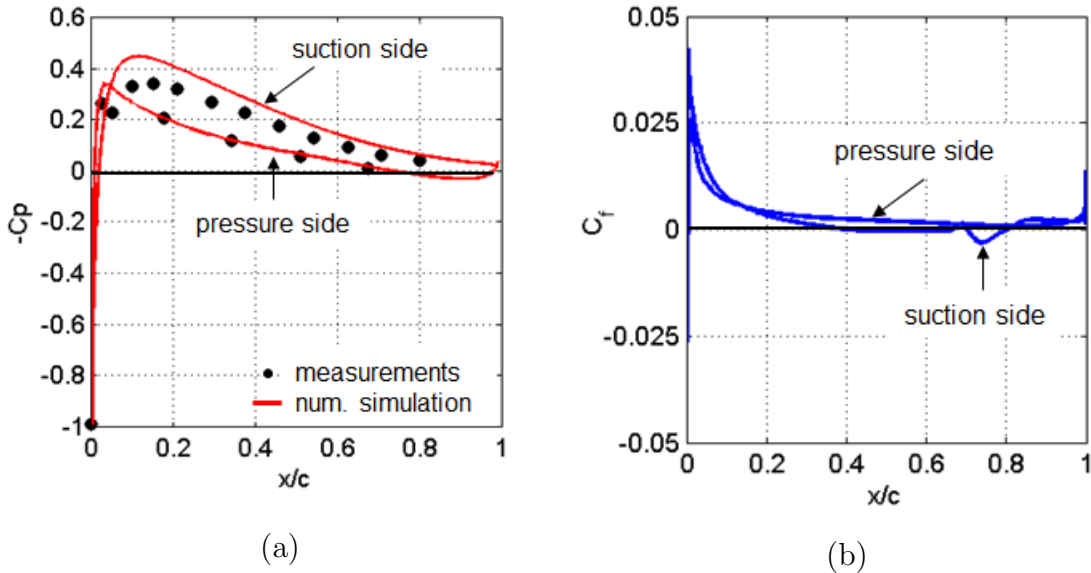


Figure 7.1: Comparison of the experimental and numerical results. ERAU (3D model in freestream at $\alpha^* = 0^\circ$) for the SD7003 airfoil at $U_\infty = 16 \text{ m/s}$ and $\alpha = 2^\circ$. (a) - pressure coefficient; (b) - skin friction coefficient.

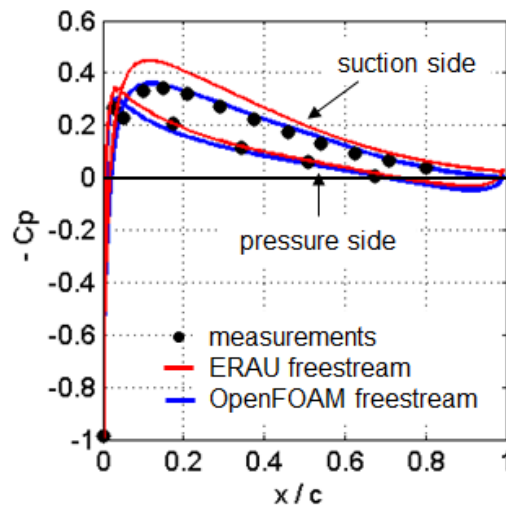


Figure 7.2: Comparison of the measured pressure coefficient at $\alpha = 2^\circ$ with numerical simulation in uniform freestream at $\alpha^* = 0^\circ$ as conducted at ERAU and when using OpenFOAM.

$\alpha^* = 0^\circ$ provided by ERAU. On the pressure side a good agreement is found. The discrepancies are more significant on the suction side so that the loading is higher for the numerical simulation. In comparison with the simulation of ERAU the results provided by OpenFOAM completely match with experiments in the figure 7.1(b).

The computed time-averaged U-velocity contours for the freestream and freejet configurations are shown in figure 7.3. The first case shows separation without reattachment on the suction side. The freejet case (figure 7.3(b)) shows that a significant deviation of the flow and changes in the near-wake occur due to the nozzle effect. It must be noted that the computation in infinite stream are 3D whereas the computation with nozzle jet are 2D.

The velocity profiles on the suction side are compared in figure 7.4. The numerical simulation produces a thicker boundary layer than in the experiment. The agreement improves closer to the trailing edge. The maxima of the rms-velocities (figure 7.4(b)) are shifted away from the wall in the simulation and also have twice higher levels in the last 10% of the chord length in comparison with the experiments. The discrepancies are systematic at all chordwise locations, therefore they cannot be attributed to positioning errors in the HWA measurements.

More details about the results of the numerical simulation can be found in [57, 9].

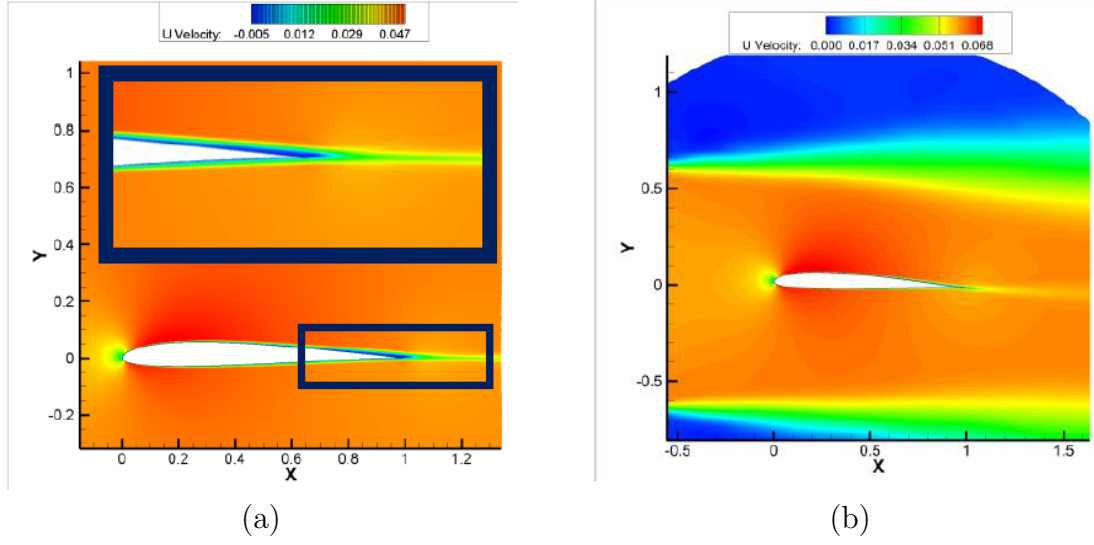


Figure 7.3: Time-average U-velocity (streamwise) contours: (a) 3D uniform ($\alpha = 0^\circ$) and (b) 2D freejet conditions ($\alpha = 2^\circ$) for the SD7003 airfoil at $U_\infty = 16 \text{ m/s}$. ERAU simulations.

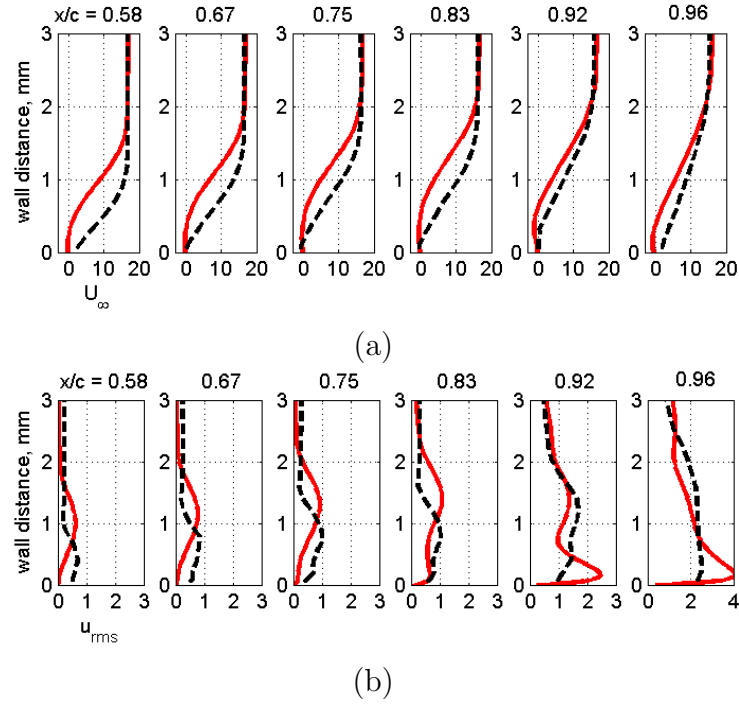


Figure 7.4: Comparison of computed velocity profiles with measured ones for the SD7003 airfoil at $U_\infty = 16 \text{ m/s}$ on the suction side. (a) - mean velocity, (b) - rms-velocity. — - numerical simulation ERAU at $\alpha^* = 0^\circ$ (uniform flow, 3D model), - - - experimental data.

7.2 Numerical Simulation in OpenFOAM

The OpenFOAM simulations was conducted in an accompanying project [67].

The numerical model was made for two geometrical configurations:

- the freestream conditions (an airfoil was embedded in a uniform flow);
- the experimental conditions (the influence of the nozzle width was accounted for).

The freestream angle of incidence corresponds to the effective angle of attack (α^*), whereas the configuration with nozzle involves the geometrical one (α). The geometrical, mathematical and numerical models are described in the appendix D.

The freestream and open-jet configurations were calculated during 11 flow times (the flow time corresponds to the time necessary for the fluid to cross the computational domain). To obtain established solutions each configuration was computed during 5.5 flow times and after that the averaging process was started for another 5.5 flow times to collect enough data.

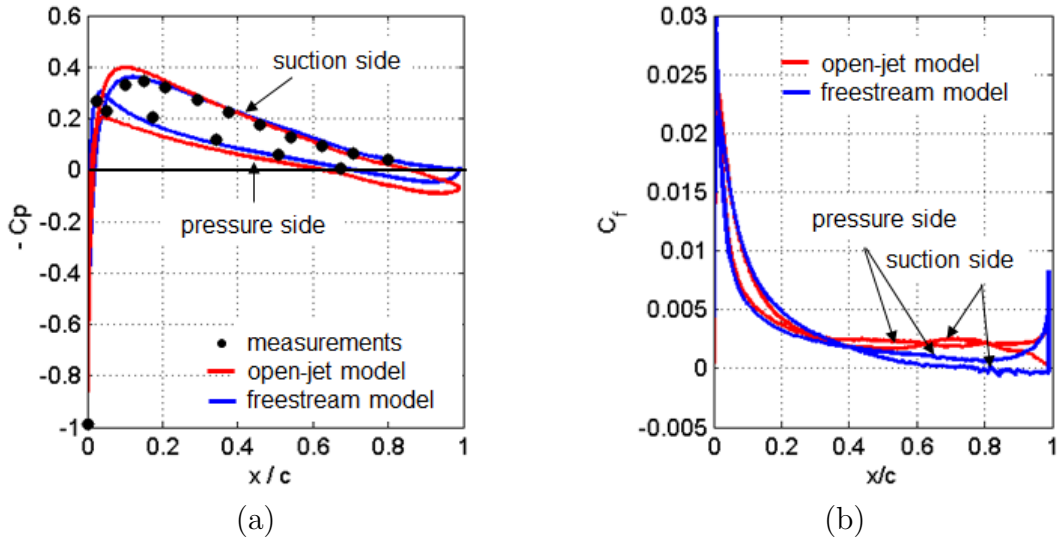


Figure 7.5: Comparison of the experimental and numerical results for the SD7003 airfoil at $\alpha = 2^\circ$ and 16 m/s. (a) - pressure coefficient distribution; (b) - skin friction coefficient.

Figure 7.5(a) shows a comparison of the measured pressure coefficient at 2° and the simulations in both configurations. The configuration with freestream was calculated at 0° and gives a surprisingly good agreement with the measurements. This suggests that the effective angle of attack $\alpha^* = 0^\circ$ corresponds to the geometrical angle $\alpha = 2^\circ$. The open-jet nozzle configuration has some overestimation on the suction side and underestimation on the pressure side close to the leading edge. But the differences of computed coefficients mainly differ close to the trailing edge. However the measurements are not available in this part of the airfoil because of the thickness.

The comparison of the mean velocity profiles (figure 7.6) confirms the agreement between results of the numerical simulation and HWA. Surprisingly, a overall better agreement is achieved by the freestream model. However, on the suction side at 98% of the chord length the open-jet simulation and the measurements show reattachment of the flow, whereas the freestream model predict a continuation of the separation bubble. This possibly can be explained by the deviation of the flow due to the influence of the nozzle in the experiment. It should be mentioned that the open-jet model has not registered any separation area on the suction side, which contradicts the experimental test. On the pressure side both models have no separation bubble in agreement with flow visualization. On the basis of the three sets of results it can be concluded that there is an attached flow on the pressure side and that the HWA produces unexpected errors for this case.

The next comparison between the calculation results and the experiment was investigated for the freestream model at $\alpha^* = 1^\circ$. The freestream model at effective angle is in clear correspondence with the experiment at $\alpha = 5^\circ$. For this comparison (figure 7.7) one can see that both freestream and open-jet case models are in acceptable agreement on the pressure side. On the suction side the freestream model has a perfect agreement with the experiment around the leading edge, but closer to the trailing edge it predicts a strong enough separation hump (from 50% to 95%) which is not present in the open-jet model. For this case the flow visualization (see section 6.5) as well as the HWA reveal the separation bubble, but far upstream from the trailing edge (from 40% to 70% of the chord length).

The streamwise velocity distribution in the freestream and open-jet models confirms the presence of the strong separation in the former and its absence in the latter (figure 7.8).

The last correspondence between the numerical case (freestream) and the experiment was observed at $\alpha^* = 2^\circ$ for the freestream and $\alpha = 7^\circ$ for the experiment (figure 7.9). Here the separation hump in the freestream is yet stronger than in

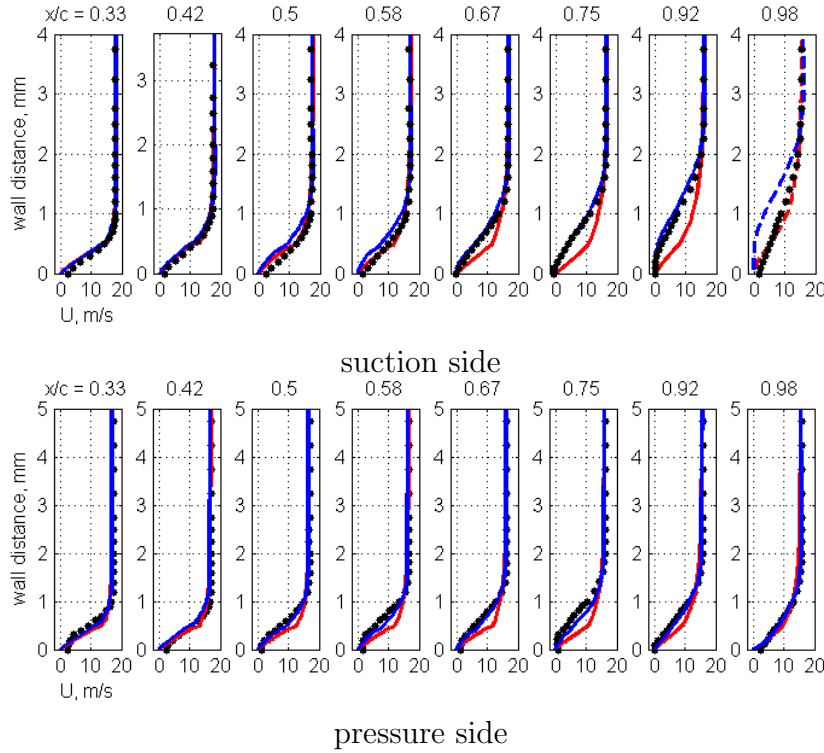


Figure 7.6: Comparison of mean velocity profiles for the SD7003 airfoil at $\alpha = +2^\circ$:
 • - ECL experiment; — - OpenFOAM freestream; — - OpenFOAM open-jet case.

the experiment despite the pressure coefficient drop in the latter. For the rest of the profile a good agreement is found.

All obtained results can be summarized in the following conclusion: the open-jet numerical model shows no separation for the cases where both the freestream model and the experiment show it, but for the higher experimental angles of attack (for example, $\alpha = +5^\circ, +7^\circ$) the freestream computation overpredicts the strength of the separation. In order to understand the cause of this behaviour of the numerical model one should analyse more precisely the environmental conditions around the airfoil, especially the wake nozzle flow in the open-jet case. This flow can be illustrated by the turbulent kinetic energy values which usually show the presence of strong mixing and turbulence (figure 7.10). Figure clearly shows the intense growth of the turbulent kinetic energy in a manner that the flow after the nozzle lips restricts the region around the airfoil. This mixing flow should raise the pressure around the airfoil and consequently block the separation from its suction side. One can see this effect in figure 7.11, where the pressure above the suction side is higher in the open-jet model than in the freestream.

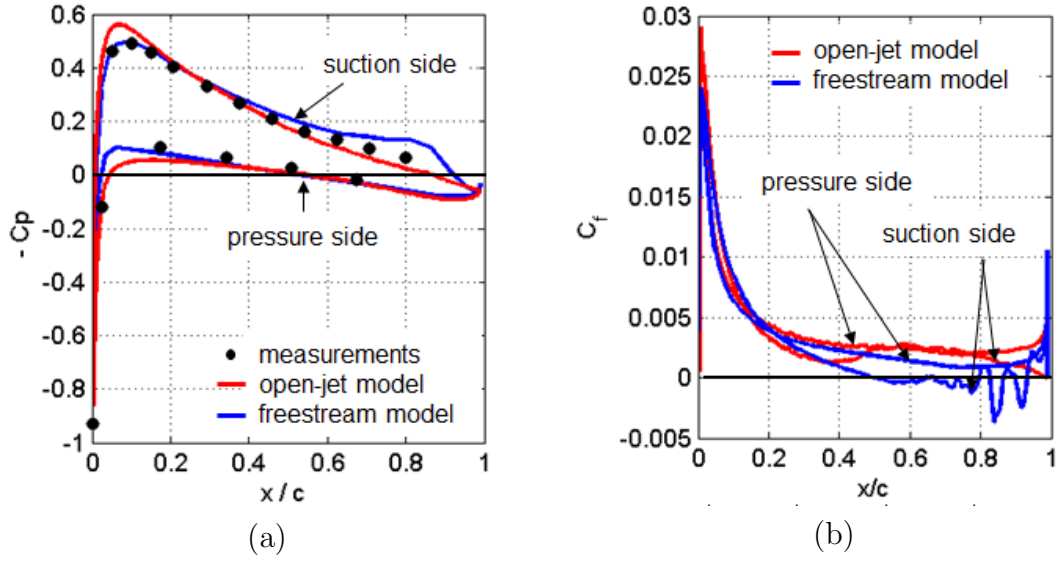


Figure 7.7: (a) - comparison of the experimental and numerical pressure coefficient distribution for the SD7003 airfoil at $\alpha = 5^\circ$ and 16 m/s. (b) - computed skin friction coefficient.

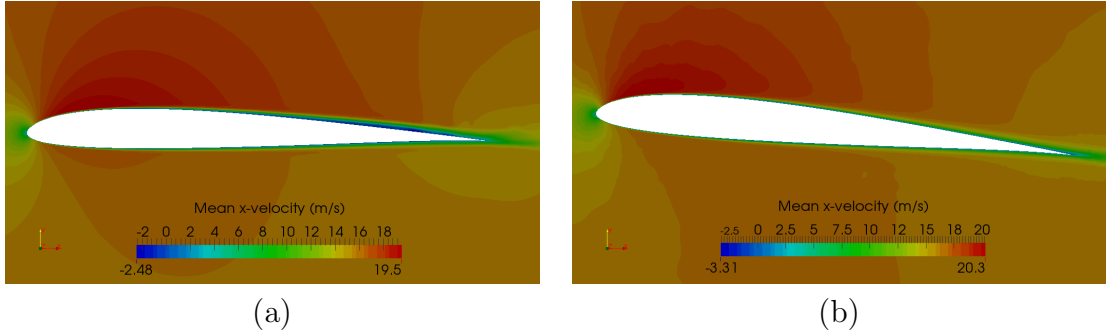


Figure 7.8: Mean streamwise velocity distribution for (a) freestream $\alpha^* = 1^\circ$ and (b) open-jet $\alpha = 5^\circ$ models.

But comparing with the experiment one should conclude that this behavior of the nozzle wake flow is excessive, maybe providing a too intense mixing. This behavior can be attributed to the weakness of RANS-model solutions which usually over-estimate the growth of the turbulent kinetic energy and the mixing intensity. The same configuration calculated with more accurate turbulence modelling (typically DES or LES) probably would solve this issue.

As a result of the numerical modelling of the airfoil at various angles of attack a matrix of correspondence between the experimental and effective angles of attack

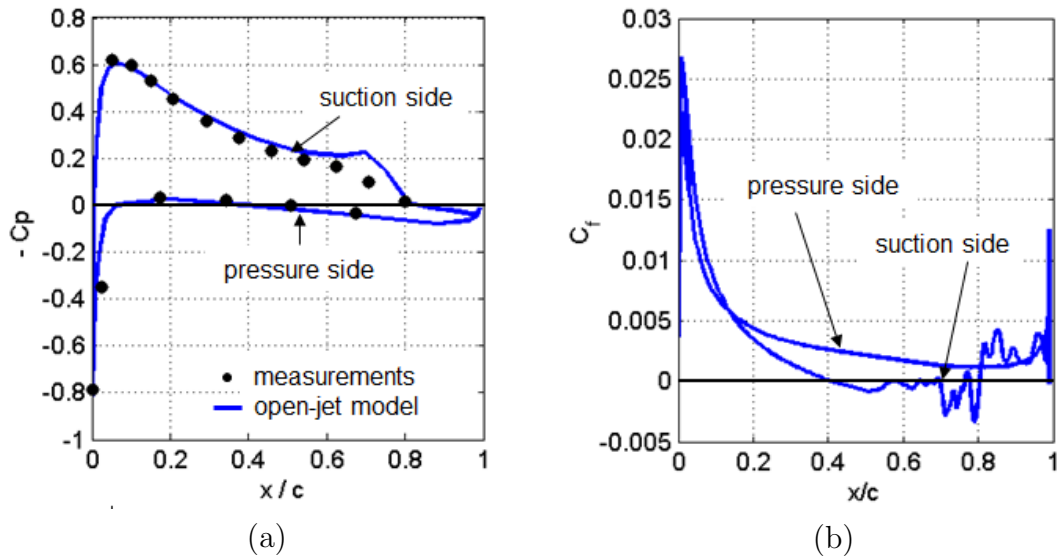


Figure 7.9: Comparison of the experimental and numerical (only freestream model) results for the SD7003 airfoil at $\alpha = 7^\circ$ and 16 m/s. (a) - pressure coefficient distribution; (b) - skin friction coefficient.

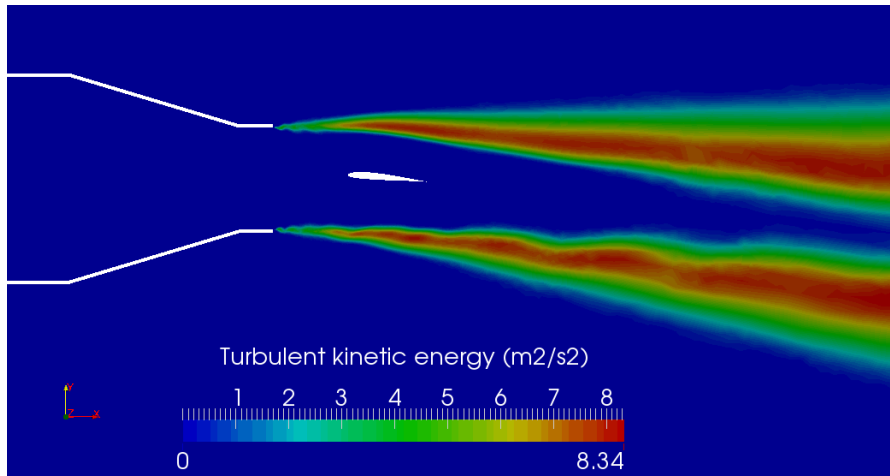


Figure 7.10: Turbulent kinetic energy at $\alpha = +5^\circ$ in the open-jet model.

was constructed (see table 7.1). Based on the analysis of the numerical results one can say that this correspondence is clear enough to be the basis of the consequent, more precise calculations and the comparison with experimental cases.

Part of the results mentioned in this chapter was presented in [67].

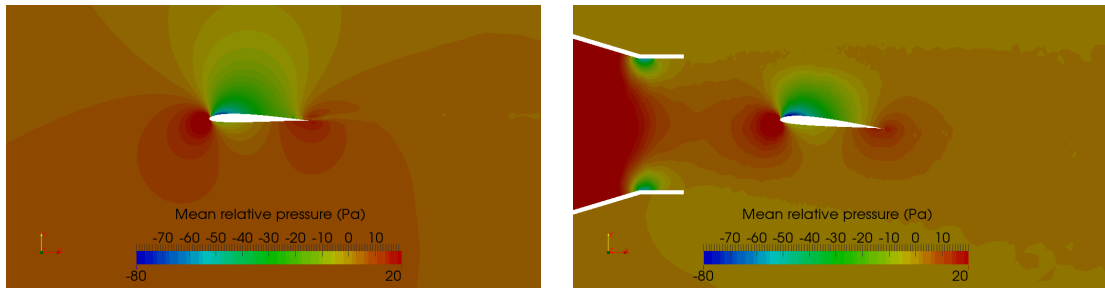


Figure 7.11: Mean pressure distribution around the airfoil for freestream $\alpha = +1^\circ$ (left) and open-jet $\alpha = +5^\circ$ (right) models.

Table 7.1: Illustrative table of the correspondence between freestream and open-jet condition angles of attack.

Freestream \ Open-jet				
	0°	$+2^\circ$	$+5^\circ$	$+7^\circ$
-1°	-	-	-	-
0°	-	X	-	-
$+1^\circ$	-	-	X	-
$+2^\circ$	-	-	-	X
$+5^\circ$	-	-	-	-
$+7^\circ$	-	-	-	-

Conclusion

The importance of the trailing-edge tonal noise produced by low-Reynolds number airfoils has been recognized in the past, particularly dealing with small-scale wind tunnel experiments. The need for its reduction when using drones and wind turbines in people's everyday life is undeniable. Therefore a deep understanding of this mechanism is needed. Despite the several decades of investigation the trailing-edge tonal noise produced by the airfoils at low-Reynolds numbers there are still some details which should be explained. The collaborative project between the Embry-Riddle Aeronautical University and the Ecole Centrale de Lyon allowed to use experimental, numerical and analytical means for understanding of the phenomenon.

The complement experimental study of the two airfoils: the NACA-0012 airfoil and the SD7003 airfoil with 12 cm chord lengths was conducted at the Ecole Centrale de Lyon and is reported as the present work. Such parameters as far-field and surface pressures, flow velocity close to the airfoils and pressure coefficient were measured. The experimental results were used for the creation of an experimental database and for comparison with numerical simulations.

The source localization performed for the SD7003 airfoil confirms that the trailing edge is the source of the observed tonal noise. Of course any location of flow unsteadiness can produce sound but the dominant sound heard in the experiment is produced by the fastest time variations of vortical patterns that occur at the trailing edge. The latter acts as a singularity. In contrast vortex dynamics developing along the smooth wall has a very low acoustic efficiency.

As the tonal noise is a very sensitive and unstable phenomenon the careful investigation of its signature depending on Reynolds numbers and angles of attack allowed to complete the tonal area provided by previous investigators for the NACA-0012 airfoil and to create this kind of plot for the SD7003 airfoil. Directivity measurements for the NACA-0012 airfoil showed a slight asymmetry in the noise signature, which can be explained by the influence of the experimental room. More details were obtained as a result of the acoustic signature measured by a microphone in the far field. For both airfoils the ladder-type structure was observed. The dominant tone was in agreement with the power law $U_\infty^{1.5}$, whereas the accompanying discrete tones coincided with the power law $U_\infty^{0.8}$.

The time-frequency analysis of the measured far-field data illustrated the existence of several regimes depending on the Reynolds number and angle of attack: regime with one strong tone, switching regime between two nonsimultaneous tones and intermittency regime with multiple tones.

The analysis of the experimental spectra and previous investigations showed that there are two components: boundary layer instabilities and feedback loop which are responsible for the tonal noise generation. The spectra of the tests with small-scale upstream turbulence which blocked generation of the feedback loop but did not destroy boundary layer instabilities had broadband hump but without tones. This proved that the feedback loop is a necessary component for the tonal noise generation. The comparison with previous measurements conducted for the NACA-0012 airfoil with 8 cm and 10 cm chord lengths showed that decreasing the chordlength led to increasing the tonal noise frequencies.

The tests with a tripping device force a laminar boundary layer to transition to turbulence and switch off the emission of tones. They showed that for the NACA-0012 airfoil at low Reynolds numbers up to 0.6×10^5 the suction side produced the tones whereas at higher flow velocities the pressure side is responsible for the tones. In the case of the SD7003 airfoil only the suction side produces tones. This depends on the existence and location of a separation bubble on each side of the airfoil. The measurements with a hot-wire anemometry and a flow visualization allowed to investigate the role of the separation bubble in the tonal noise generation. It was proved by numerous tests that if there was no separation bubble extending to the trailing edge or reaching close enough to the trailing edge then the tonal noise was absent. Indeed a rapid time variation of the vorticity carried in the oscillation boundary layers is needed for an efficient sound emission. This can only occur close to a singularity. As the location of the separation bubble strongly depends on the Reynolds number and on the angle of attack this explains the sensitivity of the tonal noise to these parameters. A more detailed explanation of the separation

Conclusion

bubble role was done by inspecting the numerical simulations conducted at the Embry-Riddle Aeronautical University. The analysis of the chordwise instability amplification showed that the separation bubble is an amplifier of the boundary layer instabilities. In other words the Tollmien-Schlichting waves generated due to viscous effects are too weak to be responsible for the tonal noise, but they provide the frequency disturbance that are strongly amplified in the separation area as the fast-developing Kelvin-Helmholtz waves associated with the inflection point of the velocity gradients. But it should be mentioned that the existence of the separation area is not a sufficient condition for the tonal noise generation. Indeed the flow visualization tests showed that a small-scale upstream turbulence did not change the onset and the location of the separation bubble, whereas it was able to suppress the tonal noise due to destruction of the acoustic feedback loop, which amplify the Tollmien-Schlichting waves.

Another measured parameter for both airfoils was the pressure coefficient which was used as a reference for comparison of numerical simulations and experimental results. For the NACA-0012 the comparison was quite good, however for the cambered SD7003 airfoil the differences were significant. This was a motivation for additional numerical simulations in OpenFOAM, which provided a nice coincidence of the measured and calculated pressure coefficients and allowed to determine an effective angle of attack for this airfoil.

In the frame of the present work the analytical prediction of the tonal far-field level with Amiet's model was made on the basis of measured surface pressures close to the trailing edge. It showed a satisfactory agreement with the experimental results, confirming the cause-to-effect relationship between the wall pressure and the radiated field. However significant discrepancies remain. They are attributed to the fact that the wall-pressure field varies rapidly in the streamwise direction for LBL instabilities, and to the fact that wall measurements can only be performed at some finite distance from the trailing edge.

On the basis of the experimental and numerical investigation the mechanism of the tonal noise generation can be described in the following way (figure 7.12). At some initial point of the airfoil the Tollmien-Schlichting instabilities start. They are moving downstream and forced to transition to Kelvin-Helmholtz waves by the separation area. These waves reach the trailing edge, scatter from it and generate acoustic waves, which move upstream. At the initial point of boundary layer instabilities the acoustic wave amplifies them at some frequencies for which the phases of both motions match and creates the feedback loop for the process. So for the tonal noise generation three components should be considered: boundary layer instabilities, separation bubble and acoustic feedback loop.

point A – starting point of boundary layer instabilities;
point B – source of the noise

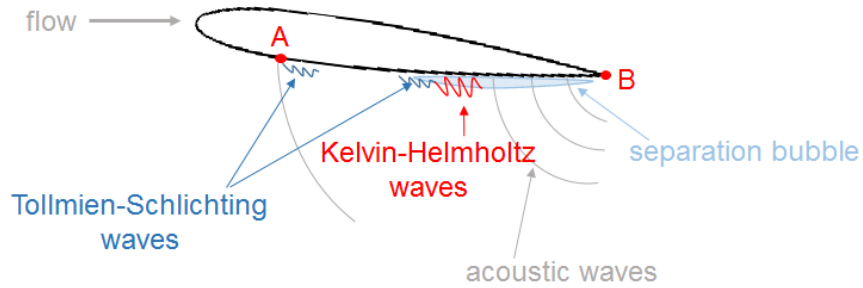


Figure 7.12: Illustration of the trailing-edge tonal noise.

The present work elucidates some details of the trailing-edge noise generation, but also put some additional questions. One of them is the explanation of the existence of the noise emission regimes. The author believes that more detailed analysis of the experimental database with advanced post-processing techniques can be one of the possible solutions. The aforementioned database can also be used for validation of future numerical simulations, which can provide more precise information about flow parameters. Moreover a more extended application of Amiet's model with experimental data as input parameters would be one way of investigating the question of the receptivity of the boundary layer to external acoustic disturbances.

Appendix A

Tables of the Parameters of Experimental Investigation

Table A.1: Flow speed range

№	No grid, m/s	Small-scale grid, m/s	Large-scale grid, m/s
1	5.4	5.3	5.9
2	5.95	5.9	6
3	6.5	6.3	6.2
4	7.1	6.7	6.5
5	7.7	7.2	6.9
6	8.25	7.7	7.3
7	8.8	8.2	7.8
8	9.4	8.8	8.4
9	10	9.4	9
10	10.6	10	9.6
11	11.2	10.7	10.3
12	11.8	11.4	11
13	12.4	12.2	11.9
14	13.6	13	12.8
15	14.7	13.8	13.7
16	15.8	14.7	14.6
17	16.9	15.5	15.4
18	18	16.4	16.1
19	18.9	17.3	16.9
20	19.1	18.2	17.7
21	19.6	19.1	18.7
22	20.9	20	19.7
23	22	20.9	20.6
24	22.8	21.8	21.5
25	23.7	22.7	22.3
26	24.8	23.7	23.3
27	26.1	24.7	24.5
28	27.5	25.7	25.7
29	28.9	26.8	27
30	30	27.8	28.2
31	30.4	28.9	29.2
32	31.4	30	30.1
33	32.7	31.2	31
34	34	32.3	31.8
35	35.5		
36	37.3		
37	38.7		

Table A.2: Conducted measurements for the NACA-0012 airfoil

Type of measurements	Measured parameters	Configuration	Angle of attack	Flow velocities, m/s
Measurements of acoustic signature	Far-field noise	A,B,C,E	0°	from 5 to 38
		A	5°	
RMPs measurements	Wall pressure	A,B,C,D	−5°, 0°, 5°	8, 11, 16, 19, 21, 25, 30, 33
		E	0°	8, 11, 16, 19, 25, 33
		F	0°	8, 11, 16, 19, 21, 25, 30, 33
Directivity measurements	Far-field noise	A	−5°, 0°	8, 11, 16, 19, 21, 25, 30, 33
		B	0°	8, 11, 16, 19, 21, 25, 30, 33
Pressure coefficient measurements	Pressure coefficient	A	−5°, 5°	19, 25
			0°	25
		B, C	−5°, 5°	19
Hot-wire anemometry	Velocity profiles	A	−5°, 5°	19
			0°	16, 19
		C	0°	19
			5°	11
		E	0°	19

Table A.3: Conducted measurements for the SD7003 airfoil

Type of measurements	Measured parameters	Configuration	Angle of attack	Flow velocities, m/s
Measurements of acoustic signature	Far-field noise	A	$-3^\circ, -2^\circ, 0^\circ, 2^\circ, 5^\circ, 7^\circ$	from 5 to 38
		B,C	$-2^\circ, 2^\circ$	
RMPs measurements	Wall pressure	A	$-2^\circ, 0^\circ, 2^\circ, 5^\circ, 7^\circ$	8, 11, 16, 19, 21, 25, 30, 33
		B,C	$-2^\circ, 0^\circ, 2^\circ$	8, 11, 16, 19, 25, 33
		D	$-2^\circ, 2^\circ$	8, 11, 16, 19, 21, 25, 30, 33
Pressure coefficient measurements	Pressure coefficient	A	$0^\circ, 2^\circ, 5^\circ$	16
			7°	8, 16
Hot-wire anemometry	Velocity profiles	A	$2^\circ, 5^\circ$	19
			2°	16

Appendix B

Complementary Experimental Results for the NACA-0012 Airfoil

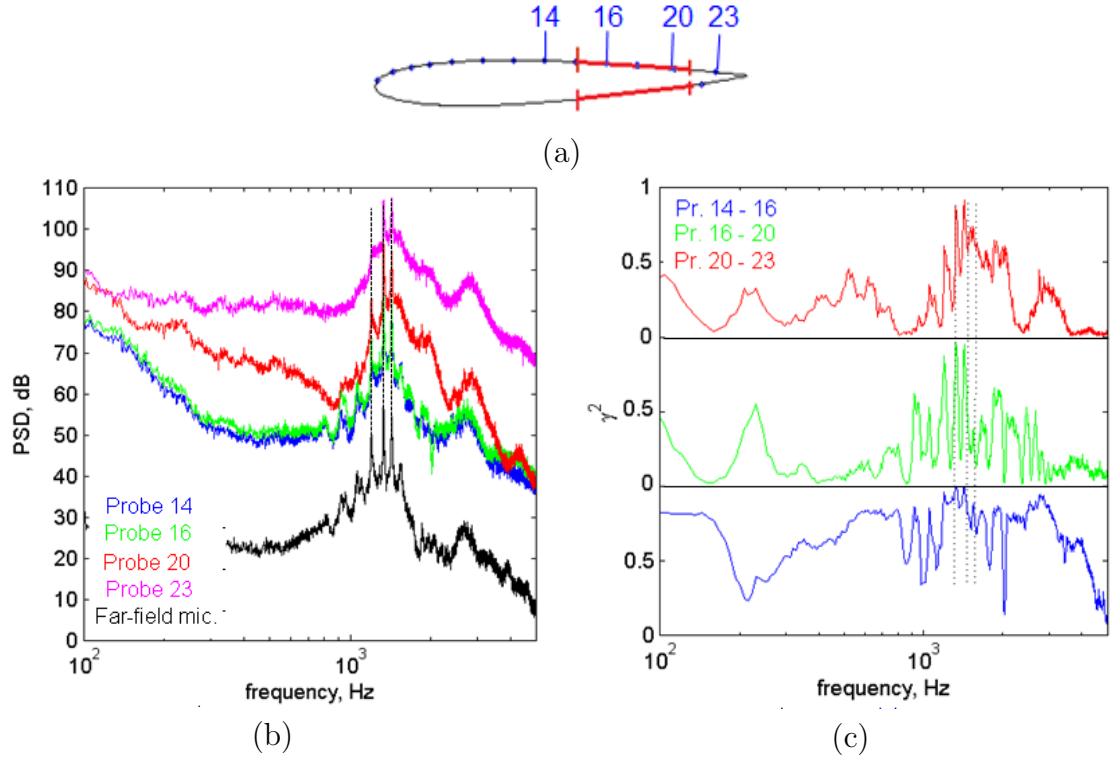


Figure B.1: The NACA-0012 airfoil at 25 m/s and zero angle of attack: (a) - location of the separation bubble; (b) - PSD plots for wall pressure probes and far-field microphone; (c) - chordwise coherence plots for doublets of wall pressure probes. Dotted lines mark tones.

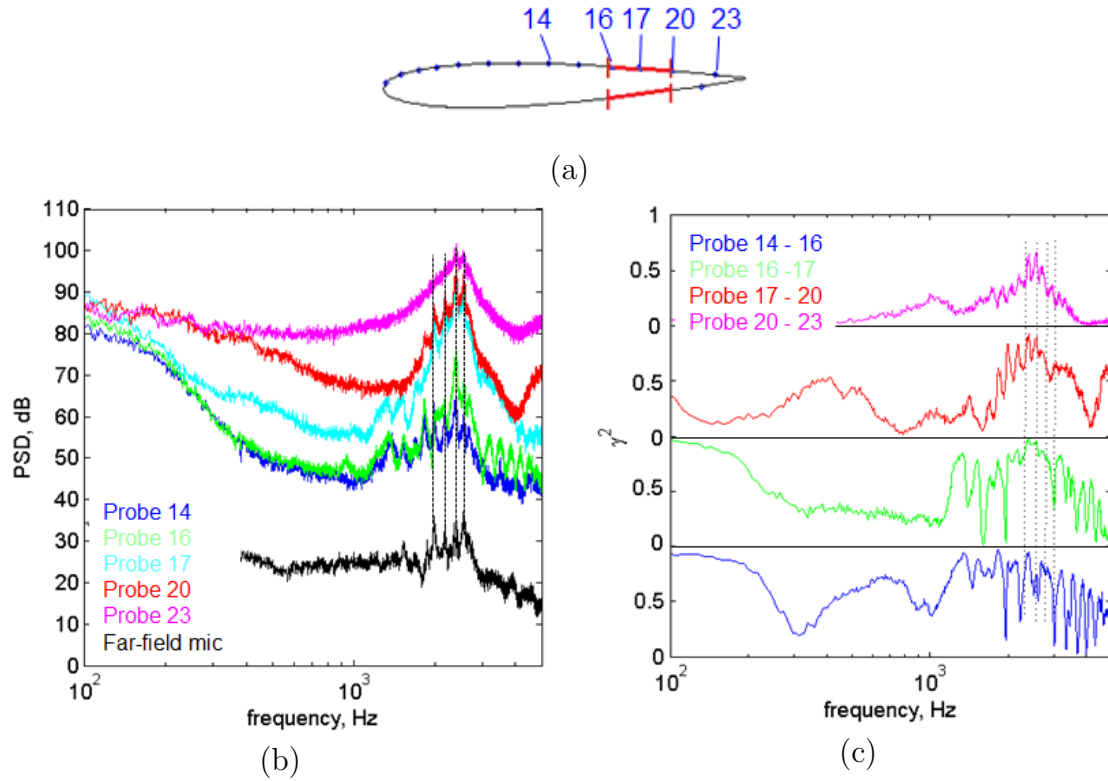


Figure B.2: The NACA-0012 airfoil at 33 m/s and zero angle of attack: (a) - location of the separation bubble; (b) - PSD plots for wall pressure probes and far-field microphone; (c) - chordwise coherence plots for doublets of wall pressure probes. Dotted lines mark tones.

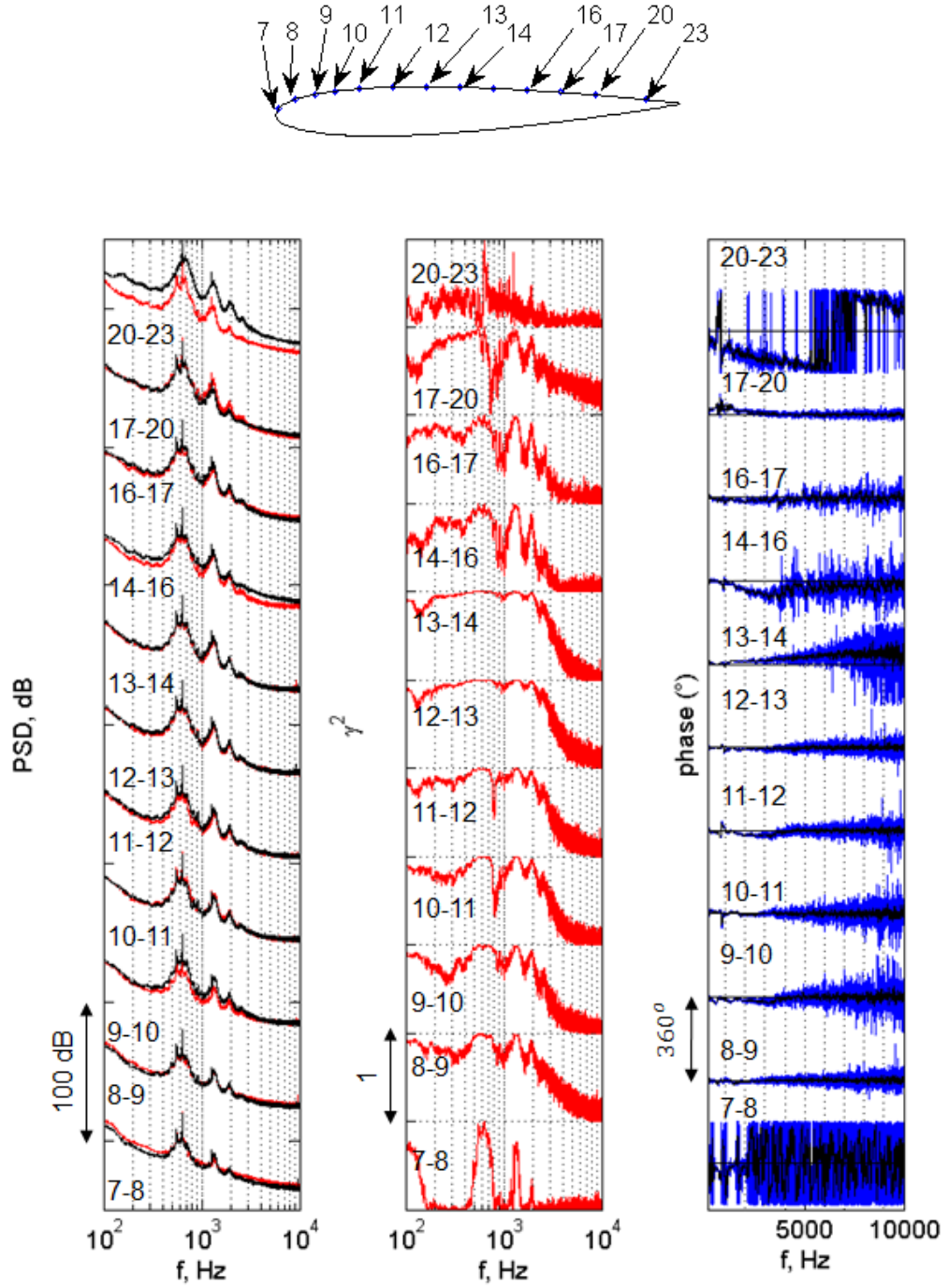


Figure B.3: Chordwise dynamic of PSD, coherence and phase of cross-spectrum of RMPs pairs for the NACA-0012 airfoil at $\alpha = 0^\circ$ and $U_\infty = 16 \text{ m/s}$.

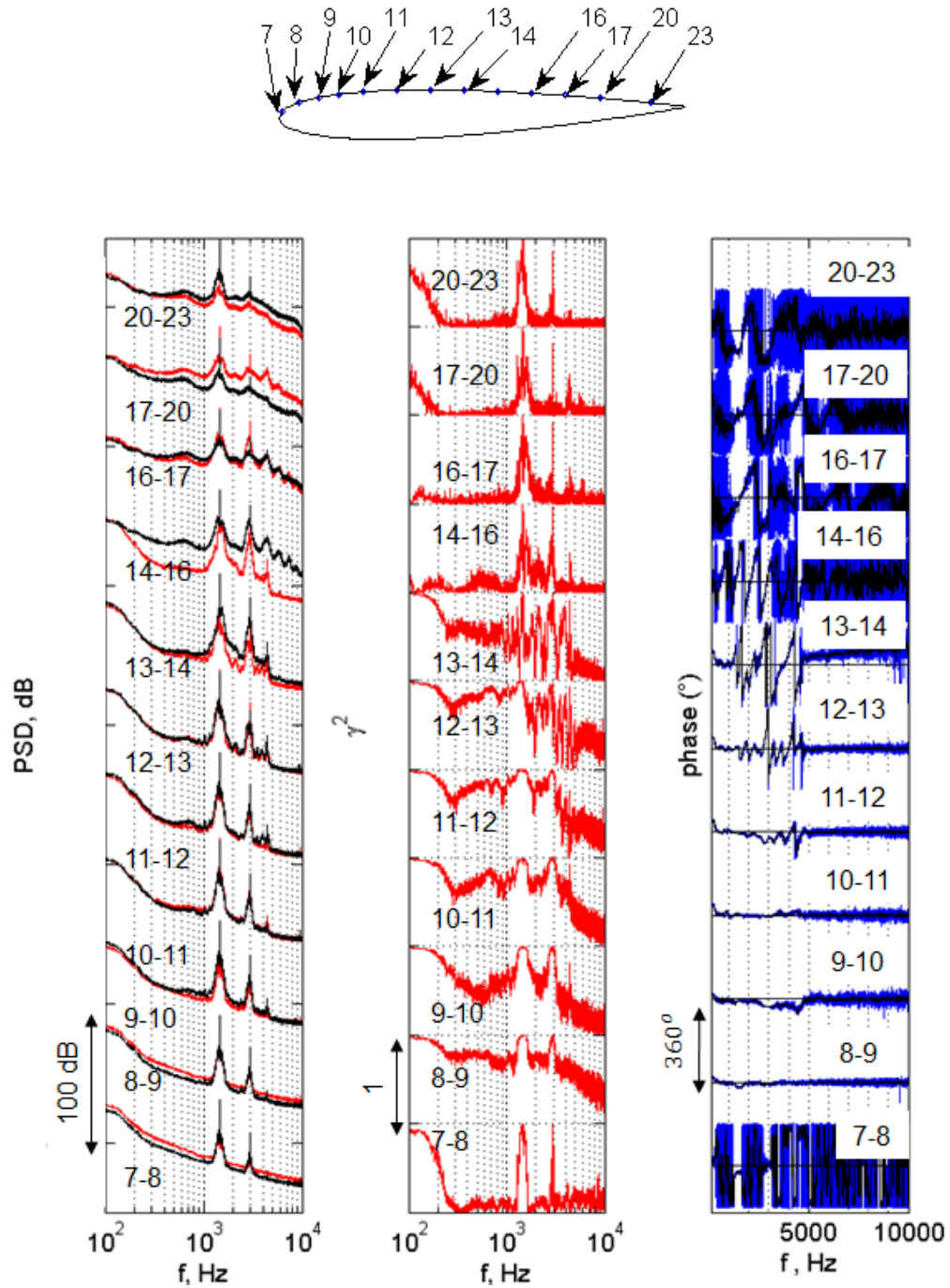


Figure B.4: Chordwise dynamic of PSD, coherence and phase of cross-spectrum of RMPs pairs on the suction side for the NACA-0012 airfoil at $\alpha = -5^\circ$ and $U_\infty = 25 \text{ m/s}$.

Appendix C

Complementary Experimental Results for the SD7003 Airfoil

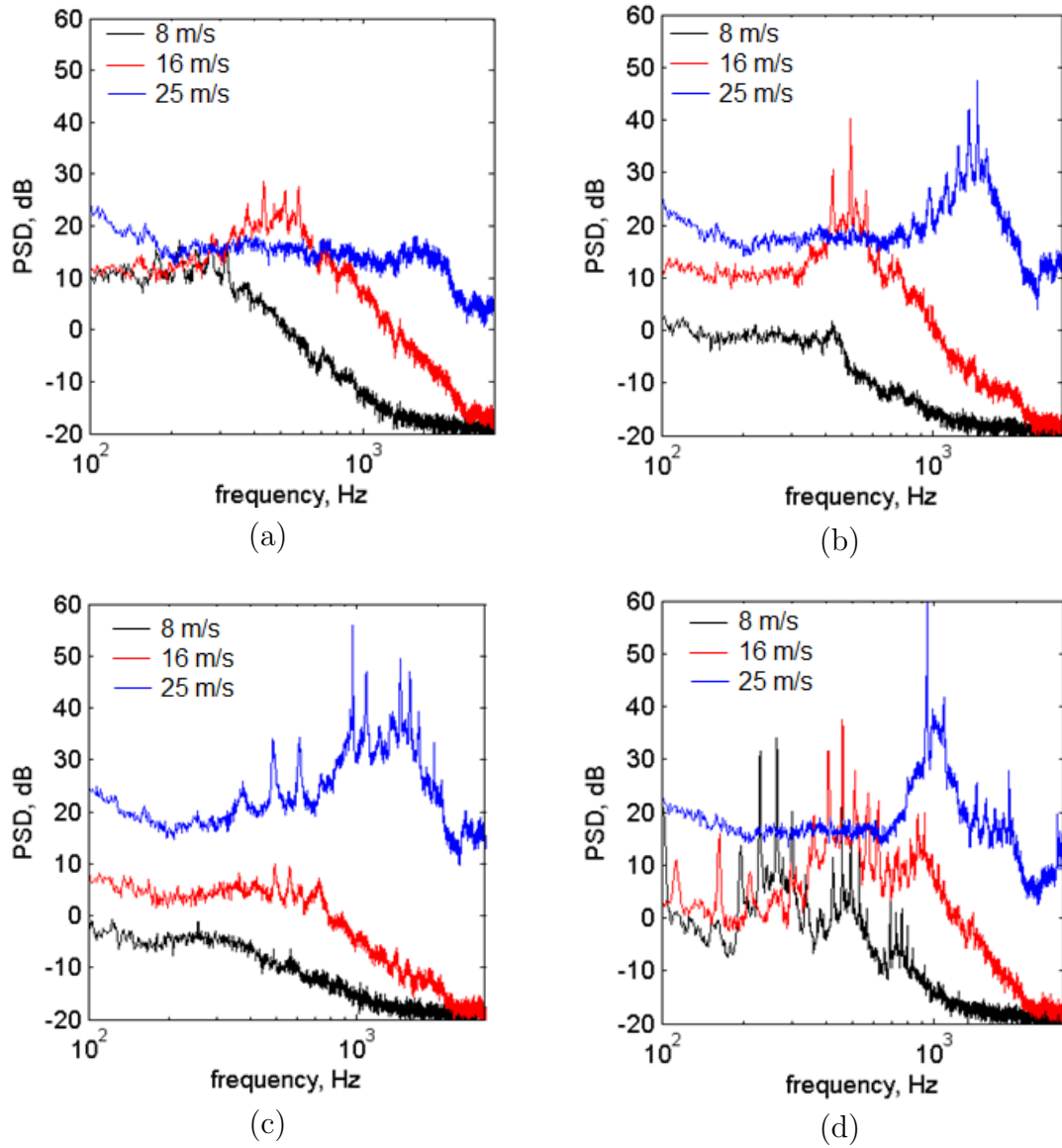


Figure C.1: PSD of the far-field microphone for the SD7003 airfoil. Configuration A at various flow velocities. (a) - at $\alpha = 5^\circ$; (b) - at $\alpha = 2^\circ$; (c) - at $\alpha = 0^\circ$; (d) - at $\alpha = -2^\circ$.

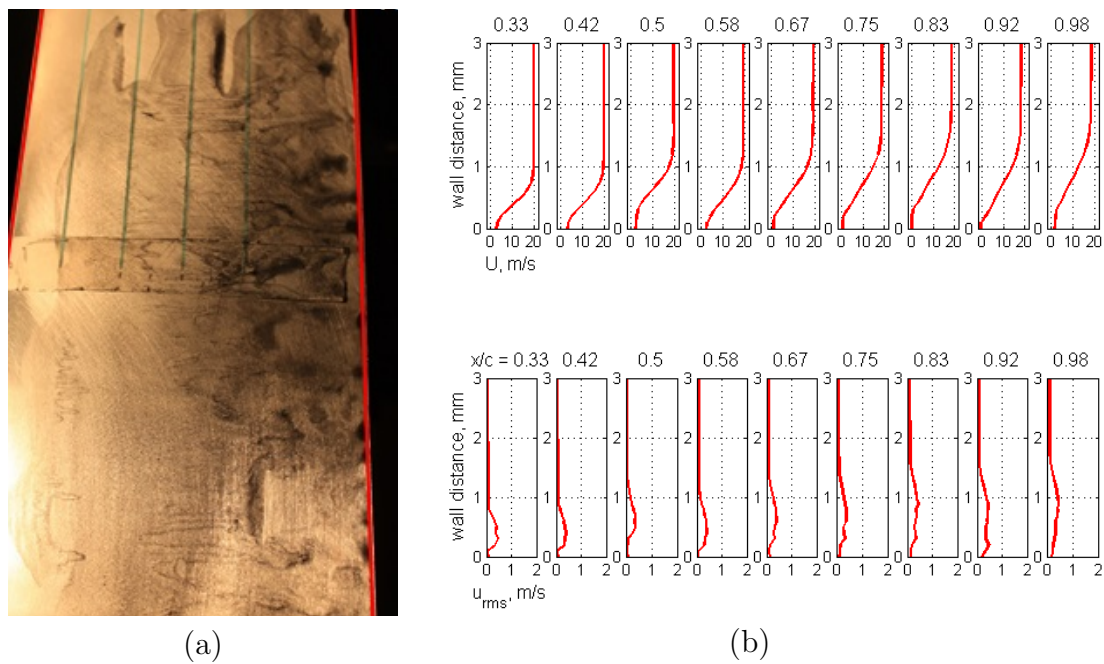


Figure C.2: Flow visualization (a) and HWA results (b) for the pressure side of the SD7003 airfoil at $\alpha = 5^\circ$ and 19 m/s. Tonal noise is not observed.

Appendix D

Numerical Simulation with OpenFOAM

In order to understand the discrepancies between the measured aerodynamic characteristic of the SD7003 airfoil and the ERAU computations it was decided to conduct additional numerical simulations, and to relate the geometrical and effective angles of attack. This part of the work was not included in the program of the thesis. It has been performed in an accompanying collaboration and appeared to be essential for the determination of the operating point of the SD7003 airfoil. This appendix gives a minimal description of the computational strategy. Readers interested in computational techniques can find more details in the list of references. It should be noted that in this chapter some items of the nomenclature differ from the previous chapters.

D.1 Geometrical Model

The numerical study was made for two geometrical configurations:

- the freestream conditions (the airfoil was modelled in a uniform flow of infinite extend);
- the experimental conditions (the influence of the nozzle was included in the computation)

The geometry of the first configuration is presented in figure D.1. The airfoil is placed at the middle of the domain, where boundary disturbances could not affect the solution in the central part. The dimensions of the domain are 16 airfoil chords in the streamwise direction and 10 chords in the crosswise direction.

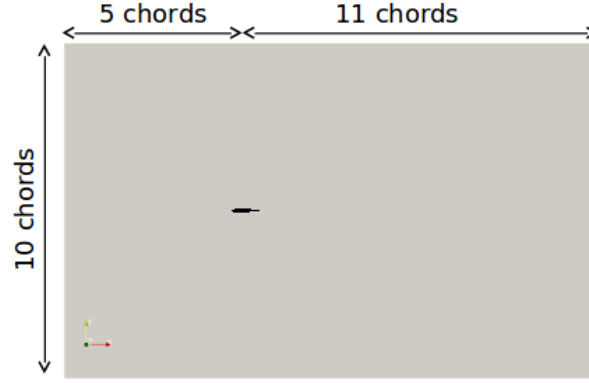


Figure D.1: View of the computational domain in the first configuration.

The second configuration (see figure D.2) includes the nozzle geometry, the airfoil and a large extent in the crosswise and streamwise directions. The height of the domain is 3.64 m (around 30 chords) and the length is 4.31 m with 29 chords downstream of the airfoil trailing edge. The airfoil geometry was rounded at the trailing edge instead of a true sharp shape (see details in figures from D.3 to D.4).

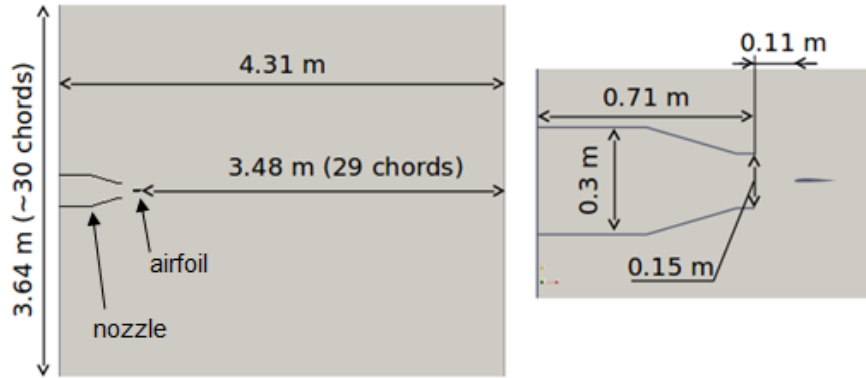


Figure D.2: View of the computational domain in the second configuration.

All numerical simulations are made in a pseudo-3D manner with a small extent in the third dimension which will be represented by just one mesh cell due to the computational code requirements. Correspondingly, the measurements which were taken on the airfoil surface (pressure coefficients) are made from the middle of the

airfoil span along all its surface which produces a continuous trace of the values aside from the point-style experimental measurements. Consequently, the clear comparison of the results are mainly provided in the corresponding locations on the airfoil surface where the measurements were actually taken in the experiments.

D.2 Mathematical Model

D.2.1 Governing Equations

The governing equations solved in the accompanying work are the three-dimensional incompressible isothermal Reynolds-averaged Navier-Stokes equations.

1) Continuity equation:

$$\frac{\partial u_j}{\partial x_j} = 0 \quad (\text{D.1})$$

2) Momentum equation:

$$\frac{\partial u}{\partial t} + \frac{\partial}{\partial x_j} (u_i u_j + p \delta_{ij} - \tau_{ij}) = 0 \quad (\text{D.2})$$

where u_{ij} is the velocity vector components; p is the thermodynamic (static) pressure; τ_{ij} is the viscous stress tensor in the following form:

$$\tau_{ij} = \nu_{eff} \left(\frac{\partial u_i}{\partial x_j} + \frac{\partial u_j}{\partial x_i} - \frac{2}{3} \frac{\partial u_k}{\partial x_k} \delta_{ij} \right), \quad (\text{D.3})$$

where δ_{ij} is the Kronecker delta; $\nu_{eff} = \nu + \nu_t$ is the effective kinematic viscosity which is sum of laminar and turbulent viscosities.

The fourth term in the turbulent viscous stress tensor ($-\frac{2}{3}k\delta_{ij}$) is neglected.

Although the governing equation system has a three-dimensional form, it is actually solved only in two directions due to the special boundary conditions and domain construction. This numerical trick is performed because of the solver

structure which is constructed for the solution of 3D problems (for more precise information see [68]).

These equations are solved using a control-volume unstructured solver based on the combination of the PISO and SIMPLE numerical schemes.

D.2.2 Turbulence Model

The system of equations D.1 - D.3 is closed via the Shear-Stress Transport (SST) turbulence model of Menter [69],[70]. This model was used to solve the freestream cases and consists in the following equations:

$$\frac{\partial k}{\partial t} + \frac{\partial u_j k}{\partial x_j} = \widetilde{P}_k - \beta^* \omega k + \frac{\partial}{\partial x_j} \left[(\nu + \sigma_k \nu_t) \frac{\partial k}{\partial x_j} \right] \quad (\text{D.4})$$

$$\frac{\partial \omega}{\partial t} + \frac{\partial u_j \omega}{\partial x_j} = \frac{\gamma}{\nu_t} \widetilde{P}_k - \beta \omega^2 + \frac{\partial}{\partial x_j} \left[(\nu + \sigma_\omega \nu_t) \frac{\partial \omega}{\partial x_j} \right] + 2(1 - F_1) \frac{\sigma_{\omega 2}}{\omega} \frac{\partial k}{\partial x_j} \frac{\partial \omega}{\partial x_j} \quad (\text{D.5})$$

where k is turbulent kinetic energy; ω is turbulent dissipation rate.

The following semi-empirical relations are used to close the model:

$$\widetilde{P}_k = \min(\mu_t S^2, 10\beta^* \omega k) \quad (\text{D.6})$$

$$F_1 = \tanh(arg_1^4) \quad (\text{D.7})$$

$$arg_1 = \min \left(\max \left(\frac{\sqrt{k}}{\beta \omega y}; \frac{500\nu}{y^2 \omega} \right); \frac{4\sigma_{\omega 2} k}{CD_{k\omega} y^2} \right) \quad (\text{D.8})$$

$$CD_{k\omega} = \max \left(2\sigma_{\omega 2} \frac{1}{\omega} \frac{\partial k}{\partial x_j} \frac{\partial \omega}{\partial x_j}; 1.0e^{-10} \right) \quad (\text{D.9})$$

The turbulent viscosity is calculated as

$$\nu_t = \min \left[\frac{k}{\omega}; \frac{a_1 k}{S F_2} \right] \quad (\text{D.10})$$

where $a_1 = 0.31$, S is the strain rate magnitude and the blending function F_2 :

$$F_2 = \tanh \left(\text{arg}_2^2 \right) \quad (\text{D.11})$$

$$\text{arg}_2^2 = \max \left(2 \frac{\sqrt{k}}{\beta^* \omega y}; \frac{500\nu}{y^2 \omega} \right) \quad (\text{D.12})$$

The coefficients of the model are defined by:

$$\phi = F_1 \phi_1 + (1 - F_1) \phi_2 \quad (\text{D.13})$$

where ϕ_1 and ϕ_2 are the coefficients of the $k - \epsilon$ and $k - \omega$ models respectively:

$$\begin{aligned} \sigma_{k1} &= 1.176; \sigma_{\omega1} = 2.000; \kappa = 0.41; \gamma_1 = 0.5532; \beta_1 = 0.0750; \beta^* = 0.09; \\ \sigma_{k2} &= 1.000; \sigma_{\omega2} = 1.168; \kappa = 0.41; \gamma_2 = 0.4403; \beta_1 = 0.0828; \beta^* = 0.09 \\ c_1 &= 10; \end{aligned}$$

However, the investigated cases are more laminar-to-transition than purely turbulent and, consequently, the use of RANS turbulent models is not strictly appropriate. The particular drawback of the eddy viscosity two-equation turbulent models is their over-prediction of the production of the turbulent kinetic energy in regions where the flow experiences significant acceleration (for example, around the airfoil leading edge) [51]. Moreover, for low-speed airfoils in a laminar upstream flow, the flow around the leading edge should remain laminar with possible subsequent transition. Despite the turbulence modeling has a minor effect on the pressure coefficient distribution around an airfoil, which can be seen, for example, in [51],[71], it affects drastically the friction and therefore should be taken into account for the comparison of the velocity profiles.

There are plenty of models which are trying to include the transition effects into the turbulence modeling staying in the region of statistical averaging paradigm. Amongst them there are models with additional equations for laminar kinetic energy [72], models based on the e^n method [71] and the local correlation transition

model [73],[74]. The latter was chosen in the current work as the most appropriate. The main advantage of this model is that it is based on local empirical correlations and may be used for arbitrary geometries including 2D and 3D cases, unlike, for example, e^n models. It is also worth noting that this model was extensively tested and showed very good results on various industrial aerodynamic models including one- and two-element airfoils, turbine blade cascades etc. Another advantage of this model is its ability to predict the transition onset location and length sufficiently accurately for a wide range of freestream turbulent intensities, either for natural or for bypass transition phenomena.

The Transition SST model incorporates two additional equations in the standard SST model, which use respectively such parameters as the intermittency (γ) and the momentum thickness Reynolds number ($\widetilde{Re_{\theta t}}$). The intermittency parameter is embedded in the SST k-equation and controls the production term, totally suppressing the production of k in laminar regions, thereby making the solution insensitive to the over-prediction of standard RANS turbulence models. In the transition region, it changes from 0 to 1 according to empirical production and destruction terms in the convection-diffusion equation.

The momentum thickness Reynolds number, in its turn, controls the production and destruction of the intermittency via a series of local empirical correlations. The convection-diffusion equation which is being solved for this parameter mainly matches the near-wall values of $\widetilde{Re_{\theta t}}$ with its freestream values obtained from the correlations. Therefore, using the general approximations for the transitional criteria one can solve very different cases of transition flow, which is why this model is the most reliable and popular amongst the others.

The intermittency equation is formulated as follows:

$$\frac{\partial \gamma}{\partial t} + \frac{\partial u_j \gamma}{\partial x_j} = P_{\gamma 1} - E_{\gamma 1} + P_{\gamma 2} - E_{\gamma 2} + \frac{\partial}{\partial x_j} \left[\left(\mu + \frac{\mu_t}{\sigma_f} \right) \frac{\partial \gamma}{\partial x_j} \right] \quad (\text{D.14})$$

The transition sources for this equation are the functions $P_{\gamma 1}$ and $E_{\gamma 1}$ where $E_{\gamma 1}$ is itself a function of $P_{\gamma 1}$. They define the transition onset position via the empirical functions as well as the transition region length. The values of these functions (and of the intermittency therefore) depend on the momentum thickness Reynolds number, which is solved by the equation (D.15).

The functions $P_{\gamma 2}$ and $E_{\gamma 2}$ are the destruction/relaminarization sources. They ensure that the intermittency will remain zero in the laminar zones or trigger the

possible relaminarization.

The boundary condition for γ should be established equal to one on all inlet and freestream boundaries. In terms of the solid walls the appropriate condition is the zero wall flux. For the outlet boundaries it is also recommended to use zero-gradient condition.

The momentum thickness Reynolds number is determined by the equation:

$$\frac{\partial \widetilde{Re_{\theta t}}}{\partial t} + \frac{\partial u_j \widetilde{Re_{\theta t}}}{\partial x_j} = P_{\theta t} + \frac{\partial}{\partial x_j} \left[\sigma_{\theta t} (\mu + \mu_t) \frac{\partial \widetilde{Re_{\theta t}}}{\partial x_j} \right] \quad (\text{D.15})$$

The source term $P_{\theta t}$ forces the transported scalar $\widetilde{Re_{\theta t}}$ to match its local value calculated from the empirical correlation outside the boundary layer. The boundary conditions for this scalar at the inlet is defined from the empirical correlation based on the turbulence intensity ([75]). For the walls one typically uses zero wall flux as well as for the outlets.

As about the numerical schemes, this model proves itself to be stable with the second-order upwind convection schemes, which are recommended in the thesis of its creator [76] and are used in the current work. For the diffusion terms the second-order linear scheme is the best option.

The model was validated on two test cases on a flat plate with two types of laminar -turbulent transition. The first one was the ERCOFTAC test case [77] and the second one case represents the Shubauer & Klebanoff experiment [78]. The results of the validation prove that the numerical model developed by Langtry and Menter can accurately predict the character of the flow with laminar/turbulent transition.

D.3 Numerical Model

The numerical model for the investigation of the aerodynamic loading of the SD7003 airfoil was constructed using the various open-source platforms which permit to construct the complete chain of numerical modeling.

The geometry sketch and the computational mesh were constructed via the SALOME platform. The numerical model as well as its solution were carried out via the OpenFOAM code with the implemented turbulence model which was described previously (section D.2).

The present section describes the computational meshes used in the calculations, the boundary conditions and the numerical schemes applied for the computation.

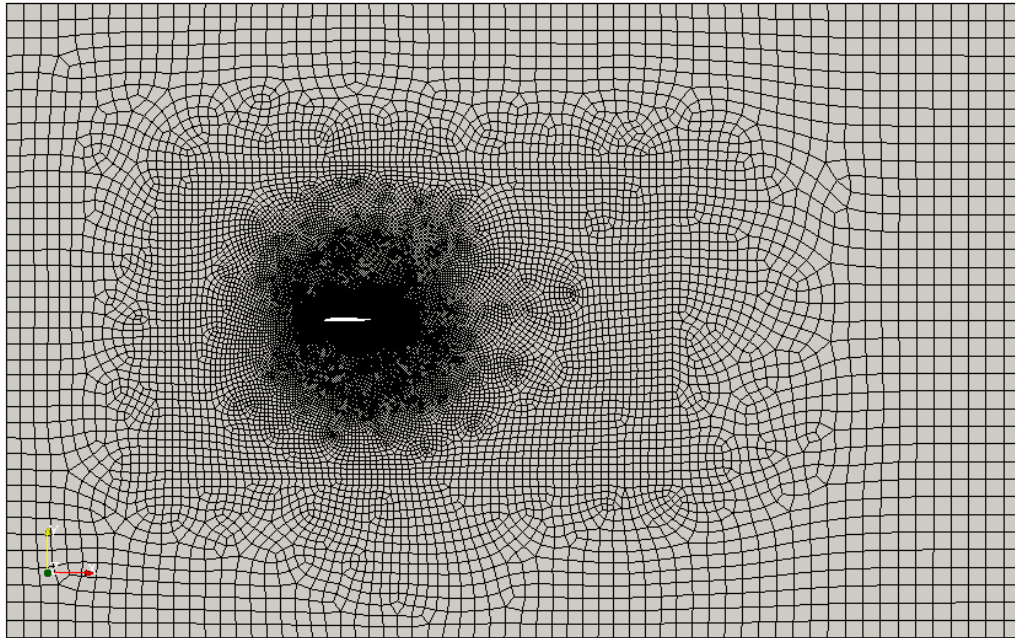
D.3.1 Computational Mesh

The mesh was constructed in SALOME and was different for the freestream case and the case with nozzle. In both cases the main purpose in the mesh construction was to ensure an acceptable compromise between the numerical accuracy and the overall mesh size. For this reason the mesh for the freestream case was constructed as hexahedral-dominant due to the simplicity of the geometry, and the second was constructed purely tetrahedral with prism layers in the region around the solid walls. The refinement of the domain for both cases was performed by different regions of interest, notably leading and trailing edge regions, wake region etc.

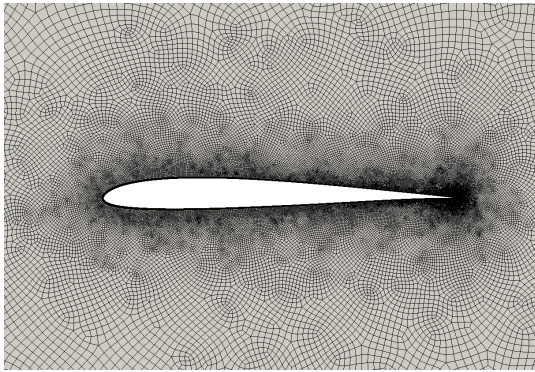
The freestream mesh is presented in figure D.3. The same pattern was used for the construction of different positions of the airfoil. The average mesh size was ≈ 66000 cells and ≈ 132000 points. For the modeling of the boundary layer 10 cell layers with a growth ratio of 1.2 were used, the Y^+ value was maintained below 1.

For the configuration with nozzle a different method of mesh construction was used in order to provide better mesh flexibility to the domain structure. This new configuration required sufficient mesh refinement not only in the region around the airfoil but also around the nozzle lips and in the wake region below and above the airfoil. In this case the mesh consisted of tetrahedrals and the boundary cells were prisms (see figure D.4). The mesh contained ≈ 39000 tetrahedrals and ≈ 87000 prisms (≈ 126000 cells in total), with 15 layers and the growth ratio of 1.1 in the boundary layers. The value of Y^+ was maintained below 0.5 due to the turbulence model requirements obtained after model validation.

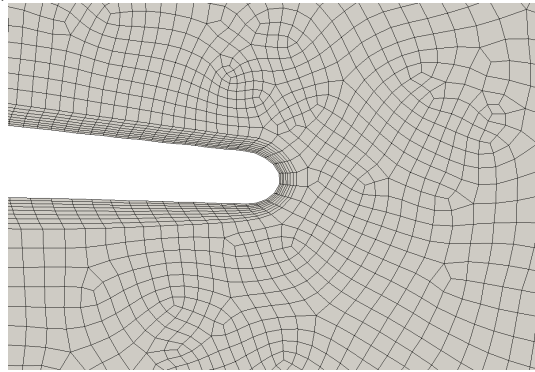
The meshes have one cell extent in the third direction due to the pseudo-3D character of the simulation.



(a)

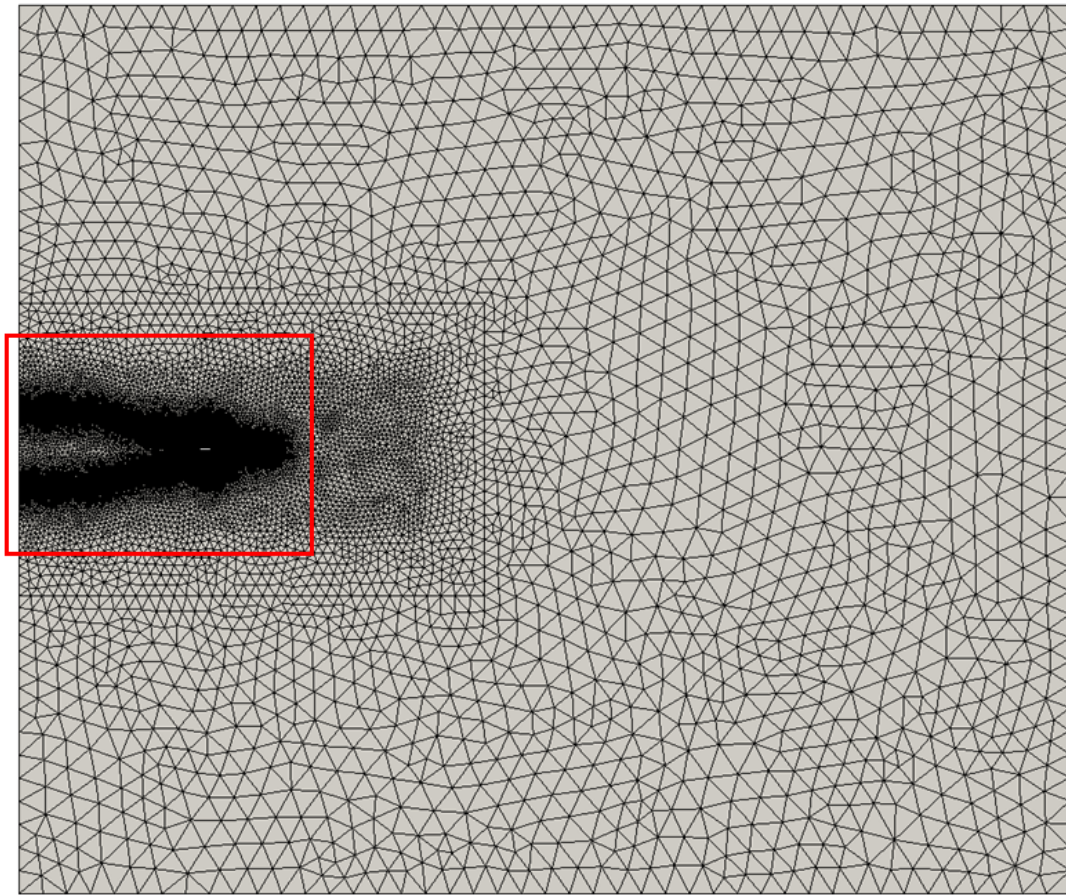


(b)

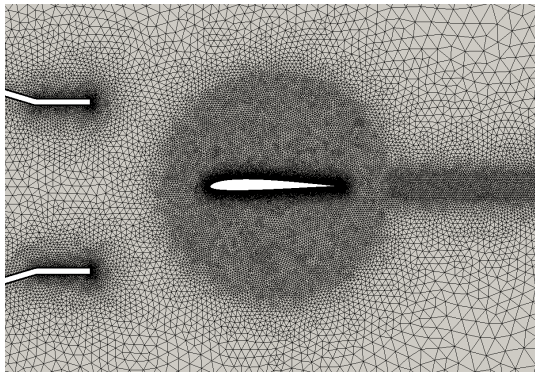


(c)

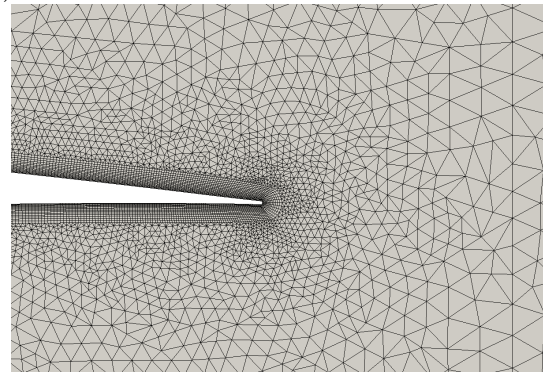
Figure D.3: (a) Computational mesh for the freestream case. Mesh views of the freestream case: (b) around the airfoil, (c) zoom around the trailing edge.



(a)



(b)



(c)

Figure D.4: (a) Computational mesh for the configuration with nozzle. Mesh views of the nozzle-flow case: (b) Mesh around the airfoil, (c) Mesh around the trailing edge.

D.3.2 Boundary Conditions

The airfoil was calculated at $Re_c = 1.26 \times 10^5$ and the angles of attack presented in the table D.1.

Table D.1: Summary of the OpenFOAM computational cases.

Configuration	Angles of attack					
Freestream	-1°	0°	+1°	+2°	+5°	+7°
Open-jet		0°		+2°	+5°	

The boundary conditions used for the simulations were different between the freestream case and the nozzle configuration. For the freestream, the uniform inlet flow with the zero-gradient slip conditions at the side boundaries was imposed in a combination with zero-gradient and pressure conditions at the outlet.

For the nozzle configuration case, it was necessary to impose inlet conditions only in the nozzle, and the application of the boundary conditions at the side and back boundaries required a special treatment. For the outlet, due to the non-uniform flow leaving the domain (because of the limited area of the nozzle exit) the imposed outlet condition also differed from the freestream case.

The character of the flow required the application of stagnation pressure at the side and outlet boundaries with the “backflow” formulation, where the velocity vector is derived from the face-normal flux component. If the value of the flux is negative (e.g. when the pressure near the boundary is smaller compared to the applied value at the boundary) then there is a local inward flux into the domain. The flexibility of such a method is due to the local cell-face estimation of the flux and therefore, non-uniform derived condition at the boundary.

For the other variables being solved in the calculation (turbulence parameters) their “atmospheric” values were imposed in case of backflow, which were calculated from the minimum supposed value of the turbulence intensity.

As the cases were incompressible, a zero value atmospheric pressure was imposed at the outlet.

The kinetic energy of turbulence imposed at the inlet was calculated as:

$$k = \frac{3}{2} (U \cdot I)^2, \quad (\text{D.16})$$

Table D.2: The general conditions for the ECL experiment.

Inlet velocity, m/s	Tu, %	Density, kg/m^3	μ , Pa·s	μ_t/μ
16	0.08	1.21	$1.84 \cdot 10^{-5}$	1

where U is the inlet velocity and I is the turbulence intensity. The value at the wall was set to zero in order to trigger the direct calculation of the boundary layer by the turbulence model.

The turbulent dissipation frequency at the inlet was calculated from the turbulent viscosity relation (eq. D.10). Its value at the wall was computed from:

$$\omega_{wall} = 10 \frac{6\nu}{\beta_1 (\Delta d_1)^2}, \quad (D.17)$$

where β_1 is the model coefficient and Δd_1 is the first cell height.

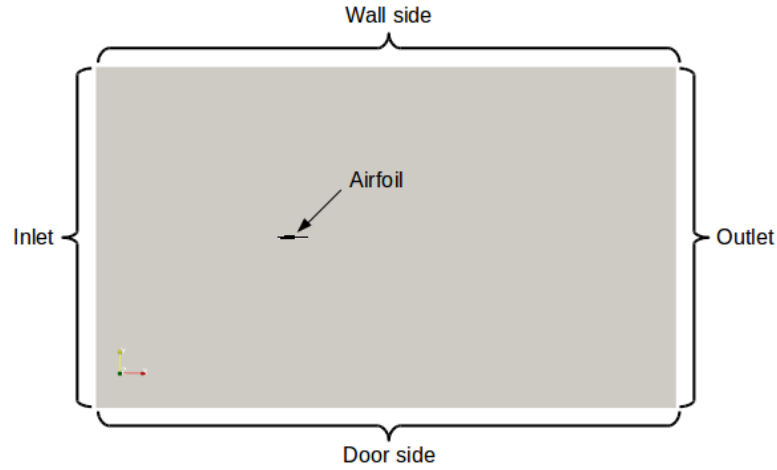


Figure D.5: Domain boundaries for the freestream case.

The boundary conditions from the figure D.5 is presented in the table D.3.

Table D.3: Boundary condition types for the freestream case.

Variable	Inlet	Door side, Wall side	Airfoil	Outlet
U	fixed value 16 m/s	zero gradient	fixed value 0 m/s	zero gradient
p	zero gradient	zero gradient	zero gradient	fixed value 0 Pa
k	fixed value $0.0002 \text{ m}^2/\text{s}^2$	zero gradient	fixed value $0 \text{ m}^2/\text{s}^2$	zero gradient
ω	fixed value 16.2 s^{-1}	zero gradient	fixed value $5.86 \cdot 10^7 \text{ s}^{-1}$	zero gradient

As said before, the nozzle configuration required somewhat different boundary conditions at the side walls and at the outlet. Instead of zero gradient conditions there was imposed an Inlet/Outlet combination (see table D.4). For the inlet, due to the convergent nozzle, one has to impose the appropriate velocity in order to obtain the necessary value at the nozzle exit. For new variables such as the intermittency and the momentum thickness Reynolds number the logic of the boundary conditions is the same as described in section D.2.

The general conditions for the second configuration are the same as for the freestream (table D.2). The domain schematic is presented in figure D.6.

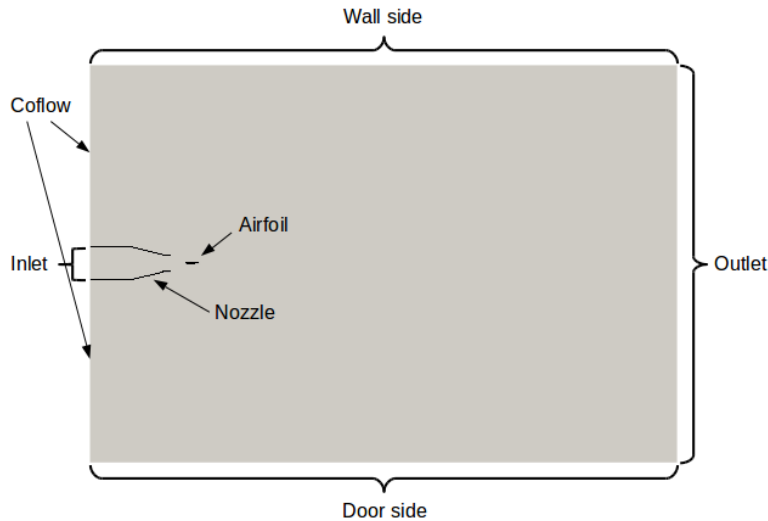


Figure D.6: Domain boundaries for the nozzle case.

Table D.4: Boundary condition types for the case with nozzle (for Inlet/Outlet the influx value is showed).

Variable	Inlet	Door side, Wall side	Airfoil, Nozzle	Coflow	Outlet
U	fixed value 8 m/s	Inlet/Outlet	fixed value 0 m/s	fixed value 0 m/s	Inlet/Outlet
p	zero gradient	fixed value 0 Pa	zero gradient	zero gradient	fixed value 0 Pa
k	fixed value $0.0001 \text{ m}^2/\text{s}^2$	Inlet/Outlet $1 \cdot 10^{-5} \text{ m}^2/\text{s}^2$	fixed value $0 \text{ m}^2/\text{s}^2$	fixed value $0 \text{ m}^2/\text{s}^2$	Inlet/Outlet $1 \cdot 10^{-5} \text{ m}^2/\text{s}^2$
ω	fixed value 5.7 s^{-1}	Inlet/Outlet 10^{-3} s^{-1}	fixed value $2.3 \cdot 10^7 \text{ s}^{-1}$	fixed value $2.3 \cdot 10^7 \text{ s}^{-1}$	Inlet/Outlet 10^{-3} s^{-1}
γ	fixed value 1	Inlet/Outlet 1	zero gradient	zero gradient	Inlet/Outlet 1
$\widetilde{Re_{\theta t}}$	fixed value 1160	Inlet/Outlet 20	zero gradient	zero gradient	Inlet/Outlet 20

D.3.3 Discretization Schemes

In terms of the discretization, the spatial and temporal terms of equations (D.1 - D.2) solved with the current numerical model were calculated with different orders of approximation:

- Divergence terms - second-order TVD scheme with van Leer limiter [79];
- Laplacian terms - second-order linear scheme;
- Temporal terms - first-order Euler scheme.

The distinction between the spatial and temporal terms was made due to the absence of the necessity to calculate high-order temporal variations of solved parameters like it is necessary in aeroacoustic simulations. For this type of expectations the first-order discretization along with a small time step ($CFL < 5$) give acceptable results without excessive computational costs.

Bibliography

- [1] Paterson, R. W., Vogt, P. G., Fink, M. R., and Munch, C. L., “Vortex noise of isolated airfoils,” *Journal of Aircraft*, Vol. 10, No. 5, 1973, pp. 296–302.
- [2] Arbey, H. and Bataille, J., “Noise generated by airfoil profiles placed in a uniform laminar flow,” *Journal of Fluid Mechanics*, Vol. 134, 1983, pp. 33–47.
- [3] Lowson, M., Fiddes, S., and Nash, E., “Laminar Boundary Layer Aeroacoustic Instabilities,” *32nd Aerospace Sciences Meeting and Exhibit*, No. 94-0358, 1994.
- [4] Arcondoulis, E., Doolan, C., and Zander, A., “Airfoil noise measurements at various angles of attack and low Reynolds number,” *Proceedings of ACOUSTICS*, 2009, pp. 23–25.
- [5] Tam, C. K., “Discrete tones of isolated airfoils,” *The Journal of the Acoustical Society of America*, Vol. 55, No. 6, 1974, pp. 1173–1177.
- [6] Longhouse, R. E., “Vortex shedding noise of low tip speed, axial flow fans,” *Journal of sound and vibration*, Vol. 53, No. 1, 1977, pp. 25–46.
- [7] Chong, T., Joseph, P., and Kingan, M., “An investigation of airfoil tonal noise at different Reynolds numbers and angles of attack,” *Applied Acoustics*, Vol. 74, No. 1, 2013, pp. 38–48.
- [8] Pröbsting, S., *Airfoil Self-Noise. Investigation with Particle Image Velocimetry*, Ph.D. thesis, Delft University of Technology, 2015.

- [9] Nguyen, L., Golubev, V., Mankbadi, R., Yakhina, G., Roger, M., and Visbal, R. M., “A Summary of High-Fidelity Numerical Studies of Flow Acoustic Resonant Interaction in Transitional Airfoils.” *22nd AIAA/CEAS Aeroacoustics Conference*, No. 2016-3030, Lyon, May 2016.
- [10] Galbraith, M. C. and Visbal, M. R., “Implicit large eddy simulation of low-reynolds-number transitional flow past the SD7003 airfoil,” *40th Fluid Dynamics Conference and Exhibit*, 28 June - 1 July 2010, Chicago, Illinois.
- [11] Hersh, A. S. and Hayden, R. E., “Aerodynamic sound radiation from lifting surfaces with and without leading-edge serrations,” *NASA CR-114370*, Vol. 197, No. 1, 1971.
- [12] Nash, E., Lowson, M., and McAlpine, A., “Boundary-layer instability noise on aerofoils,” *Journal of Fluid Mechanics*, Vol. 382, 1999, pp. 27–61.
- [13] Arcondoulis, E. J., Doolan, C. J., Zander, A. C., and Brooks, L. A., “An experimental investigation of airfoil tonal noise caused by an acoustic feedback loop,” *Proceedings of ACOUSTICS*, 2013.
- [14] Ffowcs Williams, J. and Hall, L., “Aerodynamic sound generation by turbulent flow in the vicinity of a scattering half plane,” *Journal of Fluid Mechanics*, Vol. 40, No. 04, 1970, pp. 657–670.
- [15] Amiet, R. K., “Noise due to Turbulent Flow Past a Trailing-Edge,” *Journal of Sound and Vibration*, Vol. 43, No. 3, 1976, pp. 387–393.
- [16] Howe, M., “A review of the theory of trailing edge noise,” *Journal of Sound and Vibration*, Vol. 61, No. 3, 1978, pp. 437–465.
- [17] Roger, M. and Moreau, S., “Back-scattering correction and further extensions of Amiet’s trailing-edge noise model. Part 1: theory,” *Journal of Sound and Vibration*, Vol. 286, No. 3, 2005, pp. 477–506.
- [18] Moreau, S. and Roger, M., “Back-scattering correction and further extensions of Amiet’s trailing-edge noise model. Part II: Application,” *Journal of Sound and Vibration*, Vol. 323, No. 1, 2009, pp. 397–425.
- [19] Roger, M. and Moreau, S., “Extensions and limitations of analytical airfoil broadband noise models,” *International Journal of Aeroacoustics*, Vol. 9, No. 3, 2010, pp. 273–306.
- [20] Desquesnes, G., Terracol, M., and Sagaut, P., “Numerical Investigation of the Tone Noise Mechanism over Laminar Airfoils,” *Journal of Fluid Mechanics*, Vol. 591, 2007, pp. 155–182.

- [21] Sandberg, R. and Jones, L., “Direct numerical simulations of airfoil self-noise,” *Procedia Engineering*, Vol. 6, 2010, pp. 274–282.
- [22] Jones, L. and Sandberg, R., “Numerical Investigation of Tonal Airfoil Self-Noise Generated by an Acoustic Feedback-Loop,” *AIAA 2010-3701*.
- [23] Tam, C. K. and Ju, H., “Aerofoil tones at moderate Reynolds number,” *Journal of Fluid Mechanics*, Vol. 690, 2012, pp. 536–570.
- [24] Padois, T., Laffay, P., Idier, A., and Moreau, S., “Detailed Experimental Investigation of the Aeroacoustic Field around a Controlled-Diffusion Airfoil,” *21st AIAA/CEAS Aeroacoustics Conference*, , No. 2015-2205, Dallas, June 2015.
- [25] Brooks, T. F., Pope, D. S., and Marcolini, M. A., “Airfoil Self-Noise and Prediction,” Tech. rep., 1989.
- [26] McAlpine, A., Nash, E., and Lowson, M., “On the generation of discrete frequency tones by the flow around an aerofoil,” *Journal of Sound and Vibration*, Vol. 222, No. 5, 1999, pp. 753–779.
- [27] Arcondoulis, E., Doolan, C., J., Zander, A., and Brooks, L., “A review of trailing edge noise generated by airfoils at low to moderate reynolds number,” *Acoustics Australia*, Vol. 38, No. 3, 2010, pp. 129–133.
- [28] Inasawa, A., Kamijo, T., and Asai, M., “Generation mechanism of trailing-edge noise of airfoil at low Reynolds numbers,” *Proceedings of the 13th Asian Congres of Fluid Mechanics*, 2010.
- [29] Pröbsting, S., Scarano, F., and Morris, S., “Regimes of tonal noise on an airfoil at moderate Reynolds number,” *Journal of Fluid Mechanics*, Vol. 780, 2015, pp. 407–438.
- [30] Plogmann, B., Herrig, A., and Würz, W., “Experimental investigations of a trailing edge noise feedback mechanism on a NACA 0012 airfoil,” *Experiments in fluids*, Vol. 54, No. 5, 2013, pp. 1–14.
- [31] Golubev, V. V., Nguyen, L., Roger, M., and Visbal, M. R., “On interaction of airfoil leading and trailing edge noise sources in turbulent flow,” *17th AIAA/CEAS Aeroacoustics Conference*, No. 2011-2859, Portland OR, June 2011.
- [32] Pröbsting, S., Serpieri, J., and Scarano, F., “Experimental investigation of aerofoil tonal noise generation,” *Journal of Fluid Mechanics*, Vol. 747, 2014, pp. 656–687.

- [33] Archibald, F. S., “The Laminar Boundary Layer Instability Excitation of an Acoustic Resonance,” *Journal of sound and vibration*, Vol. 38, No. 1, 1975, pp. 387–402.
- [34] Pröbsting, S. and Scarano, F., “Experimental investigation of isolated aerofoil noise,” *Proceedings of 21st International Congress on Sound and Vibration. Acoustical Society of China*, 2014.
- [35] Kingan, M. J. and Pearse, J. R., “Laminar boundary layer instability noise produced by an aerofoil,” *Journal of Sound and Vibration*, Vol. 322, No. 4, 2009, pp. 808–828.
- [36] Chong, T. and Joseph, P., “Ladder Structure in Tonal Noise Generated Around an Airfoil,” *JASA*, Vol. 131:46, 2012, pp. 1–7.
- [37] Chong, T. P., Joseph, P., and Gruber, M., “An experimental study of airfoil instability noise with trailing edge serrations,” *16th AIAA/CEAS Aeroacoustic Conference (31th AIAA Aeroacoustic Conference)*, Stockholm, Sweden, AIAA, Vol. 3723, 2010.
- [38] Nakano, T., Fujisawa, N., and Lee, S., “Measurement of tonal-noise characteristics and periodic flow structure around NACA0018 airfoil,” *Experiments in Fluids*, Vol. 40, No. 3, 2006, pp. 482–490.
- [39] Atassi, H., “Feedback in separated flows over symmetric airfoils,” Tech. rep., NASA Technical Memorandum 83758, 1984.
- [40] Pérennès, S., *Caractérisation des sources de bruit aérodynamique à basses fréquences de dispositifs hypersustentateurs*, Ph.D. thesis, Ecole Centrale de Lyon, 1999.
- [41] Pierce, A. D. et al., *Acoustics: an introduction to its physical principles and applications*, Acoustical Society of America Melville, NY, 1991.
- [42] Roger, M. and Pérennès, S., “Low-Frequency Noise Sources in Two-Dimensional High-Lift Devices,” *6th AIAA/CEAS Aeroacoustics Conference*, No. 2000-1972, Lahaina HI, 2000.
- [43] Corcos, G., “The structure of the turbulent pressure field in boundary-layer flows,” *Journal of Fluid Mechanics*, Vol. 18, No. 03, 1964, pp. 353–378.
- [44] Stewart, G., “Acoustic Transmission with a Helmholtz Resonator or an Orifice as a Branch Line,” *Physical Review*, Vol. 27, No. 4, 1926, pp. 487.

- [45] Anderson, J. D. J., *Fundamentals of aerodynamics*, McGraw-Hill Higher Education, 3rd ed., 1985.
- [46] Bailly, C. and Comte-Bellot, G., “Turbulence (CNRS éditions),” *Sciences et techniques de l’ingénieur*, 2003.
- [47] Choudhury, A. A. S., Shah, S. L., and Thornhill, N. F., *Diagnosis of process nonlinearities and valve stiction: data driven approaches*, Springer Science & Business Media, 2008.
- [48] Kim, Y. C. and Powers, E. J., “Digital bispectral analysis and its applications to nonlinear wave interactions,” *Plasma Science, IEEE Transactions on*, Vol. 7, No. 2, 1979, pp. 120–131.
- [49] Soreefan, S., *Contribution à l’étude des bruits auto-entretenus créés par un jet confiné rencontrant un obstacle*, Ph.D. thesis, 1993.
- [50] Stern, F., Muste, M., Beninati, M.-L., and Eichinger, W., E., “Summary of Experimental Uncertainty Assessment Methodology with Example,” Tech. rep., Iowa Institute of Hydraulic Research, 1999.
- [51] Moreau, S., Henner, M., I. G., Wang, M., and Roger, M., “Analysis of Flow Conditions in Freejet Experiments for Studying Airfoil Self-Noise,” *AIAA journal*, Vol. 41, No. 10, 2003, pp. 1895–1905.
- [52] Kingan, M. J., *Aeroacoustic Noise Produced by an Aerofoil*, Ph.D. thesis, University of Canterbury Christchurch, New Zealand, July 2005.
- [53] Goldstein, M. E., “Scattering of acoustic waves into Tollmien-Schlichting waves by small streamwise variations in surface geometry,” *Journal of Fluid Mechanics*, Vol. 154, 1985, pp. 509–529.
- [54] Mankbadi, R. R., “Dynamics and control of coherent structure in turbulent jets,” *Applied Mechanics Reviews*, Vol. 45, No. 6, 1992, pp. 219–248.
- [55] Padois, T., Laffay, P., Idier, A., and Moreau, S., “Tonal noise of a controlled-diffusion airfoil at low angle of attack and Reynolds number,” *The Journal of the Acoustical Society of America*, Vol. 140, No. 1, 2016, pp. EL113–EL118.
- [56] Yakhina, G., Roger, M., Jondeau, E., Golubev, V., and Nguyen, L., “Parametric Investigations of Tonal Trailing-Edge Noise Generation by Moderate Reynolds Number Airfoils. Part I Experimental Studies,” *15th AIAA Aviation Technology, Integration and Operation Conference*, No. 2015-2527, Dallas, June 2015.

- [57] Golubev, V., Nguyen, L., Hyner, W., Sansone, M., Salehian, S., Mankbadi, R., Yakhina, G., and Roger, M., “Parametric Investigations of Tonal Trailing-Edge Noise Generation by Moderate Reynolds Number Airfoils. Part II Numerical Studies,” *15th AIAA Aviation Technology, Integration and Operation Conference*, No. 2015-2528, Dallas, June 2015.
- [58] Visbal, M. R. and Gaitonde, D. V., “On the use of higher-order finite-difference schemes on curvilinear and deforming meshes,” *Journal of Computational Physics*, Vol. 181, No. 1, 2002, pp. 155–185.
- [59] Lele, S. K., “Compact finite difference schemes with spectral-like resolution,” *Journal of computational physics*, Vol. 103, No. 1, 1992, pp. 16–42.
- [60] Golubev, V. V., Nguyen, L., Mankbadi, R. R., Roger, M., and Visbal, M. R., “On Flow-Acoustic Resonant Interactions in Transitional Airfoils,” *International Journal of Aeroacoustics*, Vol. 13, No. 1, 2014, pp. 1–38.
- [61] Mankbadi, R. R., Wu, X., and Lee, S. S., “A critical-layer analysis of the resonant triad in boundary-layer transition: nonlinear interactions,” *Journal of Fluid Mechanics*, Vol. 256, 1993, pp. 85–106.
- [62] Tam, C. K. and Yu, J. C., “Trailing edge noise,” *American Institute of Aeronautics and Astronautics Paper*, , No. 75-489, 1975.
- [63] Tam, C. and Reddy, N., “Sound generated in the vicinity of the trailing edge of an upper surface blown flap,” *Journal of Sound and Vibration*, Vol. 52, No. 2, 1977, pp. 211–232.
- [64] Brooks, T. F. and Hodgson, T. H., “Trailing edge noise prediction from measured surface pressures,” *Journal of sound and vibration*, Vol. 78, No. 1, 1981, pp. 69–117.
- [65] Schlinker, R. H. and Amiet, R. K., “Helicopter rotor trailing edge noise,” *AIAA, Astrodynamics Specialist Conference*, Vol. 1, 1981.
- [66] Olson, D. A., Katz, A. W., Naguib, A. M., Koochesfahani, M. M., Rizzetta, D. P., and Visbal, M. R., “On the challenges in experimental characterization of flow separation over airfoils at low Reynolds number,” *Experiments in fluids*, Vol. 54, No. 2, 2013, pp. 1–11.
- [67] Yakhina, G., Roger, M., Kholodov, P., Nguyen, L., and Golubev, V., “An Integrated Study of Laminar Separation Bubble Effect on Tonal Noise Generation in Transitional Airfoils,” *22nd AIAA/CEAS Aeroacoustics Conference*, No. 2016-3022, Lyon, May 2016.

- [68] *OpenFOAM User Guide*, <https://openfoam.com/documentation/user-guide/>, 2015.
- [69] Menter, F., “Two-Equation Eddy-Viscosity Turbulence Models for Engineering Applications,” *AIAA Journal*, Vol. 32, No. 8, August 1994.
- [70] Menter, F., Kuntz, M., and Langtry, R., “Ten Years of Industrial Experience with the SST Turbulence Model,” *Turbulence, Heat and Mass Transfer 4*, 2003, pp. 625–632.
- [71] Hosseinverdi, S. and Boroomand, M., “Prediction of Laminar-Turbulent Transitional Flow over Single and Two-Element Airfoils,” *40th Fluid Dynamics Conference and Exhibit*, 28 June - 1 July 2010, Chicago, Illinois.
- [72] Walters, D. K. and Cokljat, D., “A Three-Equation Eddy-Viscosity Model for Reynolds-Averaged NavierStokes Simulations of Transitional Flow,” *Journal of Fluids Engineering*, Vol. 130, December 2008.
- [73] Menter, F., Langtry, R., Suzen, Y., and Huang, P., “A Correlation-Based Transition Model Using Local Variables Part I: Model Formulation,” *Journal of Turbomachinery*, Vol. 128, July 2006.
- [74] Menter, F., Langtry, R., Suzen, Y., and Huang, P., “A Correlation-Based Transition Model Using Local Variables Part II: Test Cases and Industrial Application,” *Journal of Turbomachinery*, Vol. 128, July 2006.
- [75] Langtry, R. and Menter, F. R., “Correlation-Based Transition Modeling for Unstructured Parallelized Computational Fluid Dynamics Codes,” *AIAA Journal*, Vol. 47, No. 12, December 2009.
- [76] Langtry, R. B., *A Correlation-Based Transition Model using Local Variables for Unstructured Parallelized CFD codes*, Ph.D. thesis, Universitt Stuttgart, May 2006.
- [77] Savill, A. M., “Some Recent Progress in the Turbulence Modelling of By-pass Transition,” *Near-Wall Turbulent Flows*, R. M. C. So, C. G. Speziale, and B. E. Launder, eds. Elsevier, New York, 1993, pp. 829.
- [78] Schubauer, G. B. Klebanoff, P. S., “Contribution on the Mechanics of Boundary Layer Transition,” Tech. Rep. 3489, NACA, 1955.
- [79] van Leer, B., “Towards the ultimate conservative difference scheme II. Monotonicity and conservation combined in a second order scheme,” *J. Comp. Phys.*, Vol. 14, No. 4, 1974, pp. 361–370.

AUTORISATION DE SOUTENANCE

Vu les dispositions de l'arrêté du 25 mai 2016,

Vu la demande du Directeur de Thèse

Monsieur M. ROGER

et les rapports de

M. Y. GERVAIS

Professeur - Université de Poitiers - Ecole Nationale Supérieure d'Ingénieurs de Poitiers
(ENSIP) - Laboratoire Pprime - UPR 3346 - 11 bd Pierre et Marie Curie - sp2mi-Téléport 2
86962 FUTUROSOCPE cedex

et de

M. R. MANKBADI

Professeur - Aerospace Engineering Dpartment - Embry-Riddle Aeronautical University
600 S. Clyde Morris Blvd - Daytona Beach FL 32114 - Etats-Unis

Madame YAKHINA Gyuzel

est autorisée à soutenir une thèse pour l'obtention du grade de **DOCTEUR**

Ecole doctorale MECANIQUE, ENERGETIQUE, GENIE CIVIL ET ACOUSTIQUE

Fait à Ecully, le 25 janvier 2017

P/Le directeur de l'E.C.L.
La directrice des Etudes

